TECHNISCHE
UNIVERSITÄT
DARMSTADT

Graduate School of
Energy Science
and Engineering

Degradation studies of Me-N-C catalysts for the Oxygen Reduction Reaction in Fuel Cells.

A dissertation submitted in partial fulfilment of the requirements for the degree of
Doktor-Ingenieur (Dr.-Ing.) at the Department of Material and Earth Sciences,
Technische Universität Darmstadt

Submitted by Ioanna Martinaiou (born in Athens, Greece)

catalysts
&
electrocatalysts

Dissertation approved by
Supervisor: Prof. Dr. Ulrike I. Kramm
Co-supervisor: Prof. Dr. Alessandro H. A. Monteverde Videla
Darmstadt, May 2018
D17

Degradation studies of Me-N-C catalysts for the Oxygen Reduction Reaction in Fuel Cells.

Department of Material and Earth Sciences,
Technische Universität Darmstadt

Dissertation submitted by Ioanna Martinaiou (born in Athens, Greece)

1. Report: Prof. Dr. Ulrike I. Kramm
2. Report: Prof. Dr. Alessandro H. A. Monteverde Videla

Date of thesis submission: 15 May 2018
Date of examination: 25 June 2018

Darmstadt, May 2018, D17

Martinaiou, Ioanna
Degradation studies of Me-N-C catalysts for the Oxygen Reduction Reaction in Fuel Cells
Darmstadt, Technische Universität Darmstadt
Year thesis published in TUprints: 2019
Date of the viva voce: 25.06.2018

Board of examiners

Supervisor: Prof. Dr. Ulrike I. Kramm

Co-supervisor: Prof. Dr. Alessandro H. A. Monteverde Videla

Examiner: Prof. Dr. Robert W. Stark

Examiner: Prof. Dr. Wolfram Jaegermann

Declaration

I hereby declare that the presented dissertation is based on original research and is the result of my own work. I certify that this dissertation contains no material which has been accepted for the award of any other degree in my name, in any university or other tertiary institution and, to the best of my knowledge and belief, contains no material previously published or written by another person, except where due reference has been made in the text.

Darmstadt, 15 May 2018

Martinaiou Ioanna

Acknowledgements

The work described in this thesis was carried out at the Graduate School of Excellence Energy Science and Engineering at the Technische Universität (TU) Darmstadt with financial support by the German Research Foundation (DFG) within the Excellence Initiative.

I would like to express my deepest gratitude to Prof. Dr. Ulrike Ingrid Kramm for supervising my thesis and for her scientific contribution during my PhD studies. Her critics have strongly motivated me and helped me to find and improve crucial aspects.

I furthermore thank Prof. Dr Alessandro H. A. Monteverde Videla for kindly accepting to be second reviewer and for the time he invested. I appreciate his time and scientific contribution during my research stay in Politechnico di Torino.

I would also like to thank Prof. Dr. Robert Stark and Prof. Dr. Wolfram Jaegermann for reading and evaluating my thesis. Especially, Prof. Dr. Robert Stark for letting me use the Raman microscope for the needs of my experiments during my Phd.

I would like to thank Prof. Dr. Oliver Clemens for giving me the opportunity to perform BET measurements in his laboratories.

I would like to thank Prof. Specchia for accepting me in her group in Politechnico di Torino for a Research Stay Abroad and for the nice collaboration.

Special thanks to all the ECat group, Natascha, Alish, David, Stephan, Markus, Stephen, Charlotte, Carolin, Lingmei, Sven, Pascal, Alex and Arne for a nice working time, for their input in many experiments, for the discussions, for their support during my writing process and for the many nice evenings we spend all together. It is my pleasure to work with you people! I will miss you.

Especially I would like to thank Alish and Natascha for the XPS experiments, Stephan for the Mössbauer experiments, Markus for TEM and David for BET measurements. Carolin Wittich for SEM images and Sebastian Clemenz for the nice discussions and XRD measurements.

I would like to thank also Frau Vera Becker and Dr. Tanja Drobek from the Graduate School for their support and time spent on my many questions.

I would like to thank also the people from the PhD Committee, Alish, Luis, Julian, Jan and Kristina for the organization of several events, the discussions and the nice time we spent all together in the closed meetings and in our meetings.

I would like to thank my out-of-work friends from Darmstadt, which I met during these three years, Dastin, Fre, Hedwig and the "Innerste Circle" who accepted me as a new member and spend such a nice time almost every Wednesday in the Mädelsabend, Annika, Denise, Anke, Angie, Steffi, Vicky, Anna, Kathrin and Vanessa. Thank you, it is a great pleasure to spend time with you! I would also like to thank Yann who tried to motivate me for out-of-work activities.

Last but not least my family and friends from Greece. My family, I am proud of having such great parents Kostas and Eleni Martinaiou and such a great sister Maria Martinaiou that provided me with unconditional love and support for all my life. My ”second” family I would also like to thank, Dimitra, Panagiotis, Aggelos and Alexandros with his own family now Georgia and Danai, for their support, all the discussions and welcoming in the airport. My friends from Greece, Tzoan, Ismini, Faih, Stavroula, Sandra, Maria and Virginia for supporting me all these years, for long skype calls, for the discussions serious and funny and mostly I want to thank you for all our memories and that you are in my life.

Abstract

The increasing demand for renewable energy along with the requirement of decreasing CO_2 emissions is a major challenge for the scientific community.

Fuel cells are among the most promising electrochemical devices because of their low operating temperature and high power density. The main advantage of a fuel cell is that electrical power can be produced continuously as long as the fuel supply is provided. Another important advantage is high efficiency. The efficiency of fuel cells is superior to that of combustion engines, particularly at low loads, which makes low-temperature fuel cells (0—100 °C) attractive for automotive propulsion.

State of the art catalyst for the anode as well as the cathode is typically based on platinum-supported on carbon. However, the platinum catalyst alone would account for 38-56% of the stack cost [1]. Thus the higher efficiency, in comparison to combustion engines, comes with a higher price that makes the commercialization not competitive now. As a large quantity of the precious metal is required to catalyse the oxygen reduction reaction (ORR), current research is focused on this reaction and especially on the development of alternative non-precious metal catalysts (NPMC).

In order for these catalysts to be a commercially viable solution for replacing platinum-based catalysts, they should meet two criteria, improving both activity and stability of these catalysts. Despite, several milestones that have been achieved regarding the activity of these catalysts [2– 5], stability is still relatively poor in comparison to platinum-based systems.

This dissertation focuses on the investigation of the stability of non-precious metal catalysts for oxygen reduction reaction mainly in acidic media for application in Proton Exchange Membrane Fuel Cells (PEMFCs) and Direct Methanol Fuel Cells (DMFCs). A part of this study also deals with performance determination of NPMC in alkaline media, regarding their application in Alkaline Fuel Cells (AFCs). The electrochemical tests were performed with a Rotating Disk Electrode technique. Stability refers to the ability of a system to maintain performance at constant current (or voltage) conditions, while durability refers to the ability to maintain performance following a voltage cycling.

First, a systematic study on the impact of the metal centre on durability was conducted. Thirteen Me-N-C catalysts were examined with a Start/ Stop (SSC) durability protocol in the potential range of 1.0 V – 1.5 V. Raman spectroscopy was performed before and after the durability tests and a correlation between electrochemical evaluation and Raman spectroscopy in this potential region was found.

The carbon oxidation is related to the disintegration of active MeN_4 sites that might be initiated by both: the oxidation of the surrounding graphene sheets and by a displacement of the metal out of the N_4 plane and this was evidenced by a decrease in the D_3 band.

Furthermore, a novel synthesis protocol was developed in our group and a Fe-N-C catalyst was optimized with the addition of sulfur (S) in the precursor. With respect to activity the best-off S-added catalyst and the S-free one were then examined for durability under a Load Cycle (LC) protocol (0.6 – 1.0 V) in alkaline media. A modification of both catalysts with ionic liquid (IL) was introduced by the group of Professor B. J.M. Etzold within a cooperation framework. The durability of the modified S-free catalyst was found superior to the durability of the non-modified catalyst. In the case of the S-added catalyst, the IL modification did not further improve its durability.

Finally, a third synthesis approach was developed, leading to an active Fe-N-C catalyst also with sulfur in the precursor. The stability of this catalyst was investigated in a DMFC within a research stay abroad project in collaboration with Professor S. Specchia from Politecnico di Torino and subsequently examined by post mortem Mössbauer spectroscopy. This catalyst was further evaluated with a Load Cycle durability protocol and post mortem Raman spectroscopy in our laboratories.

Included papers

PAPER I

Effect of metal species on the stability of Me-N-C catalysts during accelerated stress tests mimicking the start-up and shut-down conditions

I. Martinaiou, A. Shahraei, F. Grimm, H. Zhang, C. Wittich, S. Klemenz, S. J. Dolique, H-J Kleebe, R. W. Stark, U. I. Kramm

Electrochimica Acta 243 (2017), p.183-196

PAPER II

Influence of sulfur in the precursor mixture on the structural composition of Fe-N-C catalysts

A. Janßen, I. Martinaiou, S. Wagner, N. Weidler, A. Shahraei, U. I. Kramm

Hyperfine Interact 239: 7 (2018)

PAPER III

Improved electrochemical performance of Fe-N-C catalysts through Ionic Liquid modification in alkaline media

I. Martinaiou, T. Wolker, A. Shahraei, G-R Zhang, A. Janßen, S. Wagner, N. Weidler, R. W. Stark, B. J. M. Etzold, U. I. Kramm

Journal of Power Sources 375 (2018), p. 222-232

PAPER IV

Activity and Degradation Study of a Fe-N-C catalyst for ORR in Direct Methanol Fuel cell (DMFC)

I. Martinaiou, A.H.A. Monteverde Videla, N. Weidler, M. Kübler, D. Wallace, S. Wagner, A. Shahraei, R. W. Stark, S. Specchia, U.I. Kramm

In manuscript
Author's contributions:

Paper I is based on my work, the parts conducted by myself were: synthesis of catalysts, activity and durability characterization, as well as Raman spectroscopy. SEM, XRD and XPS measurements were conducted by co-authors. The evaluation and interpretation of SEM, XPS and XRD were carried out in co-operation with the related co-author. Theoretical calculations were conducted by a co-author. The manuscript was written by me with Professor U.I. Kramm.

Paper II is based on the work of A. Janßen during his master thesis. My contribution to this work was merely the co-supervision of the electrochemical experiments, the N_2-sorption measurements, and analysis as well as the proofreading of the manuscript.

Paper III is based on my work, the parts conducted by myself were: synthesis of catalysts, activity and durability characterization as well as Raman spectroscopy. The ionic liquid modification of the catalysts, N_2-sorption measurements, XPS, Mössbauer and FTIR spectroscopy were conducted by co-authors. This work was done within an interdisciplinary energy project including two different groups of TU Darmstadt. The manuscript was written by me with Professor U.I. Kramm.

Paper IV is based on my work, the parts conducted by myself were: synthesis of catalysts, activity and durability characterization in our laboratories, as well as activity and stability tests in a DMFC in the laboratories of Professor S. Specchia in Polytechnic di Torino, within a Research Stay Abroad project. TEM, XPS, and N_2-sorption measurements were done by co-authors. Raman spectroscopy and Mössbauer spectroscopy, measurements and analysis were conducted by me. The manuscript was written by me with Professor U.I. Kramm.

Contents

List of Figures

List of Tables

1

Introduction

1.1 Energy and the Environment

Energy plays an important role in many aspects of our lives such as water and food consumption, transportation, economic growth, land use and population growth.
In today's industrial societies, energy needs are constantly growing, and become harder to fulfill. Indicatively, the average energy consumption rate in 1980 was about 8 TW whereas in 2010 it rapidly increased to 15 TW. In Figure 1.1 the average energy consumption rate per year is shown.

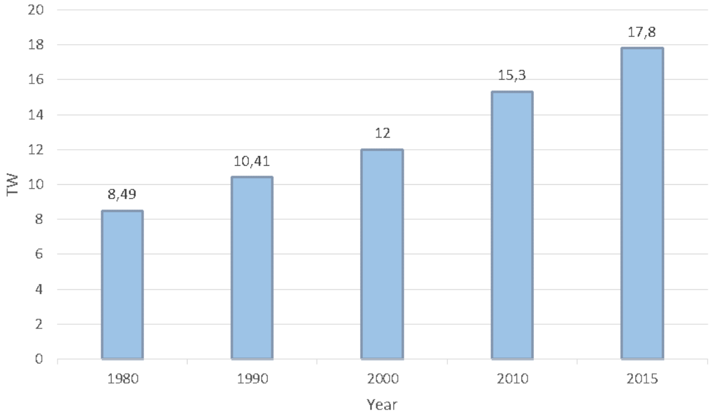

Figure 1.1: Average energy consumption rate per year [6].

Energy "production" comes mostly from the combustion of fossil fuels, and has a major impact on climate change. The increasing energy demand requires large-scale combustion of fossil fuels, which results in large quantities of carbon dioxide CO_2 released in the atmosphere. This subsequently, leads to increased greenhouse effect and consequently to global warming. Figure 1.2a and Figure 1.2b shows the global and the European CO_2 emissions per sector, respectively.

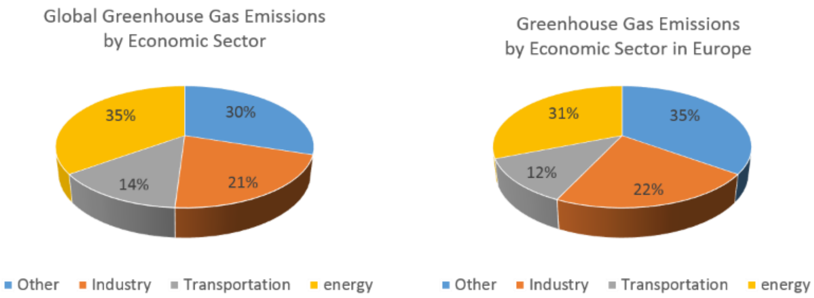

Figure 1.2: a) Scheme based on Source: [7], based on global emissions from 2010 and b) OECD 2015.

The recent Paris agreement in December 2015 among 195 countries agreed on limiting global warming to 1.5 °C , thus to prevent a global average increase of 2 °C above its pre-industrial levels [8].

The question arises on how the energy can be generated in an environmentally sustainable manner. That is, to maintain economic growth whilst providing energy security and environmental protection. J. O. Bokris in 1972 introduced the term "Hydrogen economy" which applies to the energetic, economic, ecological and societal aspects of this concept. The idea was based on converting the electrical energy delivered by nuclear stations to chemical energy, by splitting water and thereby producing hydrogen in onsite water electrolysers. After transportation to distribution stations and to final locations (houses, factories, vehicles, trains, aircrafts, etc.), the produced hydrogen would be used in an onsite fuel cell to deliver electrical energy. The advantages regarding the transportation sector were obvious: the rapidly increasing energy demand would be covered at a lower cost and without polluting the environment, while the dependence on fossil fuels would become minimal. The only drawback of this concept was the utilization of nuclear energy for the production of hydrogen via water splitting [9].

The Chernobyl accident in 1986 and the more recent accident in Fukushima in 2011 raised several concerns and alter the direction to renewable energy sources to split water and generate hydrogen [10].

The scientific community, as well as the industry counterpart, see a call to develop environmentally friendly systems, such as low ecological footprint buildings, photovoltaic systems and most recently, hydrogen-fuelled cars, buses, and other transport machinery.

In this context, the Hydrogen Council was launched at the 2017 World Economic Forum in Davos. As stated by Benoît Potier, CEO of Air Liquide: the Hydrogen Council brings together some of the world's leading industrial, automotive and energy companies with a clear ambition to explain why hydrogen emerges among the key solutions for the energy transition, in the mobility as well as in the power, industrial and residential sectors, and therefore requires the development of new strategies at a scale to support this. The goal is clearly the utilization of hydrogen as zero-carbon energy source replacing, for instance, gasoline as a transport fuel or natural gas as a heating fuel. Hydrogen is attractive because whether it is burned to produce heat or reacted with air in a fuel cell to produce electricity, the only byproduct is water.

1.2 Why Fuel Cells?

Fuel cells (FCs) are electrochemical devices that directly convert chemical energy to electrical energy. The main advantage of the fuel cell is that electrical power can be produced continuously as long as the fuel supply is provided. The major advantage of fuel cells is their high efficiency. The efficiency of fuel cells can be far superior to that of combustion engines, particularly at low loads, which makes low-temperature fuel cells (0—100 °C) attractive for urban traffic [11]. Low-temperature fuel cells are also suitable for medium-size power plants for buildings, and small-scale portable applications.

The coupling of hydrogen technology to renewable energies can be particularly fruitful. Solar and wind energies are typical examples of an irregular energy production which does not always match the energy demand. This can be avoided by storing the excess energy in the form of H_2 through water electrolysis. On demand, the H_2 can later be reconverted to electricity using fuel cells. To conclude, hydrogen could be produced anywhere where water and some source of energy coexist in order to split the water to H_2 and O_2. Fuel cells represent the most effective way to convert hydrogen into electricity. In the long-term, fuel cells will help build a sustainable production of energy only if they are fed with hydrogen, which is produced from sustainable energies.

In addition, their clean point of operation emissions, fast refuelling times and excellent energy density, render them promising for a variety of applications, the most notable of which is in the transportation sector. Hydrogen fuelled vehicles would allow to significantly cut back on the over five billion tonnes of greenhouse gas emissions (CO_2) produced by automobiles each year [12]; In addition, their high energy density can provide driving ranges of 250 miles or more, and compressed hydrogen tanks can be refilled easily in less than 5 minutes. However, for the rate of commercialization of FCs to continue to increase, three major criteria must be met concurrently: cost, performance, and durability [13].

At both the cathode and anode of a Proton Exchange Membrane Fuel Cell (PEMFC), platinum group metals (PGMs) are currently required to catalyse the desired redox reactions (hydrogen oxidation at the anode, and oxygen reduction at the cathode). As these metals are commodities and are all quite scarce, increased demand for PEMFCs will only serve to increase the price of these catalysts if the loading is not reduced significantly from current levels. Because of the sluggish kinetics of the oxygen reduction reaction (ORR) (~5 orders of magnitude slower than hydrogen oxidation kinetics) [14], the majority of the PGMs are required at the cathode. This challenge is widely recognized in the PEMFC community and has led to a strong focus on improving/ developing alternative catalysts used for the ORR at the cathode. This includes improving both the activity and utilization as well as the durability and stability of these catalysts.

1.3 Scope of the Thesis

The primary objective of this work is to investigate the degradation of Fe-N-C catalysts for Oxygen Reduction Reaction under different operation conditions. To gain more insights on the degradation mechanisms presents an indispensable basis to develop highly stable catalyst materials. Even though NPMCs for the oxygen reduction reaction have been intensively investigated in the past, the poor durability of such catalysts inevitably leads to further research.

In order to gain an improved understanding of the instability origins and the similarities/ differences of the degradation of NPMCs, electrochemical tests in Rotating Disk Electrode (RDE) under different conditions were carried out, as well as various spectroscopic techniques for the complete characterization of the NPMCs.

Firstly, we investigated NPMCs with different metal centres to unravel the effect of metal centre on the stability of these catalysts in acidic media. To the author's knowledge such investigation was not reported (with respect to stability) so far. In a next step, a novel preparation route was developed and the catalysts were further tested in alkaline media with respect to stability. Finally, in order to optimize the catalyst's structure a pure (absence of inactive species) catalyst was required. Therefore, we were able to synthesize a catalyst, free or quasi-free of inorganic species and investigate it in acidic media as well as in a Direct Methanol Fuel Cell (DMFC) with respect to stability.

The aim of this work is to gain a broader knowledge of how Fe-N-C catalysts perform in different environments (acidic, alkaline) for different fuel cell systems (PEMFCs, DMFCs, and AFCs).

2

Fuel Cells and Literature overview

2.1 Fuel Cell Principles

The idea of the fuel cell can be traced back to Sir William Grove, who is recognized as "the father of the fuel cell" [15]. In 1839 Grove found that electrolysis (using electricity to split water into hydrogen and oxygen) could be performed in reverse with the right catalyst, producing electricity. In 1842, Grove developed a stack of 50 fuel cells, which he called a "gaseous voltaic battery". However, for almost a century after Grove's discovery, the fuel cell did not make any practical progress. The next breakthrough came in the early 1960s by General Electric (GE), through the work of Thomas Grubb and Leonard Niedrach who invented the proton exchange membrane fuel cell (PEMFC) [16].

In principle, fuel cells can be divided into different types respectively to their reaction medium or their operating temperature. In this work, the focus is exclusively in low-temperature fuel cells such as proton exchange membrane fuel cells (PEMFCs) operating with hydrogen or methanol (DMFC) and alkaline fuel cells (AFCs), which are attractive for a variety of different purposes due to their efficiency, relatively low operating temperatures, and environmentally benign emissions.

The main structure of the fuel cell is independent of the fuel cell type. It consists of five different components, including a membrane which must ensure a spatial separation of the electrochemical reactions in order to prevent a direct recombination of the reactants and to avoid the formation of a short circuit, the catalyst layers for anode and cathode, to enable the half-cell reactions, the gas diffusion layers (GDLs) which sit outside the catalyst layers and facilitate transport of reactants into the catalyst layer, as well as removal of product water, and the bipolar plates (BP) which terminate the fuel cell at both the anode and cathode side and guarantee the structural integrity, electric current distribution, heat-distribution/cooling and gas supply via incorporated gas channels. The assembly of the electrodes and the membrane is referred to as membrane electrode assembly (MEA). In addition, gaskets must be added around the edges of the MEA to make a gas-tight seal [17].

2.1.1 Fuel Cell Types

Proton Exchange Membrane Fuel Cell (PEMFC)

Figure 2.1 shows a schematic representation of a Proton Exchange Membrane Fuel Cell (PEMFC). The conversion of chemical energy to electrical energy in a PEM fuel cell occurs through a direct electrochemical reaction. A PEMFC delivers high power density and offers the advantage of low weight and volume, compared to other fuel cells.

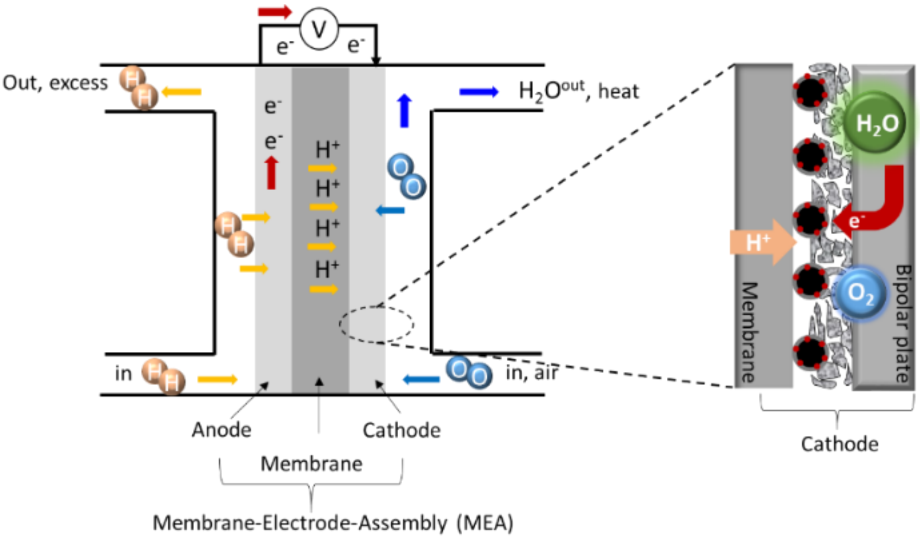

Figure 2.1: Scheme of a polymer electrolyte fuel cell and simplified structure of the cathode side of the MEA. Figure inspired by [18].

In the PEMFC, hydrogen oxidation reaction (HOR) takes place at the anode side (Equation 2.1), and oxygen reduction reaction (ORR) occurs at the cathode (Equation 2.2).

$$H_2 + 4e^- \rightarrow 4H^+ + 4e^- \qquad (E_0 = 0.00\ \text{V vs. SHE}) \tag{2.1}$$

$$O_2 + 4e^- + 4H^+ \rightarrow 2H_2O \qquad (E_0 = 1.23\ \text{V vs. SHE}) \tag{2.2}$$

$$2H_2 + O_2 \rightarrow 2H_2O \qquad (E_0 = 1.23\ \text{V vs. SHE}) \tag{2.3}$$

Following the hydrogen oxidation reaction, the generated protons will diffuse across the electrolyte membrane towards the cathode. In PEMFC systems, the electrolyte membrane is Nafion, a perfluorinated sulfonic acid membrane developed by DuPont. The state of the art for both half-cell reactions are platinum-based catalysts. However, due to ORR sluggish kinetics, the cathode requires higher loadings of the catalyst than the anode [19]. The major drawback of platinum-based catalysts is the limited availability and high cost, contributing to the overall production cost of the fuel cell system [20].

PEM fuel cells can generate power from a fraction of a watt to hundreds of kilowatts and can be used for several applications such as transportation (cars, buses with a power range of 10 to 100 kW), backup power (telecommunication systems with a power range of 2 to 10 kW) and small portable power (cell phones, laptop computers, battery replacements with a power range of 1W to 100 kW) [21].

Especially, with respect to the high energy density of hydrogen, the application of PEMFCs in the transportation sector has gained the greatest interest. In 1995, Ballard Power Systems demonstrated the first fuel cell-powered bus. Later the development of fuel cell vehicles (FCVs) continued by other companies like Honda, who have successfully demonstrated the Honda FCX Clarity in 2008 Hyundai, who presented the ix35 FCEV in 2014, and Toyota who introduced the first mass-produced fuel cell car, the Toyota Mirai in 2015.

Direct Methanol Fuel Cell (DMFC)

Direct Methanol Fuel Cells (DMFCs) are a particular type of PEMFC where methanol is used as fuel instead of hydrogen [22].

The DMFC enables the direct conversion of the chemical energy stored in the chemical bonds of methanol (CH_3OH) to electrical energy, with water and carbon dioxide as main products (Equation 2.6). At the anode, methanol is oxidized to carbon dioxide, protons, and electrons (Equation 2.4). The protons diffuse through the membrane (Nafion) to the cathode, in order to react with oxygen and the transferred electrons to water, which is also the product in the PEMFC (Equation 2.5).

$$CH_3OH + H_2O \rightarrow CO_2 + 6H^+ + 6e^- \qquad (E_0 = 0.02 \text{ V vs. SHE}) \tag{2.4}$$

$$3/2\ O_2 + 6H^+ + 6e^- \rightarrow 3H_2O \qquad (E_0 = 1.23 \text{ V vs. SHE}) \tag{2.5}$$

$$CH_3OH + 3/2\ O_2 \rightarrow CO_2 + 2H_2O \qquad (E_0 = 1.21 \text{ V vs. SHE}) \tag{2.6}$$

Compared to the more well-known H_2 -PEMFCs, DMFCs present several intriguing advantages as well as a number of challenges.

Methanol has a high energy density thus making DMFCs good candidates for small portable applications, in addition, the most important advantage is that methanol can integrate effectively with transmission and distribution systems that are already in existence [23,24].

Among the challenges for commercialization of DMFCs, the electrocatalyst holds a major part. Until now, Pt-alloyed noble metal catalysts remain the best choice for activating the methanol oxidation reaction (MOR) at the DMFC anode. When using a pure Pt catalyst, the MOR is not completely realized because of the formation and subsequent irreversible absorption of CO (poisoning of Pt). This can be limited by the addition of a second metal such as Ru, Sn, Co, Ni. For Pt-Ru catalysts, the oxophilic nature of Ru is believed to promote the formation of hydroxyl adsorbates on its surface, which can then react with carbon monoxide adsorbed on the platinum atoms [25].

At the cathode side, the replacement of Pt with non-precious Me-N-C catalysts (group of NPMC) is necessary not only because of the high cost and high loading but also because Me-N-C catalysts are unaffected by methanol crossover [26–28].

DMFCs are mostly suitable for off-grid power generation (with a power range of 10 to 75 W) or in regions with frequent power outages and portable applications including computers, notebooks, cell phones, cameras (in the power range of 5 to75 W) [21].

Demonstrations for notebooks have been developed by Toshiba, Hitachi, Panasonic, Samsung, Sanyo and LG (50–250 cm^3, 10–75 W mostly driven direct by methanol) [29].

Alkaline Fuel Cell (AFC)

Alkaline Fuel Cells which operate with an anion exchange membrane are called Anion Exchange Membrane Fuel Cells (AEMFCs) and are similar to PEMFCs in that they use hydrogen and oxygen as fuel and generate electricity through the HOR (Equation 2.6) and ORR (Equation 2.7). In contrast to PEMFCs, hydroxyl ions (OH^-) pass from the cathode towards the anode, instead of protons diffusing from anode to cathode. Rather than a polymeric membrane, AEMFCs use a liquid electrolyte of potassium hydroxide (KOH) which has a very good conductivity for hydroxyl anions (OH^-). The reactions at the anode and cathode are HOR and ORR, as in a PEMFC, but in alkaline media, the reactions are slightly different:

$$2H_2 + 4OH^- \rightarrow 4H_2O + 4e^- \qquad (E_0= 0.83 \text{ V vs. SHE}) \qquad (2.6)$$

$$O_2 + 2H_2O + 4e^- \rightarrow 4OH^- \qquad (E_0= 0.40 \text{ V vs. SHE}) \qquad (2.7)$$

$$2H_2 + O_2 \rightarrow 2H_2O \qquad (E_0= 1.23 \text{ V vs. SHE}) \qquad (2.8)$$

Famously, alkaline fuel cells were used by NASA for a number of space missions including providing power for the Shuttles. They boast a higher current density than PEMFCs and have been shown to have good performance with a very low loading of precious metal catalysts. McLean et al. [30] outlines two of the major challenges that have hindered the use of AFCs.

AEMFCs are promising on a cost basis mainly because cheap and abundant non-precious metals are viable catalysts. The kinetics of the ORR on these catalysts are faster in alkaline than in acidic media. Even metal-free electrocatalysts can reach high activity and selectivity toward ORR in alkaline media [31,32].

A major issue with AEMFCs is the membrane/ electrolyte and electrode degradation which are caused by the formation of carbonate/bicarbonate on the reaction of OH^- ions with CO_2 contamination in the oxidant gas stream [33].

Today, the Anion Exchange Membrane Fuel Cell (AEMFC) is an attractive alternative to acidic Proton Exchange Membrane Fuel Cells. This development has been supported by demonstrations of power densities almost equal to power densities achieved in PEMFCs with membranes of similar thickness and while using non-precious metal catalysts as cathodes [34].

2.1.2 PEM Fuel Cell Thermodynamics

The net reaction in a fuel cell fed with H_2 and O_2 can be described with Equation 2.9

$$H_2 + \tfrac{1}{2} O_2 \rightarrow H_2O \qquad (2.9)$$

For every mole of H_2 fuel consumed, the cell consumes ½ mole of O_2 and produces one mole of H_2O. When the oxidation and reduction reaction occur separately, two mole of electrons are generated.

The standard potential (E^0) for the H_2/O_2 cell reaction is determined by the change in Gibbs free energy (ΔG^0) of all reactants and products,

$$E^0 = -\frac{\Delta G^0}{n\,F} \qquad (2.10)$$

where n is the number of exchanged electrons (in this case, n=2) and F is Faraday's constant (96485 $C \cdot mol^{-1}$). At the typical 80 °C of an operative PEM fuel cell and a pressure of 1 atm, the formation of liquid water gives $\Delta G = -237.1\ kJ \cdot mol^{-1}$, while vapour water gives $\Delta G = -228.5\ kJ \cdot mol^{-1}$ therefore: $E^0 = 1.23$ V (25°C) and $E^0 = 1.18$ V(80°C), respectively.

To calculate electrode potentials differing from the standard conditions, the Nernst equation for the H_2/O_2 cell can be written,

$$E = E^0 + \left(\frac{RT}{nF}\right) ln\left(\frac{p_{H_2} \cdot p_{O_2}^{1/2}}{p_{H_2O}}\right) \tag{2.11}$$

where E is the cell potential at non-standard conditions, R is the gas constant (8.314 J $mol^{-1}K^{-1}$) and p the partial pressures of H_2, O_2 and H_2O in atm.

As for the system's maximum theoretical efficiency η, this is typically defined as the ratio between Gibbs free energy ΔG and enthalpy (or heating value) ΔH (reflecting the maximum extractible work)

$$\eta = \frac{\Delta G}{\Delta H} \tag{2.12}$$

At the typical operating conditions the formation of liquid water supplies ΔH = -285.8 kJ·mol^{-1} and for the formation of gas water ΔH = -241.83 kJ·mol^{-1}, the cell's theoretical (and therefore maximum) efficiency at this temperature and atmospheric pressure would be of ~ 80 and ~90%, respectively [35].

2.1.3 Deviations of the Thermodynamic potential: Overpotential

In reality, the efficiency of the PEM fuel cell is typically closer to 50% (vs. ~20% in internal combustion engines) because its operative potential E is systematically below the theoretical value E^0 estimated above. The difference between the experimentally determined electrode potential (E) for a given current density and the theoretical potential (E^0) is called overpotential (η).

$$\eta = E - E^0 \tag{2.13}$$

An operative fuel cell features three main overpotential contributions to the total voltage loss. Each one of these predominates at a different operational regime and potential / current "region" of the cell's polarization curve, as shown in Figure 2.2 [35,36].

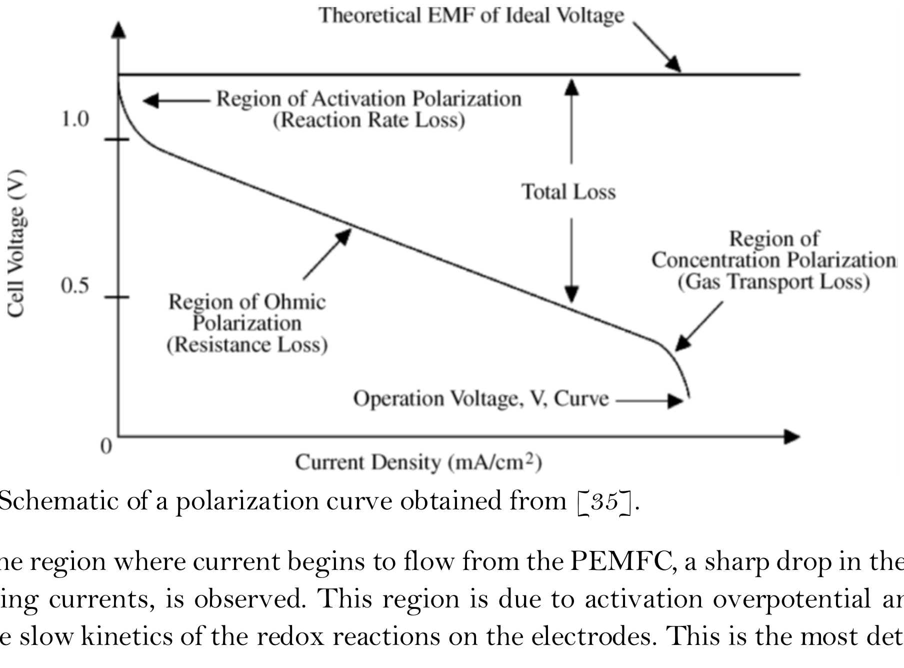

Figure 2.2: Schematic of a polarization curve obtained from [35].

Moving to the region where current begins to flow from the PEMFC, a sharp drop in the cell voltage, with increasing currents, is observed. This region is due to activation overpotential and is directly related to the slow kinetics of the redox reactions on the electrodes. This is the most detrimental and important cause of voltage drop in PEMFCs, contributed primarily by the cathode due to the very sluggish ORR kinetics in comparison to the HOR which contributes negligible losses. Using more effective catalysts with deliberately designed nanostructures can serve to overcome these irreversible voltage losses.

The region displaying a linear loss of cell voltage with increasing currents in the polarization curve provided in Figure 2.2 is due to ohmic losses. The sources of resistance in PEMFCs can arise from the polymer electrolyte/membrane, the cell connections or the bipolar plates. These issues can be mitigated by appropriate selection of materials, including electrode structures with high conductivity. Finally, at high current densities, the voltage of the PEMFC will drop off dramatically as observed in Figure 2.2. This is because the necessary electrode reactions are proceeding at a faster rate than the reactants can be delivered to the catalyst surface. Using pure reactant feeds, or increased gas pressures can help to mitigate this occurrence, but also using well-designed catalyst layer conducive to good reactant flow and accessibility will increase the current densities attainable in a PEMFC system [35,37].

Therefore, the real cell voltage can be expressed by subtracting the voltage drops caused by the various losses from the ideal thermodynamically predicted voltage [35]

$$E = E^0 - \eta_{act} - \eta_{Ohmic} - \eta_{mass} \tag{2.14}$$

Where: E: real cell voltage, E^0: thermodynamically predicted voltage of fuel cell, η_{act}: activation losses due to electrode kinetics, $\eta\mathrm{o}_{hmic}$: ohmic losses due to ionic and electronic conduction, η_{mass}: mass transport losses of reactant gases.

2.1.4 Electrode Kinetics

When current flows, a deviation from the open circuit potential occurs corresponding to the electrical work performed by the cell. The deviation from the equilibrium value is called the overpotential and has been given the symbol η. One of the reasons for the deviation of the potential from the equilibrium value is the finite rate of the reaction at the electrodes. For a redox reaction at one electrode, the current density (j) is given by the Butler-Volmer equation:

$$\mathrm{j} = \mathrm{j}_0 \left[\underbrace{\exp\left(\frac{\alpha \mathrm{nF}}{\mathrm{RT}}\eta\right)}_{\text{Anodic current}} - \underbrace{\exp\left(\frac{(1-\alpha)\mathrm{nF}}{\mathrm{RT}}\eta\right)}_{\text{Cathodic current}}\right] \tag{2.15}$$

As shown in Figure 2.3 the current density increases exponentially with a rising overpotential and the slope depends on the exchange current density j_0 as well as on the charge transfer factor α. The value of α is theoretically between 0 and 1, and most typically for the reactions on a metallic surface it is around 0.5. The value of the exchange current density depends on speed of the electrode reaction: a slow reaction will require a larger overpotential for a given current, than a fast reaction.

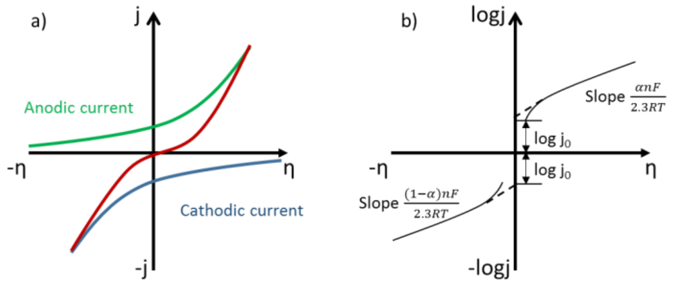

Figure 2.3: a) Graphical representation of the anodic current (green line), cathodic current (blue line) and Butler- Volmer equation (red line). b) Graphical representation of the Tafel equation with the current plotted on a logarithmic scale.

The Butler-Volmer equation is unwieldy to use in the form given in Equation 2.15. Hence it is simplified for two important cases, related to (i) large overpotentials, that is $|\eta| > 100$ mV and (ii) small overpotentials, that is $|\eta| < 10$ mV.

large overpotentials: $|\eta| > 100$ mV

$$j = j_0 \exp\left(\frac{\alpha nF}{RT}\eta\right), \quad (\eta > 0) \tag{2.16}$$

$$j = j_0 \exp\left(\frac{(1-\alpha)nF}{RT}\eta\right), (\eta < 0) \tag{2.17}$$

small overpotentials: $|\eta| < 10$ mV

$$j = j_0 \frac{nF}{RT}\eta \tag{2.18}$$

A plot of log j vs. η is called a Tafel plot. Evaluation of the slope of the linear Tafel region enables the charge transfer factor α to be evaluated, whereas the exchange current density j_0 is obtained from the intercept at $\eta = 0$ [14].

2.1.5 Issues of PEMFC Commercialization

PEM fuel cells may be more efficient and respectful to the environment than the internal combustion engines currently used in cars, but they will only represent an alternative to this well-established technology if their manufacturing cost is accordingly competitive.

Durability and cost are the primary challenges to fuel cell commercialization and must be met concurrently. As shown in Figure 2.4 the most expensive component of a fuel cell stack it is the catalyst. The high cost of Pt has been one of the major barriers to the widespread commercialization of PEMFCs.

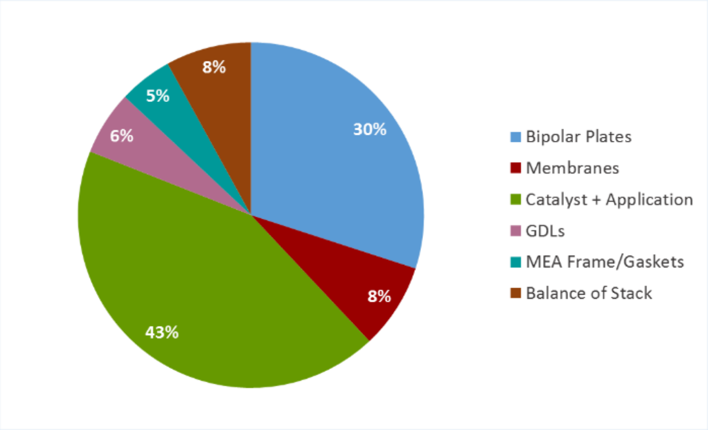

Figure 2.4: PGM Stack Cost Breakdown (500,000 systems/year) [1].

The platinum utilization status for 2015 is 0.16 g of Pt per kW as defined by the U.S. Department of Energy (U.S. DOE), whereas the target for 2020 decreases at 0.125 g of Pt per kW. Based on this target and under the assumption that all cars in the future would be powered by PEMFCs, a global annual production of 72 million (current annual automobile production) PEMFC cars rated at 50 kW each would require a steady Pt demand of 625 tons a year.

Table 2.1: Information on targets from [38].

Characteristic	Units	2015 Status	2020 Targets
Platinum group metal total content (both electrodes)	g/kW @ 150 kP (abs)	0.16	0.125
Platinum group metal (PGM) total loading (both electrodes)	mg PGM/cm^2 electrode area	0.13	0.125

In year 2017, the global platinum metal reserves is 69000 tons, and 95 % is located in South Africa [39].

In recent years, the global Pt production has only been ca. 200 tons a year [39].

Based on these numbers, it is clear that the platinum recycling rate must be very high for such a fleet to be sustainable. Under such market pressure, the platinum cost would likely rise significantly. Platinum catalyst alone would account for 38-56% of the stack cost [1].

Therefore, significant interest is shown in developing non-precious metal catalyst (NPMC) to help either reduce or eliminate the Pt in PEMFCs. Since the ORR is 5 orders of magnitude slower than the HOR, the cathode of a PEMFC typically contains 80-90% of the total Pt in the PEMFC [14,39].

2.2 Development of New Materials as Catalysts for ORR

2.2.1 Understanding of the Oxygen Reduction Reaction (ORR)

In spite of the considerable effort expended in trying to unravel the fundamental aspects of the O_2 electroreduction reaction, many details about the mechanism are not fully understood. This is due to the complexity of ORR as a four-electron transfer process, which involves the formation of different intermediates.

The electrochemical reduction of oxygen can follow two essential different pathways (direct: Equation 2.19, indirect: Equation 2.21) depending on the electrode material. The direct pathway involves the rupture of the O-O bond.

Oxygen reduction proceeds either by the direct 4-electron path (H_2O) or by the indirect 2- electron path (H_2O_2)
The direct four-electron reduction pathway:

➔ in acidic media: $O_2 + 4H^+ + 4e^- \rightarrow 2H_2O$ $E_o = 1.229$ V vs. SHE (2.19)
➔ in alkaline media: $O_2 + 2H_2O + 4e^- \rightarrow 4OH^-$ $E_o = 0.401$ V vs. SHE (2.20)

The indirect two-electron peroxide pathway:

➔ in acidic media: $O_2 + 2H^+ + 2e^- \rightarrow 2H_2O_2$ $E_o = 0.670$ V vs. SHE (2.21)
➔ in alkaline media: $O_2 + H_2O + 2e^- \rightarrow HO^-{}_2 + OH^-$ $E_o = -0.065$V vs. SHE (2.22)

Peroxide formation during O_2 reduction can be followed by its reduction

➔ in acidic media: $H_2O_2 + 2H^+ + 2e^- \rightarrow 2H_2O$ $E_o = 1.770$ V vs. SHE (2.22)
➔ in alkaline media: $HO^-{}_2 + H_2O + 2e^- \rightarrow 3OH^-$ $E_o = 0.867$ V vs. SHE (2.23)

The 2-electron peroxide reaction is undesired, not only because it involves the production of less current per O_2 molecule, but also because of its H_2O_2 yield which can degrade the membrane or catalyst if desorbed. Of course, if this reaction happens 100 % efficiently it will give the same result as the 4-electron path, namely water formation. If hydrogen peroxide is reduced before it is desorbed, no difference will be noticed with the 4-electron path [40,41].

Oxygen Reduction Mechanism on Metal Electrodes

The oxygen molecule has a bond strength corresponding to $\Delta H_f = -498.7$ kJ mol^{-1}. Compared to C-C bond (-334 kJ mol^{-1}), the H-H bond (-431 kJ mol^{-1}) and the C-H bond (-160 kJ mol^{-1}) [41], it becomes clear that oxygen reduction at ambient temperature (or at the 80 °C of an operational PEM fuel cell) is a slow reaction that needs to be catalysed in order to proceed at an energetically-profitable rate.
The oxygen binding involves binding with the d-orbitals of the central metal-ion of the MeN_4 sites. In acidic media the mechanism of the oxygen reduction, is commonly supposed to follow a modified redox pathway according to Van Veen et al. [42]:

$Me(III) + e^- \rightarrow Me(II)$ (2.24)
$Me(II) + O_2 + H^+ \rightarrow Me(II)\text{-}O_2H$ (2.25)
$Me(III)\text{-}O_2H + e^- \rightarrow$ intermediates (2.26)

In alkaline media according to Zagal et al. [40] the redox mechanism is presented as follows:

$Me(III)\text{-}OH + e^- \rightarrow Me(II) + OH^-$ (2.27)
$Me(II) + O_2 \rightarrow Me(III)\text{-}O_2^-$ or $Me(II)\text{-}O_2$ (2.28)
$Me(III)\text{-}O_2^- + e^- \rightarrow Me(II)$ + intermediates (2.29)

According to literature the adsorption of an oxygen species on the surface of the metal particles is necessary for electron transfer. In principle, ORR starts with the O_2 binding on the Me(II) [40,43].
The potential-determining step is the step with the least favorable equilibrium potential. The difference in the equilibrium potential of the potential-determining step and the overall equilibrium potential is the thermodynamic overpotential η. As ORR happens only on specific active sites of the catalyst, the type of metal and its surface are of crucial importance.

2.2.2 Concept of Non-Precious Metal Catalysts (NPMC)

Interestingly, the complex oxygen reduction is also a fundamental part of our own respiratory metabolism, which yet performs this reaction without resorting to high operative temperatures or precious metals to boost its kinetics. The enzyme responsible for this ORR catalysis in eukaryotes is called cytochrome c oxidase (CcO) and, it initially inspired the research on Fe- N- C materials as catalysts for the ORR [44]. Me-N-C and in particular Fe-N-C catalysts are the group of NPMCs this thesis focuses on.

Non-precious metal catalysts (NPMC), which are less expensive materials than platinum (noble metal), such (Fe, Co, Ni etc.) have been studied for over 50 years now and tremendous improvements in both performance and durability were achieved. A major milestone in the development of N_4 chelates as catalysts for the ORR presents the findings of Jasinski et al. in 1964, who reported first the ORR activity of catalysts based on the active center of haemoglobin [45]. It was shown that cobalt phthalocyanine supported on carbon in alkaline media could be used as a cathode electrocatalyst for O_2 reduction [46].

Ten years later in 1976—1977 Jahnke et al. [47] and Bagotzky et al. [48] who discovered that the heat-treatment of various cobalt or iron macrocycles impregnated on active carbon improves activity and/or stability. Another milestone achieved in 1989 by Gupta et al. [49] who demonstrated that highly active Me-N-C catalysts can be synthesized by pyrolyzing ($T > 700$ °C) a precursor mixture consisting of a separate metal, carbon and nitrogen sources instead of the complex macrocycles.

Although the heat-treatment of these materials was shown to increase the activity and stability, it also resulted in a loss of their original structure. Consequently, the heterogeneous morphology of the heat-treated catalysts leads to the questioning of the exact nature of the active site [50].

Researchers have tried many methods to develop new efficient NPMCs including non-pyrolysed transition metal macrocycles [51], conductive polymer based-complexes (pyrolysed and non-pyrolysed) [52], (transition metal chalcogenides [53], metal oxide/carbide/nitride materials [54–56], and pyrolysed non-precious Me-N-C (with Me = Fe, Ni, Co, etc.) catalysts [2, 57–63].

It should be pointed out that the latter Me-N-C based catalysts are the largest subclass of catalysts studied for the ORR due to their very promising performance in acidic media.

Currently proposed Structures for Active Sites

Due to the complex heterogeneous morphology of the Me-N-C catalysts, the nature of the active sites is still not fully understood and under scientific debate. During the last decade, there were mainly three different structures of active sites identified and discussed: the nitrogen-coordinated transition metal (FeN_4) sites, some metal-free, with heteroatoms (mostly graphitic or pyridinic N) doped in carbon, sites (CNx) and encapsulated iron species in carbon (Fe_xC/C).

Metal-free CN_x-sites

The concept of metal-free CNx structures are the active sites was first proposed by Wiesener in 1986 [64] and was followed by other authors [65–68].

A typical example of a metal-free catalyst by Popov's group [69] was prepared with Ketjen Black (EC-300) oxidized in HNO_3. Several nitrogen precursors were used to functionalize the carbon black, namely, melamine formaldehyde (MF), urea formaldehyde (UF), thiourea formaldehyde (TUF), and selenourea formaldehyde (SeUF). The mixture was then pyrolysed at various temperatures (400-1000 °C) in inert atmosphere. Electrochemical tests under acidic conditions showed that the best performing catalyst was the one heat treated at 800 °C with selenourea as the nitrogen precursor. The onset potential of this catalyst was 0.76 V and the half-wave potential ($E_{1/2}$) < 0.6V. The authors used Inductively Coupled Plasma Mass Spectrometry (ICP-MS) to prove that indeed no metal was present in the catalyst. However, traces of iron were found present in the catalyst (0.00002 wt.%). Dodelet's group has shown that even very low iron content can, in fact, result in non-negligible catalytic activity for ORR in acid medium [70], and additionally in their work found that N-doped carbon with metal, exhibits higher activity (about 20 mV higher V_{onset}) of the N-doped carbon prepared without metal. Nevertheless, even though this "metal-free" catalyst showed some ORR activity, in reality is far below the activity obtained by metal containing catalysts (FeN_x or CoN_x).

In another case[71], "metal-free" catalysts were prepared with a nitrogen precursor and with either Co, Ni and/or Fe precursors, but for which, according to the authors, the ORR properties do not derive from metal-containing sites, but are the result of the nitrogen-doped carbon obtained during their synthesis. In this case, all of the ORR active sites in these catalysts, are of the CNx type, and the metals are only intermediates which are removed during acid leaching. However, in most cases the acid leaching step is not fully complete (metallic ions are adsorbed in the carbon support), resulting to low metal loadings present in the final catalysts. Therefore, the question rise on how to be sure that metal does not participate in the obtained ORR activity?

Fe-carbide sites

Another class of active sites such as iron carbide nanorods, iron carbide functionalized melamine, or iron carbide nanoparticles, prepared by high pressured pyrolysis, encased by graphitic layers, with little surface nitrogen or metallic functionalities [72,73]. Iron carbides confined inside carbon nanotubes (CNTs) [74], or the coexistence of Fe/Fe_3C nanocrystals and $Fe\text{-}N_x$ [75] or Fe_3C/C [76] have been suggested that may also reduce O_2 electrochemically.

Hu et al. [76] reported an onset potential of 0.90 V a half-wave potential ($E_{1/2}$) of 0.73 V and an activity decay of 40 mV in terms of $E_{1/2}$ after 31500 cycles (140 h) of cycling between 0.6 and 1.0 V under N_2 atmosphere. According to the authors, it was clear that since the Fe_3C nanoparticles, which are encased by graphitic layers, are not in direct contact with the electrolyte or O_2, hence they cannot be the direct ORR active sites. However, they are proposed to play a synergetic role in activating the outer surface of the graphitic layers towards the ORR as shown in Figure 2.5.

In a following work [77], it was found that the heat-treatment temperature plays a critical role in the formation of hollow morphologies of microspheres consisting of graphitic layer encapsulated Fe_3C nanoparticles and ORR active sites of the catalysts. The authors suggest that catalysts pyrolysed at different temperatures (Fe/C-700 °C and Fe/C-800 °C) contain a different ORR active site and the synergetic interaction between Fe_3C nanoparticles and the protective graphitic layers has a key role in the ORR. The Fe/C-800 °C catalyst retained the high activity performance after a stability test of 2000 cycles between 0.6 and 1.0 V, this time under O_2- saturated acidic environment. A 17 mV negative shift in terms of $E_{1/2}$ was observed.

Strickland et al. [78] in 2014 prepared a MOF based FePhen@MOF catalyst with high activity in acidic media in which the Fe-N coordinated site is absent. The authors attribute the high activity to subsurface Fe/Fe_xC nanoparticles and verified their suggested structures with in-situ X-ray absorption spectroscopy (XAS) measurements and Mössbauer spectroscopy. Although the Fe based catalyst showed a high activity and stability (to the range of 0.6—1.0 V) during a stability protocol in the range of 1.0—1.5 V a loss of 270 mV is observed after 6200 cycles. The authors then claim that some of the Fe/Fe_xC nanoparticles covered by fewer graphitic sheets are exposed to the acidic environment and are dissolved. This process would then allow some of the dissolved Fe-ions to either (a) adsorb on nitrogen sites that are doped into the carbon matrix to form the FeN_x active site or (b) form Fe^{III} hydroxides ($Fe(OH)_3$) as proposed by Goellner et al. [79]

FeN_4 sites

Notwithstanding the above suggestions of the nature of active sites, the main focus has been given to the FeN_4 sites, due to the fact that significantly higher activity is achieved in acidic media, in the presence of such sites.

Based on Mössbauer and X-ray absorption spectroscopy, van Veen and his collaborators proposed that the chelates metal-N_4 moiety is retained in the heat treatment, and actually binds to the carbon support [41,42,42,80,81]

During the 1990's, other groups backed van Veen's hypothesis of a MeN_4 resembling site. Savy and Savinell et al. prepared Fe or Co napthophthalocyanines [82–84] and porphyrins [85,86] with various loadings and different carbon blacks, they characterized their catalysts with Infrared (IR) spectroscopy, X-ray photoelectron spectroscopy (XPS) and rotating disk electrode (RDE) and suggested that the Me-N_4 moiety remains intact when heat-treated up to 500 °C.

The group of Dodelet, through time-of-flight secondary-ion mass spectrometry (ToF SIMS), initially proposed that the nature of the catalytic sites involved a coordination between the transition metal ion, nitrogen, and carbon support, in the form of $MeN_xC_y^+$. In pursuing, the realization of the true nature of the catalytic site they prepared different precursors one for the metal and one for the nitrogen in order to identify the role and importance of each component: the metal, the nitrogen atoms, and the carbon support. It was found that active catalysts were obtained only when both Fe and N precursors were in the reactor at the same time. There was no catalytic activity from only C-N or C-Fe precursors. It is clear that in these catalysts metallic Fe and iron carbide were not the catalytic sites [87].

In the case of Fe based catalysts synthesized from either iron^{II} acetate (FeAc) or iron porphyrin (ClFeTMPP), followed by heat-treatment in Ar between 400 and 1000 °C two different catalytically active sites were observed, namely FeN_2/C and FeN_4/C [88,89].

Later however, Dodelet's group has revised their proposed active site configurations claiming that the majority of active site structures consist of an FeN_4/C (labelled by the authors as FeN_{2+2}/C) configuration bridging two adjacent graphene crystallites [90].

The active sites was proposed to be hosted in micropores of the catalyst materials and with deliberate carbon support selection and synthesis methods to obtain ideal nanostructure configurations, active site densities can be improved. This would adequately explain previous studies correlating ORR activity to the presence of Fe ions coordinated by four nitrogen atoms observed through Mössbauer analysis [90].

Koslowski et al. [91] have investigated the influence of porphyrin structure on the ability to directly or indirectly catalyse the ORR. They prepared various iron porphyrin (FeTMPP) and H_2TMPP based catalysts using a foaming agent technique. Both iron (II) oxalate and sulphur were used in the synthesis and the prepared catalyst materials were heat-treated under N_2 at 800 °C. To modify the structure of the catalysts as well as their composition, various post-treatments using HNO_3, H_2O_2, N_2, and CO_2 were carried out on the prepared catalyst. This allowed the influence of structure and composition on catalytic activity to be investigated. The structural changes were investigated using Mössbauer spectroscopy and their influence on catalyst activity was studied using the rotating ring disk electrode (RRDE) technique. They found that the generic catalysts that went through a few post-treatments had a number of atomic Fe centres that correlated well with kinetic current density as measured in the RRDE. Specifically, it was found that the total number of in-plane Fe-N_4 moieties implanted in a graphene type matrix relates directly to the current density for a given potential for the reduction of oxygen to water.

Kramm et al. [60] prepared various iron porphyrin based catalysts using different heat- treatment temperatures. The authors extensively characterised these materials by bulk elemental analysis, X-ray photoelectron spectroscopy and Mössbauer spectroscopy in order to gain insight into the impact of synthesis technique on the resultant catalyst properties and the variations in ORR activities. The conclusion drawn by the authors was that improvements in the ORR activity, and by extension the average TOF of the NPMC materials were due to increase in the electron density of the nitrogen coordinated metal ion centres proposed to be the active site structure. Higher nitrogen contents in the carbon support materials were linked to increased electron densities of the Fe-ions.

Kramm et al. in a later work [92], in combination with Dodelet's group reported a detailed active site investigation using NPMCs. Different catalysts were prepared by impregnating iron acetate in carbon black and heat-treated at 950 °C in ammonia. The authors used plenty of techniques to characterize their catalysts, such as Mössbauer spectroscopy, EXAFS, TEM, XRD, neutron activation analysis (NAA) and combustion analysis. The most common notion for a metal-based active site is that Fe ions are coordinated by four nitrogen species. This includes the FeN_4 or FeN_{2+2} structures. Of these different species, it is the FeN_4 and the N-FeN_{2+2} that were found to be responsible for ORR activity. Particularly, the N-FeN_{2+2} structure was unique to catalysts that were subjected to a heat-treatment in ammonia.

Regarding the iron carbides as active sites, Kramm [93] found that the formation of iron carbide related to the graphitization of carbon leads to the decomposition of FeN_4-centers. The author suggested that such decomposition can be avoided by the addition of sulfur to the original precursor since iron sulfide species (FeS, Fe_2S_3) which are formed instead of iron carbide can be removed completely with an etching step due to their good acid solubility. In a later work by Kramm et al. [94] the role of sulfur was elucidated. The authors concluded that sulfur has no beneficial effect on activity performance by itself, but it prevents iron-carbide formation during the heating process. The iron carbide formation causes the disintegration of FeN_4 sites as shown by structural characterization. The catalysts prepared without sulfur addition showed a much lower concentration of FeN_4-centers.

In addition, this case was verified by Ferrandon et al. [95] where the authors prepared catalysts in the absence and in the presence of a sulfur-based oxidant in the aniline polymerization and found that the absence of sulfur led to an increase in the amount of iron carbide formed during the heat-treatment and a decrease in the number of FeN_4 centres, thus contributing to an indirect beneficial role of sulfur in the catalyst synthesis.

A recent work by Choi et al. [96] shed a light on this topic. The authors prepared four different groups of catalysts, namely metal-free N-C, electrolyte-exposed Fe particles, FeN_xC_y moieties and Fe@N-C and tested them under acidic conditions for peroxide reduction reaction (PRR) a key intermediate during O_2-reduction. The authors elucidated the ORR and PRR reactivity concluding that FeNxCy mostly catalyses direct $4e^-$ ORR, but also releases a minor fraction of H_2O_2. Fe@N-C produces a higher fraction of H_2O_2 in comparison to FeN_xC_y. The released H_2O_2 is then reduced to H_2O in a second step, either on FeN_xC_y or Fe@N-C. Surface-exposed Fe particles and N groups without subsurface Fe are PRR inactive (Figure 2.5). PRR catalysis is highly desirable for catalysts with multiple Fe species present, in order to improve the durability of Fe-N-C catalysts as H_2O_2 production is considered to lead to significant degradation during fuel cell operation.

In conclusion, with the intense debate on the exact nature of active sites still remaining, leads to the conclusion that the ORR active site structure (Figure 2.5) is material dependent and relates to the particular synthesis procedures and conditions used. A short summary could be that one can now control the synthesis conditions and obtain Fe-N-C catalysts with exclusively FeNxCy, [97,98]only Fe@N-C particles [78], or their combination [57,58] in order to design controllable Fe-N-C catalysts and improve the activity and most important to gain some insights on the durability.

It is of importance though to mention, that catalysts containing FeN_x sites are found to be more active in acidic media, as well as when the structure is pure, more accurate and straight forward results can be drawn.

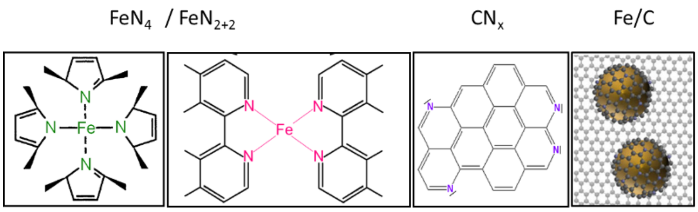

Figure 2.5: Schematic representation of the proposed active sites existing in literature [92].

Overview on Me-N-C Synthesis and Performance

During the last years, significant progress has been achieved regarding the improvement of the activity, selectivity, and stability of these Me-N-C catalysts. With a large number of scientific publications concerning Me-N-C catalysts, various notions have been portrayed regarding their activity and active sites. In the present work, the most important breakthroughs, regarding activity performance and evidence of the nature of the active sites, will be mentioned.

Most of currently studied Me-N-C catalysts are prepared by pyrolyzing a composite that was mixed with iron salts, nitrogen–carbon precursors, and high-surface-area supports, followed by an acidic leaching (AL) and a second heat-treatment (HT).

In 2011, a carbon-supported iron-based catalyst (Fe-N-C) from Dodelet's group achieved power densities comparable with that of a Pt-based catalyst [2]. This Fe-N-C catalyst displayed the highest (in that time) ORR activity with a volumetric current density of 99 A cm^{-3} at an iR-free cell voltage of 0.8 V (with initial maximum performance: 0.90 W cm^{-2}), significantly higher than 2.7 A cm^{-3} determined for the previously presumed best non-precious metal catalyst from their group in 2008 [90,99]

The group of Zelenay investigated the non-pyrolysed Co-polypyrrole-C systems which showed a respectable durability, however, the ORR activity was low [100]. Later the authors shifted toward high-temperature systems synthesized using pre-dominantly iron, cobalt, and heteroatom polymer precursors (polypyrrole and polyaniline) where the obtained ORR activities found to be much higher [101,102].

In 2011, Wu et al. [58] prepared a FeCo-PANI/C on Ketjen Black carbon support catalyst. The catalyst material was heat-treated at 900 °C then acid leached in 0.5 M H_2SO_4 at 85 °C for 8 h, followed by a second pyrolysis in nitrogen in order to remove any surface inactive metallic species or residues. Through fuel cell testing, the catalyst containing a mixture of iron and cobalt was found to provide the best performance and stability, most notably a maximum power density of 0.55 Wcm^{-2} at a cell voltage of 0.4 V and excellent durability performance after 700 h (~4 weeks) of potential hold at 0.4 V (with initial maximum performance: 0.55 W cm^{-2}).

In 2014 Serov et al. [103], prepared a Fe-8CBDZ-DHT-NH_3 catalyst by a sacrificial support method. Carbendazin (a nitrogen precursor) and iron nitrate (the iron precursor) were added to a dispersion of fumed silica in water. After evaporation of the solvent, the obtained solid was then subjected to a first heat-treatment at 800 °C under N_2 atmosphere. The resulting material was acid leached. After being rinsed with distilled water, the material was then subjected to a second 30 min heat-treatment, at 950 °C under NH_3 atmosphere, to obtain the Fe- 8CBDZ- DHT- NH_3 catalyst. The ORR catalytic activity of Fe-8CBDZ-DHT-NH_3 is attributed to FeN_x centres formed during the heat-treatment. This catalyst showed a significant performance of 0.56 W cm^{-2}.

In 2015 a significant breakthrough was achieved by Shui et al. [3], reporting the highest volumetric activity and improved fuel cell durability of an iron-based nanofiber framework. In their work, the authors prepared a carbon-based nanofibrous catalyst by electrospinning with a high-density of active sites hosted in micropores as well as with an improved mass transfer via macropores. This catalyst design led to astonishing high volumetric activities of 450 A cm^{-3} at 0.8 V (with initial maximum performance: 0.90 W cm^{-2}).

In another work in 2015, Wang et al. [104], prepared a Fe/N/C-SCN catalyst. This catalyst was prepared by carbon black (KJ600) that was first functionalized with sulfophenyl groups. Polymethylphenylenediamine (PmPDA) was coated on the functionalized carbon black through oxidative polymerization of mPDA monomer by APS $(NH_4)_2S_2O_8$ in the presence of $FeCl_3$. After $Fe(SCN)_3$ was added, the resulting material was subjected to the sequence of a first pyrolysis step at 950 °C under Ar, acid leaching, and a secondary pyrolysis step again at 950 °C under Ar to obtain the catalyst. This catalyst showed an activity of 23 A g^{-1} at 0.80 V in an acidic environment (with initial maximum performance: 0.94 W cm^{-2}).

In 2016 Wang et al.[5], prepared an iron-doped in ZIF-8 catalyst, by wet mixing, washing and a heat-treatment step at 1000 °C for 1 h. The obtained catalyst was tested in a half-cell and the RDE measurements showed an onset potential of 0.95 V and a half-wave potential ($E_{1/2}$) of 0.82 V. The authors performed also a stability test (cycling between 0.6 – 1.0 V) which showed an activity decay of just 40 mV loss in terms of half-wave potential after 10000 cycles. Directly converting Fe-doped metal-organic frameworks into highly active and stable Fe-N-C catalysts for oxygen reduction in acid.

In 2017 a work by Zhang et al. [105], demonstrated an additional high performed catalyst by pyrolyzing a mixture of $Zn(NO_3)_2$ and $FeSO_4$ with the addition of multiwall-carbon-nanotube (MWCNT). A high performance of 17.22 A g^{-1} at 0.8 V in acidic media was achieved (with initial maximum performance: 0.82 W cm^{-2}) making this catalyst comparable with the highest performing NPMC reported so far.

The highest performing catalyst to date is PAN-Fe03-1000NH_3 prepared by Chokai et al. [4], in 2014. Firstly, the authors polymerized acrylonitrile, which then as polyacrylonitrile (PAN) was heated at 230 °C for 1 h under air. Then PAN was dispersed in a solution of $FeCl_2 \cdot 4H_2O$ in tetrahydrofuran (THF). The initial Fe loading was 0.3 wt % to obtain PAN-Fe03. The resulting material was pyrolysed at 600 °C for carbonization. It then was ball-milled for dispersion. The dispersed sample was first activated at 800 °C for 1 h and then at 1000 °C for 1h in NH_3 to become the final catalyst. This catalyst was prepared without acid leaching. This catalyst has a surface area of 1096 m^2g^{-1}.

The fuel cell testing of this catalyst resulted in open circuit voltages of 0.97 V and a current density at 0.6 V displayed over 1.0 A cm^{-2} (with initial max power: 0.98 W cm^{-2}). A short durability test was performed which showed that approx. 90% of the property was retained for 400 min with a fixed voltage at 0.8 V.

Table 2.2: Summary of NPMC with the highest reported power densities in PEMFCs. HT corresponds to Heat-Treatment and AL to Acid Leaching.

Name of NPMC	**Synthesis**	**Max. Power density W cm^{-2}**	**Ref.**
FeAc-Phen-MOF	HT1: 1050 °C, AL, HT2: 950 °C (NH_3)	0.90	[2]
FeCo-PANI/KB	HT1: 900 °C, AL, HT2: 900 °C	0.55	[58]
Fe-8CBDZ-DHT-NH_3	HT1: 800 °C, AL, HT2: 950 °C (NH_3)	0.56	[103]
Fe/N/CF	HT1: 1000 °C(NH_3), AL, HT2: 700 °C (NH_3)	0.90	[3]
Fe/N/C-SCN	HT1: 950 °C, AL, HT2: 950 °C	0.94	[104]
Fe-N-C	HT1: 80 °C, HT2: 150 °C (NH_3)	0.82	[105]
PAN-Fe03-1000NH_3	HT1: 800 °C, HT2: 1000 °C, HT3: 950°C	0.97	[4]
Zn(ligand)$_2$TPIP	HT1: 1050 °C, AL, HT2: 950 °C (NH_3)	0.62	[106]

These main achievements were based on in-depth structure-to-property correlations of the factors that improve significantly the ORR activity of these catalysts, namely the presence of MeN_4 sites [60,81,91,92,97,98,107], the presence of nitrogen moieties assigned to $N_{pyrid.}$ [99] and N_{Me-N} [60,89,108,109].

Additionally as one can recognise from the discussion above, to point out the importance of the precursor's composition, the metal species and the carbon morphology for the ORR activity and stability [58,108,110–112]

Me-N-C in Alkaline Media

The performance of Me-N-C catalysts in alkaline media is significantly higher in comparison to acidic media. Thanks to the -59 mV change in the potential per every pH unit, the operation potential of an ORR catalyst is expected be ca. 0.83 V lower in a 1.0 M solution of a strong base than in 1.0 M solution of a strong acid. Such potential shift influences the double layer structure and the electric field at the electrode-electrolyte interface, altering the adsorption strength of neutral species [113].

Decreased anionic adsorption in alkaline media is expected to help the kinetics of electrocatalytic reactions including ORR [114].

A variety of NPMCs have shown comparable corrosion resistance in alkaline media to that of precious metals, which makes them particularly suitable for alkaline fuel cells [113].

Wu et al. [115] (reported the ORR performance of three different PANI-derived catalysts prepared with Fe, Co and without metal in an alkaline electrolyte. The best performing catalyst was found to be the Co-based catalyst containing a large amount of Co_9S_8 particles surrounded by nitrogen-doped graphene sheets, which showed a performance superior to that of a Pt/C reference catalyst.

Moreover, it is known that even metal-free electrocatalysts can reach high activity and selectivity toward ORR. In this context, Liang et al. [116] developed a metal-free electrocatalyst as an alternative to Pt/C that revealed the highest ORR activity in alkaline media among all reported metal-free ORR catalysts.

Methanol Tolerance

Methanol (MeOH) crossover from the anode to the cathode in the Direct Methanol Fuel Cell (DMFC) is responsible for significant deactivation of Pt cathode catalysts. Compared to Pt- based catalysts, NPMCs are poor oxidation catalysts, of methanol oxidation in particular, which makes them highly methanol-tolerant.

A wide variety of studies have shown that NPMCs are tolerant to methanol concentration, even up to 10.0 M MeOH [117]. High methanol tolerance of a NPMC was also demonstrated by Piela et al. with a heat-treated CoTMPP catalyst which was tested at various concentrations 0.0 to 5.0 M MeOH. The CoTMPP catalyst retained its activity for methanol concentration up to 5.0 M, thus making it an attractive candidate for the cathode in DMFCs [118].

Li et al. [119] tested the activity of a Fe-PANI-rGO catalyst in sulfuric acid with a variation in methanol concentration from 0.0 to 17.0 M MeOH. The catalyst was capable of tolerating highly-concentrated methanol, up to 4.0 M, without significant performance loss. This NPMC exhibited superior ORR activity and stability in DMFC with a current density > 0.1 A cm^{-2} at 0.4 V. In another work from Sebastian et al. [28] a triple heat-treated Fe-N-C catalyst showed very good performance even with 10 M MeOH. Best results found for 90 °C and 5.0 M MeOH. In addition, a 100 h durability test (at 0.3 V) under these conditions results in 50% decay of the NPMC and 45% decay for the Pt/C.

Recently Park et al. [117], synthesized a nanosized graphene derived Fe/Co-N-C catalyst which was tested in acidic media and showed high methanol tolerance up to 10.0 M. The maximum power density achieved was 32 mW cm^{-2} with a relatively low content of PtRu anode catalyst. The authors did not provide any durability/stability data.

2.2.3 Studying the Degradation in PEMFC

Durability remains one of the primary challenges facing fuel cells today. The loss of performance with operation time is a serious barrier to the real-world use of PEMFCs. Great efforts have been made to improve the durability of FCs in the last decade as significant studies have been conducted in this regard by industry, government, and academia. The United States Department of Energy (DOE) has been among the most active in terms of organizing and support FC research and studies published through their Fuel Cell Technologies Program have become valuable guides for researchers and industry [120]

Since the mid-2000s there have been durability targets for PEMFC. Currently, the targets for 2020 are 5000 hours of operation with < 10% loss of performance for automotive applications and 60,000 hours operation for stationary power systems [120].

Table 2.3: Targets for Pt and NPMC for transportation applications [121].

Characteristic	Units	2015 Status	2020 Target
Platinum group metal (pgm) total loading (both electrodes)	mg PGM/ cm^2 electrode area	0.13	0.125
Mass activity	A / mg PGM @900 $mV_{iR\text{-}free}$	> 0.5	0.44
Loss in initial catalytic activity	% mass activity loss	66	< 40
Loss in performance at 0.8 A / cm^2	mV	13	<30
Electro catalyst support stability	% mass activity loss	41	< 40
Loss in performance at 1.5 A/cm^2	mV	65	< 30
PGM-free catalyst activity	A / cm^2 @900 $mV_{iR\text{-}free}$	0.016	> 0.044

In addition, the objectives include efficiencies of 65% and 45% for automotive and small-stationary uses. Though there are a number of degradation pathways related to system or stack components, the main reason for loss of FC performance is degradation of the catalysts and membrane [122,123]. The lifetime of PEM-fuel cells is primarily affected by the harsh potential differences applied during Start-stop operation and steep transient load cycling (leading to water management and gas transport problems) [122]. PEMFCs for automotive applications go through thousands of cycles during normal operation of the vehicle over the expected lifespan of 10 years [124]. These cycles include a combination of load or voltage and start/stop cycles. In this context, a huge variety of protocols has been proposed to test stability/durability of the fuel cell system. **Stability refers to the ability of the system to maintain performance at constant current (or voltage) conditions, while durability refers to the ability to maintain performance following a voltage cycling.**

Briefly, the most commonly applied are those recommended by the Fuel Cell Commercialization Conference in Japan in 2011 Figure 2.6 [124,125].

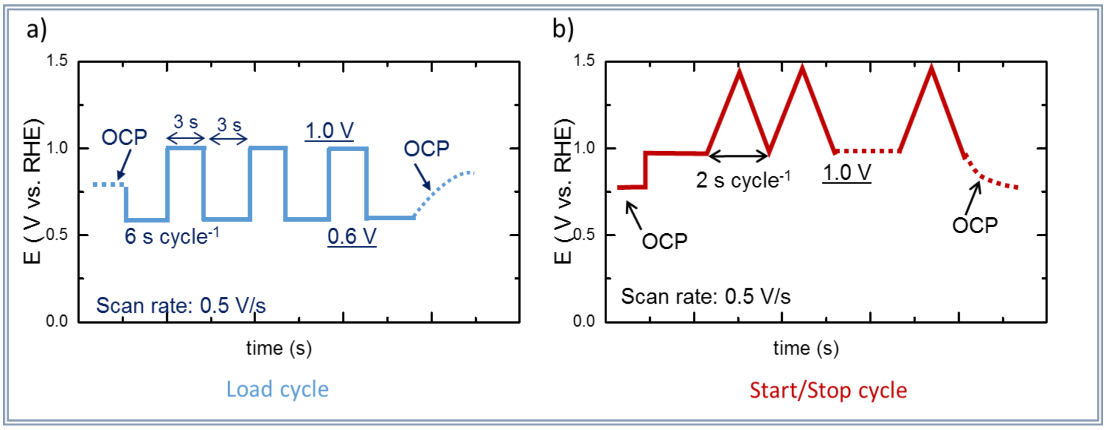

Figure 2.6: Schematic representation of potential-cycle durability test protocols as suggested by FCCCJ. a) Load cycle and b) start/stop protocol, reproduced by [125].
Load cycle protocol

The durability protocols are focused on understanding the material degradation under relevant automotive cycles and correlating single cell durability to the stack level. The widest potential range of each cell in the stacks can be approximately between 0.6—1.0 V vs. RHE in actual FCVs. The load cycle protocol simulates the peak load and OCV/idle using a square wave profile with a 3-second hold at each potential. The lowest potential corresponds to the potential at peak power (about 0.6 V) and the upper potential corresponds roughly to open circuit potential (OCP). The upper potential is known to have a significant impact on catalyst degradation [124,125].

Start/Stop protocol

Automotive PEMFC must be tolerant to frequent shut-down/start-up cycles. During the shut-down of a fuel cell, both the anode and cathode chambers get filled with ambient air from the atmosphere. In the anode during start-up when hydrogen flows in, an H_2/air boundary is created. This causes a local fuel starvation, thus leading to a high potential difference of up to 1.5 V on the cathode, causing carbon corrosion and oxygen evolution at the cathode electrode and oxygen reduction in the anode as seen in Figure 2.7. The processes that take place, referred to as reverse current mode [126]. Under these conditions, the electrochemical oxidation of the carbon support is believed to play an important role in the degradation of the catalyst. Therefore in this durability protocol, a cathode potential range of 1.0—1.5 V vs. RHE, a triangular wave, and a 2-second cycle period is applied to accelerate the degradation and shorten the evaluation time [124,125].

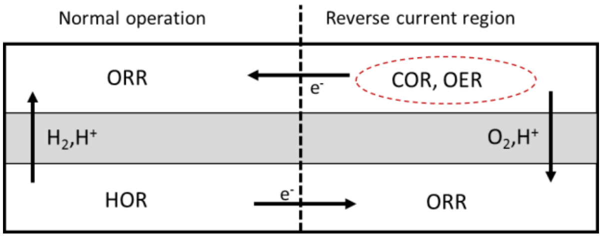

Figure 2.7: Illustration of the “reverse current” mechanism [126].

Origin of Catalyst Instability in Low-Temperature Fuel Cells

While a comprehensive body of work exists on the degradation mechanisms of Pt particles supported on carbon or non-carbon supports [127,128], few such investigations have focused on Me-N-C catalysts. In the following, the degradation mechanisms as suggested by literature will be reported, however not all of them have been investigated in the current thesis.

Factors such as the synthesis conditions (heat-treatment temperature, gas atmosphere, and acid leaching), the transition metal utilized (Co, Fe, bimetallic, or other metals), and the active site structure have a significant impact on catalyst stability and specific degradation mechanisms.

Therefore, it is not surprising, given the large variety of synthetic approaches and the complexity of the final structure of NPMCs that a mechanistic understanding of catalyst degradation is not a simple work. Moreover, it has been suggested that possibly there are two mechanisms of performance loss. One occurring in a short time frame and one occurring in a longer period. This was observed by Proietti et al. [129] that the most rapid performance loss occurs within the first several hours of operation, followed by a more gradual decay in performance.

However, several suggested mechanisms (Figure 2.8) found in the literature are discussed in the following.

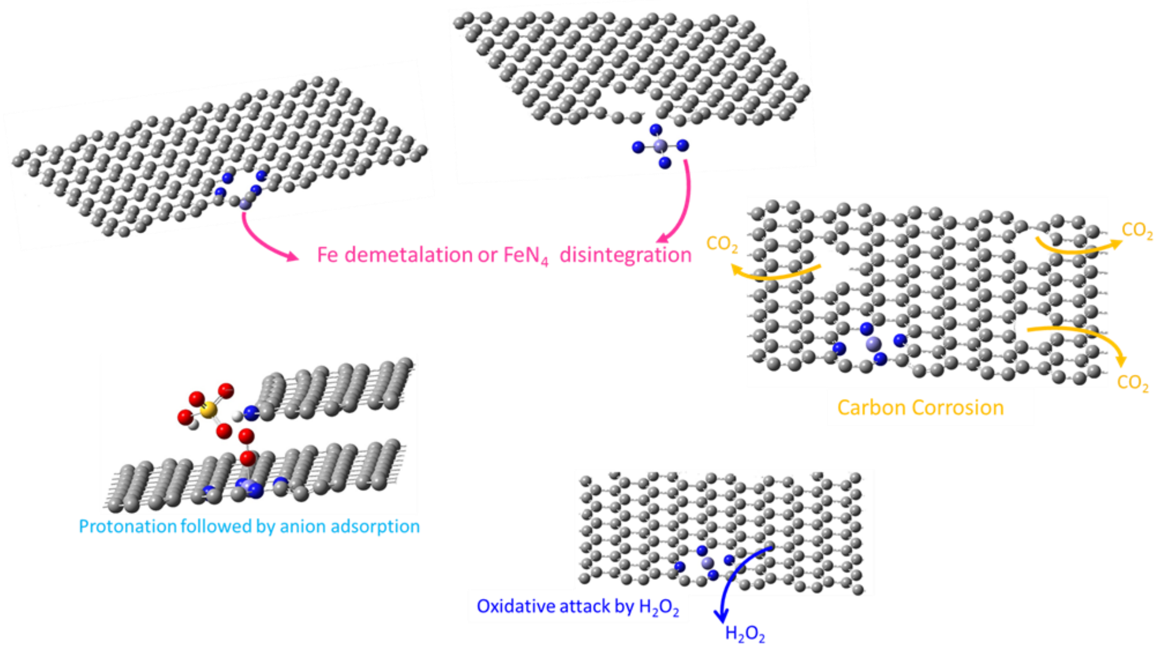

Figure 2.8: Possible degradation mechanisms.

1. Fe Demetallation or Disintegration of FeN_4 Active Sites

The ORR must start with the adsorption of the oxygen molecule on the catalytic site, i.e. on top of the Fe^{II} (most-acknowledged oxidation state at the beginning of O_2-electroreduction) [40,43,130,131]. This O_2-adsorption and pulling of an electron from the site actually lead to a first reasonable cause for the catalyst's instability [132].

Indeed, the transition in iron's oxidation state, from Fe^{2+} to Fe^{3+}, causes the contraction of the ion's radius and its displacement above the chelate plane. The oxidized Fe^{3+} is, therefore, farther from its coordinating nitrogen environment (N_4), in a stretched state that may lead to its detachment and the literal demetallation of the active sites [133].

This hypothesis was suggested by a work of Baranton et al. [134] where the authors tested non- pyrolysed iron phthalocyanine and found that Fe^{2+} was oxidized to Fe^{3+} in the presence of O_2, making its ionic radius shorter thus leading to a less stable iron species in the macrocycle. Interestingly, this mechanism was observed only in the presence of O_2 whereas in the presence of inert gas the catalyst was found very stable.

However, it is believed that iron (or other metal) is strongly bonded to the surrounding nitrogen making the metal cation stable in its environment [100,135,136].

Deng et al. [74] prepared metallic Fe nanoparticles encapsulated within the compartments of pea-pod like CNTs (Pod(N)-Fe) which exhibit high long-term stability under both steady current and steady voltage modes. The stable behaviour of the catalyst is attributed to the avoidance of direct contact with harsh environments including acid medium, oxygen, and sulfur contaminations.

Due to the general belief of demetallation being harmful to a stable operation of PEMFCs, Choi et al. [137] worked on minimizing this effect of operando demetallation by preparing Fe-N-C catalysts free from inactive Fe particles or by effectively removing them by electrochemical treatment after synthesis. Fe demetallation from catalysts containing mostly or only FeNxCy moieties was significantly reduced without any activity loss implying the stability of such moieties in acidic environment at 1.0 – 0.0 V RHE. Short durability tests showed that operando Fe demetallation is not a primary degradation mechanism for their Fe-N-C catalysts during 5– 50 h operation.

Varnell et al. [138] attributed the high activity of their H_2-treated catalyst to the Fe particles encapsulated by N-doped carbon. These Fe particles are disordered and nanostructured, which enhances their catalytic properties due to the increased surface to bulk ratio, and are made stable in acid by their encapsulation as shown by XAS studies.

In the most recent work by Chenitz et al. [139] the authors make a novel hypothesis for the instability issues regarding PEMFC operation. After numerous experimental work and suggestions (which will be discussed in the following) the authors presume that responsible for the initial fast decay of catalyst performance is the fact that the FeN_4-like active sites which are located in the micropores never reach an equilibrium between iron ion in and out of the FeN_4- like site resulting in the demetallation of these sites in the micropores.

This work is based on a previous work by Glibin and Dodelet [140] in which the authors determined the thermodynamic stability of FeN_4C_{12} associated to OH adsorption or other equivalent reaction intermediates in acid. The evaluated Fe-based catalyst was found to be chemically stable in acid. These conclusions are valid for systems in the state of chemical equilibrium. However, when iron ions exit the system according to Le Chatelier's principle may lead to the destruction of the electrocatalytic site.

According to the authors, the micropores of their catalysts are open-end and slit-shaped with hydrophobic walls, thus water flowing in the micropores does not interact with the walls and successfully exits the micropores providing the dissolved oxygen and protons for ORR. The dissolved oxygen is adsorbed on the catalytic site and explains the initial high activity. However, any Fe ion, which is released by the sites, will be transported out of the micropores through the water stream until all sites found in the micropores are demetallated leading to the fast initial decay of activity. Particularly, for water molecules to quickly move through the hydrophobic walls of the micropores, the size of the latter should be > 0.7 nm.

The demetallation mechanism has been widely known since NPMCs were first discovered and is related to the thermodynamic instability of Fe and Co in the acidic, oxidizing environment of a PEMFC cathode. Besides, the direct demetallation of the catalytic site, another degradation pathway of the active sites is caused indirectly by electrochemical corrosion of the carbonaceous support of the catalyst. This mechanism of stability loss is explained in the following.

2. Carbon oxidation

Carbon is thermodynamically susceptible to oxidation to carbon dioxide (standard potential of 0.207 V) in typical fuel cell operation. The reaction (Equation 2.30) is kinetically hindered to a great extent, however, is known to be severely enhanced by increasing temperature and potential [141].

$$C + 2H_2O \rightarrow CO_2 + 4H^+ + 4e^- \qquad (E_0 = 0.207\ V) \qquad (2.30)$$

In a work by Goellner et al. [79] a Fe-N-C catalyst was prepared by Fe acetate, phenanthroline and MOF heat-treated under Ar at 1050°C followed by an acid leaching. The authors reported that the degradation of active sites and carbon corrosion occur in parallel at high potentials and is enhanced at temperatures higher than room temperature leading to decayed ORR kinetics.

Regarding the stability of Me-N-C catalysts Kramm et al found in a previous post-mortem analysis of a Fe-N-C catalyst prepared by Fe acetate, phenanthroline and MOF, heat-treated at 1050 °C, acid leached and heat treated for a second time at 500 °C, a carbon burn-off and a destruction of FeN_4 induced by cycling the catalyst in a potential range of 0.8 V to 1.2 V in a fuel cell (H_2/O_2 at 80 °C) [142]

In another work, Ferrandon et al. [143] correlate also the Fe loss with the potential sequence. The authors observed that the greatest loss of Fe occurs during potential transitions between approximately 0.6 V and 0.4 V, where Fe is reduced from $Fe^{3+}$to Fe^{2+}. Despite faster initial dissolution rates at 0.6 V, more Fe is lost after extended holds at 0.4 V versus 0.6 V. These observations were made on a PANI–Fe–C catalyst, prepared with additional Ketjenblack EC 300J, subjected on a first heat treatment at 900 °C, followed by acid leaching and a second heat-treatment at 900 °C.

Choi et al. [144] investigated a Fe-N-C catalyst (derived from MOF, Fe acetate, and phenanthroline) using a Scanning Flow Cell (SFC) coupled with ICP-MS and DEMS varying the temperature and the potential range. The authors report that demetallation of Fe species and carbon oxidation occur at low (< 0.7 V) and high (0.9 V) potentials, respectively and that Fe demetallation does not directly lead to activity decay, even though it can potentially cause damage to the PEMFC system. However, carbon oxidation can directly cause the destruction of the carbon surface, and indirectly lead to the destruction of the active sites.

The increased degree of graphitization in NPMCs is linked with improved stability. This could be due to the enhanced resistance to corrosion. In this context, improved stability has been reported by using highly graphitized support materials such as carbon nanotubes [145] or graphene materials [146].

In a work of Charreteur et al. [147] it was found that catalysts (FeTMPPCl) heat-treated under NH_3 are very active but not stable. The stability of their catalysts was explained by the graphitization that would protect the active sites, including the carbon atoms near the active sites, against oxidative attack when current is produced. This hypothesis is based on the suggestions by Schulenburg et al. [135] and Tributsch et al. [112] where the authors propose that active sites are probably embedded in graphene layers.

In addition, Wu et al. [58] reported that the formation of graphene sheets appears to be closely associated with the improved durability of PANI-derived catalysts. According to the authors, the graphitization apart from contributing to the active site formation may also enhance the electronic conductivity and corrosion resistance of the carbon-based catalysts.

It becomes apparent that a high degree of graphitization is required in order to obtain stable catalysts, however, at high temperatures an extreme surface loss is observed. It is necessary to balance these contradicting findings in order to prepare both active and stable catalysts.

3. Oxidative attack by H_2O_2/ impact of selectivity on stability

This degradation pathway is based on the formation of H_2O_2 as byproduct of the ORR. As we described before, ORR can proceed either by an overall four-electron reduction mechanism to form water or by a two-electron mechanism forming hydrogen peroxide (H_2O_2) species. Thus the selectivity which depends on the precursors and type of metal species [100,148,149] of the Me-N-C catalysts plays a key role. The loss of the metallic ion in the Me-N-C sites leaves behind free metal ions, which can form radical oxygen species with the presence of H_2O_2. This reaction is known as Fenton's reaction:

$$Fe^{2+} + H_2O_2 + H^+ \rightarrow Fe^{3+} + {}^{\cdot}OH + H_2O \text{ [150]} \qquad (2.31)$$

The radical oxygen species are highly reactive and can oxidize the active moieties like the N heteroatoms, which can be responsible for catalyst deactivation and decomposition [135,151]

The hydroxyl free radicals are the main cause of peroxide related degradation, especially when using carbonaceous materials, where the radical attack leads to carbon corrosion and to the loss in conductivity [146,152,153].

Furthermore, upon release from the catalyst layer, these species can cause instability issues also to the membrane due to their highly oxidizing nature [154].

In a most recent work by Banham et al. [155,156] a galvanostatic mode was employed in order to test the stability of a MEA as this most closely represents the operating mode in a commercial portable/backup power fuel cell product. The authors consider several instability mechanisms such as demetallation of NPMC, attack by H_2O_2 (and/or free radicals), protonation of the active site or protonation of N species neighbouring the active site, followed by anion adsorption and micropore flooding. These mechanisms were previously proposed by different groups and are summarized by Banham et al. [157].

According to these results, the authors doubt the demetallation, the micropore flooding, and the active-site protonation/anion binding as being a large contributor to instability, at least for the family of NPMCs evaluated in their work. The authors favour the oxidation of the carbon/active sites. Based on the results obtained, it is unlikely that carbon corrosion occurs electrochemically at a significant rate at potentials < 0.6 V. Thus, their primary hypothesis for the rapid performance decay of their catalyst is the chemical attack of carbon/active sites by H_2O_2 or by radicals. However, these results do not preclude the possibility that other mechanisms are also occurring.

In addition, a work by Goellner et al. also attributes the instability of NPMC in the formation of highly-oxidizing radical species through a mechanism similar to the Fenton reaction for Fe or Co/N/C catalysts which are placed at the cathode side of a PEMFC [158].

Lefevre and Dodelet [159] treated pyrolysed porphyrin-derived Fe-N-C catalysts or Fe-salts under various conditions, with a 5% H_2O_2 in H_2SO_4. They reported a loss of ORR activity for all materials, with the magnitude of activity loss being sample dependent. This degradation was attributed to the oxidation/attack of the active site structures by H_2O_2 itself, or radical species formed by the simultaneous presence of H_2O_2 and Fe ions. In addition, the authors were able to determine that the total Fe content has a crucial role with NPMCs having a higher Fe content to be more stable.

Koslowski et al. [91] obtained contradicting results for pyrolysed N_4-macrocycle complexes, where negligible performance loss was observed after treating Me-N-C catalyst materials in concentrated H_2O_2 for ten minutes at room temperature.

In addition, even though Dodelet's group earlier attributed the origin of catalyst instability in acid medium to the release of peroxide during ORR, in a later work by Charreteur et al. [147], they found that their stable catalyst releases high peroxide amounts. The NH_3 treated catalyst shows low H_2O_2 amounts but is very unstable. Indeed, domains that are more graphitic involve an improved conductivity that may prevent the active site from remaining as Fe^{3+} and demetallizing, hence linking the instability to the mechanism.

In addition Zhang et al. [160] recently reported that by lowering the Fe content of a Fe-N-C catalyst to 50 ppm, a Fenton reaction was not an important cause of instability for the rapid initial performance loss of such catalysts.

This point out, that the impact of H_2O_2 species on NPMC stability is material dependent. Nevertheless, a mitigation strategy to overcome this issue is the acid leaching which often results in much higher ORR activity thanks to the removal of unstable and unreactive phases from the porous catalyst, which leads to an exposure of additional active sites. The acid leaching or the second heat-treatment does not influence the type of active sites but the relative content might change [91,161].

4. Protonation followed by a possible anion adsorption of the Active Site

In 2011 Dodelet's group [136], reported that for the catalysts prepared under NH_3 (even using small amounts) and tested in acidic environment, the surface nitrogen species neighbouring (not part) of the active site are the source of the loss of catalytic activity during fuel cell operation. The performance loss was due to protonation of the aforementioned surface nitrogen species, followed by anion binding. Once anion binding occurred, a decrease in ORR activity was observed. Eventually, the activity of the acid-resistant FeN_4 sites is restored after a thermal or chemical treatment due to the removal of the anion.

This mechanism leads to the deactivation of some catalytic centres as soon as the catalyst is exposed to the electrolyte and therefore could be considered as deactivation mechanism and not really as a degradation mechanism because this process is already reflected in the initial activity of a catalyst and the catalyst can often be reactivated.

5. Flooding of micropores

This mechanism was proposed by the group of Dodelet initially to help explain the rapid initial (< 20 hours) decay in performance. It is believed that as current is generated; water can start to fill the micropores of the NPMC. As for some NPMCs the active sites are hosted in micropores, flooding of the micropores should result in substantial mass transport limitations, which means the diffusion of oxygen will be lowered [152,160].
According to the authors, after a first decay common to all electrocatalysts that they prepared, only a Fe-N-C (NC Por_0.8 -1150 Ar + NH_3) catalyst (prepared with MOF and chloroiron-tetramethoxyporphyrin at 1050 °C) showed an improvement in durability attributable to a decrease in water flooding of the catalytic sites, particularly those located in micropores [162].
To support their hypothesis in a later work the authors clarified the role of iron in the first rapid decay of the activity excluding iron (through a Fenton reaction with H_2O_2) as the origin of the first rapid decay of these catalysts in fuel cells. The authors also concluded that H_2O_2 itself is also not at the origin of instability. A slow electro-oxidation of the carbonaceous support of the catalyst, lasting about 15 h at 0.6 V in H_2/O_2 fuel cell and transforming the initially hydrophobic catalyst layer into a hydrophilic one, could explain the first fast instability at 0.6 V of NC_Ar + NH_3 and also that of all other MOF catalysts, leading to micropore flooding, which is inducing mass transport problems [160].
This hypothesis was criticized by Banham et al. [156] along with a more recent work by the group of Dodelet [139] as discussed above for the demetallation mechanism.

It is important to note, that it is possible the lack of durability of most Me-N-C catalysts will have more than one origin, complicating, therefore, the resolution of this problem. In the following, the recent progress achieved in durability/stability in PEMFCs is summarized.

Table 2.4: Summary of some of today's most durable/stable Fe-N-C catalysts. RDE corresponds to Rotating Disk Electrode results and MEA to Membrane Electrode Assembly, which means these results, were obtained in PEMFCs.

Name of NPMC	Protocol used	RDE or MEA	Performance loss	Ref.
PANI-FeCo-C	0.6 -1.0 V, N_2, 30000 cycles	MEA	20 % (in current density @ 0.8 V)	[58]
Fe/N/CF	0.6 -1.0 V, Ar, 35000 cycles	RDE	7.9 mV in $E_{1/2}$	[3]
Fe-N-C	0.1 – 0.4 V, O_2, 5000 cycles	RDE	0 %	[144]
	0.6 – 0.9 V, O_2, 5000 cycles		30%	
	1.2– 1.5 V, O_2, 5000 cycles		40%	
FeIM/ZIF-8	0.0 -1.1 V, Ar, 10500 cycles	RDE	10 mV in $E_{1/2}$	[106]
Fe-3PEI	0.2 -1.1 V, O_2, 5000 cycles	RDE	12.3 % in $E_{1/2}$	[163]
Fe-N-C	@ 0.5 V for 50 h	MEA	< 5 % (in current density @ 0.5 V)	[97]
Fe-PANI/C-Mela	0.39 -1.04 V, O_2, 10000 cycles	RDE	< 5 % (in current density @ 0.65 V)	[164]
	@ 0.6 V for 100 h	MEA	> 80 % (in current density @ 0.6 V)	
Pod(N)-Fe	@ 0.45 V for 150 h	MEA	< 5 % (in current density @ 0.45 V)	[74]
PANI-Fe-C	@ 0.4 V for 200h	MEA	< 5 % (in current density @ 0.4 V)	[143]
	@ 0.6 V for 200h		50 % (in current density @ 0.6 V)	
Fe-N-C	0.9 – 1.4 V, N_2, 900 cycles	RDE	40 mV in $E_{1/2}$	[79]
Fe-N-C	@ 0.5 V for 100h	MEA	15 % (in current density @ 0.5 V)	[2]
PAN-Fe03-1000NH3	@ 0.8 V for 7h	MEA	10 % % (in current density @ 0.8 V)	[4]
Fe/C-800	0.6 -1.0 V, O_2, 2000 cycles	RDE	< 5 mV in $E_{1/2}$	[77]

In summary, careful design and synthesis of Me-N-C materials are very important in order to produce highly active and stable catalysts. The type of precursor materials utilized, including the type of the metal and its nominal content in the final catalyst structure are very important parameters influencing ORR activity and stability/durability. In addition, the heat-treatment conditions, specifically the pyrolysis temperature, time and gas employed will result in performance variations, with the optimal conditions being material dependent.

3

Experimental Part

This chapter is divided into two main sections. Firstly, the preparation of Me-N-C catalysts by three different synthesis routes is described. The electrochemical evaluation of activity and durability is described, followed by physicochemical characterization methods of the catalysts with a variety of techniques in order to gain useful information on the structure and morphology of the studied catalysts.

3.1 Synthesis of the Me-N-C catalysts for Oxygen Reduction Reaction

It was already shown in the 1980s that ORR-active Me-N-C catalysts can be synthesized by mixing independent iron, nitrogen and carbon precursors followed by a heat-treatment step at temperatures > 600 °C [49]. This precursor approach was followed for the preparation of all catalysts prepared for the scope of this thesis. The synthesis route was the same for all catalysts following the mixing of a metal, nitrogen and carbon precursor, pyrolysed at a temperature ($\geq$ 800 °C), followed by an acid leaching step and a second heat treatment ($\geq$ 800 °C). The materials and steps involved are summarized in the following sections.

3.1.1 Synthesis 1. Me-N-C (MOF + MeAc + Phen)

The first project dedicated to this thesis was to investigate the effect of metal species on the stability of Me-N-C catalysts. To prepare the catalysts a synthesis route adapted by the work of Proietti et al.[2], that led to the most active Fe-N-C catalyst of that time, was followed. The synthesis of the catalysts was done by mixing a metal organic framework (MOF) with different metal acetates (MeAc) and 1,10 phenanthroline (Phen). The metals that were used are Fe, Co, Cu, Ni, Mn, Cr, Mo, Zn, Ru and bimetallic combinations of Fe&Co, Mn&Co, Mo&Co, and Ni&Co all with 2 wt% metal in the precursor.The bimetallic catalysts had a molar ratio of Me_1:Me_2 of 1 in the precursor. In the following, the mixture was heat treated at 950 °C under nitrogen for 2 hours. After cooling down an acid leaching was performed in 2 M HCl for 4 hours and the final catalysts were obtained after a second heat-treatment under the same conditions. A schematic figure of the preparation is presented in Figure 3.1.

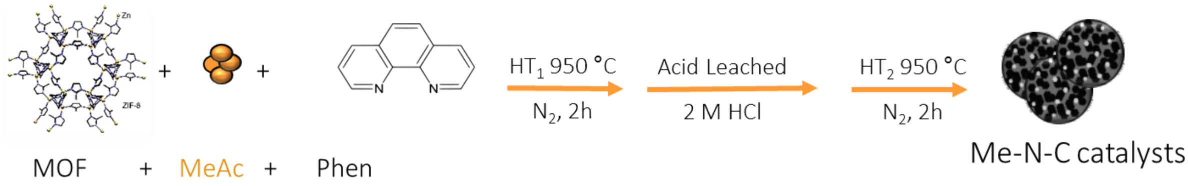

Figure 3.1: Preparation method of MOF-based Me-N-C catalysts.

For each synthesis, 2 mmol Z1200 was mixed with 1.5 mmol 1,10 phenanthroline and 0.25 mmol metal acetate in a mortar until a homogeneous mixture was obtained. The precursor mixture was then filled into a quartz boat and placed in an oven where it was heat-treated with a ramp of 450 °C · h^{-1} in inert gas atmosphere to 950 °C. After 2 hours, the sample was cooled down (< 80 °C) and transferred to 2 M HCl for acid leaching. The acid leaching was accelerated by placing the solution in an ultrasonic bath for about 1 h. After additional 3 h in the acid, the sample was filtered, rinsed with deionized water and dried (overnight). For the second heat-treatment, the conditions were identical to the first heat treatment.

3.1.2 Synthesis 2. Fe-N-C (DCDA + FeAc + Phen (±S))

The second project was to investigate the influence of sulfur addition on the precursors. It was shown by Herrmann et al. [149], Kramm et al. [94], and Ferrandon et al. [143], that the introduction of sulfur in the precursor mixture hinders the formation of inactive iron species (e.g. iron carbides) in the final catalysts. In addition, Kicinski et al. [163], showed that sulfur addition leads to an enhanced specific surface area of the catalysts. In principle, in the range of investigated pyrolysis temperatures, it has been observed that inactive iron species such as iron carbides are formed which are believed to compete with the active FeN_4 site formation [94,143]. In this context, a new preparation approach was employed with the use of iron acetate (FeAc), dicyandiamide (DCDA) as the pore-forming agent, 1,10 phenanthroline (Phen) as the nitrogen and carbon source and sulfur (S) as the promoting agent. It is important to note that a reference catalyst without the addition of sulfur was prepared for reasons of comparison.

For the preparation of the catalysts, 2.85 mmol Phen were mixed with 20.0 mmol DCDA and 0.76 mmol FeAc in a mortar until a homogeneous mixture was obtained. In case of sulfur addition, the S-pellets were added to the precursors and thoroughly mixed as indicated in Figure 3.2. In this project, the sulfur to iron molar ratio (S to Fe ratio) was varied between 0.0 - 2.45.

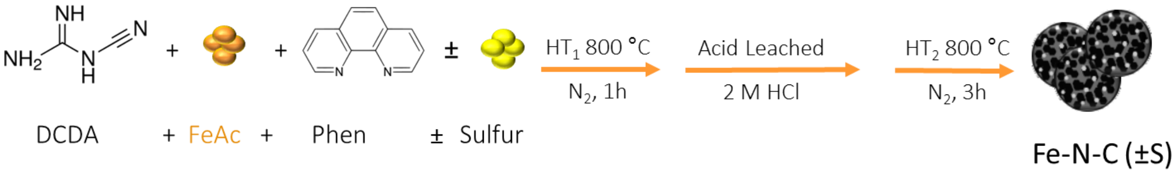

Figure 3.2: Preparation method of DCDA-based Fe-N-C (±S) catalysts.

The precursor mixture was then filled into a quartz boat and placed in an oven where it was heat-treated with a ramp of 300 °C · h^{-1} in inert gas atmosphere. In a first step, the pyrolysis temperature was kept at 300 °C for 30 minutes, in the second step, at 500 °C for 30 minutes and for the final step at 800 °C for 1 hour. The sample was cooled down (< 80 °C) and transferred to 2M HCl for acid leaching. The acid leaching was accelerated by placing the solution in an ultrasonic bath for about 1 h. After 12 h the sample was filtered, rinsed with deionized water and dried (overnight).

The reference catalyst and the best performing one of the S-addition series (S to Fe ratio of 0.82) were additionally (separately) heat-treated with a heating ramping rate of 600 °C · h^{-1} in inert atmosphere and at a pyrolysis temperature of 800 °C where the samples were kept for 3 hours.

3.1.3 Synthesis 3. ^{57}Fe-N-C (DCDA + FeAc + PANI(S))

For the third project, polyaniline, which represents a favorable combination of aromatic rings connected via nitrogen-containing groups, was selected as a promising template compound for nitrogen and carbon [58].

For the preparation of polyaniline, 90 mmol aniline was mixed with 264 mmol of the oxidant ammonium peroxydisulfate (APS) $(NH_4)_2S_2O_8$, in 0.5 M HCl and let to polymerize for 24h below 4 °C. The solvent evaporated at 150 °C for 24 h. This means the residuals of APS remain in the PANI precursor.

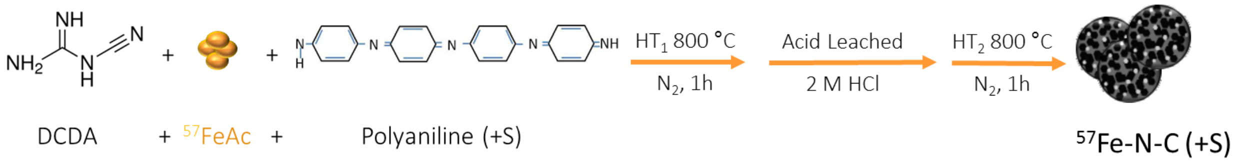

Figure 3.3: Preparation method of PANI-based ^{57}Fe-N-C (+S) catalyst.

In the following, 116 mmol of polyaniline was mixed with 3.4 mmol iron acetate, 1.1 mmol iron (57) acetate, and 418 mmol dicyandiamide (DCDA) in a mortar until a homogeneous powder was obtained. The powder mixture was first heat-treated up to 800 °C for 1 hour with a ramping rate of 300 °C · h^{-1} under inert atmosphere. Intermediate steps at 300 °C for 30 minutes and at 500 °C for 30 minutes were performed. After cooling down the catalyst was transferred in 2 M HCl for acid treatment where it was placed for 1h in the ultrasonic bath and in total 12 hours. In the following, the product was filtered and washed with distilled water until a neutral pH was achieved. After drying at 80 °C overnight the catalyst was heat treated again at 800 °C for 1 h in inert atmosphere with a heating ramp of 600 °C · h^{-1}.

Table 3.1: Summary of chemical compounds used for the different preparation methods.

List of materials	Chemical formula and Molecular weight	Company
Basolite Z1200	$(C_8H_{10}N_4Zn)$, 225.4 g/mol	Sigma Aldrich
1.10 Phenanthroline	$C_{12}H_8N_2$, 180 g/mol	Sigma Aldrich
Dicyandiamide	$C_2H_4N_4$, 84 g/mol	Alfa Aesar
Aniline	$C_6H_5NH_2$, 93 g/mol	Alfa Aesar
Ammonium peroxydisulfide, 98%	$(NH_4)_2S_2O_8$, 228 g/mol	Alfa Aesar
Sulfur, 99%	S_8, 32 g/mol	Carl Roth
Iron acetate	$Fe(CH_3COO)_2$, 174 g/mol	Alfa Aesar
^{57}Iron acetate	$^{57}Fe\ (CH_3COO)_2$, 175 g/mol	Por-Lab
Cobalt acetate, 99%	$Co(CH_3COO)_2 \cdot 4H_2O$, 249 g/mol	Alfa Aesar
Copper acetate, 99%	$Cu(CH_3COO)_2$, 182 g/mol	Alfa Aesar
Manganese acetate, 98%	$Mn(CH_3COO)_2$, 173 g/mol	Alfa Aesar
Nickel acetate, 99%	$Ni(CH_3COO)_2 \cdot 4H_2O$, 248 g/mol	Alfa Aesar
Chromium acetate trimer	$(CH_3COO)_7Cr_3(OH)_2$, 603 g/mol	Alfa Aesar
Molybdenum acetate dimer	$Mo_2(CH_3COO)_4$, 428 g/mol	Alfa Aesar
Ruthenium acetylacetonate, 97%	$C_6H_{12}O_6Ru$, 281 g/mol	Sigma Aldrich

3.2 Characterization of Me-N-C catalysts for Oxygen Reduction Reaction

This section deals with the general electrochemical evaluation and structural characterization procedures used in this thesis. In the first part, the performance (activity and durability) determination methods, such as Cyclic Voltammetry (CV) and Rotating Disk Electrode (RDE) of Me-N-C catalysts are described. In the second part, the structure and morphology characterization techniques, such as N_2-sorption measurements, Transmission Electron Microscopy (TEM), X-Ray Photoelectron Spectroscopy (XPS), Mössbauer spectroscopy and Raman spectroscopy are introduced.

3.2.1 Electrochemical Characterization of Me-N-C catalysts

Firstly, to better understand the electrocatalytic processes, one has to elevate the theories of electrode-electrolyte interaction. At an electrode surface, two fundamental electrochemical processes that produce current can be distinguished: the so-called Faradaic process (charge transfer) as a result of chemical reaction at the electrode which is proportional to the Faradaic current, and the non-Faradaic current (no charge transfer) which is caused due to change in double layer when potential is altered. The non-Faradaic current is the background current in voltammetric measurements. While the Faradaic processes are of main interest for an electrochemical investigation, the effect of non-Faradaic processes must be taken into account as well [164].

In this work, for easier comparison with data given in the literature, the potential is always given vs. the Reversible Hydrogen Electrode (RHE). RHE is defined as a subtype of the Standard Hydrogen Electrode (SHE) and corresponds to

$$E = 0.0000\,V - 0.0591 * pH \qquad (3.1)$$

Depending on the environment of the experiments, the corresponding potential can be calculated. In this work, the potential was experimentally measured in the electrolyte by a voltammeter.

Ink preparation:

In order to perform the electrochemical evaluation of the Me-N-C catalysts, a catalyst ink is required. In this thesis, the preparation of the catalyst ink is always the same and includes 5 mg of the catalyst powder, 25 µl of Nafion solution (5 wt.%), 83 µl distilled water and 142 µl of ethanol. The mixture is placed in an ultrasonic bath for 30 minutes until a homogeneous solution is obtained. In the following, the ink is placed in a vortex for ca. 1 minute and in an ultrasonic needle for final dispersion for about 30 seconds.

Electrode preparation

5 µl of the catalyst ink that served as working electrode, was placed on the glassy carbon disc (A= 0.1963 cm^2) of the electrode and dried. The catalyst loading in all cases was 0.5 mg cm^{-2} and the Nafion to catalyst ratio was 0.25. A homogeneous catalyst deposition onto the glassy carbon disk electrode is very important in order to obtain reliable and reproducible data.
A glassy carbon rod and a silver/silver chloride Ag/AgCl/(3M KCl) were used as counter and reference electrodes, respectively.

Cyclic Voltammetry (CV)

Cyclic voltammetry is a method, which involves sweeping the electrode between two potential limits at a known sweep rate. By convention, the positive going current is the anodic and the negative going current is the cathodic. At the beginning, the working electrode is held at some potential, E_i, where no electrode reactions occur. During measurement, the potential is swept linearly at a rate ν between two limiting potentials E_1 and E_2. The same sweep rate is normally chosen for the forward and reverse sweep. The corresponding current is recorded as a function of the varying potential [164].
In this work, cyclic voltammetry is applied to investigate the presence (if the case) of a redox transition of the metals in the absence of oxygen. The measurements were carried out in a conventional three-electrode cell (Figure 3.4) connected to three electrodes (working, reference and counter) immersed in an electrolyte solution. The potentiostat applies and maintains the potential between the working (WE) and the reference electrode (RE), while at the same time measuring the current at the working electrode. Charge flows between the working electrode and the counter electrode (CE). A recording device (e.g. a computer) is used to record the resulting cyclic voltammograms as a graph of current versus potential. If a reduction reaction takes place at the WE, an oxidation reaction occurs at the CE with the same reaction rate [164,165].

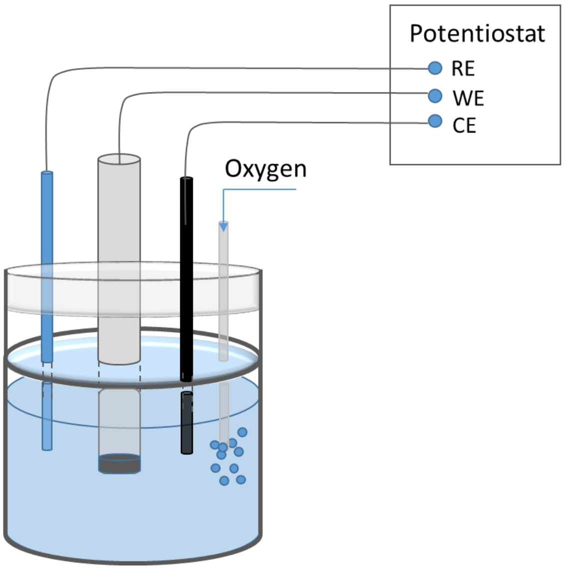

Figure 3.4: Schematic configuration of a three-electrode electrochemical cell.

Prior to the CV measurements, the electrolyte solution was saturated with N_2 in order to remove any reactive species. In the following, the CV curves were obtained by cycling the potential between 1.0 to 0.0 V with a scan rate of 300 mV s^{-1}, 100 mV s^{-1}, and 10 mV s^{-1}. As an example of the information provided by cyclic voltammetry, a CV curve of a Fe-N-C (S) catalyst is given in Figure 3.5. It becomes apparent, that a pair of peaks at ca. 0.70 V vs. RHE can be observed, some publications associate the peak with the metal centred Fe^{2+} / Fe^{3+}redox peak of the active site [166,167].
Ramaswamy et al. [166] reported a relationship with the position of the redox peak and the activity of the catalyst. The charge associated with this peak was used to determine the number of active sites and hence the site density.
It has to be noted that this peak can also be associated with a quinone/hydroquinone couple on the carbon surface [168].

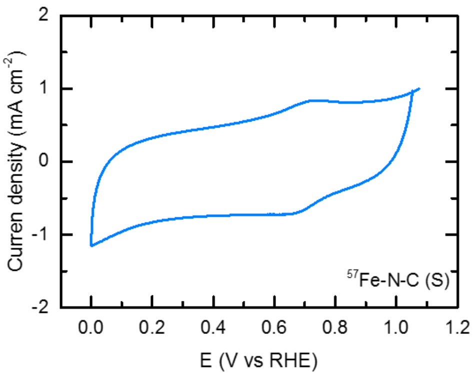

Figure 3.5: Cyclic Voltammogram of the ^{57}Fe-N-C (S) catalyst in N_2-saturated 0.1 M H_2SO_4 electrolyte, with 10 mV s^{-1} scan rate.

Rotating Disk Electrode (RDE)

The rotating disc electrode is a well-established technique and has been used in order to evaluate the activity and durability of the catalysts for the ORR in acidic or alkaline media. RDE is a technique based on controlled convection by rotating the working electrode in the electrolyte solution. The working electrode rotates with an angular velocity (ω in rounds per minute), drawing up the electrolyte along with the electrochemically active substances (in this case oxygen) towards the rotation axis as seen in Figure 3.6a, and flinging it out radially. This technique leads to better transport of reactants towards the electrode surface [164].

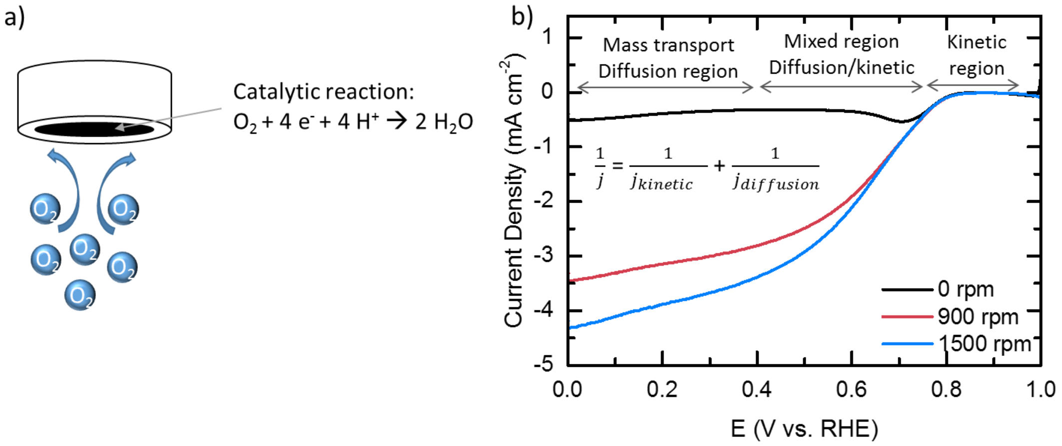

Figure 3.6: a) Schematic representation of the working electrode while rotating [93] and b) RDE curves of the Fe-N-C catalyst in O_2-saturated 0.1 M H_2SO_4 electrolyte, with 10 mV s^{-1} scan rate and 0, 900 and 1500 rpm. The regions of diffusion and kinetic controlled process are marked.

In this work, the controlled mass transport of the reactants is achieved by setting the working electrode during the experiment into rotation (0, 900 and 1500 rpm) as seen in Figure 3.6b. It can be seen by the polarization curves within the diffusion-controlled region, that by increasing the rotation velocity the mass transfer is improved and the diffusion plateau is shifted to higher current density values (absolute values). This plateau is known as the mass transfer limited region of the voltammetry profile where the rate of the ORR reaction is limited by the availability of oxygen at the electrode surface.

The diffusion limiting current density increases in magnitude with increasing ω according to the Levich equation:

$$j_{Diff,lim} = 0.62 \cdot z \cdot c_O \cdot F \cdot A \cdot D^{\frac{2}{3}} \cdot v^{-\frac{1}{6}} \cdot \omega^{\frac{1}{2}} = B \cdot c_O \cdot \omega^{1/2} \tag{3.2}$$

where z is the number of exchanged electrons, c_O is the concentration of dissolved oxygen in the electrolyte, F is the Faraday constant, A is the electrode's geometric area, D is the diffusion coefficient, ω is the rotation velocity, v is the kinematic viscosity of the electrolyte and B is the Levich constant ($B = 0.62 \cdot z \cdot F \cdot A \cdot D^{\frac{2}{3}} \cdot v^{-\frac{1}{6}}$).The equation is derived from the description of the Nernst diffusion layer (δ):

$$\delta = 1.61 \cdot \omega^{-1/2} \cdot v^{1/2} \cdot D^{1/3} \tag{3.3}$$

and Fick's first law:

$$j_{Diff} = z \cdot F \cdot A \cdot c_O \frac{D}{\delta} \tag{3.4}$$

The total current density (j) can be calculated form the kinetic current density j_{kin} and the diffusion limiting current density j_{Diff} according to:

$$\frac{1}{j} = \frac{1}{j_{kin}} + \frac{1}{j_{Diff,lim}} \tag{3.5}$$

The current density can be derived by a simplified from considering only the reduction current from the Butler-Volmer equation (valid due to high overpotential η):

$$j = -j_0 \cdot exp\left(-\frac{\alpha_C \cdot z \cdot F}{R \cdot T} \cdot \eta\right) \tag{3.6}$$

where j_0 is the exchange current density (current at zero overpotential), α_c is the cathodic charge transfer coefficient, R is the universal gas constant, T the temperature and η the overpotential.
The kinetic current density can be calculated by the combination of Equation 3.2 and Equation 3.5:

$$j_{kin} = \frac{j \cdot j_{Diff,lim}}{j_{Diff,lim} - j} \tag{3.7}$$

In this work, the diffusion limiting current density and the total current density can be experimentally determined by the RDE technique. Regarding the diffusion limiting current density it is determined experimentally and not with the theoretical value of a four-electron reduction to water. The RDE plots, which show j_{Diff} (mA cm^{-2}), correspond to the current density corrected for the capacitance current (non-Faradaic process)).

The kinetic current density is then calculated by the as measured current (j, used as the total current) and the $j_{Diff,lim}$ (at 0.0 V):

$$j_{kin} = \frac{j \cdot j_{Diff,lim}}{j_{Diff,lim} - j} \tag{3.8}$$

The mass related kinetic current density (A g^{-1}) is determined by:

$$Jkin = \frac{j_{kin}}{m_{cat}} \tag{3.9}$$

with m_{cat} the catalyst loading in the working electrode which is 0.5 mg cm^{-2}.
From the RDE curves the onset (E_{Onset}) and the half-wave potential ($E_{1/2}$) can also be determined. The onset potential is defined at <-0.1 mA cm^{-2} and the half-wave potential corresponds to the half of the maximum diffusion limiting current. The kinetic current density is usually taken at 0.75 V if not stated otherwise.

In the following the activity and durability protocols used in this work are given.

Table 3.2: Activity protocol.

Type of scan	rpm	Potential range / V vs. RHE	gas	Sweep rate / mV/s	No of sweeps
CV	0	1,0 … 0,0	N_2	300	20*
CV	0	1,0 … 0,0	N_2	100	2
CV	0	1,0 … 0,0	N_2	10	1
OCP	0	About 15 min	O_2	-	-
CV	0	1,0 … 0,0	O_2	10	1
CV	900	1,0 … 0,0	O_2	10	1
CV	1500	1,0 … 0,0	O_2	10	1

* Only for initial activity

Table 3.3: Load Cycle durability protocol.

Type of scan	rpm	Potential range / V vs. RHE	gas	Sweep rate / mV/s	No of sweeps
		Activity Protocol			
Bihold 3s at 0.6, Bihold 3 s at 1.0 V	0	0.6 ….1.0	O_2		**1000**
		Activity Protocol			
Bihold 3s at 0.6, Bihold 3 s at 1.0 V	0	0.6 ….1.0	O_2		**1000**
		Activity Protocol			
Bihold 3s at 0.6, Bihold 3 s at 1.0 V	0	0.6 ….1.0	O_2		**1000**
		Activity Protocol			
Bihold 3s at 0.6, Bihold 3 s at 1.0 V	0	0.6 ….1.0	O_2		**1000**
		Activity Protocol			
Bihold 3s at 0.6, Bihold 3 s at 1.0 V	0	0.6 ….1.0	O_2		**1000**
		Activity Protocol			

Total: 5000 "cycles"

Table 3.4: Start/ Stop durability Protocol.

Type of scan	rpm	Potential range / V vs RHE	gas	Sweep rate / mV/s	No of sweeps
			Activity Protocol		
CV	0	1.0 …1.5	O_2	500	**1000**
			Activity Protocol		
CV	0	1.0…1.5	O_2	500	**1000**
			Activity Protocol		
CV	0	1.0 …1.5	O_2	500	**1000**
			Activity Protocol		
CV	0	1.0…1.5	O_2	500	**1000**
			Activity Protocol		
CV	0	1.0….1.5	O_2	500	**1000**
			Activity Protocol		

Total: 5000 cycles

3.2.2 Structural Characterization of Me-N-C catalysts

The large variety of characterization techniques applied in this thesis allowed the determination of the surface properties, porous distribution and composition of the Me-N-C catalysts and their subsequent correlation to their electrochemical features.

N_2-sorption measurements

In order to determine the specific surface area and the pore size distribution, N_2 sorption measurements were employed.

The Brunauer-Emmett-Teller (BET) theory describes the physical adsorption of gas molecules on a solid surface. The BET theory can be derived by the Langmuir theory, which is a theory for monolayer molecular adsorption, considering multilayer adsorption when there is no interaction between each adsorption layer and the Langmuir theory can be applied to each layer [169].

For pressures in the range $0.05 \leq P/Po \leq 0.35$, the BET equation is described as:

$$\frac{P}{V \cdot (P_0 - P)} = \frac{1}{V_m \cdot C} + \frac{(C-1)}{V_m \cdot C} \cdot \frac{P}{P_0} \tag{3.10}$$

where P and P_0 are the equilibrium and the saturation pressure of adsorbates at the temperature of adsorption, V is the adsorbed gas quantity (cm^3), V_m is the monolayer adsorbed gas quantity (cm^3) and C is the BET constant as a function of the heat adsorption for the first layer (E_1) and for the second and higher layers (E_L) and is given by [169]:

$$C = exp\left(\frac{E_1 - E_L}{R \cdot T}\right) \tag{3.11}$$

The measurements were performed in a Quantachrome Autosorb 3-B instrument, started with the weighing of a certain mass of catalyst powder (typically between 50 and 80 mg) that was subsequently placed in a specially designed tube and out-gassed by heating it for 12 hours at 200 °C. This was followed by the measurement of the N_2-sorption isotherm, in which the sample container is introduced in a bath of liquid nitrogen. Subsequently, nitrogen gas enters the tube with a controlled flow. Induced by the adsorption of nitrogen on the surface of the catalyst the content of nitrogen within the gas phase decreases and as a consequence, the pressure is lower compared to a reference cell that is connected in the system. The difference in pressure is due to the adsorption of nitrogen in the samples, whereby the pressure ratio P/P_0 is related to the size of the pores in which nitrogen is adsorbed. The adsorption and desorption isotherms were recorded at 77 K in the range of $0.05 \leq P/P_0 \leq 0.1$

The shape of the resulting isotherm provides information about the adsorbent's porous features. For this purpose, a general IUPAC classification consisting of six different types of isotherms are shown in Figure 3.7.

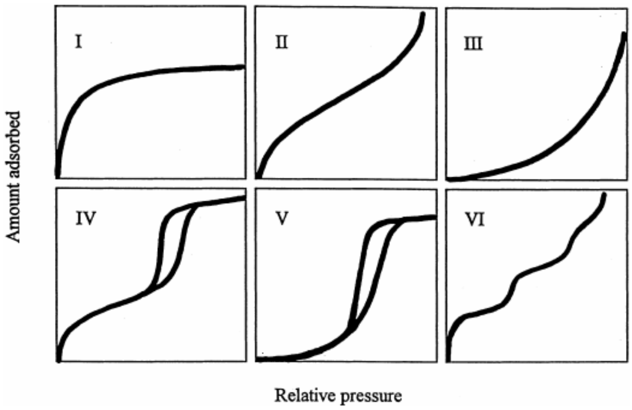

Figure 3.7: General classification of sorption isotherms [170].

According to Herrmann et al. [171] and Kramm et al. [161] the kinetic current density is related to the surface area of mesopores (20—500 Å) whereas Dodelet's group [172] found a correlation towards the micropore (≤ 20 Å) surface area. In order to evaluate the fraction of different pore sizes and their influence on the oxygen reduction reaction, the V-t method was used to distinguish the surface area related to micro- and mesopore surface area.

Transmission Electron Microscopy (TEM)

Transmission electron microscopy uses high energy electrons (up to 300 kV accelerating voltage) which are accelerated to nearly the speed of light. An image is formed from the interaction of the electrons transmitted through the specimen; magnified and focused onto an imaging device, such as a fluorescent screen, on a layer of photographic film. The imaging mode provides a highly magnified view of the micro- and nanostructure and ultimately, in the high-resolution imaging mode a direct map of atomic arrangements can be obtained (high-resolution EM = HREM). The diffraction mode (electron diffraction) displays accurate information about the local crystal structure [173].
Regarding the TEM technique used for characterization of Me-N-C catalysts, it is a very useful tool, for studying the structure of the catalysts. TEM can be used in order to investigate the microstructure of the samples, to identify the carbon phases (amorphous, turbostratic) and more importantly how the metal is embedded in the carbon support. Typical TEM images of carbon-based materials can be seen in Figure 3.8.

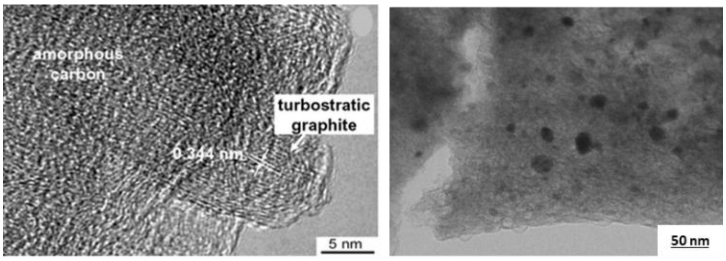

Figure 3.8: TEM images of carbon phases (left) image taken by Dimovski et al [174]. Synthesis of graphite by chlorination of iron carbide at moderate temperatures, and (right) of a Fe-N-C catalyst with iron embedded in carbon

In this work, the catalyst powder was immersed in ethanol and sonicated for 10 minutes in an ultrasonic bath, then, a small drop was placed on a copper grid (Plano S147-4) and kept for drying at room temperature. Measurements were conducted by a FEI CM 20 ST system equipped with a LaB6

Filament and a SDD-EDS detector. The maximum resolution of the system is 2.3 Å. M. Kübler performed the TEM measurements.

X-Ray photoelectron spectroscopy (XPS)

X-Ray photoelectron spectroscopy (XPS) is a surface characterization technique that can analyse a sample to a depth of 2 to 5 nanometers (nm). XPS provides information about the chemical structure and composition of a sample surface and requires Ultra-High Vacuum (UHV) conditions. A surface is irradiated with X-rays (usually monochromatic Al Kα of 1486.6 eV or Mg Kα of 1253.6 eV)) in vacuum [175]. When an X-ray photon hits and transfers this energy (hv) to a core-level electron, it is emitted from its initial state with a kinetic energy (E_{kin}). The photoelectron's kinetic energy dependent on the core electron's binding energy (E_B) which is a direct measure of the energy required to remove the electron from the material and is specific to the orbital of the element from which it came, and taking into account the work function (ϕ) of the spectrometer, the binding energy can be therefore calculated according to [176]:

$$E_B = hv - \varphi - E_{kin} \tag{3.12}$$

By comparing the measured binding energies with the literature data of reference compounds, one can gain information about possible bond structures.

For the investigation of Me–N–C catalysts, the changes of C, N, Me can be followed in the 1s spectra of nitrogen, carbon, or oxygen. Whereas, the analysis of Me 2p regions are more complicated due to the low metal concentrations and the lower sensitivity in comparison to N1s. Therefore, the analysis of the N1s region is used to identify structural changes or to assign specific N types as active sites. Several authors assign specific N types such as pyridinic or pyrrolic with the participation of a metal atom, like MeN_x, to active centres [136,177].

In this work, X-Ray photoelectron spectra (XPS) were measured at DAISY Fun in the group of Prof. Jaegermann with a Specs Phoibos 150 hemispherical analyzer and a Specs XR50M Al Ka X-ray source (E = 1486.7 eV). Before the measurements, the catalyst powder was pressed on an indium foil and transferred into the high-vacuum system. Spectra were analyzed using CasaXPS. Peaks were fitted using a Shirley background and a mixed Gauss/Lorentz peak. A. Shahraei and N. Weidler performed the measurements and the data analysis.

Mössbauer spectroscopy

The physical principle of this technique is based on the observed resonance absorption of γ- rays. A nucleus with Z protons and N neutrons in an excited state of energy E_a undergoes a transition to the ground state of energy E_g by emitting a gamma quantum of energy E_a-E_g. The gamma quantum may be absorbed by the nucleus of the same kind (same Z and N) in its ground state, whereby a transition to the excited state of energy E_a takes place (resonance absorption). The subsequent transition to the ground state emits a conversion electron e^- or a gamma quantum (resonant fluorescence) [178].

In the case of freely moving atoms or molecules, a recoil momentum is imparted to the decaying nucleus upon emission of a gamma quantum, whereby the emission line is shifted by the recoil energy to lower energy. The same recoil phenomenon occurs in the absorbing nucleus but with opposite direction, i.e. the absorption line is shifted to higher energy by the same amount of recoil energy [179].

In other words, the recoil effect reduces the transition energy for the emission process and increases the transition energy for the absorption process. Due to the recoil effect, the resonant absorption between the emission and absorption lines is not observable. Resonance can be measured by Mössbauer when emission and absorption lines are brought to sufficient overlap (not too narrow nor too large). To achieve this the iron nuclei has to be embedded in solid, under these conditions the recoil effect can be minimized. In order to compensate for the energy loss of the gamma quanta due to the recoil effect, the source and the absorber move relative to each other according to the Doppler Effect [178].

The interaction between a nucleus and its surrounding environment is known as a hyperfine interaction. These interactions are very small compared to the energy levels of the nucleus itself but the extreme energy resolution of the Mössbauer effect enables these interactions to be observed.

In principle, three kinds of hyperfine interactions may be observed in a Mössbauer spectrum: (i) the electric monopole interaction between protons of the nucleus and electrons (mainly s electrons) penetrating the nuclear field, (ii) electric quadrupole splitting between the nuclear quadrupole moment and an inhomogeneous electric field at the nucleus, and (iii) the magnetic dipole interaction between the nuclear magnetic dipole moment and a magnetic field at the nucleus.

(i) The electric monopole interaction results in the isomer shift (δ_{ISO}) which provides information on the oxidation state, spin state, and bonding properties such as covalence and electronegativity.

(ii) The quadrupole splitting (ΔE_Q or ε) refers to oxidation state, molecular symmetry and bond properties.

(iii) The magnetic-dipole interaction (H_0) gives information on the magnetic properties of the material under study [178].

Magnetic dipole interaction and electric quadrupole interaction may be present in a material simultaneously (together with the electric monopole interaction, which is always present). In Figure 3.9 the Mössbauer parameters as described by the hyperfine interactions are presented.

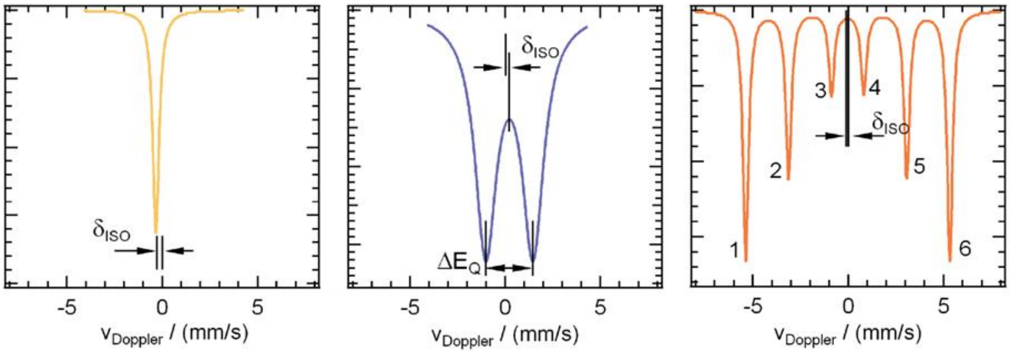

Figure 3.9: Mössbauer spectra of (a) an electric monopole interaction, (b) an electric quadrupole interaction, and (c) a magnetic interaction on the energy levels of excited and ground states. Graph taken by [177].

To date, Mössbauer spectroscopy on Fe-N-C catalysts has been well established. This spectroscopic technique is a very powerful tool for the identification of the active species in the catalysts, which is a topic of debate in the NPMC community, as discussed in chapter 2.2.2. In a Mössbauer spectrum of a Fe-N-C catalyst one can observe doublets, a singlet or sextets. The presence of FeN_4 sites give rise to a doublet independent of their oxidation and spin states. The singlet is evidence of superparamagnetic iron, and sextets are related to the formation of different inorganic byproducts. These iron species are usually not of importance for the overall ORR activity, but one can extract important information on the processes that take place during the catalyst preparation [177].

In this work, the Mössbauer measurements were performed with a Wissel instrument with a 100 mCi $^{57}Co/Rh$ source. The samples were prepared and measured under standard conditions and the isomer shifts were determined relative to α-Fe at 298 K. In the case of the powder catalyst 100 mg were filled into a PTFE sample holder, all Mössbauer spectra were fitted with Lorentzian lines using the program Recoil. The goodness-of-fit was indicated by the reduced χ^2 value, which would be unity for perfect agreement between the calculated fit curve and the observed spectrum. The fitting process was done without fixing or limiting the range of any spectral parameter in the iteration procedure. The Mössbauer measurements and data analysis for the Paper II were performed by S. Wagner, further experiments and analysis were conducted by me.

Raman spectroscopy

In 1928, Sir C.V. Raman documented the phenomenon of inelastic scattering and in 1930 he won the Nobel Prize for the discovery of the effect named after him. As a monochromatic light (laser) hits a sample and interacts with molecular or crystal vibrations (phonons), Raman scattering occurs. When the elastically scattered light has the same energy as the incident light it is called Rayleigh scattering. If the system gains energy during this process, the scattered light loses this amount of energy and the system reaches a higher energy state (higher energy level) than it had before, it is called Stokes scattering. In case the transition starts from an excited vibrational state and ends in the ground state, the scattered photons gain energy and it is called anti-Stokes scattering. The latter process is rarer as most molecules at room temperature are in the ground state [180,181].

Regarding the Me-N-C catalysts studied in this work, these materials are carbon-based, thus Raman spectroscopy is a suitable technique to characterize the structure of the samples. In particular, Raman spectroscopy provides information on the type of the carbon (graphitic, diamond-like, amorphous etc.) [182], the graphene layer extension [183] and the content of disordered carbon [184]. In a typical Raman spectrum (Figure 3.10) two prominent bands corresponding to the D (1350 cm^{-1}) and G band (1590 cm^{-1}) are shown.

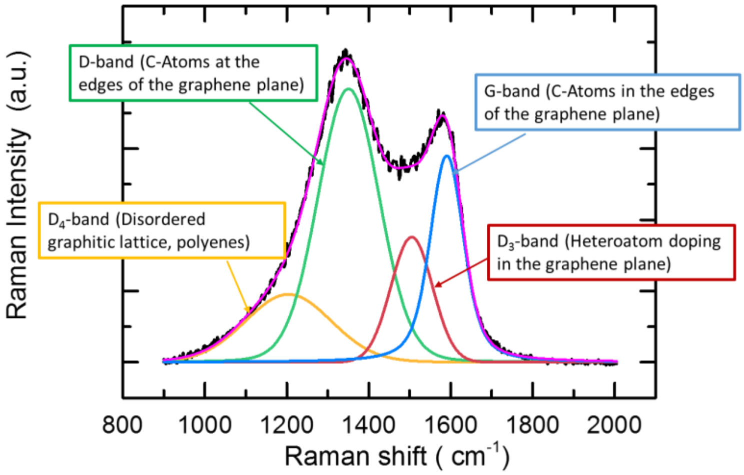

Figure 3.10: Typical Raman spectra of a Fe-N-C catalyst including the deconvoluted bands.

According to F. Tuinstra and J. L. Koenig [183] single crystals of graphite show one single line approximately at 1580 cm^{-1} which is referred as the G-band and is due to E_{2g} symmetry mode and is related to the C=C sp^2 (in-plane) bond stretching vibrations. In the Raman spectrum of all other carbon-based materials like activated charcoal, carbon black, and vitreous carbon a second line appears near 1360 cm^{-1} (D-band) produced by breathing vibrations of aromatic rings with A_{1g} symmetry mode [182,185–188].

The G-band and D-band are related to vibrations inside a graphene layer and vibrations at the edges of graphene layers, respectively. Therefore, the dominance of the G-band can be related to the high order of the graphite material. Large and homogeneous graphene layers are stacked above each other so that only a small contribution of vibrations at the edge of a graphene layer is found. When the graphite is cracked down (e.g. by ball milling), one will observe a decrease of the G-band and increase of the D-band. Therefore, the intensity ratio of D to G band (I_D/I_G) is extensively used in literature as a descriptor of the degree of graphitization [149,189–193].

In contrast to graphitic carbons, the spectra of the pyrolysed samples show that besides these two bands of the spectra two other signals appear which are typical for amorphous carbons. From the comparison with the literature, these bands can be assigned to small molecules, sp^2- hybridized carbons (D_4, 1200 cm^{-1}), and built-in defects caused by heteroatom doping (D_3 1500 cm^{-1}) [149,188,194].

In particular, for the D_3 band at approximately 1500 cm^{-1}, several authors studying metal phthalocyanines and metal porphyrins correlate this band to be sensitive to the type of the central atom [195,196] with changes in the electronic structure, the core size [197] and the bond distance (e.g. porphyrin centre to pyrrole N distance) [198]

There are several publications on Me-N-C catalysts that discuss the effect of carbon morphology of these catalysts on ORR activity, indicating that Raman spectroscopy is essential for the optimization of the structure and thus for the performance of these catalysts [199,200].

In this work an alpha 300R confocal Raman microscope from WiTec (Ulm, Germany) with a grid of 600 lines mm^{-1} using an excitation laser (532.2 nm) with a laser power of 1 mW was used in order to obtain the Raman spectra of the Me-N-C catalysts. The range of the measured spectra spreads from 0 to 4000 cm^{-1}, however since in most cases in the second order region (between 2200 and 3500 cm^{-1}) of the spectra were only broad bands (if so) visible, the deconvolution of the bands was applied only in the first order region (< 2200 cm^{-1}). The spectra were acquired by performing 10 scans, each with integration time of 10 s. A minimum of two positions were measured per sample to determine the average spectrum. The spectra were fitted assuming the presence of four bands for the catalysts using voigtian lines. The bands can be assigned as G band (1580 cm^{-1}), D band (1360 cm^{-1}), D_3 band (1500 cm^{-1}) and D_4 band (1200 cm^{-1}). The assignment of these bands to different carbon contributions is given in the discussion part.

The goodness-of-fit was indicated by the reduced χ^2 value, which would be unity for perfect agreement between the calculated fit curve and the observed spectrum. Typically, values between 1 and 5 were achieved. The fitting process was done without fixing or limiting the range of any spectral parameter in the iteration procedure and in addition, the Full Width at Half Maximum (FWHM) was considered to be of the same order of magnitude for each of the corresponding bands.

4

Results and Discussion

In this chapter, the most important results obtained during this work are reported in the form of publications, followed by an overall summary of the best Fe-based catalysts, characterized electrochemically and structurally under identical conditions in acidic media, which is related to Proton Exchange Membrane Fuel Cell application. The sequence of the sub-chapters follows the progress of the work carried out in these three years. Paper I and Paper II are related to Proton Exchange Membrane Fuel Cell (PEMFC) application, Paper III is related to Alkaline Fuel Cell (AFC) application and paper IV to Direct Methanol Fuel Cell (DMFC) application.

PAPER I The adsorption energy of oxygen species on a transition-metal surface has been correlated to the position of the d-band center (ε_d) with respect to the Fermi level (ε_F) (known as the d-band center model). According to this model, the metal–adsorbate (e.g. M-$_{O_{ads}}$) bond is weaker when the distance between the Fermi level and the d-band center (e_F-e_d) is larger [201–203].
Thus, the d-band center can be used (instead of the adsorption energy of a species on the surface) as an activity descriptor [127].
In this context, we chose to investigate most of the 3d transition metals of the first row of the periodic table and some of the 4d transition metals of the second row in order to study the effect of the metal centre on the durability of non-precious metal catalysts for the oxygen reduction reaction (ORR) in acidic media.

PAPER II In order to further enhance the activity and durability of Me-N-C catalysts towards ORR, a better understanding of the active sites towards ORR is required. The most commonly recognised structure of the active sites in Me-N-C catalysts is the coordination of a transition metal ion to nitrogen (MeN_x), especially FeN_4 sites. It has been reported by several authors that the doping of heteroatoms for example sulfur, shows positive effects on the performance of Fe- N-C catalysts.

The motivation of this work is to unravel the effect of sulfur on the active sites of Fe-N-C catalysts by Mössbauer spectroscopy, prepared with a novel synthesis approach developed by our group and subsequently derive a more rational design with respect to the durability of Fe- N-C catalysts.

PAPER III Since PEMFCs operate in a corrosive environment, the selection of electrocatalysts is limited to noble metals. One of the solutions enabling the use of inexpensive electrocatalytically active materials is switching from proton conductive membranes and ionomers to hydroxyl conductive ones. Such as low-temperature, polymer electrolyte fuel cells called Alkaline Fuel Cell (AFC). Operation with hydroxyl ions allows the use of catalysts derived from abundant 3d transition metals, such as iron, cobalt, nickel etc. Following the outcome of our previous work (section 4.2), we chose the catalyst where the S-addition was optimized, for durability testing in an alkaline environment. In a collaborative work with the group of Professor B. J. M. Etzold from the Chemistry Department of the TU Darmstadt, this catalyst was modified with the introduction of an ionic liquid.

PAPER IV Direct methanol fuel cell (DMFC) has recently drawn attention because of its unique advantages, such as high fuel energy density, facile liquid fuel storage, low working temperature, simpler system structure, and low emission of pollutants. In this project, we study a new preparation method with polyaniline as the nitrogen and carbon source. This promising catalyst is tested in a DMFC within a Research Stay Abroad in the group of Professor. S. Specchia in Politecnico di Torino, Italy (October-November 2017).

4.1 Effect of metal species on the stability of Me-N-C catalysts during accelerated stress tests mimicking the start-up and shut-down conditions

Electrochimica Acta 243 (2017) 183–196

Contents lists available at ScienceDirect

Electrochimica Acta

journal homepage: www.elsevier.com/locate/electacta

Effect of metal species on the stability of Me-N-C catalysts during accelerated stress tests mimicking the start-up and shut-down conditions

Ioanna Martinaiou [a,b], Ali Shahraei [a,c], Fabian Grimm [a], Hongbin Zhang [d], Carolin Wittich [a,e], Sebastian Klemenz [a,f], Stephanie J. Dolique [a,f], Hans-Joachim Kleebe [e], Robert W. Stark [g], Ulrike I. Kramm [a,b,c,*,1]

[a] *TU Darmstadt, Graduate School of Excellence Energy Science and Engineering, Jovanka-Bontschits-Str. 2, 64287 Darmstadt, Germany*
[b] *TU Darmstadt, Catalysts and Electrocatalysts, Department of Materials- and Earth Science, Jovanka-Bontschits-Str. 2, 64287 Darmstadt, Germany*
[c] *TU Darmstadt, Catalysts and Electrocatalysts, Department of Chemistry, Jovanka-Bontschits-Str. 2, 64287 Darmstadt, Germany*
[d] *TU Darmstadt, Theory of Magnetic Materials, Department of Materials- and Earth Science, Alarich-Weiss-Str. 16, 64287 Darmstadt, Germany*
[e] *TU Darmstadt, Geomaterial Science, Department of Materials- and Earth Science, Schnittspahnstraße 9, 64287 Darmstadt, Germany*
[f] *TU Darmstadt, Eduard-Zintl-Institute for Physical and Inorganic Chemistry, Alarich-Weiss-Str. 12, 64287 Darmstadt, Germany*
[g] *TU Darmstadt, Physics on Surfaces, Department of Materials- and Earth Science, Alarich-Weiss-Str. 16, 64287 Darmstadt, Germany*

ARTICLE INFO

Article history:
Received 19 January 2017
Received in revised form 25 April 2017
Accepted 25 April 2017
Available online 1 May 2017

ABSTRACT

Currently, Me-N-C catalysts are the most prominent alternative to Pt/C catalysts for the oxygen reduction reaction in acidic media. It is well known that the achievable activity and selectivity strongly correlates with the nature of metal species. However, so far the effect of the metal species on the stability of these catalysts was not investigated systematically. In this work, a group of 13 different Me-N-C catalysts were investigated with respect to their activity and stability in accelerated stress tests mimicking the start-up and shut-down conditions (AST_SSC). A strong correlation between the nitrogen content assigned to different MeN_4 sites and the D_3 band from Raman spectroscopy is found. Moreover, we were able to correlate changes in the D_3 band and variations in the displacement of the metal atoms out of the N_4 plane with the losses in ORR activity. Based on these findings, we propose a model for the degradation of Me-N-C catalysts during accelerated stress tests mimicking the start-up and shut-down conditions.

1. Introduction

Proton exchange membrane fuel cells (PEMFC) are among the most promising electrochemical devices for hydrogen based energy supply in automotive propulsion owing to their low operating temperature and high power density. Nowadays, state of the art catalysts for the anode as well as the cathode are typically platinum-based catalysts supported on carbon. However, the limited abundance of Pt and the steadily increasing price lead to the conclusion that this cannot be a long term solution for an affordable PEMFC.

Despite, the recent improvements on reducing Pt loading, the fact is that the cathode requires most of the Pt content in order to facilitate the sluggish oxygen reduction reaction (ORR). Thus, a lot of effort has been put in replacing the precious metal catalysts with cheaper alternatives [1].

In 1964, Jasinski [2] discovered that N_4 metal chelates can reduce oxygen in alkaline media. Other Co- and FeN_4 macrocycles were later found to catalyse the ORR in alkaline or acid media [3]. A heat-treatment of such macrocycles between 500 and 900 °C in inert atmosphere was found to greatly improve their stability and activity [4,5].

Lately, most emphasis has been given in pyrolysed non-precious metal catalysts involving independent nitrogen, carbon and metal sources. Due to the importance of all these three components, these catalysts are labelled Me-N-C catalysts. During the last years, significant progress has been achieved regarding the improvement of the activity, performance and stability of these Me-N-C catalysts: in 2009 Lefevre et al. prepared carbon-supported iron-based catalysts (Fe-N-C) with current densities close to the Pt-based reference catalyst [6]. In 2011, another Fe-N-C catalyst again from

---

[*] Corresponding author.
E-mail address: kramm@ese.tu-darmstadt.de (U.I. Kramm).
[1] ISE member

http://dx.doi.org/10.1016/j.electacta.2017.04.134
0013-4686/

Dodelet's group achieved power densities comparable with that of a Pt-based catalyst [7]. In 2011 the best stability was demonstrated for a carbon-based (Fe,Co)-PANI-C catalyst that exhibited good long-term performance for 4 weeks of potentiostatic measurement at 0.4 V [8]. Moreover, in 2015 a significant breakthrough was achieved by Shui et al. reporting the highest volumetric activity and improved fuel cell durability of an iron-based nanofiber framework. In their work, they prepared a carbon-based nanofibrous catalyst by electrospinning with a high density of active sites hosted in micropores as well as with improved mass transfer via macropores. This catalyst design led to astonishing high volumetric activities of 450 A cm^{-3} at 0.8 V [9]. These main achievements were based on a better understanding of the factors that improve the ORR activity of these catalysts, namely the presence of MeN_4 sites [10–12], and the presence of nitrogen moieties assigned to N_{pyrid}. and N_{MeN} [11,13,14]. In addition, in Charreteur et al. [15] it was discussed that the $N_{pyrid.}$ species are all integrated at the edges of graphene layers, as the fwhm of the D band in Raman spectra correlated with the amount of nitrogen integrated in the carbon support. Based on this and previous findings, it was concluded that the active site is formed in micropores, bridging two adjacent graphene layers, each contributing by two N_{pyrid} atoms towards the fourfold coordination of this FeN_4 site.

Recent results also point to the importance of the precursor's composition, the metal species and the carbon morphology for the ORR activity and stability [8,9,16–19]. Despite, the progress made in activity of these type of catalysts, stability is still insufficient for fuel cell application. The instability issues are considered as an ongoing challenge.

Besides gas contaminants that might cause performance losses on the anode, the degradation of the cathode catalyst layer from carbon corrosion during start-up and shut-down conditions is the dominant process. In a recent paper, Choi et al. (2015) [20] demonstrated that for a Fe-N-C catalyst the leaching of iron particles and carbon oxidation occur at low (0.7 V) and high (> 0.9 V) potentials, respectively. In addition, carbon oxidation directly lead to a destruction of active sites [20]. This confirms previous findings by the authors where a significant loss of activity was correlated with the loss of iron from active FeN_4 sites in a post-mortem Mößbauer spectroscopic study [21]. In an acidic electrolyte the oxidation of carbon thermodynamically starts at ca. 0.2 V. Due to kinetic hindrance; however, it is usually not necessary to take carbon oxidation into account in the potential range related to standard PEMFC operation conditions [22]. It was shown, that during the start-up and shut-down conditions (SSC) of the PEMFC a large increase in the anode potential is observed. This increase is caused by air that diffuses into the anode compartment during the shut-down period. In the following start-up, also oxygen is reduced in the anodic compartment. The processes are referred to as reverse current mode [23] as they cause an anodic counter reaction and potentials of up to 1.5 V in the cathodic compartment (therefore reverse current). The high potential causes carbon corrosion and possibly oxygen evolution in the cathode.

In fact, Goellner et al. (2014) published a study on the degradation mechanisms of a Fe-N-C catalyst, stating that the degradation of active sites and carbon corrosion occur in parallel at high potentials and is enhanced at temperatures higher than room temperature [24].

During the high potentials various scenarios may contribute towards the overall activity loss of the Me-N-C catalysts: (i) carbon oxidation, (ii) impact of selectivity on stability and (iii) intrinsic stability of MeN_4 sites.

(i) Carbon oxidation: For recent approaches in the preparation of Me-N-C catalysts the carbon is formed during the heat-treatment in parallel with the formation of active sites. As usually not the overall metal content contributes to the active site formation, it is reasonable that excess metal can have a strong impact on the formed carbon morphology. The variations in the metal species can cause variations in the extent of carbon oxidation [25].

(ii) Selectivity: The selectivity of Me-N-C catalysts depends on the precursors and type of metal species [16,26,27]. The ORR can proceed either with a 4-electron reduction mechanism to form water or with a 2-electron mechanism to form hydrogen peroxide (H_2O_2):

$$O_2 + 4e^- + 4H^+ \rightarrow 2H_2O(\text{directreduction}), \qquad (E_0 = 1.23\,V) \qquad (1)$$

$$O_2 + 2e^- + 2H^+ \rightarrow H_2O_2(\text{indirectreduction}). \qquad (E_0 = 0.68\,V) \qquad (2)$$

It was found that catalysts with a higher yield of hydrogen peroxide usually exhibit a lower stability due to the oxidative power of hydrogen peroxide [28,29]. Jaouen et al. investigated the effect of various metals within the preparation of Me-N-C catalysts and found the following order of decreasing hydrogen peroxide formation during ORR: Mn > Ni > Cr > Me-fee, Cu > Co > Fe [26]. Based on this finding one can assume that Mn-based catalysts exhibit a limited stability whereas Fe-based catalysts should give best long-term stability.

(iii) Intrinsic stability of MeN_4 sites: Based on the different ionic radii and occupation of 3d orbitals of the various metal centers also their ability to remain in the coordination environment provided by the N_4 core can change. A first idea on this might be provided by the comparison of the stability of non-pyrolysed macrocycles applied for the ORR in acidic environment. Here it was reported that a molecular hardness can be calculated from the difference between electron affinity of the oxygen molecule and the ionization potential of the MeN_4 site. The higher the ionization potential of the MeN_4 site is, the higher the resulting activity, but the smaller the stability of the desired site [30,31].

Consequently, similar pronounced changes in the stability of the MeN_4 sites in Me-N-C catalysts can be expected.

Based on this, the aim of this work is to study the effect of metal species on the stability of the Me-N-C catalysts in accelerated stress tests (AST) mimicking Start-up and Shut-down conditions (SSC), as suggested by the Fuel Cell Conference Japan (FCCJ) [32].

As discussed above, previous results suggest that carbon oxidation is an important parameter contributing to the activity decay induced by AST_SSC. Therefore, beside X-ray induced photoelectron spectroscopy (XPS) the catalysts were characterised by Raman spectroscopy before and after the stability tests in order to clarify the impact (of AST_SSC) on changes in the carbon morphology, and to find possible correlations between the structural parameters and the ORR activity and stability.

2. Experimental

2.1. Catalyst synthesis

In order to investigate the role of the metal center on the stability of Me-N-C catalysts with respect to AST_SSC we considered most of the 3d transition metals of the first row of the periodic table and some of the 4d transition metals of the second row. To prepare the catalysts we adapted the brilliant synthesis route described by Proietti et al. [7] that led to today's most active Fe-N-C catalysts.

Proietti's protocol was changed in the following points: 1. The pyrolysis temperature was kept at 950 °C to avoid decomposition of MeN_4 sites that is strongly accelerated for temperatures $T \geq 950$ °C [11,33], 2. The heat-treatment involved a ramp in contrast to a flash pyrolysis, to enhance the ORR performance [34]. 3. An acid leaching step was performed after the first pyrolysis in order to remove inactive metal species that might have been formed during the heat-treatment [17,35,36]. 4. The second heat-treatment was performed in N_2 instead of ammonia in order to avoid the fast

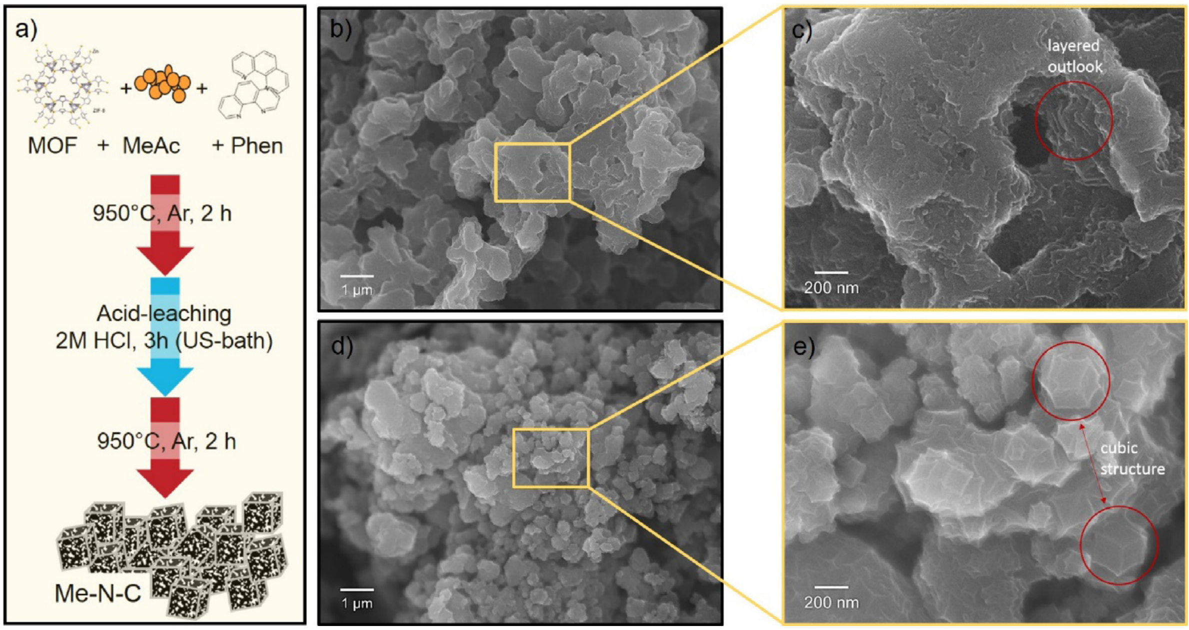

Figure 1. Description of the catalyst synthesis (a) with SEM images of Fe-N-C (b, c) and Zn-N-C (d, e).

degradation assigned to ammonia treatments [6,37–41]. Figure 1a provides a schematic illustration of the preparation process of the Me-N-C catalysts.

Commercial Basolite precursor (Z1200 (Sigma Aldrich)) was used as a structure forming agent with large accessible surface area, phenanthroline as nitrogen and carbon precursor together with the different metal acetates (Me = Co, Fe, Cu, Mn, Ni, Cr, Mo, Ru, and bimetallic (Co,Me) with Me = Fe, Mn, Mo, Ni).

For each synthesis, 2 mM Z1200 was mixed with 1.5 mM 1,10 phenanthroline and 0.25 mM metal acetate in a mortar until a homogeneous mixture was obtained. This procedure results in about 2 wt% metal in the precursor for each catalyst. The precursor mixture was than filled into a quartz boat and placed in an oven where it was heated with a ramp of 450 °C h^{-1} in inert gas atmosphere to 950 °C. After 2 hours the sample was cooled down (< 80 °C) and transferred to 2 M HCl for acid leaching. The acid leaching was accelerated by placing the solution in an ultrasonic bath for about 1 h. After 3 h the sample was filtered, rinsed with deionized water and dried. For the second heat-treatment the conditions were identical to the first heat-treatment.

In Figure 1b, c and Figure 1d, e SEM images of two representative Me-N-C catalysts are shown. For some catalysts the cubic structure of the MOF is resembled by the carbon morphology where as for other catalysts the morphology, as for example can be seen in Figure 1c, became more distorted resulting in a more layered appearance.

It was found that – in contrast to previous reports [7] – even after in total 4 h at 950 °C the samples contained between zero to 3.3 wt% Zn, with the exception of Mo-N-C that contained 8 wt% Zn, as summarized in Table 1. For better estimate of the contribution of Zn or ZnN_4 sites towards ORR activity and stability, a Zn-N-C reference catalyst was prepared by using Zn acetate instead of the other metal acetates. For bimetallic catalysts the molar ratio of Co:Me was 1:1, but keeping the same overall amount of metal. All catalysts are labelled Me-N-C catalysts, for bimetallic catalysts (Co,Me)-N-C.

2.2. Characterisation

2.2.1. Electrochemical measurements

The RDE measurements were performed in a three-compartment cell with glassy-carbon tip used as counter electrode, a reversible H_2 and an Ag/AgCl/(3 M KCl) electrode as reference electrodes and a glassy carbon disk with the catalyst as working electrode. In all experiments, the catalyst loading was 0.5 mg cm^{-2} with a Nafion-to-catalyst ratio of 0.25. All experiments were carried out at RT in 0.1 M H_2SO_4 electrolyte.

For the activity evaluation the electrolyte was first purged with N_2 for about 15 minutes in order to remove any reactive species, then the potential was swept between 1.0 and 0.0 V vs. RHE with sweep rates of 300 mV s^{-1} (20 scans), 100 mV s^{-1} (2 scans) and 10 mV s^{-1} (1 scan). After saturation with O_2 the open circuit potential (OCP) was determined and finally the activity measurements were applied in the same potential range as given above with a sweep rate of 10 mV s^{-1} and 0 rpm, 900 rpm and 1500 rpm. In this work all activity data are plotted for rpm1500 and the potentials are all calculated versus the reversible hydrogen electrode (RHE).

To define ORR activity, we used the mass based kinetic current density, in units of A g^{-1} that was calculated according to equation (3):

$$i_K = j_{kin} \cdot m_{cat}^{-1} \tag{3}$$

In this equation j_{kin} is the kinetic current density and m_{cat} the catalyst loading (0.5 mg cm^{-2}). The loading usually used for non-precious metal catalysts is larger than for Pt catalysts as it is required to obtain the typical shape of the RDE curves but also to have sufficient material for Raman spectroscopy after the stability tests. The kinetic current density j_{kin} (mA cm^{-2}) was determined according to equation (4):

$$j_{kin}(U) = j(U) \cdot j_{Diff,\mathrm{lim}} \cdot (j_{Diff,\mathrm{lim}} - j(U))^{-1}. \tag{4}$$

In this equation $j(U)$ represents the current density corrected for the capacity current and $j_{Diff,lim}$ is as-measured diffusion limiting current density. For those samples which did not yield the typical sigmoid curve as it is common for RDE experiments, the current density at U = 0 V was set as diffusion limiting current density. For the capacity current correction, the current density measured in N_2 saturated electrolyte was subtracted from the current density measured in O_2 saturated electrolyte.

The determination of the onset potentials at defined conditions is very important for the evaluation of the catalytic activity and even more for the comparison of different catalysts.

Table 1
Metal and nitrogen contents (in wt%) for all Me-N-C catalysts investigated in this work. Atomic N:Me ratio was determined for all catalysts including all metal species present in the catalyst. From DFT calculations the values of bond distance $d_{Me\text{-}N}$, displacement out of the N_4-plane and formation energy ΔE are given. Critic values (with respect to MeN_4 formation) are indicated in bold letters.

(wt%)	Co	Fe	Cu	Mn	Ni	Ru	Mo	Zn	Cr	Co, Fe	Co, Mn	Co, Mo
N	7.9	8.5	9.2	9.3	9.8	6	4.8	7.8	3.2	9.4	7.9	5.8
Metal	2.3	3	2.9	2.9	3.5	5.9	0.5	5.3	3.5	1.3	0.2	0.2
Co (bi)										1.5	4	0.4
Zn	3.2	0	3.1	3.1	3.3	2.4	8	0	1.3	3.2	3.4	1.1
N:Me	6.4	11.3	7.1	6.6	6.4	4.5	**2.7**	6.9	**2.6**	6.9	4.6	16.1
d_{MeN} (nm)	0.186	0.189	0.192	0.191	0.187	0.195	**0.203**	0.195	0.195	-	-	-
$a_{Me\text{-}N4\text{-}plane} \cdot 10^{-3}$ (nm)	1.1	1.0	1.1	0.00	0.3	19.9	**80.1**	1.1	0.5	-	-	-
ΔE (eV)	−2.71	−2.36	−1.43	−2.81	−2.73	−0.51	**0.20**	−2.31	−2.71	-	-	-

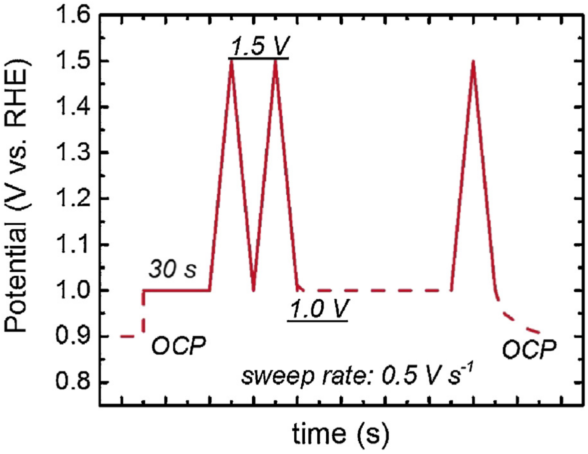

Figure 2. Conditions for the accelerated stress test protocol (AST) mimicking the start-up and shut-down conditions.

In our case, we defined the onset potential as that potential where $j(U) \leq$ -0.1 mA cm^{-2}. The stability of each catalyst was evaluated by an AST_SSC as proposed by the Fuel Cell Conference in Japan in 2011 [32]. As indicated in Figure 2 it consists of a potential cycling between 1 and 1.5 V vs. RHE with a sweep rate of 500 mV s^{-1}.

During AST_SSC the electrolyte was saturated with oxygen to combine possible deactivation by carbon oxidation and active site destruction due to ORR. In total 5000 cycles were performed and the activity was evaluated by the activity protocol after 250, 500, 1000, 1500, 2500 and 5000 cycles.

2.2.2. Raman spectroscopy

For the Raman measurements of the as-prepared catalysts a drop of the catalyst ink was placed onto a silica disk. For the catalysts after stability testing, the remaining catalyst was scratched from the working electrode and placed on a silica disk with a drop of deionized water. The measurements were done with an alpha 300R confocal Raman microscope from WiTec (Ulm, Germany) with a grid of 600 lines mm^{-1} using an excitation laser (532.2 nm) with a power of 1 mW. The range of the measured spectra spreads from 0 to 4000 cm^{-1}.

The spectra were acquired by performing 10 scans, each with integration time of 10 s. A minimum of two to four positions were measured per sample to determine the average spectrum. The spectra were fitted assuming the presence of four bands for the catalysts using voigtian lines. The bands can be assigned as G-band (1580 cm^{-1}), D-band (1360 cm^{-1}), D_3-band (1500 cm^{-1}) and D_4-band (1200 cm^{-1}). The assignment of these bands to different carbon contributions is given in the discussion part. It should be noted that for none of the catalysts investigated in this study a pronounced formation of D*-band intensity – assigned to oxidized carbon – was found, in contrast to studies of AST_SSC of Pt/C catalysts and some other Me-N-C catalysts [16,25].

For better comparison, the intensity of the spectra was normalized to the G-band maximum.

2.2.3. X-ray diffraction (XRD)

X-ray diffraction measurements were used as additional measure of possible inorganic metal residuals. Measurements were done with a StadiP (Stoe & Cie. GmbH, Darmstadt) diffractometer in transmission geometry either with a position sensitive detector using MoKα1-radiation (λ = 0.070930 nm) (Ge[111] monochromator) or with a Mythen-1K detector (Dectris, Baden, Switzerland) using CuKα1-radiation (λ = 0.15406 nm).

2.2.4. X-ray induced photoelectron spectroscopy (XPS analysis)

The X-ray photoelectron spectra of the samples were acquired with a XRC 1000 M X-ray source providing Al-Kα X-rays with excitation energy of 1486.7 eV provided by SPECS GmbH – Surface Analysis and Computer Technology. The catalyst powder was pressed onto an indium foil and sealed on the sample holder. The spectra were recorded with SpecsLab2 Version: 2.78-r28574. Finally, the reflected beam was analyzed by HAS 3500 plus from SPECS. For the survey scans, an energy step of 1 eV was applied and two scans were overlaid. For the N1s scan, an energy step of 0.05 eV was applied and 100 scans were overlaid. For all samples an elemental composition was derived from XPS data.

2.2.5. SEM images

SEM was performed on a JEOL JSM 4600F instrument that provides a high resolution of 1.4 nm (1 kV) – 1 nm (15 kV). SEM images of 3 different areas on the sample were acquired.

2.2.6. DFT calculations

To shed more light into the underlying mechanism of our study, we have performed first principles calculations based on density functional theory (DFT). All the calculations are performed using the plane-wave pseudo-potential method as implemented in the VASP code [42] where the exchange-correlation function is parameterised using the GGA approximation [43]. Supercells with dimensions of 4 X 3 X 1 with respect to the unit cell of graphene have been used for all transition metal hybrid systems, with the atomic positions relaxed by minimizing the forces on each atom below 0.005 eV/Angstrom. To guarantee convergence, a γ-centered k-mesh of 3 × 4 × 1 (7 × 8 × 1) has been considered in the optimisation (self-consistent) calculations, whereas the energy cutoff is taken to be 500 eV. It is noted that all the calculations are done with large enough initial magnetic moment, which allows the magnetic ground state.

2.2.6.1. Bond distances and displacement out-of-plane. From the aforementioned description of the optimisation of the hybrid systems bond distances between the transition metal and coordinating

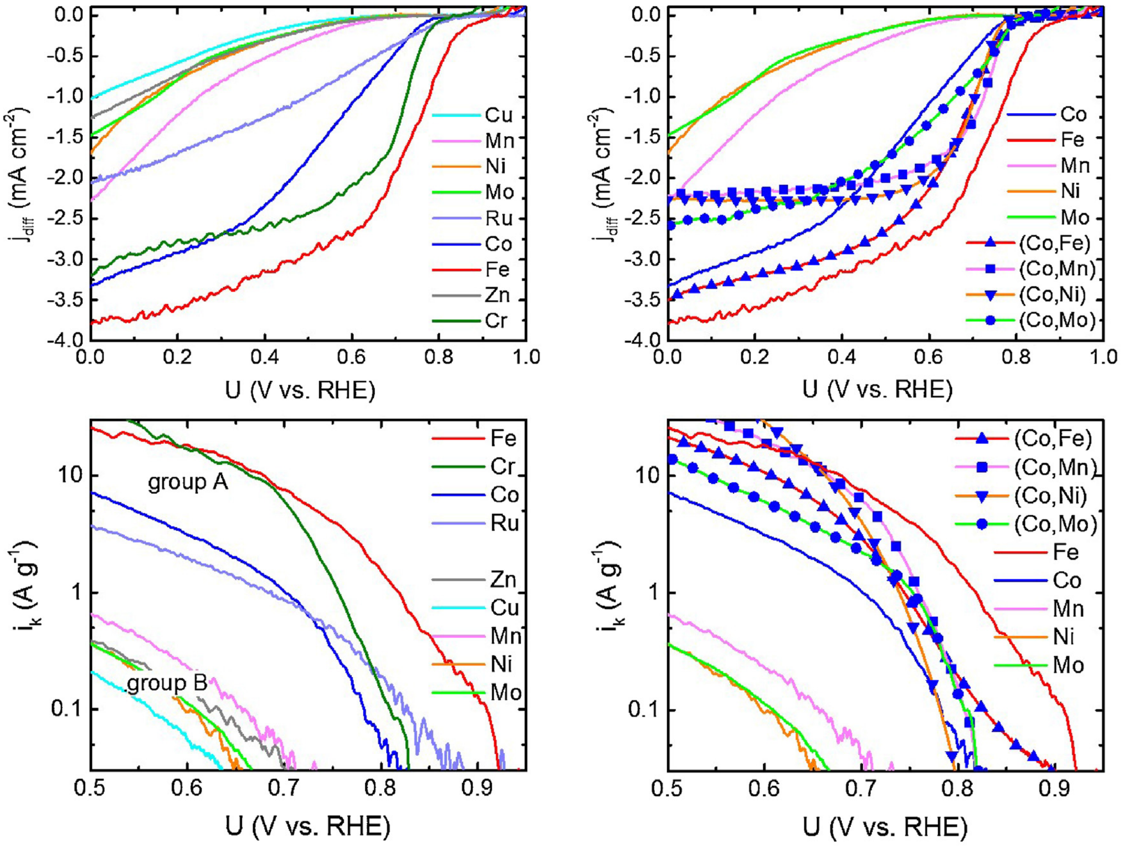

Figure 3. Linear sweep voltammograms (a), (b) and Tafel plots (c),(d) of all investigated Me-N-C catalysts in O_2 saturated 0.1 M H_2SO_4, 1500 rpm, with a scanning rate of 10 mV s^{-1} and catalyst loading of 0.5 mg cm^{-2}.

nitrogen atoms $d_{Me\text{-}N}$ can be obtained. In addition to this, depending on the ionic radii also variations within the displacement of the metal ion out of the N_4-plane $a_{Me\text{-}N4plane}$ can be deduced.

2.2.6.2. Calculation of the stability of MeN$_4$ sites integrated in graphene layers. To estimate the stability of the Me-N-C hybrid systems, the formation energy is evaluated following

$$\Delta E = E(\text{hybrid}) - E(\text{Me}) - E(\text{Me-free}), \tag{5}$$

where E(hybrid) is the total energy for the Me-N-C hybrid system after full atomic relaxation, E(Me) the energy per metal atom (Co, Fe, Mn, Cu, Ni, Ru, Mo, Cr, Zn) in the experimental crystal structure, and E(Me-free) the energy of $C_{26}N_4$ after relaxation.

2.2.6.3. Calculation of adsorption energies. The absorption energies relevant to the oxygen reduction reaction are calculated using Eqs. (1)–(6) in Calle-Vallejo et al. [44]. For all the intermediates (*OOH, *O, *OH), the crystal parameters are fully optimized as stated above, followed by evaluation of the total energies.

3. Results and discussion

The preparation of all catalysts was conducted from precursors containing 2 wt% of the desired metal species and 16.8 wt% Zn (from the MOF, Z1200) that was intended to be completely removed during heat-treatment based on the results given in Proietti et al. [7]. Table 1 summarises the metal contents (in wt%) of the final catalysts as well as nitrogen contents, all determined from XPS. The results indicate that on the one hand, Zn remains in the carbon framework of all catalysts even after 4 h at 950 °C - the only exception is Fe-N-C. On the other hand, except for Mo-N-C and Cr-N-C the atomic ratio N:Me > 4 would in principle enable a fourfold N-coordination of all metal atoms present within our catalysts. The atomic N:Me ratio was estimated considering all metals found for a particular sample and dividing the given metal contents by the related molar mass. The obtained “molar fractions” of metals were summed up. Similarly, the molar fraction of nitrogen was determined and divided by the sum of molar fractions of metals to obtain the atomic N:Me ratio. For example, in case of Mn-N-C the calculation was as followed:

$$\Sigma[\text{Me}] = 2.9\,\text{wt\%}_{\text{Mn}} \cdot \left(54.9\,\text{g mol}^{-1}\right)^{-1}$$

$$+3.1\,\text{wt\%}_{\text{Zn}} \cdot \left(65.4\,\text{g mol}^{-1}\right)^{-1} = 0.0474\,\text{mol\%}\,g_{\text{cat}}^{-1}$$

$$[\text{N}] = 9.3\,\text{wt\%}\,\text{N} \cdot \left(14\,\text{g mol}^{-1}\right)^{-1} = 0.664\,\text{mol\%}\,g_{\text{cat}}^{-1}$$

$$[\text{N}] : [\text{Me}] = 0.664/0.0474 = \mathbf{6.63}$$

In addition to this, various DFT calculations were performed considering the model system of these catalysts, as described above. The obtained Me-N bond distances d_{MeN}, displacements out of the N_4 plane $a_{Me\text{-}N4plane}$ and the energy difference ΔE from eq. (5) are added in Table 1. If the energy difference ΔE is negative the hybrid system is stable, whereas a positive value means the system is thermodynamically unstable. However, we need to point out that this calculation does not consider any kinetic effects or side products during heat-treatment. Hence, even if ΔE < 0 eV, it is not certain, that indeed only MeN$_4$ sites are formed. As can be seen in Table 1, in all cases except molybdenum the formation of MeN$_4$ sites is thermodynamically possible. This explains, why the Mo contents in Mo-N-C and (Co,Mo)-N-C were rather low. As indicated by the XPS results for Cr-N-C, most likely also some metal or metal nitride/carbide particles were formed. However, these have

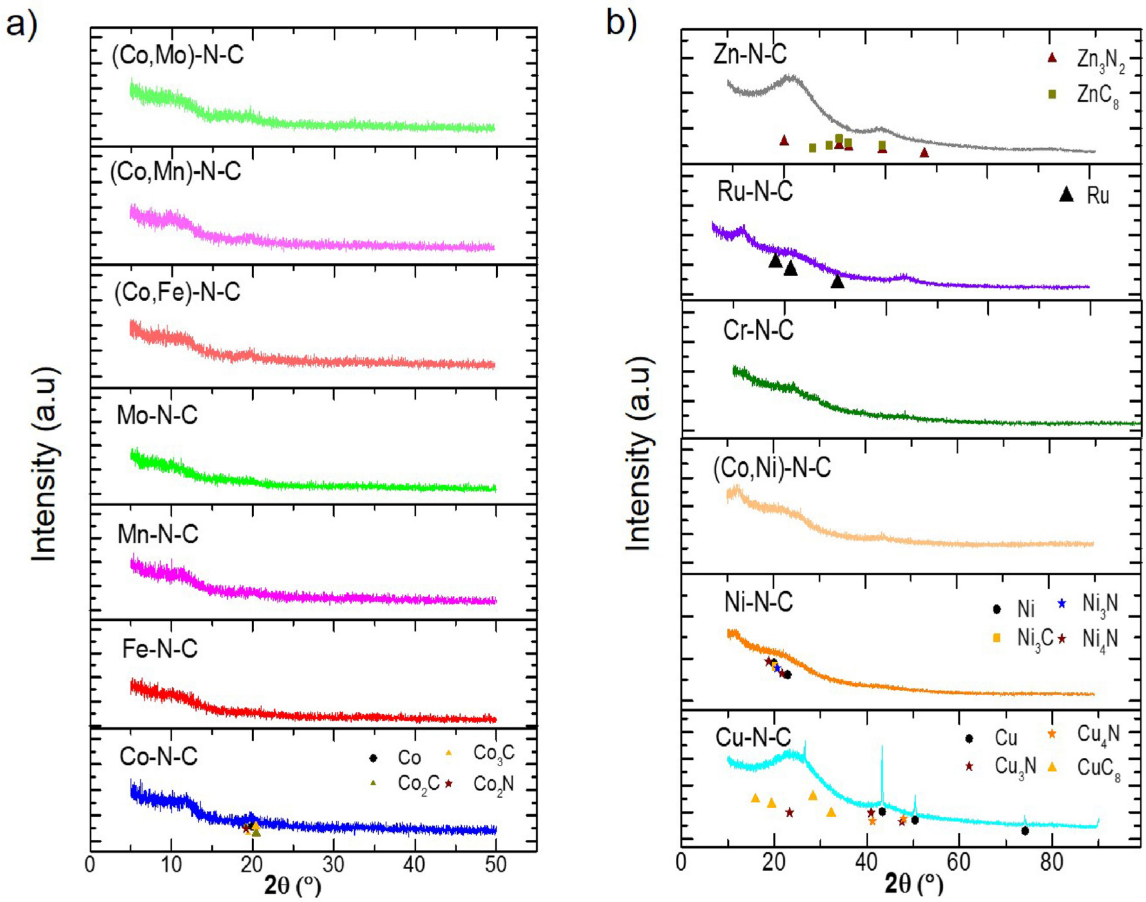

Figure 4. X-ray diffractograms of all Me-N-C catalysts. Measurements were performed (a) with Mo-K$_{\alpha1}$ radiation (λ = 0.071 nm) and (b) with Cu-K$_{\alpha1}$ radiation (λ = 0.15406 nm).

to be well distributed and small, as the sample exhibited mostly x-ray amorphous behavior as will be shown later (Figure 4).

In the following, the results from structural characterisation and theoretical calculations should be used in order to define activity descriptors for the overall group of investigated Me-N-C catalysts, in the first part 3.1.

In the second part 3.2 the focus is directed to the degradation of Me-N-C catalysts under accelerated stress test conditions mimicking the start-up and shut-down conditions (AST_SSC) and related conclusions.

3.1. Impact of the metal species on ORR activity

In order to clarify the role of metal species on the ORR activity RDE experiments were conducted in 0.1 M H_2SO_4. Figure 3a and 3b give the RDE curves of monometallic and bimetallic catalysts, respectively.

However, we have to point out that none of the investigated catalysts reaches the expected diffusion limiting plateau related to a four-electron transfer process at the given catalyst loading. This feature is already well-known for Me-N-C catalysts [45].

Therefore, the diffusion limiting current densities cannot be discussed as straight forward compared to other electrocatalysts. Nevertheless, for group B catalysts and most bimetallic catalysts (except (Co,Fe)-N-C) the possibility of a reduction to hydrogen peroxide might have to be considered, at least to some extent.

In Figure 3c and 3d the Tafel plots are given for the mono- and bimetallic catalysts. The achieved ORR activity trend for the metal species is similar to the ones obtained by other groups working on Me-N-C catalysts [19,46–51] even though in this study completely different precursors were used as compared to literature data. This underlines that for Me-N-C catalysts prepared from various types of precursors similar electrochemical trends can be achieved making it likely that also findings on degradation origins (part 2) might be transferred from one preparation approach towards another.

An important point to notice is the low performance of the Zn-N-C reference catalyst. As given in Table 1, even though unintended, nearly all Me-N-C catalysts contained zinc. However, as the ORR activity of Zn-N-C was low (group B metal) a major contribution of ZnN_4 sites with regard to the ORR activity (and stability) of the other Me-N-C catalysts can be excluded, but might affect the average diffusion limiting current density.

The motivation for the preparation of bimetallic catalysts was given by previous findings by one of us and other groups that bimetallic catalysts showed improved activity and stability in comparison to monometallic catalysts [8,17,19,52,53]. Indeed, our bimetallic (Co,Me)-N-C catalysts with Me of group B metals (Mn, Ni, Mo) revealed an improved ORR activity in comparison to their monometallic counterparts. However, this did not apply for (Co,Fe)-N-C which basically reflected the average performance of the monometallic Fe-N-C and Co-N-C. Hence, if there is any significant improvement it seems to be related to an improvement of the kinetics of some specific group B metals.

In order to verify to what extent crystalline phases were formed within our catalysts, X-ray diffraction was performed on all catalysts. As shown in Figure 4 most of the catalysts reveal the expected x-ray amorphous behavior that is typical for Me-N-C catalysts.

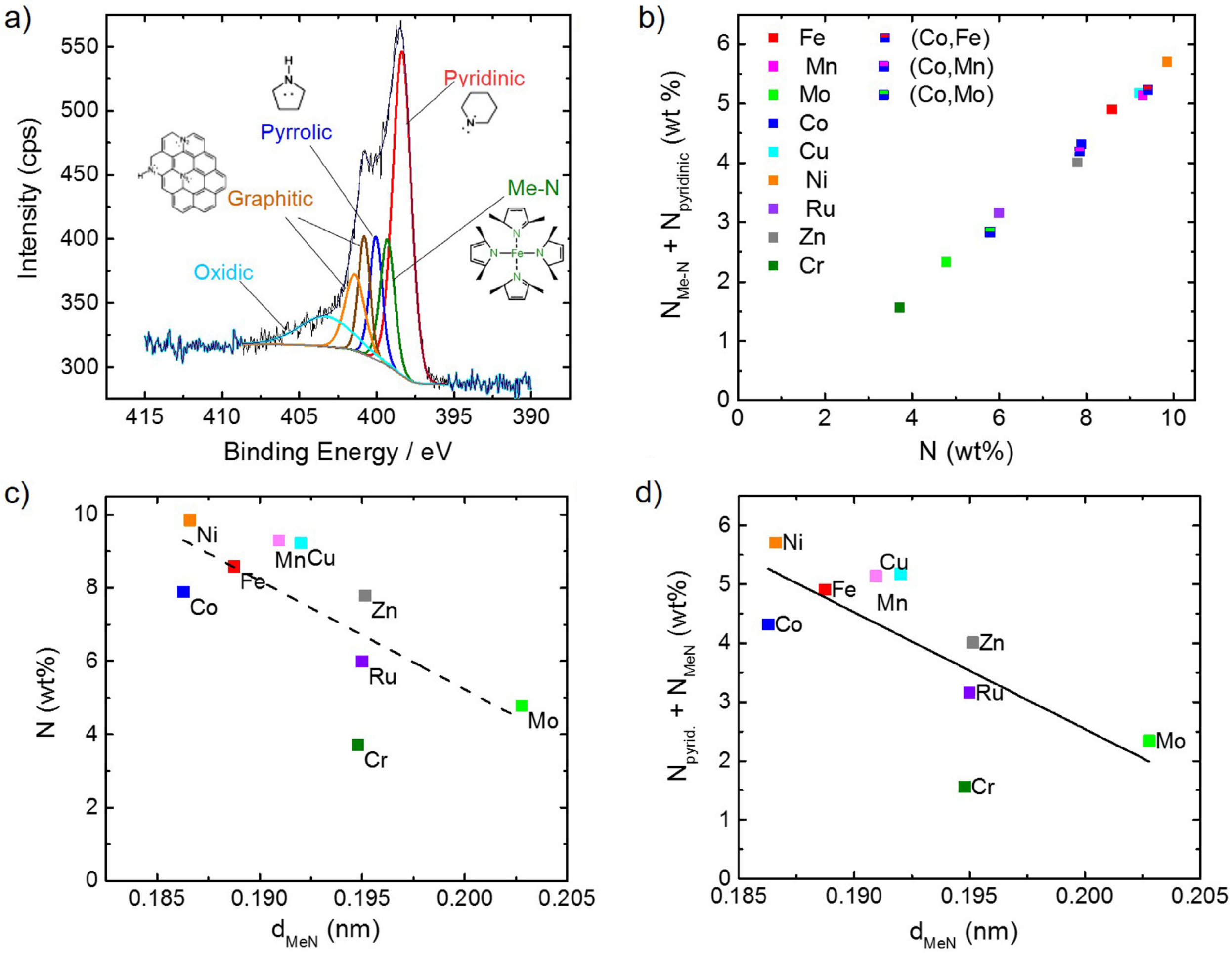

Figure 5. High resolution N 1s XP spectrum of the bimetallic (Co,Fe)-N-C catalyst (a), and N content in $N_{pyrid.}$ plus N_{MeN} vs. the total nitrogen content (b). In (c) and (d) the total nitrogen content and the sum of $N_{pyrid.}$ plus N_{MeN}, respectively, was correlated with the bond distance obtained from DFT calculations.

Interestingly, the most intense reflexes were found for Cu-N-C and were assigned to Cu nanoparticles. However, even Mo-N-C is x-ray amorphous. In Co-N-C some Co nanoparticles are found that could eventually be present in all bimetallic catalysts, as well as a slight increase in intensity is found at $2\theta = 20^{\circ}$.

Different spectroscopic techniques can help identifying the structural composition and morphology of the catalysts, thus giving important information on improving the requirements for designing active catalysts.

The surface-near composition of the various metal based catalysts was studied using XPS. In Figure 5a the N1s XP spectrum of the bimetallic (Co,Fe)-N-C catalyst was fitted with six peaks: pyridinic (N_{pyrid}, 397.5–398.8 eV), Me–N (N_{MeN}, 398.5–400.5 eV), pyrrolic (N_{pyrrol}, 400–401.5 eV), two graphitic peaks (N_{graph}, 401–403 eV), and oxidic (N_{ox}, 402.5–405 eV) [54,55].

In Figure 5b the weight percentage of nitrogen assigned to the N_{pyrid} plus $N_{Me\text{-}N}$ peaks is correlated to the overall nitrogen content. As discussed in the introduction in different papers nitrogen assigned to N_{pyrid} and $N_{Me\text{-}N}$ were attributed to the ORR active MeN_4 sites in Me-N-C catalysts [11,14]. Here, we find a distinct correlation, indicating that the relative fraction of MeN_4 moieties assigned to N_{pyrid} and/or N_{MeN} is about the same for all catalysts (on average about 54%). In addition to this, we tried to correlate the overall nitrogen content (Figure 5c) and the nitrogen content assigned to the sum of $N_{pyrid.}$ plus N_{MeN} (Figure 5d) with the bond distance obtained from DFT calculations. A slightly better correlation is found for the sum of N_{MeN} plus N_{pyrid}. The data indicate that less nitrogen content related to different types of MeN_4 sites is kept within the catalyst if the bond distance between the metal atom and the coordinating nitrogen atoms is increasing too much. In addition, these data are in line with previous findings that showed smaller nitrogen contents for the heat-treated H_2N_4-macrocycles in comparison to MeN_4 macrocycles heat-treated at similar temperatures (for T > 500 °C) [59,60].

The metal-nitrogen bonding stabilises the nitrogen in the carbon framework, so far the bond distance is not too large.

For the oxygen reduction reaction it is assumed that the electron transfer takes place stepwise together with the related proton transfer. The intermediates OOH, O and OH are adsorbed during the process of oxygen reduction to water [66,67] whereas OOH will be the only adsorption intermediate for an indirect reduction to hydrogen peroxide. Based on this consideration, the kinetic current density was correlated to the adsorption energy of OOH on MeN_4 sites in Figure 6.

As can be seen for most of the metals (except Mo) the kinetic current density becomes higher with decreasing adsorption energy.

Raman spectroscopy was used in order to obtain information on the structure and the morphology of the Me-N-C. In Figure 7 the spectra of the as-prepared catalysts are given. The Raman spectra are typical for amorphous carbons. The Raman spectrum is divided in the first-order region ($<2200\,cm^{-1}$) and in the second-order region (between 2200 and $3500\,cm^{-1}$) [57]. The two characteristic bands of carbon-based materials are the G-band (for Graphite) at around $1580\,cm^{-1}$ and the D-band (for Defect) at

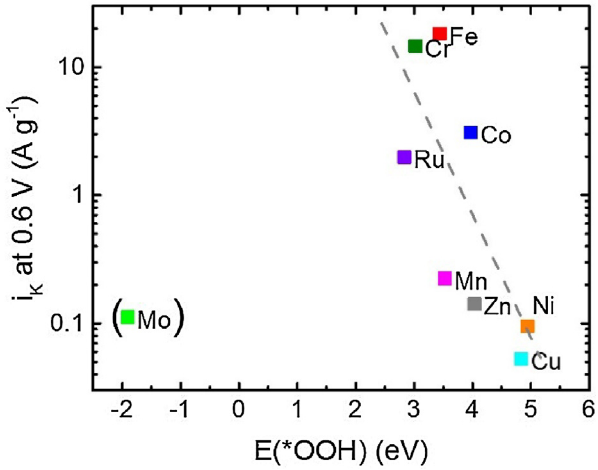

Figure 6. Mass-based kinetic current density (0.6 V) as a function of the adsorption energy of *OOH on various monometallic MeN_4 sites (The higher the E(*OOH) value the stronger the OOH binding is).

around 1360 cm^{-1}. The first corresponds to an ideal graphitic lattice vibration mode with E_{2g} symmetry and the second to disordered graphite with a vibration mode of A_{1g} symmetry, vibrations at the edges of a graphene layer or close to defects (e.g. heteroatoms) [58]. Moreover, additional bands appear at about 1200 cm^{-1} (D_4) due to polyenes and at 1500 cm^{-1} (D_3) due to defective carbon that possibly includes organic molecules, molecular fragments or functional groups [61,62]. An additional band at about 1750 cm^{-1} (D*) can be observed as a small shoulder in our spectra after AST_SSC and is assigned to the oxidation of carbon with the formation of surface groups [25,63–65].

All observed second-order Raman bands are assigned to overtones and combination modes of the first-order bands [58,68]. The second order bands occur at ~ 2700 cm^{-1} (2*D), ~ 2450 cm^{-1} (2*D_4) and ~ 2950 cm^{-1} (G + D). Most of the catalysts show only broad bands in the second order range. However these bands are well pronounced for Ru > (Co,Fe) > Cr illustrating the higher degree of order in comparison to the other catalysts.

In various works by Dodelet's group it was shown that pyridinic nitrogen atoms that were integrated into the carbon network by a pyrolysis in ammonia lead to a more intense and broadened D-band [37,69]. As mentioned in the introduction part, this finding and others led to the conclusion that the active sites are hosted in micropores, with two adjacent graphene layers contributing each two pyridinic nitrogen atoms for the fourfold coordination (MeN_{2+2} sites, compare Figure 14, sketch of active site at the bottom left). Also here, there are indications of an increasing D-band intensity with increasing content of N_{pyrid} as shown in Figure 8a (R^2 = 0.245). It should be pointed out that correlation attempts with N_{pyrrol}, sum of N_{graph} and N_{oxidic} did not give similar good results (not shown). Also correlation attempts of the fwhm of the D-band with the overall N content did not succeed.

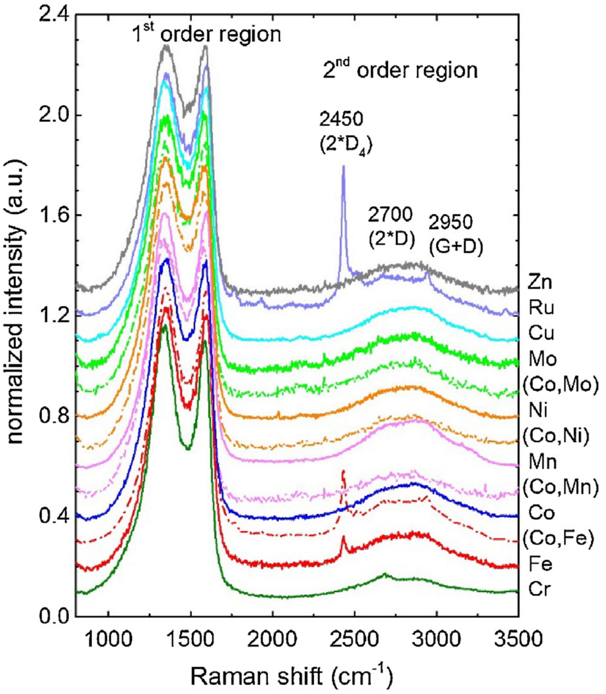

Figure 7. Raman spectra of all investigated as-prepared catalysts. The colour code is identical to Figure 3, whereas bimetallic catalysts are plotted in dashed lines coloured similar to the 2nd metal species (Fe, Mn, Ni or Mo).

However, a better correlation is achieved if the sum of nitrogen content assigned to $N_{pyrid.}$ and $N_{Me\text{-}N}$ is plotted versus the normalized D_3 band intensity as given in Figure 8b (R^2 = 0.475, with an intercept (*x*,*y*) = 0,0). As explained above the D_3-band contributes of defects expressed by functional groups within the graphene layers. Based on the good correlation given in Figure 8b we propose that

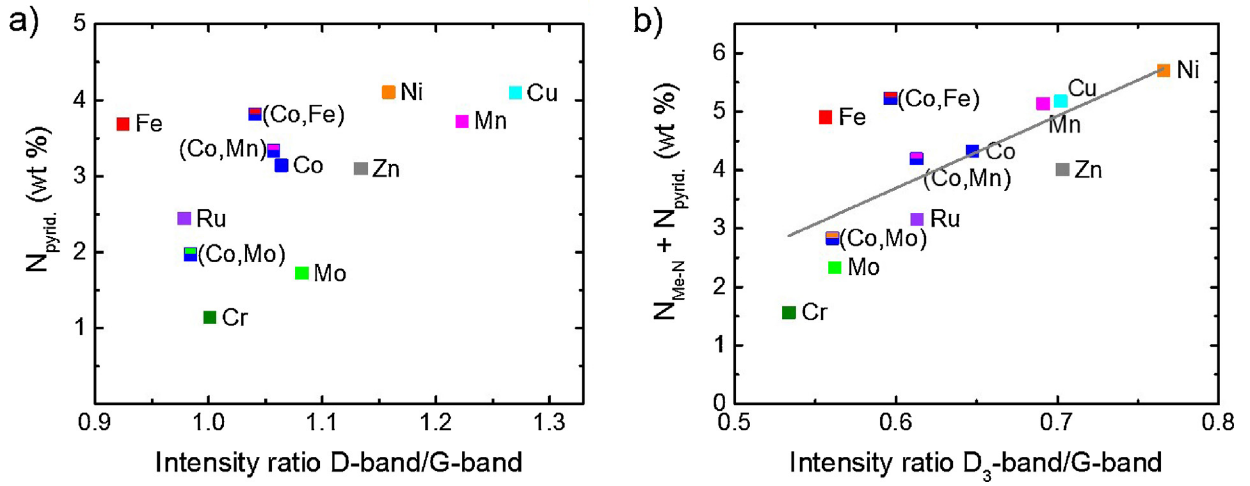

Figure 8. Comparison of the nitrogen content assigned to N_{pyrid} vs. the intensity ratio of D-band/G-band (a), and sum of nitrogen contents assigned to $N_{pyrid.}$ plus N_{MeN} vs. the intensity ratio of D_3-band/G-band (b).

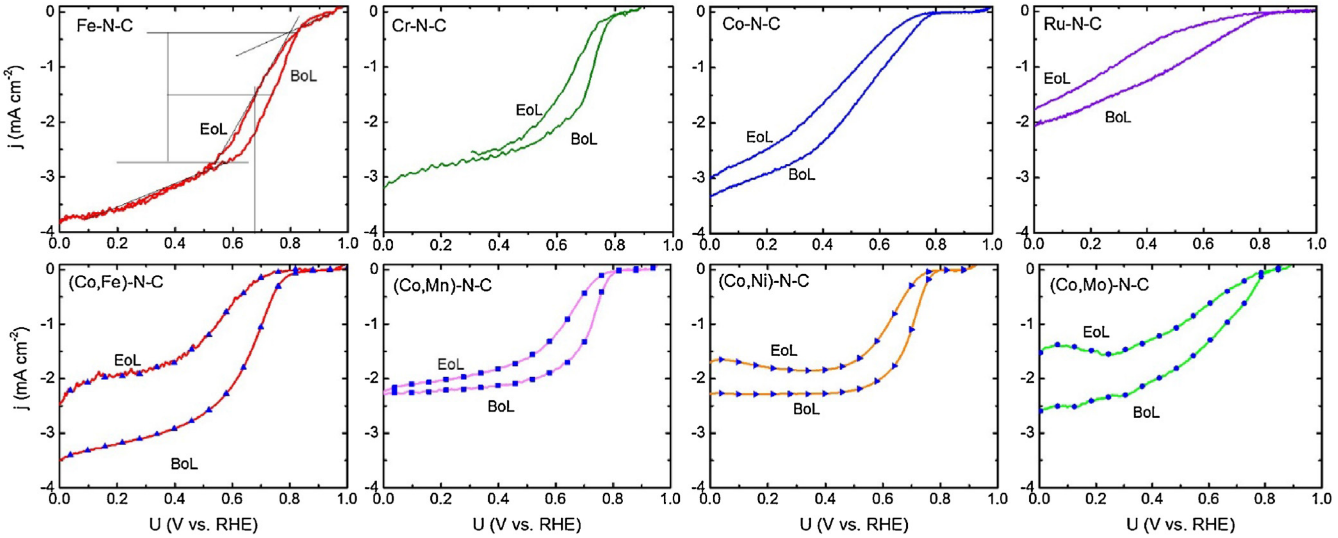

Figure 9. Beginning of Life (BoL) and End of Life (EoL) RDE curves of the group A mono- and bimetallic catalysts obtained at 1500 rpm.

the MeN_4 sites reflect defects within graphene layers contributing towards the D_3-band intensity. Also here, correlation attempts with N_{pyrrol}, N_{graph} and N_{oxidic} were not successful.

That means, while Dodelet's group assigned the $N_{pyrid.}$ as part of active sites to a descriptor defined by the D-band, in our case the best correlation is found between the nitrogen contents that can be related to different MeN_4 sites and the D_3-band. How to explain the difference to the previous findings by Dodelet's group? Considering the catalysts that led to the aforementioned conclusion on FeN_{2+2} sites, their nitrogen contents, iron contents and the Mößbauer signatures are available for identically prepared catalysts [38,56]. Based on Mößbauer data and iron contents, for the most active catalyst in the referred work the amount of FeN_4 plus FeN_{2+2} sites added up to ~0.14 wt% [38]. Consequently with a ratio of 1:4 and a ratio of molar masses of 56 g mol^{-1} to 14 g mol^{-1}, also the same weight percentage of nitrogen is required to form these FeN_4 plus FeN_{2+2} sites. The overall nitrogen content of this catalyst is about 3.5 wt% with about 25% assigned to $N_{pyrid.}$ [55], this makes 3.5 wt% × 25% = 0.875 wt% $N_{pyrid.}$ in this catalyst. Hence, only a partial fraction of $N_{pyrid.}$ can be assigned to iron-nitrogen coordination (<0.14/0.875 = 16%), whereas most of it has to be attributed to metal-free $N_{pyrid.}$ functionalities. Note, that the value will be even lower than 16%, as part of the FeN_4 sites are mesomeric coordinated by pyrrolic nitrogen atoms and assigned to the N_{MeN} peak [11]. Therefore, the correlation that was found by Charreteur for the nitrogen content and the D-band might have their main origin by the metal-free $N_{pyrid.}$ sites, whereas our results indicate that $N_{pyrid.}$ seems to contribute to the D_3-band intensity similar as N_{MeN}.

Based on the indications provided by Figure 8b, we conclude that the D_3-band can be used as activity descriptor which is related to $N_{pyrid.}$ and N_{MeN} contents that both can contribute to the formation of MeN_4 sites for the different Me-N-C catalysts. Furthermore, the error in the correlation as well as the intercept on a positive D_3/G intensity ratio indicate that there are additional contributions to this band that are not expressed by $N_{pyrid.}$ functionalities or MeN_4 sites.

3.2. *Stability in accelerated stress tests mimicking the start-up and shut-down conditions (AST_SSC)*

Regarding the stability of Me-N-C catalysts we found in our previous post-mortem analysis of a Fe-N-C catalyst, carbon burn-off and a destruction of FeN_4 were induced by cycling the catalyst in a potential range of 0.8 V to 1.2 V in a fuel cell (H_2, O_2 at 80 °C) [21]. Induced by a variation of the metal species the carbon morphology can change due to the different capability of the metal species to induce the formation of specific carbon structures [70]. Indeed the Raman spectra in Figure 7 illustrate that a higher degree of order is observed for Ru-N-C and (Co,Fe)-N-C. Even more likely, it appears that the type of metal center within the N_4 coordination will have an impact on the intrinsic stability of active MeN_4 sites.

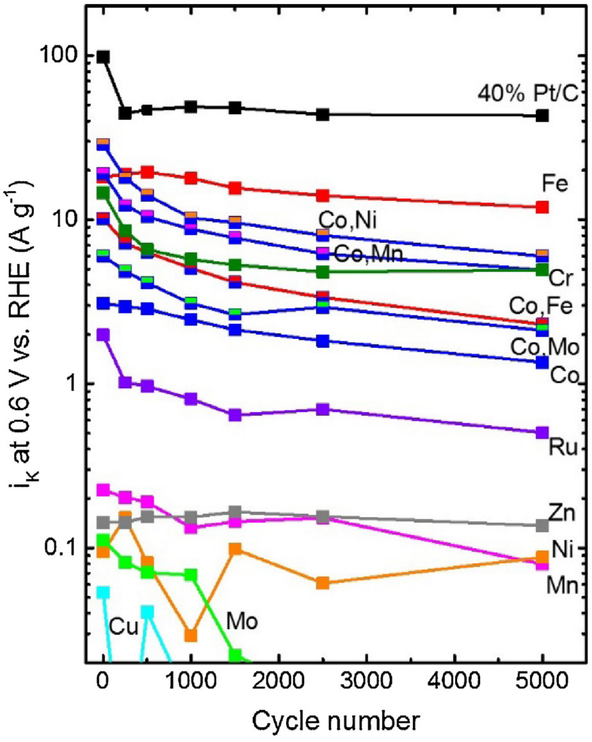

Figure 10. ORR activity at 0.6 V vs. number of SSC cycles (compare Figure 2). RDE was done in O_2 saturated 0.1 M H_2SO_4, 1500 rpm, with a scanning rate of 10 mV s^{-1} and catalyst loading of 0.5 mg cm^{-2}.

Therefore, in order to verify to what extend the type of metal center influences the stability during accelerated stress tests mimicking the start-up and shut-down conditions (AST_SSC) the related protocol as recommended by the Fuel Cell Conference Japan (FCCJ)

Table 2
Half wave potential ($E_{1/2}$) of Beginning and End of Life of mono-and bimetallic catalysts of group A.

$E_{1/2}$ (V)	Fe	Cr	Co	Ru	Co,Fe	Co,Mn	Co,Ni	Co,Mo
BoL	0.75	0.71	0.59	0.55	0.68	0.73	0.70	0.64
EoL	0.68	0.63	0.50	0.42	0.56	0.65	0.62	0.56
$\Delta E_{1/2}$	0.07 ± 0.01	0.08 ± 0.01	0.09 ± 0.02	0.13 ± 0.02	0.12 ± 0.04	0.08	0.08 ± 0.01	0.08

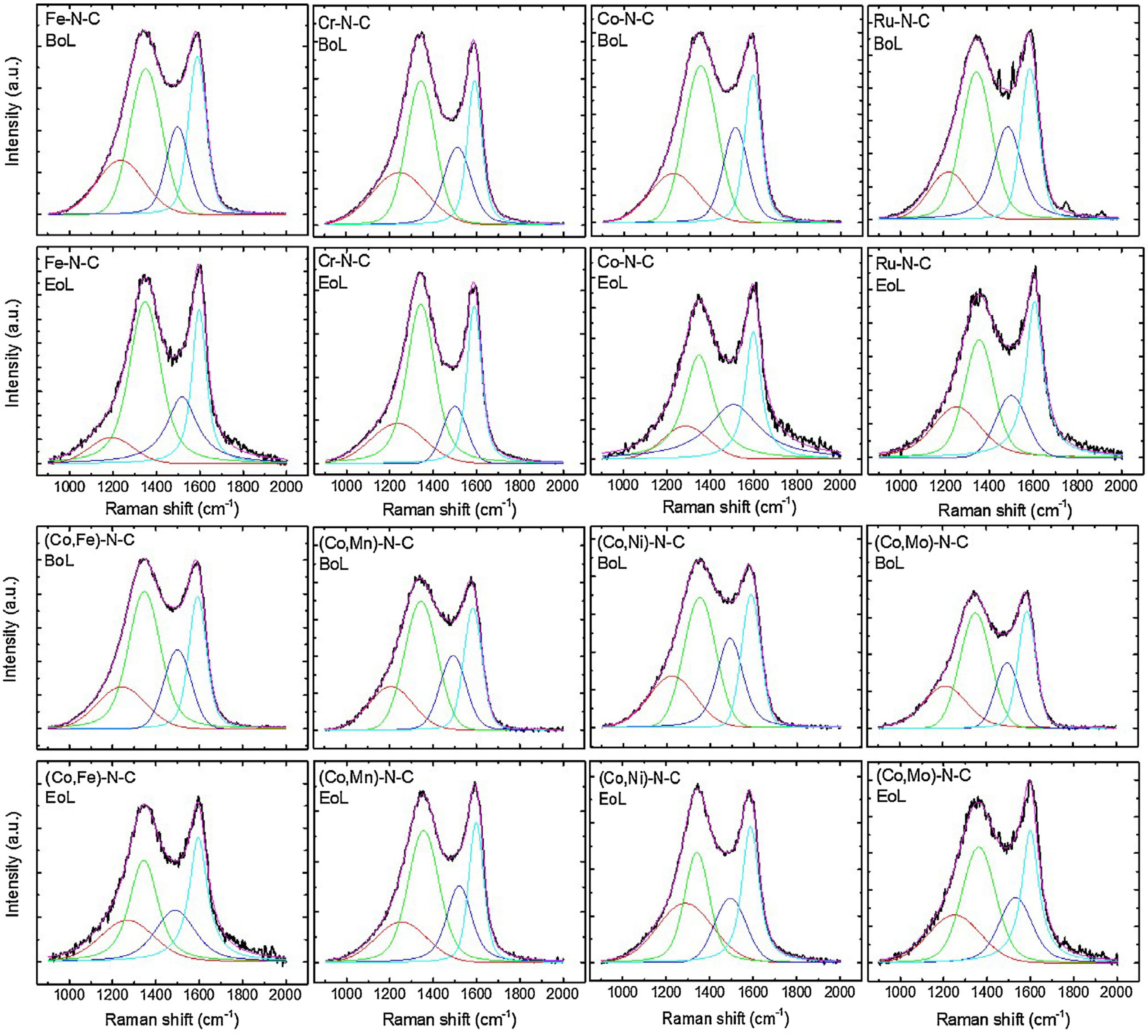

Figure 11. Raman spectra of all group A catalysts at their beginning of life (BoL) and end of life (EoL) including the deconvolution.

was applied [32]. We have to admit, that based on the different fractions of zinc that remained even after in total 4 h of heating at 950 °C and including an acid leaching, the obtained results on stability for the different Me-N-C catalysts might change, if those catalysts are prepared indeed free of any Zn impurity. While it is clear from the activity data of Zn-N-C that Zn and possible ZnN_4 sites are not affecting the activity of our group A metals, it could be possible that Zn or ZnN_4 sites affect the stability of MeN_4 sites or of the carbon support in a positive or negative way. However, we believe that the zinc impurities in our group A catalysts might change absolute values of activity or structural changes, but not the overall trends, derived in the following.

In Figure 9 the Beginning of Life (BoL) and End of Life (EoL) RDE curves are given for all group A catalysts. In case of Fe-N-C it is indicated how the half-wave potential $E_{1/2}$ was determined. Figure 9 shows that the catalysts exhibit rather different ORR performance and also stability, as illustrated by the change in half wave potential and changes in the diffusion limiting area. In most of the cases, the ORR polarisation curves recorded at 1500 rpm reveal a decrease in the diffusion limiting current density after performing the AST_SSC indicating the degradation / partially deactivation of the catalyst. Interestingly, while the BoL curve of (Co,Fe)-N-C could nearly be calculated from Fe-N-C and Co-N-C data (as sum of the current densities of 50% Fe-N-C plus 50% Co-N-C), the EoL polarisation curve of

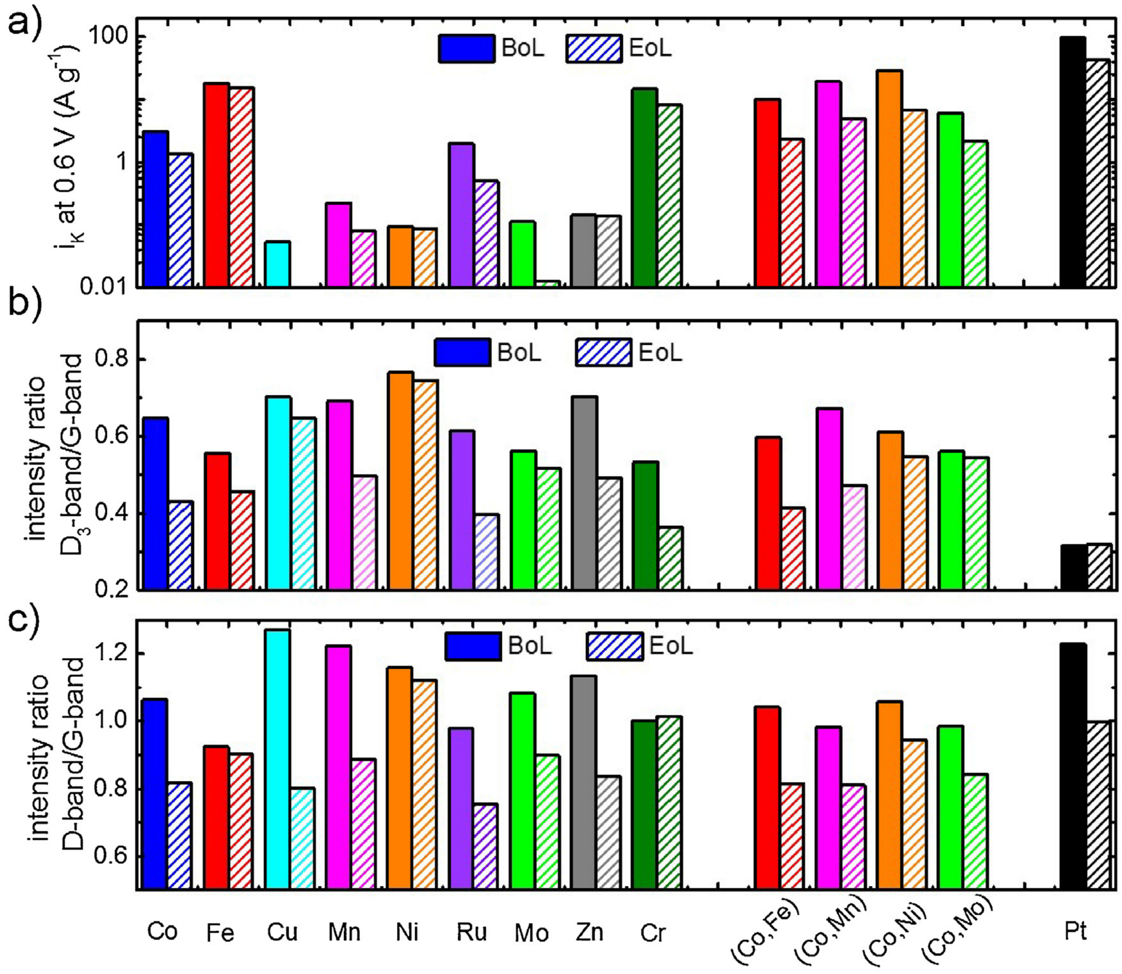

Figure 12. a) Overview of ORR activity (i_K at 0.6 V) and intensities of the b) D_3-band and c) D-band normalized to the G-band for all monometallic and bimetallic catalysts as well as Pt/C at the Beginning of Life (BoL) and End of Life (EoL).

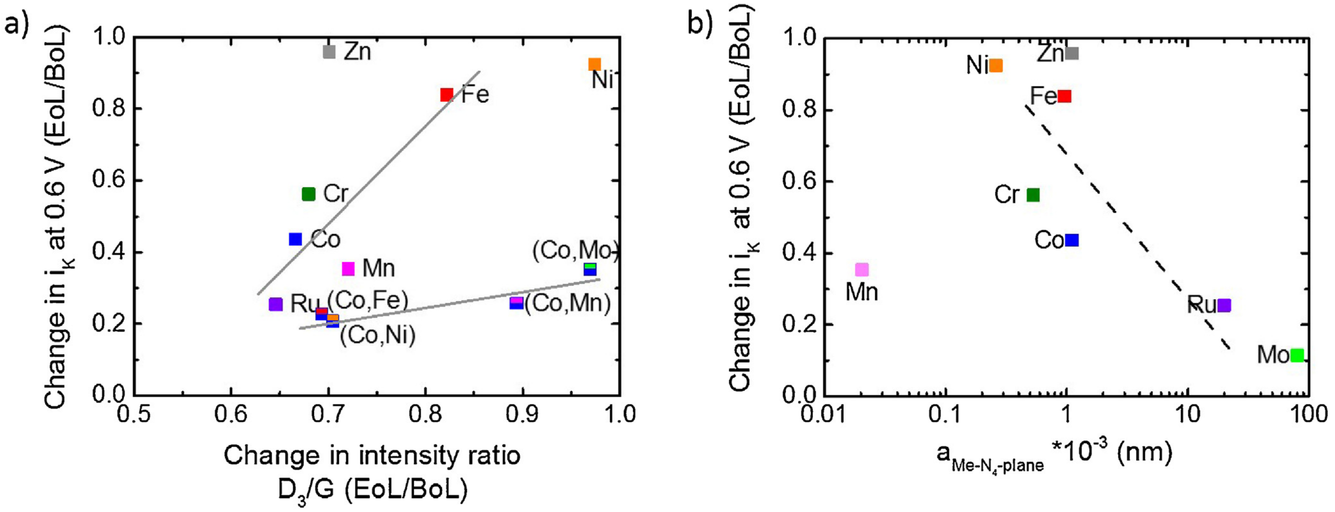

Figure 13. Comparison of the relative remaining ORR activity versus the relative change of the normalized D_3-band intensity (a) and vs. the displacement of the metal out of the N_4-plane (b).

(Co,Fe)-N-C shows a significantly stronger degradation in comparison to the individual Fe-N-C and Co-N-C catalysts. It should also be noted that the EoL curve for Cr-N-C is only plotted down to a potential of 0.2 V, since below this potential a specific adsorption of hydrogen is observed, hindering an appropriate subtraction of the nitrogen scan in this potential region.

The values of BoL and EoL half-wave potentials ($E_{1/2}$) are summarised for these catalysts in Table 2. It becomes apparent that for

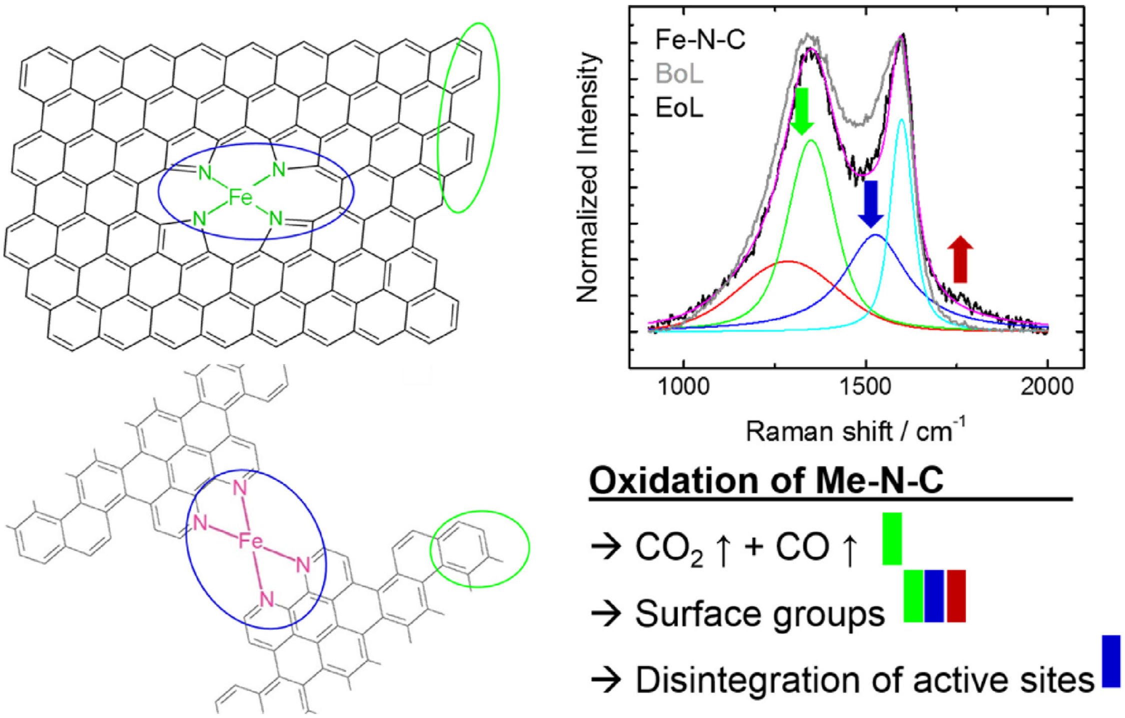

Figure 14. Proposed model for the Me-N-C deactivation by accelerated stress tests mimicking the start-up and shut down conditions: beside oxidation of the carbon (formation of surface groups and release as Co and CO_2) a partial disintegration of MeN_4 sites (either in-plane or at the edges) occurs.

most of the catalysts the potentials are reduced by about 80 mV. The strongest decrease occurs for Ru-N-C and (Co,Fe)-N-C.

In Figure 10 the change of ORR activities at 0.6 V is given as a function of AST_SSC cycle numbers. A Pt/C catalyst is also shown for comparison. It should be noted that the Pt/C catalyst was also measured in sulfuric acid with the high catalyst loading of 0.5 mg cm^{-2} as it is common for non-precious metal catalysts, in order to have sufficient material for post-mortem Raman measurements after the AST_SSC.

For Figure 10 a potential of 0.6 V was chosen in order to be able to compare all catalysts (including group B) at the same potential. It is clear from this graph that the Cu-N-C and Mo-N-C are the two least stable catalysts. Indeed, it is known for MoN_4 macrocycles that they are not applicable in acidic electrolyte but only in alkaline solution [31].

As indicated by our own results and results of other groups, bimetallic catalysts were found to be more stable than monometallic catalysts [8,17]. However, such an improvement cannot be confirmed for the bimetallic catalysts investigated in this work.

Based on the above, it can be concluded that an improved performance of bimetallic catalysts is not a general feature but is related to the distinct combination of metal species and/or to other preparation parameters that still have to be worked out.

In Figure 11 the deconvolution of the Raman spectra of all group A catalysts are shown for the first order region at BoL and EoL. In addition to this, Pt/C and group B metals were investigated. For Pt/C the usual features of a decreasing D-band intensity and increase in D*-band intensity was monitored (not shown) [25]. However, in the case of Me-N-C catalysts also a decrease of the D_3-band intensity was observed.

This is even better illustrated in Figure 12 which summarises the related values of the mass-based kinetic current density (0.6 V) and the normalised intensities of D_3/G and D/G bands.

Two main changes can be identified that appear to be induced by the AST_SSC:

(a) A decrease of the D-band intensity is found for all Me-N-C catalysts (except Cr-N-C)
(b) A decrease of the D_3-band intensity as observed for all Me-N-C but not for Pt/C.

While changes of the D-band and D*-band are intensively discussed in the literature on the stability of carbon blacks or Pt/C catalysts during AST_SSC [25,63–65] the observation of a decreasing D_3-band is special for the group of Me-N-C catalysts.

As Figure 8b gives a very well defined correlation between the nitrogen content assigned to those nitrogen species that are proposed to be involved in MeN_4 active sites ($N_{pyrid.}$ and N_{MeN}) and the normalized D_3-band intensity, we assume that the decrease in the normalized D_3-band intensity indicates a loss of MeN_4 sites induced by the AST_SSC.

Indeed, it was shown by Goellner et al. [24] that the disintegration of FeN_4 sites in Fe-N-C catalysts is initiated by the oxidation of the carbon, when cycled in a potential range 0.9 V to 1.4 V. The carbon corrosion rate determined for different temperatures correlated with the activity decay of the investigated Fe-N-C catalyst. The release of the metal is also confirmed by the stability tests discussed by Choi et al. [20] and our post-mortem studies of the degradation of a Fe-N-C catalyst during potential cycling in a PEMFC (0.8 V to 1.2 V) [21]. Hence, the data provided in literature support our thesis on the role of the carbon support specifically for Me-N-C catalysts and as expressed by the decrease of the D_3-band intensity.

This is further supported by the correlation between the relative change in ORR activity and the relative change of the normalised D_3-band intensity, as given in Figure 13. The group B metals are also more randomly distributed, but group A metals give some correlations. Interestingly, the slopes of mono- and bimetallic catalysts are different. This could indicate that for bimetallic catalysts an additional factor was contributing to the overall current losses. As the presence of cobalt was one common ground, one might hypothesise some connection to cobalt at the origin of the changed slope. Further investigation will be required.

In addition to this it was tried to correlate the activity losses with descriptors assigned to our MeN_4 sites as derived from DFT calculations. As shown in Figure 13b, the relative part of remaining activity correlates with the out-of-plane displacement of the metal atom towards the N_4-plane for all monometallic catalysts except manganese. However, as the remaining activity correlates with this property related to the metal center, it seems that the displacement of the metal might be at the origin of the activity losses most probably due to a disintegration of the active MeN_4 sites. This would be in contrast to Goellner's conclusions were it was said that the carbon oxidation (and not an intrinsic instability of MeN_4 sites) is at the origin of active site destruction [24]. However, Goellner et al. studied only a Fe-N-C catalyst at different operation temperatures for the accelerated stress tests, whereas here a significant larger number of Me-N-C catalysts were considered.

Considering the previous findings on carbon oxidation during AST_SSC in combination with our results on these D_3-band changes we thus suggest the degradation scheme given in Figure 14 for the deactivation of Me-N-C catalysts during AST_SSC.

In general, the oxidation of disordered carbon (decrease of D-band intensity) can cause an overall oxidation to CO_2 and CO and leads to the formation of surface oxides. This phenomenon is visible for both Pt/C catalysts and the Me-N-C catalysts. Beside this phenomenon, a decrease of the D_3-band intensity is observed exclusively for Me-N-C catalysts.

In our current model, the D_3-band intensity is related to the disintegration of active MeN_4 sites that might be initiated by both: the oxidation of the surrounding graphene sheets and by a release of the metal out of the N_4 core that is induced by the displacement of the metal out of the N_4-plane causing significant activity losses during start-up and shut-down conditions.

4. Conclusions

In this work the effect of the metal species on the activity and the stability of Me-N-C catalysts was investigated. Our results indicate that the formation of MeN_4 sites is thermodynamically likely to happen for all investigated metals, except Mo. The amount of nitrogen that can be kept in the catalyst during the pyrolysis depend on the metal nitrogen bond distance. A correlation of the nitrogen contents assigned to N_{pyrid} and N_{MeN} (both assigned to different MeN_4 sites, compare Figure 14) with the intensity of the D_3-band provides strong evidence that the D_3-band intensity is composed in parts by vibrational modes assigned to the integration of different types of MeN_4 sites in graphene layers.

The AST_SSC conditions do cause considerable alterations of the D-band and D_3-band intensities. Correlations of activity losses were found with the decrease of the D_3-band intensity and with the displacement of the metal atoms out of the N_4-plane. Therefore, it can be concluded that the degradation of the Me-N-C catalysts under such oxidising conditions is governed by the carbon oxidation and the disintegration of the MeN_4 sites as indicated by the decrease of the D_3-band intensity.

Acknowledgements

The possibility to do X-ray induced photoelectron spectroscopy at the DAISY-FUN system of Wolfram Jaegermann's group at TU Darmstadt is gratefully acknowledged. Technical support by Sabine Hess is greatly acknowledged. Financial Support by the German Research Foundation (DFG) via the Excellence initiative TU Darmstadt Graduate School of Excellence Energy Science and Engineering (ESE) (GSC1070) is also gratefully acknowledged.

References

[1] U.I. Kramm, P. Bogdanoff, S. Fiechter, in: R.A. Meyers (Ed.), Encyclopedia of Sustainability Science and Technology, Springer New York, New York, NY, 2012, pp. 8265–8307.
[2] R. Jasinski, Nature 201 (1964) 1212–1213.
[3] H. Jahnke, M. Schonborn, G. Zimmermann, Topics in current chemistry 61 (1976) 133–181.
[4] J.A. van Veen, J.F. van Baar, C.J. Kroese, J.G.F. Coolegem, N. de Wit, H.A. Colijn, Berichte der Bunsengesellschaft für physikalische Chemie 85 (1981) 693–700.
[5] V.S. Bagotzky, M.R. Tarasevich, K.A. Radyushkina, O.A. Levina, S.I. Andrusyova, Journal of Power Sources 2 (1978) 233–240.
[6] M. Lefevre, E. Proietti, F. Jaouen, J.-P. Dodelet, Science (New York, N.Y.) 324 (2009) 71–74.
[7] E. Proietti, F. Jaouen, M. Lefèvre, N. Larouche, J. Tian, J. Herranz, J.-P. Dodelet, Nat Comms 2 (2011) 416.
[8] G. Wu, K.L. More, C.M. Johnston, P. Zelenay, Science 332 (2011) 443–447.
[9] J. Shui, C. Chen, L. Grabstanowicz, D. Zhao, D.-J. Liu, Proceedings of the National Academy of Sciences of the United States of America 112 (2015) 10629–10634.
[10] U.I. Koslowski, I. Abs-Wurmbach, S. Fiechter, P. Bogdanoff, J. Phys. Chem. C 112 (2008) 15356–15366.
[11] U.I. Kramm, I. Abs-Wurmbach, I. Herrmann-Geppert, J. Radnik, S. Fiechter, P. Bogdanoff, J. Electrochem. Soc 158 (2011) B69–B78.
[12] A. Zitolo, V. Goellner, V. Armel, M.-T. Sougrati, T. Mineva, L. Stievano, E. Fonda, F. Jaouen, Nature materials 14 (2015) 937–942.
[13] M. Lefèvre, J.P. Dodelet, P. Bertrand, J. Phys. Chem. B 104 (2000) 11238–11247.
[14] F. Jaouen, S. Marcotte, J.-P. Dodelet, G. Lindbergh, J. Phys. Chem. B 107 (2003) 1376–1386.
[15] F. Charreteur, F. Jaouen, S. Ruggeri, J.-P. Dodelet, Electrochimica Acta 53 (2008) 2925–2938.
[16] U.I. Kramm, A. Zana, T. Vosch, S. Fiechter, M. Arenz, D. Schmeißer, J. Solid State Electrochem. (Journal of Solid State Electrochemistry) 20 (2016) 969–981.
[17] N.R. Sahraie, U.I. Kramm, J. Steinberg, Y. Zhang, A. Thomas, T. Reier, J.-P. Paraknowitsch, P. Strasser, Nat Commun 6 (2015) 8618.
[18] A. Serov, K. Artyushkova, E. Niangar, C. Wang, N. Dale, F. Jaouen, M.-T. Sougrati, Q. Jia, S. Mukerjee, P. Atanassov, Nano Energy 16 (2015) 293–300.
[19] H. Tributsch, U.I. Koslowski, I. Dorbandt, Electrochim. Acta 53 (2008) 2198–2209.
[20] C.H. Choi, C. Baldizzone, J.-P. Grote, A.K. Schuppert, F. Jaouen, K.J.J. Mayrhofer, Angew. Chem. Int. Ed 54 (2015) 12753–12757.
[21] U.I. Kramm, M. Lefevre, P. Bogdanoff, D. Schmeisser, J.-P. Dodelet, J. Phys. Chem. Lett. 5 (2014) 3750–3756.
[22] K. Sasaki, M. Shao, R. Adzic, in: F.N. Büchi, M. Inaba, T.J. Schmidt (Eds.), Polymer Electrolyte Fuel Cell Durability, Springer New York, New York, NY, 2009, pp. 7–27.
[23] C.A. Reiser, L. Bregolia, T.W. Patterson, J.S. Yi, J.D. Yang, M.L. Perry, T.D. Jarvi, Electrochem. Solid-State Lett 8 (2005) A273–A276.
[24] V. Goellner, C. Baldizzone, A. Schuppert, M.T. Sougrati, K. Mayrhofer, F. Jaouen, Phys. Chem. Chem. Phys 16 (2014) 18454–18462.
[25] A. Zana, J. Speder, N.E. Reeler, T. Vosch, M. Arenz, Electrochimica Acta 114 (2013) 455–461.
[26] F. Jaouen, J.P. Dodelet, J. Phys. Chem. C 113 (2009) 15422–15432.
[27] I. Herrmann, U.I. Kramm, J. Radnik, S. Fiechter, P. Bogdanoff, J. Electrochem. Soc 156 (2009) B1283–1292.
[28] R. Borup, J. Meyers, B. Pivovar, Y.S. Kim, R. Mukundan, N. Garland, D. Myers, M. Wilson, F. Garzon, D. Wood, P. Zelenay, K. More, K. Stroh, T. Zawodzinski, J. Boncella, J.E. McGrath, M. Inaba, K. Miyatake, M. Hori, K. Ota, Z. Ogumi, S. Miyata, A. Nishikata, Z. Siroma, Y. Uchimoto, K. Yasuda, K. Kimijima, N. Iwashita, Chem. Rev 107 (2007) 3904–3951.
[29] M. Lefèvre, J.P. Dodelet, P. Bertrand, J. Phys. Chem. B 106 (2002) 8705–8713.
[30] R.G. Pearson, Proceedings of the National Academy of Sciences 83 (1986) 8440–8441.
[31] J.H. Zagal, F. Bedioui, J.-P. Dodelet, N4-Macrocyclic Metal Complexes, Springer New York, New York, NY, 2006.
[32] A. Ohma, K. Shinohara, A. Iiyama, T. Yoshida, A. Daimaru, ECS Trans. 41 (2011) 775–784.
[33] A.L. Bouwkamp-Wijnoltz, W. Visscher, J.A.R. van Veen, E. Boellaard, A.M. van der Kraan, S.C. Tang, J. Phys. Chem. B 106 (2002) 12993–13001.
[34] V. Armel, J. Hannauer, F. Jaouen, Catalysts 5 (2015) 1333–1351.
[35] G. Wu, C.M. Johnston, N.H. Mack, K. Artyushkova, M. Ferrandon, M. Nelson, J.S. Lezama-Pacheco, S.D. Conradson, K.L. More, D.J. Myers, P. Zelenay, J. Mater. Chem 21 (2011) 11392–11405.
[36] U.I. Kramm, I. Herrmann-Geppert, J. Behrends, K. Lips, S. Fiechter, P. Bogdanoff, J. Am. Chem. Soc 138 (2016) 635–640.
[37] F. Charreteur, F. Jaouen, J.-P. Dodelet, Electrochimica Acta 54 (2009) 6622–6630.
[38] U.I. Kramm, J. Herranz, N. Larouche, T.M. Arruda, M. Lefèvre, F. Jaouen, P. Bogdanoff, S. Fiechter, I. Abs-Wurmbach, S. Mukerjee, J.-P. Dodelet, Phys. Chem. Chem. Phys 14 (2012) 11673.
[39] U.I. Kramm, M. Lefèvre, N. Larouche, D. Schmeisser, J.-P. Dodelet, J. Am. Chem. Soc 136 (2014) 978–985.

[40] U.I. Kramm, I. Herrmann-Geppert, P. Bogdanoff, S. Fiechter, J. Phys. Chem. C 115 (2011) 23417–23427.
[41] H. Meng, N. Larouche, M. Lefèvre, F. Jaouen, B. Stansfield, J.-P. Dodelet, Electrochimica Acta 55 (2010) 6450–6461.
[42] http://www.vasp.at, http://www.vasp.at.
[43] Perdew, Burke, Ernzerhof, Physical review letters 77 (1996) 3865–3868.
[44] F. Calle-Vallejo, J.I. Martínez, J. Rossmeisl, Phys. Chem. Chem. Phys 13 (2011) 15639–15643.
[45] A. Bonakdarpour, M. Lefevre, R. Yang, F. Jaouen, T. Dahn, J.-P. Dodelet, J.R. Dahn, Electrochem. Solid-State Lett 11 (2008) B105–B108.
[46] C.W. Bezerra, L. Zhang, K. Lee, H. Liu, A.L. Marques, E.P. Marques, H. Wang, J. Zhang, Electrochimica Acta 53 (2008) 4937–4951.
[47] H. Peng, F. Liu, X. Liu, S. Liao, C. You, X. Tian, H. Nan, F. Luo, H. Song, Z. Fu, P. Huang, ACS Catal 4 (2014) 3797–3805.
[48] A.H. Monteverde Videla, S. Ban, S. Specchia, L. Zhang, J. Zhang, Carbon 76 (2014) 386–400.
[49] H.-J. Zhang, X. Yuan, L. Sun, X. Zeng, Q.-Z. Jiang, Z. Shao, Z.-F. Ma, International Journal of Hydrogen Energy 35 (2010) 2900–2903.
[50] H. Jahnke, M. Schönborn, G. Zimmerman, The Electrochem. Soc (1974) 303–319.
[51] P. He, M. Lefevre, G. Faubert, J.-P. Dodelet, J. New Mat. Electrochem. Systems 2 (1999) 243–251.
[52] S. Li, L. Zhang, J. Kim, M. Pan, Z. Shi, J. Zhang, Electrochimica Acta 55 (2010) 7346–7353.
[53] I. Herrmann, U.I. Kramm, S. Fiechter, P. Bogdanoff, Electrochimica Acta 54 (2009) 4275–4287.
[54] U.I. Kramm, in: X. Feng (Ed.), Nanocarbons for Advanced Energy Conversion, Wiley-VCH Verlag GmbH & Co. KGaA, Weinheim, Germany, 2015, pp. 117–148.
[55] F. Jaouen, J. Herranz, M. Lefèvre, J.-P. Dodelet, U.I. Kramm, I. Herrmann, P. Bogdanoff, J. Maruyama, T. Nagaoka, A. Garsuch, J.R. Dahn, T. Olson, S. Pylypenko, P. Atanassov, E.A. Ustinov, ACS Appl. Mater. Interfaces 1 (2009) 1623–1639.
[56] F. Jaouen, J.-P. Dodelet, Electrochimica Acta 52 (2007) 5975–5984.
[57] R.J. Nemanich, S.A. Solin, Phys. Rev. B 20 (1979) 392–401.
[58] A. Sadezky, H. Muckenhuber, H. Grothe, R. Niessner, U. Pöschl, Carbon 43 (2005) 1731–1742.
[59] M.R. Tarasevich, K.A. Radyuskina, Materials Chemistry and Physics 22 (1989) 477–502.
[60] D. Scherson, A.A. Tanaka, S.L. Gupta, D. Tryk, C. Fierro, R. Holze, E.B. Yeager, R.P. Lattimer, Electrochimica Acta 31 (1986) 1247–1258.
[61] T. Jawhari, A. Roid, J. Casado, Carbon 33 (1995) 1561–1565.
[62] A. Cuesta, P. Dhamelincourt, J. Laureyns, A. Martínez-Alonso, J. Tascón, Carbon 32 (1994) 1523–1532.
[63] Y. Hiramitsu, H. Sato, H. Hosomi, Y. Aoki, T. Harada, Y. Sakiyama, Y. Nakagawa, K. Kobayashi, M. Hori, Journal of Power Sources 195 (2010) 435–444.
[64] S. Sze, Atmospheric Environment 35 (2001) 561–568.
[65] M. Hara, M. Lee, C.-H. Liu, B.-H. Chen, Y. Yamashita, M. Uchida, H. Uchida, M. Watanabe, Electrochimica Acta 70 (2012) 171–181.
[66] I.C. Man, H.-Y. Su, F. Calle-Vallejo, H.A. Hansen, J.I. Martínez, N.G. Inoglu, J. Kitchin, T.F. Jaramillo, J.K. Nørskov, J. Rossmeisl, ChemCatChem 3 (2011) 1159–1165.
[67] M.T. Koper, Journal of Electroanalytical Chemistry 660 (2011) 254–260.
[68] Y. Wang, D.C. Alsmeyer, R.L. McCreery, Chem. Mater 2 (1990) 557–563.
[69] F. Jaouen, F. Charreteur, J.P. Dodelet, J. Electrochem. Soc 153 (2006) A689–A698.
[70] H. Marsh, A.P. Warburton, J. Appl. Chem 20 (1970) 133–142.

4.2 Influence of sulfur in the precursor mixture on the structural composition of Fe-N-C catalysts

Hyperfine Interact (2018) 239:7
https://doi.org/10.1007/s10751-017-1481-z

Influence of sulfur in the precursor mixture on the structural composition of Fe-N-C catalysts

A. Janßen[1] · I. Martinaiou[1,2] · S. Wagner[2] · N. Weidler[2] · A. Shahraei[1,3] · U. I. Kramm[1,2,3]

Abstract Fe-N-C catalysts were prepared by a new synthesis protocol at 800 °C with subsequent acid leaching. The effect of sulfur was investigated by a systematic study in which the molar S/Fe ratio in the precursor was varied from 0.0 to 2.45. The obtained catalysts were evaluated for their ORR activity in 0.1 M H_2SO_4. In addition, the specific BET surface area was determined from N_2 sorption measurements and structural characterization was made by Mößbauer spectroscopy. Catalysts contain FeN_4 moieties and inorganic iron species. Structure activity correlation indicate a dominance of the ferrous low-spin FeN_4 site for the ORR activity. This is in agreement with previous findings. In addition, the optimum in terms of ORR activity is in the same S/Me range as found for porphyrin-based catalysts. However, in contrast to previous conclusions of an avoidance of iron carbide formation by sulfur addition, a very high S/Fe ratio is required to obtain a catalyst free of iron carbide. Further work is required to identify the parameter that indeed enables inhibition of iron carbide formation.

Keywords Fe-N-C catalysts · Electrocatalysis · Mößbauer spectroscopy · Oxygen reduction reaction (ORR)

This article is part of the Topical Collection on *Proceedings of the International Conference on the Applications of the Mössbauer Effect (ICAME 2017), Saint-Petersburg, Russia, 3–8 September 2017*
Edited by Valentin Semenov

✉ U. I. Kramm
kramm@ese.tu-darmstadt.de

[1] Graduate School of Excellence Energy Science and Engineering, Technische Universität Darmstadt, Otto-Berndt-Str. 3, 64287 Darmstadt, Germany

[2] Department of Materials- and Earth Sciences, Technische Universität Darmstadt, Alarich-Weiss-Str. 2, 64287 Darmstadt, Germany

[3] Department of Chemistry, Technische Universität Darmstadt, Alarich-Weiss-Str. 8, 64287 Darmstadt, Germany

1 Introduction

In proton exchange membrane fuel cells (PEMFC), today platinum supported on carbon (Pt/C) catalysts are the state-of-the-art materials to accelerate the hydrogen oxidation reaction (HOR) and oxygen reduction reaction (ORR). The two half-cell reactions are given in (1) and (2).

$$\text{HOR:} \qquad H_2 \rightarrow 2\,H^+ + 2\,e^- \tag{1}$$

$$\text{ORR:} \qquad O_2 + 4\,H^+ + 4\,e^- \rightarrow 2\,H_2O \tag{2}$$

One major problem that hinders a commercialization of PEMFC is the high cost contributions assigned to Pt/C. About 25% of the overall costs for a PEMFC system to be implemented in cars is attributed to the catalysts [1]! While the HOR is a fast reaction, the ORR is kinetically hindered. That is why about 80% of the used platinum amount are required on the cathodic side for the ORR. Hence, in order to reduce costs it is most effective to reduce the platinum loading or to substitute platinum on the cathode. Higher activity per gram platinum is for instance reached for platinum alloy catalysts, core-shell catalysts, shape controlled nanocrystals or nanoframes of platinum [2]. Nevertheless, in all cases still platinum is used as catalyst, even though it was already defined years ago as a critical raw material by the European Union (EU) [3].

There are different groups of non-precious metal catalysts (NPMC) that showed an activity for the oxygen reduction reaction in acidic environment. So far, Fe-N-C catalysts were the most promising NPMCs [4–7]. In early years Fe-N-C (or in general Me-N-C) were prepared by the pyrolysis of porphyrins or other MeN_4 macrocycles in order to improve ORR activity and stability [8–12]. The today's most active Fe-N-C catalysts are prepared from independent iron, nitrogen and carbon precursors [4, 5, 7]. A major advantage is the possibility to tune iron, nitrogen and carbon contents in the precursor independently from each other.

For porphyrin-based catalysts we were able to show by Mößbauer spectroscopy that only one distinct type of FeN_4 site dominates the ORR activity [13–15]. Later, this type of active site was confirmed for alternative preparation approaches [6, 16–20]. Nevertheless, it should be mentioned that other Fe-based catalysts did not give indication of the presence of FeN_4 sites. Instead, the activity was attributed to iron carbide and/or graphene layers surrounding iron carbide particles [21–23]. This illustrates two important aspects: 1st even though similar precursors might be used the obtained structural composition depends on individual ratios, and pyrolysis conditions (specifically temperature T, time t and pressure p) and 2nd the assignment of ORR activity is complex but required for further optimization of the catalysts.

Zitolo et al. showed for the first time a preparation with the exclusive presence of FeN_4 sites. Catalysts were obtained by a short pyrolysis at 900 °C with low iron content without further conditioning [20]. For another catalyst that indicated at room temperature again only the presence of FeN_4 sites, low-temperature Mößbauer spectroscopy indicated the presence of small fractions of iron oxide nanoparticles [24]. At room temperature these nanoparticles lead to a doublet with Mößbauer parameters that cannot be resolved from the doublet related to the ORR active FeN_4 moiety. Performing an acid leaching avoids the presence of these iron oxide nanoparticles [24]. This underlines the importance of acid-leaching steps in order to enable the removal of acid soluble by-products.

A simple preparation with almost homogeneous composition can be achieved by the oxalate supported pyrolysis of porphyrins with subsequent acid leaching [13]. Performing a second heat-treatment in forming gas (N_2/H_2) with a second acid-leaching enables a high density and exclusive presence of FeN_4 moieties in Fe-N-C as shown recently by X-ray diffraction, X-band electron paramagnetic resonance spectroscopy (EPR) and Mößbauer spectroscopy by us [25].

To the best of our knowledge, the oxalate-supported pyrolysis of porphyrins was the first preparation attempt that worked with an inorganic structure forming agent instead of a carbon support [26]. For cobalt porphyrin pyrolyzed in the presence of iron oxalate and sulfur it was shown that sulfur addition enables significant higher activities in a S/Me range of 0.2 to 0.4 [27]. In a first work, the improved performance was assigned to three aspects: 1st a better solubility of the inorganic by-products that are formed during the pyrolysis, 2nd an enhanced specific BET surface area and 3rd changes in the electronic structure of the surrounding carbon that becomes amorphous by S-addition to the precursor [28]. Also Kiciński et al. recently showed that S-addition can enhance the specific BET surface area [29]. However, further work focusing on the oxalate-supported pyrolysis of iron porphyrin confirmed the improved activity while the surface area was almost identical. Instead, by the combination of in-situ high-temperature X-ray diffraction (HT-XRD), thermogravimetry coupled with mass-spectroscopy (TG-MS) and a detailed characterization of the catalysts we were able to show that without S-addition iron carbide formation coincides with the destruction of FeN_4 sites [30]. Thermodynamic calculations for $S/Fe = 0.37$ confirmed that iron carbide gets only stabilized at temperatures above 810 °C. Without S-addition, in the oxalate-supported pyrolysis iron carbide is formed at about 580 °C [30]. Hence, S-addition enables a simple preparation with relatively homogeneous composition (in terms of FeN_4 sites vs. inorganic iron species) of the catalysts. The improving effect was attributed to the hindrance of supersaturation of iron clusters with carbon by sulfur addition [31]. For this process, sulfur has to adsorb on iron [32].

Based on previous studies, in this work we optimized the ratio of S/Fe in the precursor in order to enable a maximum in current density and the aim of achieving a homogeneous catalyst composition.

2 Experimental part

2.1 Catalyst preparation

For the preparation of the catalysts, 2.85 mM 1,10-phenanthroline (Phen) were mixed with 20.0 mM dicyandiamide (DCDA) and 0.76 mM iron acetate (FeAc) in a mortar until a homogeneous mixture was obtained. In case of sulfur addition, the S-pellets were added to the other precursors and thoroughly mixed. In this work the molar sulfur to iron ratio was varied between $S/Fe = 0.0$ to $S/Fe = 2.45$.

The obtained precursor was filled in a quartz boat and placed in a tube furnace. The overall oven program was run in inert gas atmosphere. The sample was heated with a ramp of 5 K min^{-1} up to 300 °C (30 min), 500 °C (30 min) and then finally to 800 °C (60 min). Then the oven was cooled down (<80 °C) before the sample was transferred into 2 M HCl. To accelerate the reaction, the solution was placed for 1 h in an Ultrasonic (US) bath, before it was left overnight. Then the catalyst was filtered and washed with 1.5 l distilled water before the filter cake was dried overnight. The yield was determined from the catalyst weight after drying toward the initial precursor mass (except sulfur). In sample label the S/Fe ratio is indicated as value. For example Fe-N-C_0.82 is the label of the sample prepared with $S/Fe = 0.82$.

2.2 Electrochemistry

In order to investigate the catalytic performance of the electrocatalysts, measurements with a rotating disk electrode (RDE) setup were performed in 0.1 M H_2SO_4. The RDE electrode equipped with a glassy carbon disk ($A_{geo} = 0.1963\ cm^2$) was used as working electrode, a glassy carbon rod and a (Ag/AgCl/3 M KCl) electrode were used as counter and reference electrode. All potential values of this work are given with respect to the standard hydrogen electrode (SHE). In a first step, a catalyst ink was prepared. Therefore, 5 mg of catalyst powder were mixed with 250 μl of a 0.5 wt% Nafion solution in H_2O/EtOH. The suspension was placed in an ultrasonic (US) bath for 15 min, followed by mixing on a Vortexer for 1 min. Both steps were repeated, before the ink preparation was finished with a treatment for about 1 min with a US homogenization needle. 5 μl of this ink were drop casted on the RDE electrode and allowed to dry. The resulting catalyst loading is 0.509 $mg_{cat}\ cm_{geo}^{-2}$.

The overall current in an RDE experiment constitute of the current contributions assigned to oxygen reduction reaction and a capacity current that is attributed to the charging of the electrochemical double layer. The capacity current can be measured by performing the experiments in N_2-saturated electrolyte. In a first place, the catalyst was cycled until steady state was reached in a potential range of 0.0 to 1.2 V(SHE). Then the capacity current was determined by a cathodic linear sweep voltammetry (LSV) with a sweep rate of 10 mV s^{-1}.

Afterwards the electrolyte was saturated with oxygen until a constant value for the open circuit potential was reached (approx. 10–15 min). A LSV in O_2-saturated electrolyte was performed for a rotation speed of 1500 rounds per minute (rpm) with the same conditions as in N_2. After subtracting the capacity current density, the kinetic current density j_{kin} was determined from (3):

$$j^{-1} = j_{kin}^{-1} + j_{diff}^{-1} \tag{3}$$

In this equation, j denotes the capacity corrected overall current density and j_{diff} the diffusion limiting current density. In this work the absolute value of the kinetic current density at a potential of 0.75 V is defined as ORR activity and used for comparison of the different catalysts. An exemplary RDE measurement is given in Fig. 1.

2.3 Physico-chemical characterization

In order to determine the BET surface area of the catalysts, N_2 sorption was measured at 77 K. Previous to the measurements the samples were degassed at 200 °C overnight. Measurements and data analysis were performed with an AUTOSORB instrument from Quantachrome.

Mößbauer spectroscopy was made in transmission mode using a Co/Rh source and a scintillation detector for data acquisition. Calibration of the velocity scale was made with respect to alpha-iron at room temperature. Samples were measured in a velocity range of 6 mm s^{-1}. Lorentzian site analysis was performed to determine Mößbauer parameters. Assignment of iron species was made by comparison to literature data.

3 Results and discussion

3.1 Effect of S/Fe ratio on yield and surface area

As described in the introduction it is the aim to prepare highly active Fe-N-C catalysts with the presence of FeN_4 centers and carbon black, only. Inorganic iron impurities can lead to higher yields and block pores so that less active sites are accessible during ORR.

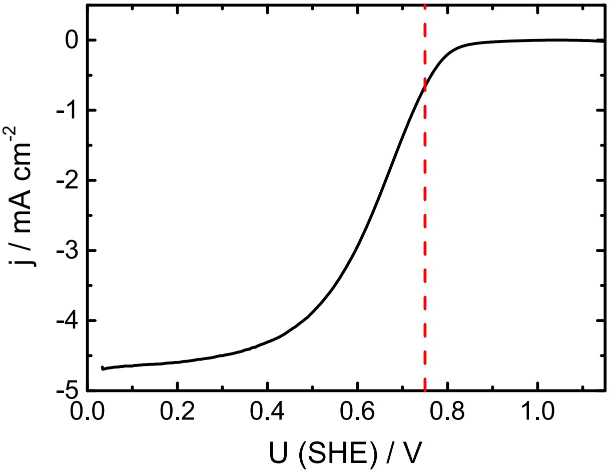

Fig. 1 Exemplary linear sweep voltammetry (LSV) of Fe-N-C_0.82. The potential of 0.75 V is indicated with a dashed line and used for reasons of comparison of different catalysts

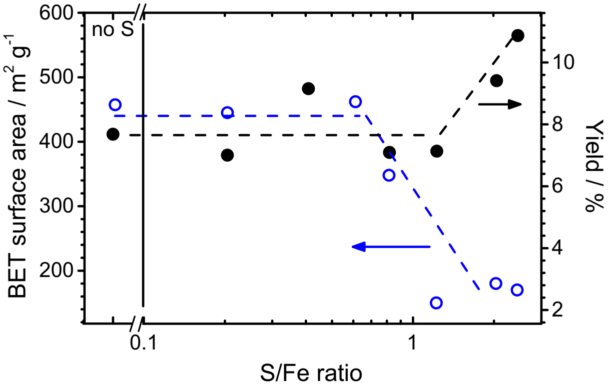

Fig. 2 BET surface area (○) and yield (●) as a function of the S/Fe ratio

Therefore, in Fig. 2 the yield and BET surface area of the different catalysts are given as a function of S/Fe ratio. It can be noted that the yield remains almost constant up to a S/Fe ratio of 1.2. Above this ratio it increases and reaches a maximum of 12%. Contrary, the BET surface area remains constant up to a ratio of S/Fe = 0.6 and starts already to decrease for higher S/Fe ratios. Above S/Fe = 1.0 the BET surface area remains at a low level of <200 m^2 g^{-1}. The trends of yield and BET surface area indicate that most probably inorganic iron species are formed at high S/Fe ratios as it will be confirmed by structural characterization.

3.2 Effect of S/Fe ratio on the oxygen reduction reaction

In order to study the impact of sulfur addition on the electrochemical performance of the catalysts the ORR activity was determined, the obtained values are given in Fig. 3 as a function of S/Fe ratio.

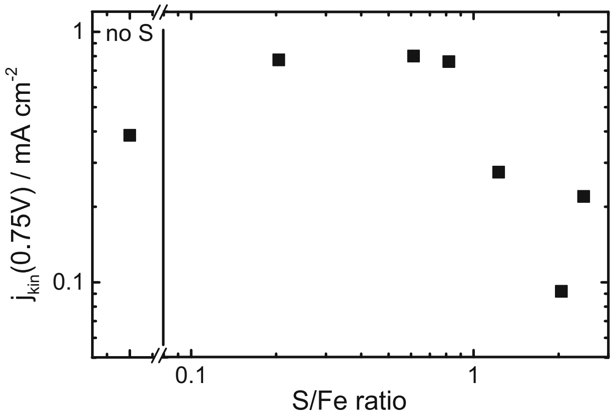

Fig. 3 Kinetic current density at 0.75 V as a function of S/Fe ratio

Induced by sulfur addition, the ORR activity is almost doubled in comparison to the S-free catalyst. Again, above a ratio of S/Fe = 1 the activity drops down and remains at a low level. This drop in ORR activity correlates well with the obtained increases in yield and drop in BET surface area. It can be assumed that the lower ORR activity of the S-free sample might be related to iron carbide formation whereas at high S/Fe ratios iron sulfide species might have been formed. In order to evaluate this statement, the catalysts were checked for the type of iron species present in the catalyst.

3.3 Effect of S/Fe ratio on the structural composition

Mößbauer spectroscopy has proven to be the most suitable technique for the characterization of iron sites in Fe-N-C catalysts. The big advantage is that beside crystalline phases also amorphous structures and in specific FeN_4 sites can be identified. The Mößbauer spectra of the S-free catalyst, with the highest S/Fe ratio and of the most active catalyst (Fe-N-C_0.82) are shown in Fig. 4. The averaged Mößbauer parameters of all three catalysts are summarized in Table 1.

In case of Fe-N-C_0.0 the typical Mößbauer signature of S-free catalysts is obtained. The material is dominated by iron carbide (Sext2), but small lines assigned to alpha-iron are seen as well (Sext1, indicated by arrows) are indicated as well [30, 33]. It is interesting to note, that for the S-free sample the absorption area assigned to FeN_4 sites is significantly larger in comparison to the S-free porphyrin-based Fe-N-C catalysts [30]. On the one hand, this could be attributed to the significant larger nitrogen fraction in the precursor, on the other hand the significant better thermal stability of pyridinic nitrogen in comparison to pyrrolic nitrogen could be at the origin [34].

Fe-N-C_0.0 also contains about 10% of an iron species that was not possible to assign. Fits were performed considering two different approaches. In a first approach a sextet was implemented beside the already known structure. In such a case the isomer shift was indicative of a ferrous high-spin state with a magnetic field of 8.3 T ($X^2 = 2.7$). An even better fit was obtained assuming a further doublet (here labeled D3, compare Table 1, $X^2 = 1.9$). Also here, the isomer shift indicates a high-spin site, with an unusual large quadrupole splitting. In Fig. 4a the model assuming a doublet species was plotted (note: the absorption area of the unknown species accounts in both fit approaches to about 10%).

Fig. 4 Mößbauer spectra for Fe-N-C_0.0 (**a**), Fe-N-C_0.82 (**b**) and Fe-N-C_2.45 (**c**)

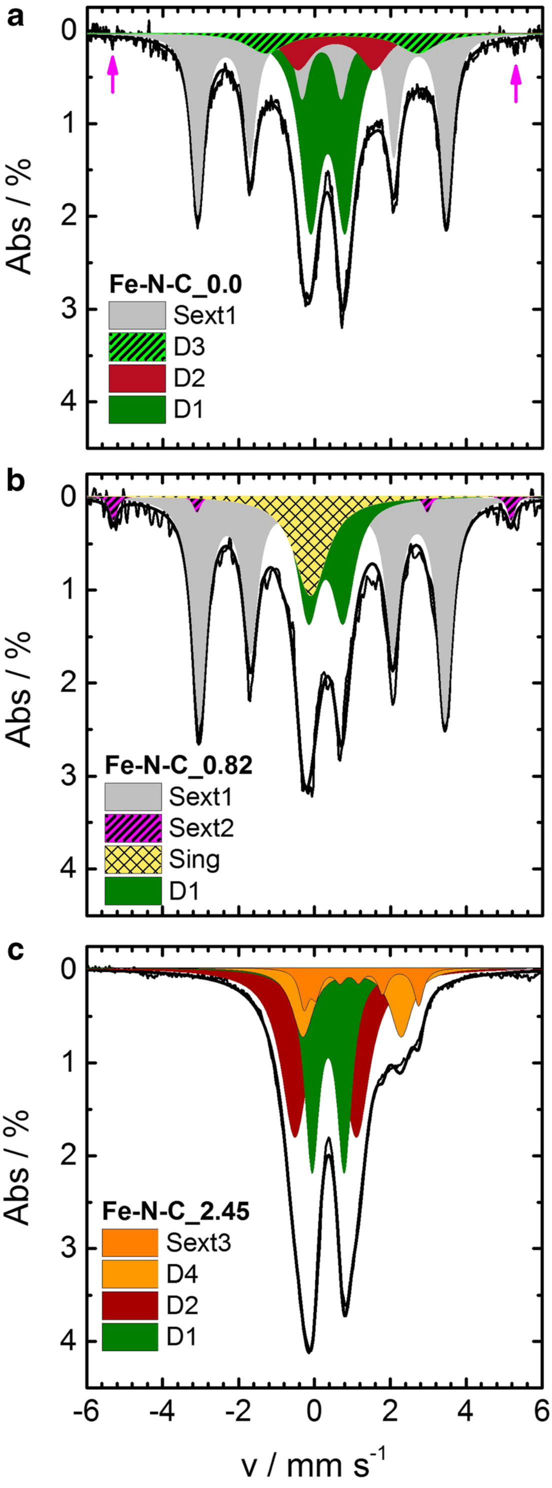

Table 1 Summary of the Mößbauer parameters for the three investigated catalysts and assignment to iron species

	δ_{iso}	ΔE_Q	fwhm	Magn.	Area /%			Assignment
	/mm s^{-1}			Field/T	_0.00	_0.82	_2.45	
Sing	−0.10	–	0.70	–	–	15.1	–	Nano-Iron
D1	0.34	0.90	0.60	–	37.2	22.9	30.4	FeN$_4$, 2+, LS
D2	0.43	1.81	0.86	–	9.7	–	45.8	FeN$_4$, 2+, MS
D3	0.71	4.01	1.2 *	–	7.7	–	–	Unknown
D4	0.99	2.59	0.70	–	–	–	15.9	Nano-Fe$_3$S$_4$
Sext1	0.19	<0.01	0.42	20.2	45.4	58.6	–	Fe$_3$C
Sext2	−0.06	–	0.24	32.5	–	3.4	–	α-Fe
Sext3	1.08	0.16	0.32	9.4	–	–	7.9	Nano-Fe$_3$S$_4$
					Fe-contents from XPS/wt%			
					0.66	2.41	0.95	

For the most active catalyst Fe-N-C_0.82 the composition was surprising. Even though—based on our previous study [30]—the temperature was in a range where an inhibition of iron carbide formation by sulfur addition was expected, the catalyst still contained iron carbide. So far, iron carbide was only found in S-added catalysts when the temperature exceeded 810 °C [16]. Thermodynamic calculations in our previous work showed that this temperature is the lower limit for the thermodynamic stability of iron carbide in the presence of sulfur. The calculations were made for the S-containing precursor composition of the oxalate-supported pyrolysis [30].

In this work, only for the highest sulfur content, the catalyst Fe-N-C_2.45 was free of iron carbide. In this case, however, two additional iron sites (D4, Sext3) were found. Based on the large isomer shift and due to the presence of excess sulfur, both D4 and Sext3 are assigned to nanoparticles of ferrous iron sulfide [16, 17].

3.4 Correlation of structural composition and ORR activity

As discussed in the introduction the D1 motif was assigned as ORR active site by us and others. In contrast, other groups prepared catalysts even free of the D1 motif but ORR active. Activity was assigned to iron carbide and/or graphene layers surrounding iron carbide structures. Regarding our catalysts, all samples contain the D1 motif, but the Sext1 motif is absent in Fe-N-C_2.45. Therefore, an exclusive ORR activity of the Sext1 motif can be excluded.

From the absorption area of a Mößbauer site and the iron content of the catalyst one can estimate the amount of iron assigned to each motif. We have to assume a homogeneous distribution of iron in our catalysts, as iron contents are only available from X-ray induced photoelectron spectroscopy. The related iron contents were determined for the D1 and Sext1 motif.

In terms of activity, we already concluded from Figs. 1 and 2 that the surface area that is available for ORR catalysis is changing with the variation of S/Fe-content. Therefore, the kinetic current density related to the specific BET surface area is a better measure for a comparison of the three catalysts. Based on the kinetic current density and the catalyst loading on the GC electrode (0.509 mg_{cat} cm_{geo}^{-2}) a mass-based kinetic current density can

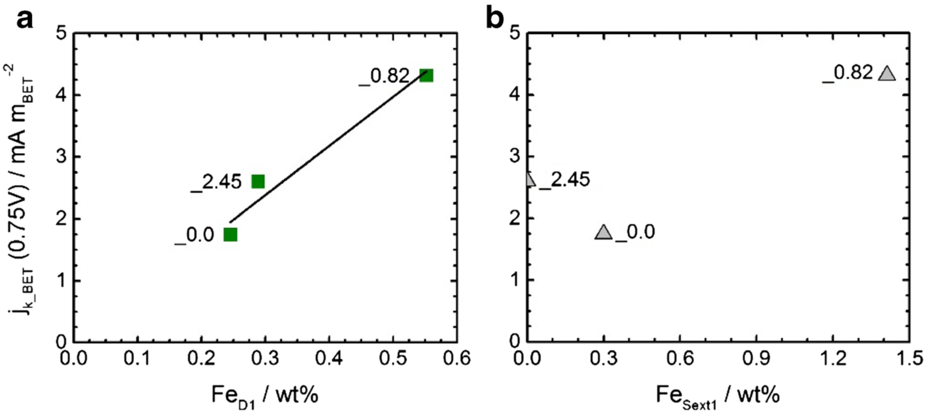

Fig. 5 Correlation of the specific BET surface area related kinetic current density j_{k_BET} with the estimated iron content assigned to D1 (**a**, 🟩) and Sext1 (**b**, ▲)

be determined (in A g_{cat}^{-1}) that can then be related to the specific BET surface area (in m_{BET}^2 g^{-1}) to get a value j_{k_BET} that gives the kinetic current density in relation to the specific BET surface area (in mA m_{BET}^{-2}). Please note: to avoid confusion between the geometric area of the glassy carbon disk and the BET surface area we implemented the subscript BET for the specific BET surface area.

In Fig. 5 the specific BET surface area related kinetic current density j_{k_BET} is plotted as a function of the iron content assigned to the D1 motif (a) and the Sext1 motif (b). While the correlation of the D1 motif goes straight through zero, there is no trend assigned to the Sext1 motif. This does not necessarily exclude a contribution of iron carbide species to the ORR activity but makes it unlikely. Hence, the observations made for this preparation are in agreement with our previous works.

4 Conclusions

In this work the effect of sulfur was investigated for a new preparation attempt to prepare Fe-N-C catalysts for the oxygen reduction reaction. Several Fe-N-C catalysts were prepared with nominal S/Fe ratios (in precursor) of 0.0 to 2.45. The catalysts without sulfur, with the maximum in activity and with the highest sulfur content were structurally analyzed in detail. In fact, only for the highest S/Fe ratio a catalyst free of iron carbide was obtained, whereas at lower values—and especially also in the range of maximum activity—catalysts contained iron carbide. The results indicate that instead of S/Fe ratio another parameter seems to be of more importance in terms of the possibility of avoiding iron carbide formation.

It is shown that similar to previous conclusions also here, the amount of ORR active D1 sites (ferrous FeN_4, low spin) dominates the catalytic activity of these catalysts. With the aim of achieving a homogeneously composed catalyst with high activity additional work is required to define the parameter that determines whether iron carbide is formed or not.

Acknowledgements Financial support by the German Research Foundation (DFG) for the Graduate School of Excellence Energy Science and Engineering (GSC1070), the Federal Ministry of Education and Research (BMBF) via the projects NUKFER (05K16RD1) and StRedO (03XP0092) is gratefully acknowledged.

References

1. Frank de Bruijn, A., Janssen, G.J.M.: Encycl. Sustain. Sci. Technol. 7694 (2014)
2. Banham, D., Ye, S.: ACS Energy Lett. **2**, 629 (2017)
3. European Commission: Report on critical raw materials for the EU (2014)
4. Proietti, E., Jaouen, F., et al.: Nat. Commun. **2**, 416 (2011)
5. Wu, G., More, K.L., et al.: Science **332**, 443 (2011)
6. Kramm, U.I., Lefèvre, M., et al.: J. Am. Chem. Soc. **136**, 978 (2014)
7. Shui, J., Chen, C., et al.: Proc. Natl. Acad. Sci. USA **112**, 10629 (2015)
8. Bae, I.T., Tryk, D.A., Scherson, D.A.: J. Phys. Chem. B **102**, 4114 (1998)
9. Blomquist, J., Lang, H., et al.: J. Chem. Soc., Faraday Trans. **88**, 2007 (1992)
10. Bouwkamp-Wijnoltz, A.L., Visscher, W., et al.: J. Phys. Chem. B **106**, 12993 (2002)
11. Jahnke, H., Schönborn, M., Zimmermann, G.: Topics Curr. Chem. **61**, 133 (1976)
12. Scherson, D.A., Tanaka, A.A., et al.: Electrochim. Acta **31**, 1247 (1986)
13. Koslowski, U.I., Abs-Wurmbach, I., et al.: J. Phys. Chem. C **112**, 15356 (2008)
14. Kramm, U.I., Abs-Wurmbach, I., et al.: J. Electrochem. Soc. **158**, B69 (2011)
15. Kramm, U.I., Herrmann-Geppert, I., et al.: J. Phys. Chem. C **115**, 23417 (2011)
16. Ferrandon, M., Kropf, A.J., et al.: J. Phys. Chem. C **116**, 16001 (2012)
17. Sahraie, N.R., Kramm, U.I., et al.: Nat. Commun. **6**, 8618 (2015)
18. Zhang, S., Liu, B., Chen, S.: Phys. Chem. Chem. Phys. **15**, 18482 (2013)
19. Zhu, Y., Zhang, B., et al.: Angew. Chem., Int. Ed. **53**, 10673 (2014)
20. Zitolo, A., Goellner, V., et al.: Nat. Mater. **14**, 937 (2015)
21. Hu, Y., Jensen, J.O., et al.: Angew. Chem. Int. Ed. **53**, 3675 (2014)
22. Varnell, J.A., Tse, E.C.M., et al.: Nat. Commun. **7**, 12582 EP (2016)
23. Strickland, K., Miner, E., et al.: Nat. Commun. **6**, 7343 (2015)
24. Sougrati, M.T., Goellner, V., et al.: Catal. Today **262**, 110 (2016)
25. Kramm, U.I., Herrmann-Geppert, I., et al.: J. Am. Chem. Soc. **138**, 635 (2016)
26. Bogdanoff, P., Herrmann, I., et al.: J. New Mater. Electrochem. Syst. **7**, 85 (2004)
27. Herrmann, I.: Doktorarbeit. Freie Universität, Berlin (2005)
28. Herrmann, I., Kramm, U.I., et al.: J. Electrochem. Soc. **156**, B1283 (2009)
29. Kiciński, W., Dembinska, B., et al.: Carbon **116**, 655 (2017)
30. Kramm, U.I., Herrmann-Geppert, I., et al.: J. Mater. Chem. A **2**, 2663 (2014)
31. Marsh, H., Warburton, A.P.: J. Appl. Chem. **20**, 133 (1970)
32. Grabke, H.J., Moszynski, D., et al.: Surf. Interface Anal. **34**, 369 (2002)
33. Greenwood, N.N., Gibb, T.C.: Mössbauer Spectroscopy, 1st edn. Chapman and Hall Ltd., London (1971)
34. Pels, J.R., Kapteijn, F., et al.: Carbon **33**, 1641 (1995)

4.3 Improved electrochemical performance of Fe-N-C catalysts through Ionic Liquid modification in alkaline media

Journal of Power Sources 375 (2018) 222–232

Contents lists available at ScienceDirect

Journal of Power Sources

journal homepage: www.elsevier.com/locate/jpowsour

Improved electrochemical performance of Fe-N-C catalysts through ionic liquid modification in alkaline media

Ioanna Martinaiou [a, b, 1], Thomas Wolker [c, 1], Ali Shahraei [a, b], Gui-Rong Zhang [c], Arne Janßen [a, b], Stephan Wagner [a, b], Natascha Weidler [a, b], Robert W. Stark [d], Bastian J.M. Etzold [c, **], Ulrike I. Kramm [a, b, *]

[a] *TU Darmstadt, Catalysts and Electrocatalysts, Department of Material and Earth Sciences and Department of Chemistry, Jovanka-Bontschits-Str. 2, 64287 Darmstadt, Germany*
[b] *Graduate School of Excellence Energy Science and Engineering, Jovanka-Bontschits-Str. 2, 64287 Darmstadt, Germany*
[c] *TU Darmstadt, Ernst-Berl-Institut für Technische und Makromolekulare Chemie, Alarich-Weiss-Straße 8, 64287 Darmstadt, Germany*
[d] *TU Darmstadt, Physics on Surfaces, Department of Materials- and Earth Science, Alarich-Weiss-Str. 16, 64287 Darmstadt, Germany*

HIGHLIGHTS

- Modification of two types of Fe-N-C catalysts by an ionic liquid.
- IL modification leads to improved activity and stability for a sulfur-free catalyst.
- Strong correlation between the double layer capacitance and the activity.

GRAPHICAL ABSTRACT

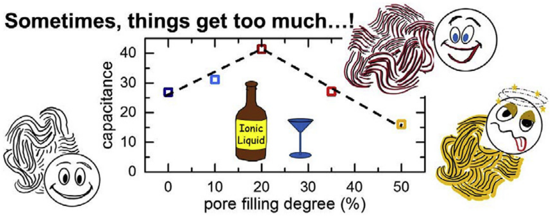

ARTICLE INFO

Article history:
Received 17 May 2017
Received in revised form
5 July 2017
Accepted 6 July 2017
Available online 20 July 2017

Keywords:
Fe-N-C catalyst
Oxygen reduction reaction
SCILL
Ionic liquid modification
Non-PGM catalyst

ABSTRACT

It is well known that Fe-N-C catalysts reach a significantly better ORR activity in alkaline compared to acidic electrolyte. This advantage makes the material of interest for application in alkaline fuel cells. Beside this, for Pt/C catalyst it is known that the performance in acid can be significantly enhanced through ionic liquid modification following the Solid Catalysts with Ionic Liquid Layer (SCILL) concept. In our current study we combine both advantages and investigate for two Fe-N-C catalysts prepared either with or without sulfur in the precursor mixture the effect of IL modification. The unmodified catalysts are characterized using X-ray induced photoelectron spectroscopy (XPS), ^{57}Fe Mößbauer and Raman spectroscopy as well as N_2 sorption. The electrochemical behavior of the unmodified catalyst and with different pore-filling degrees of ionic liquid (IL) is analysed with respect to double layer capacitance, ORR activity and stability in accelerated stress tests mimicking the load-cycle conditions.

1. Introduction

The oxygen reduction reaction (ORR) is a fundamental reaction with a crucial importance in a variety of applications such as fuel cells, metal-air batteries and other electrochemical energy technologies. The sluggish and complex kinetics of this reaction; however, require the use of precious Pt group catalysts in order to avoid high efficiency losses. This leads to increased costs on these

---

* Corresponding author. TU Darmstadt, Catalysts and Electrocatalysts, Department of Material and Earth Sciences and Department of Chemistry, Jovanka-Bontschits-Str. 2, 64287 Darmstadt, Germany.

** Corresponding author. TU Darmstadt, Ernst-Berl-Institut für Technische und Makromolekulare Chemie, Alarich-Weiss-Straße 8, 64287 Darmstadt, Germany.

E-mail addresses: etzold@tc1.tu-darmstadt.de (B.J.M. Etzold), kramm@ese.tu-darmstadt.de (U.I. Kramm).

[1] Both authors contributed equally.

http://dx.doi.org/10.1016/j.jpowsour.2017.07.028

energy conversion/storage devices especially in fuel cell technologies [1]. In order to overcome the cost barrier, a lot of effort has been put in replacing the precious Pt-based catalysts with less expensive alternatives. The so-called non-precious metal catalysts (NPMCs) especially the family of transition metal-nitrogen-carbon (Me-N-C) catalysts represent the most promising candidates as alternatives to the costly Pt catalysts.

Recently, significant advances have been made regarding the activity, performance and stability of these Me-N-C catalysts in acidic media [2–9]. The major problem of NPMCs in acidic electrolyte is their poor stability, which is usually attributed to the corrosion of the carbon support as well as the destruction of active sites of the catalysts induced by hydrogen peroxide, a product of the $2e^-$ reduction of O_2. Regarding the alkaline media, since the mid-1960s alkaline fuel cells (AFCs) have played a leading role in fuel cell technologies due to their high power densities, long lifetimes and high efficiencies that they provide. The chemical reactions in alkaline solution are [10]:

$$O_2 + 2H_2O + 4e^- \rightarrow 4OH^- \ (E_0 = 0.401\ V) \quad (1)$$

$$O_2 + H_2O + 2e^- \rightarrow HO^-{}_2 + OH^- \ (E_0 = -0.065\ V) \quad (2)$$

$$HO^-{}_2 + H_2O + 2e^- \rightarrow 3OH^-. \ (E_0 = 0.68\ V) \quad (3)$$

In 2013 Brocato et al. [11] investigated the effect of pH (1–13.7) on the ORR efficiency of Fe-phenanthroline catalysts using a rotating ring-disk electrode (RRDE) setup. They found that between pH 1 and pH 7 the half wave potential was not affected, however between pH 7 and pH 13.7 they observed a linear increase. Indeed, it is known for the group of Me-N-C catalysts that their performance in alkaline is either equal or exceeds the performance in acidic electrolyte [6,12–14]. In 2011 He et al. developed a bicore CuFe/C electrocatalyst for ORR in alkaline media and they found similar performance to commercial Pt/C electrocatalyst with much lower metal loading [15].

Recently, Titirici published data on a metal based, N-doped carbon capsule catalyst which showed outstanding performance in both acidic and alkaline media. In particular, they pointed out the importance of N-doping of the carbon matrix ($N_{pyrid.}$, $N_{quaternary}$), presence of Fe-N coordination sites and a large surface area, that was mainly mesoporous in their catalyst. For this catalyst, Alkaline Anion-Exchange Membrane Fuel Cell (AAEMFC) and RDE measurements gave similar good activity [16].

Moreover, it is known that in alkaline media even metal-free electrocatalysts can reach high activity and selectivity toward ORR. In this context, Liang et al. developed a metal-free electrocatalyst as an alternative to Pt/C that revealed the highest ORR activity in alkaline media among all reported metal-free ORR catalysts [17].

Regarding the role of sulfur, our own results showed that the use of sulfur within the precursor mixture is advantageous as more active MeN_4 sites remain intact [18,19]. Sulfur-addition changes the carbon morphology [18] and – so far optimised – suppresses carbide formation [19]. The carbide formation was correlated with the disintegration of MeN_4 sites during the heat-treatment in that work.

Another approach from Zelenay group using Co-S-N-C catalyst leads to an improved activity and stability for the oxygen reduction reaction in alkaline media compared to their Fe-N-C and a Pt/C reference catalyst [20].

Recently, Kicinski et al. investigated a broader group of catalysts prepared as Fe-N-C, Fe-O-C, Fe-S-C and mixtures thereof in order to study the effect on the structural composition of the final catalysts, their morphologies and ORR activities in alkaline [21]. The authors concluded that beside the aforementioned effects, sulfur-addition leads to a tremendous increase of the specific surface area of the catalysts. In its optimum the BET surface area was 4.5 times larger compared to a similarly prepared catalyst without sulfur-addition. The importance of electrochemical accessible surface area was pointed out in Gupta et al. [22]. They prepared different PANI-based Fe-N-C catalysts under the addition of a further N-precursor and found a strong correlation between carbon morphology, in terms of surface area, porosity, and degree of graphitization and ORR activity [22].

While in all aforementioned approaches the precursor compositions – and therefore the overall number of active MeN_4 sites or its accessibility – were changed it is also demonstrated that the electrocatalytic properties can be tuned by varying the microenvironment at the surface of the electrocatalyst [23–25]. A successful implementation of this approach is to modify electrocatalysts by coating their inner surface with a controlled amount of ionic liquids (ILs) which have already been widely applied in electrochemistry due to their high ionic conductivity, broad electrochemical window and good chemical stability [26]. Such a “Solid Catalyst with Ionic Liquid Layer (SCILL)” concept was invented by Etzold et al., in 2007 [27], and meanwhile has been proven to be highly effective to enhance catalytic activity and selectivity in many heterogeneous catalytic reactions, e.g., hydrogenation of limonene, citral and acetylene, and isomerization of *n*-octane [28,29]. Pioneering work transferring this SCILL concept to electrocatalysis was realized by Erlebacher and his co-workers by introducing a hydrophobic protic IL ([MTBD][NTf2]) into the pores of nanoporous PtNi materials [30,31]. By testing these IL modified materials for ORR they found that the intrinsic activity of the SCILL material for ORR is enhanced by a factor of 2–3 in comparison to the pure nanoparticles and rationalized this result with the high oxygen solubility of the IL [30,31]. Moreover, the SCILL concept in electrocatalysis is studied in detail by some authors of the current work, by systematically incorporating different amounts of IL into the pores of a commercial Pt/C catalyst [32]. We found surprisingly the fact that both the ORR activity and stability of the IL modified Pt/C catalysts in acidic electrolyte are sensitive to the degree of IL filling. A partial IL filling (i.e., 50%) was identified as optimum, where the mass transfer resistance of the IL does not outweigh the boosting effect [32]. In another study this boosting effect could also be observed for the more common IL [BMIM][NTf_2], leading to an activity increase by a factor 3 in comparison to the unmodified Pt/C catalyst [33]. This effect was explained with the prevention of catalyst poisoning by oxygenated species through the hydrophobic IL rather than the increased oxygen solubility.

In this paper we investigated for Fe-N-C catalysts prepared with and without sulfur-addition the influence of IL modification on the electrocatalytic properties of the materials at alkaline conditions. To avoid interaction of the proton at the C2-position of the imidazolium cation $[BMIM]^+$ with OH^- in alkaline media, the C2-position was methylated $[BMMIM]^+$. Using the same anion like in the aforementioned IL finally the IL [BMMIM][NTf_2] was employed for the modification in alkaline media. We thus demonstrate that the SCILL approach can be successfully transferred to non-precious metal ORR catalysts and in alkaline electrolyte. Our results show a new way to enhance the catalytic properties in terms of activity and stability for a possibly higher performance and stability in alkaline fuel cells.

2. Experimental

2.1. Synthesis

2.1.1. Preparation of sulfur-free (−S) and sulfur-added (+S) catalysts

In a typical synthesis of a sulfur-free catalyst, 2.25 mmol of iron acetate were mixed in a mortar with 8.5 mmol of 1,10-phenanthroline and 61.3 mmol of dicyandiamide until a homogeneous mixture was obtained. The precursor mixture was filled into a quartz boat and placed in the oven for the first heat treatment. The sample was heated with a ramp of 300 °C h^{-1} in inert atmosphere to 800 °C. After 1 h the sample was cooled down (<80 °C) and transferred to 2 M HCl for acid leaching for 12 h. The sample was then washed with deionized water until neutral pH was reached and dried at 85 °C overnight. A second heat treatment was performed with the same heating rate up to 800 °C for 3 h. The final solid material was ground manually in a mortar.

The preparation of the sulfur-added catalyst was almost identical, except that in a first step 1.8 mmol of sulfur were ground in the mortar before adding all other precursor species.

In the following "−S" and "+S" will be used as short indicators for the catalysts prepared without and with sulfur-addition to the precursor.

2.1.2. Synthesis of Fe-N-C (±S) SCILL systems

SCILL systems were prepared by coating the as-prepared catalysts (±S) with the ionic liquid [BMMIM][NTf2]. In a typical synthesis the amount of IL corresponding to the desired pore filling degree was dissolved in 10 ml of isopropanol. This solution was then mixed with approximately 40 mg of the catalyst under intense stirring at room temperature. After 20 min ultrasonic treatment of this mixture, the volatile solvent isopropanol was slowly removed from the slurry through rotary evaporation under low vacuum (137 mbar, 60 °C) and followed by further evaporation at 5 mbar vacuum. Finally, the sample was dried overnight in a vacuum oven (5 mbar, 60 °C). In the following, the degree of pore-filling with ionic liquid is indicated with a number after IL. For example IL 20 refers to a sample, where 20% of the pores were filled with the ionic liquid. An exemplary calculation of the pore filling degree for S-free_IL20 catalyst is given below:

The IL pore filling degree (IL_PFD) is given by the volumetric ratio of IL and catalyst:

$$\mathrm{IL\_PFD} = V_{IL} \cdot V_{cat}^{-1} \tag{4}$$

The volume that is occupied by the IL can be calculated from the density (of 1.43 g cm^{-3}) and used mass for the IL modification.

For example, for the S-free_IL20 sample 9.2 mg IL were used for the modification. This corresponds to a volume of

$$V_{IL} = (9.2 \times 10^{-3}\ \mathrm{g})\ \mathrm{x}\ (1.43\ \mathrm{g\ cm^{-3}})^{-1} = 6.43 \times 10^{-3}\ \mathrm{cm^3} \tag{5}$$

This volume was used to modify 61.7 mg of the S-free catalyst. As the catalyst has a pore volume of 0.49 cm^3 g^{-1}, we can calculate the volume that corresponds to the used mass.

$$V_{cat} = (61.7 \times 10^{-3}\ \mathrm{g})\ \mathrm{x}\ (0.49\ \mathrm{cm^3\ g^{-1}}) = 30.23 \times 10^{-3}\ \mathrm{cm^3} \tag{6}$$

The IL pore filling degree is given by the volume ratio of IL and pore volume:

$$\mathrm{IL\_PFD} = V_{IL} \cdot V_{cat}^{-1} = (6.43 \times 10^{-3}\ \mathrm{cm^3})\ \mathrm{x}\ (30.23 \times 10^{-3}\ \mathrm{cm^3})^{-1} = 0.213 = 21.3\% \tag{7}$$

2.2. Electrochemical characterization

The electrochemical measurements were performed with a glassy carbon (GC-) working electrode (A = 0.196 cm^{-1}), a GC-counter electrode and a Hg/HgO reference electrode. In all experiments the catalyst loading was 0.5 mg cm^{-2} with a Nafion to catalyst ratio of 0.25. All experiments were carried out at RT and 0.1 M NaOH. For the activity evaluation the electrolyte was first purged with N_2 for about 15 min, then the potential was swept between 1.0 and 0.0 V vs. RHE with a sweep rate of 300 mV s^{-1} (20 scans, for activation), 100 mV s^{-1} (2 scans, for determination of the capacity) and 10 mV s^{-1} (1 scan, for background correction of RDE data). After saturation with O_2 the open circuit potential (OCP) was determined and finally the activity measurements were applied in the same potential range as given above with a sweep rate of 10 mV s^{-1} and 0 rpm, 900 rpm and 1500 rpm.

In order to calculate the kinetic current density j_k, in a first step the linear sweep voltammogram (LSV) under oxygen was corrected for capacity contributions by subtracting the LSV obtained in N_2 saturated electrolyte. Then, the kinetic current density was determined according to equation (8).

$$j_k\,(U) = j\,(U) \cdot j_{Diff,lim} \cdot (j_{Diff,lim} - j(U))^{-1} \tag{8}$$

In this equation j(U) is the current after background correction and $j_{Diff,lim}$ is the current density value of the diffusion limiting plateau. In samples where this plateau was not observed, $j_{Diff,lim}$ was taken as the current density at U = 0 V vs. RHE (the lowest investigated voltage). All data were iR corrected.

For the stability evaluation the load cycle durability test as proposed by the Fuel Cell Commercialization Conference in Japan in 2011 [34] was slightly modified (O_2-saturated instead of N_2 saturated electrolyte, 1650 and 15,000 cycles instead of 400 000). After OCP a stepped potential protocol is applied, where in each cycle the potentials of 0.6 V and 1.0 V were held for 3 s. Hence, one stability needed 6 s. In total 1650 cycles were performed and the activity was evaluated by measuring the activity protocol after 100, 200, 350, 500, 850 and 1650 cycles.

In the following, all potentials refer to the reversible hydrogen electrode (RHE) and activity data are plotted for rpm1500.

2.3. Structural characterization

2.3.1. Raman spectroscopy

For the Raman measurements of the as-prepared catalysts a drop of the catalyst ink was placed onto a silica disk. The measurements were done with an alpha 300R confocal Raman microscope from WiTec (Ulm, Germany) with a grid of 600 lines mm^{-1} using an excitation laser (532.2 nm) with a power of 1 mW. The range of the measured spectra spreads from 0 to 4000 cm^{-1}. The spectra were acquired for each sample by performing 10 scans at three different positions, each with integration time of 10 s. These three measurements were used to calculate the average spectra as shown in the Results and Discussion part. Curve fitting for the determination of spectral parameters was performed including four peaks. In the fitting, the G-band ca. 1580 cm^{-1} is assigned to the stretching of the C-C bond in graphitic materials, the D-band ca. 1360 cm^{-1} is assigned to vibrations at the edges of graphene planes or close to defects, the D_3-band ca. 1500 cm^{-1} is assigned to defective carbon and D_4-band ca. 1200 cm^{-1} which is assigned to polyenes [35].

2.3.2. X-ray induced photoelectron spectroscopy (XPS)

X-ray photoelectron spectra (XPS) were measured with a Specs Phoibos 150 hemispherical analyzer and a Specs XR50M Al K_α X-ray source (E = 1486.7 eV). The catalyst powder was pressed on a thin indium foil and sealed on a sample holder. For the survey scans, an energy step of 1 eV has been applied and two scans were overlaid. For the N1s scans, 100 scans with energy step of 0.05 eV were overlaid. Spectra were analysed using CasaXPS and peaks were fitted using a Shirley background and a mixed Gauss/Lorentz peak.

2.3.3. ^{57}Fe Mössbauer spectroscopy

The Mößbauer measurements were performed with a MS96 from RCPTM with a 100 mCi 57Co/Rh source and a scintillation detector. Samples were measured at room temperature and the isomer shifts were determined relative to α-Fe at 298 K. All Mößbauer spectra were fitted using the software Recoil.

2.3.4. N_2 sorption measurements

The textural properties were analysed by conducting nitrogen sorption measurement at 77 K on a Micromeritics 3Flex Physisorption instrument. The surface area was estimated using the Brunauer-Emmett-Teller (BET) equation using 3Flex software (Ver. 4.02). Pore size distributions were calculated using the “Nitrogen on Carbon with Slit/Cylinder pores adsorption” QSDFT kernel implemented in VersaWin Software (Ver. 1.0). The pore volume of both unmodified catalysts was used to calculate the required amount of IL to reach the desired pore filling degree.

2.3.5. FTIR spectroscopy

FTIR measurements were performed on a VERTEX 70 spectrometer (Bruker). The catalysts were ground with KBr and then pressed to obtain wafers that were analysed in the spectrometer in transmission mode.

3. Results and discussion

3.1. Structural characterization of as-prepared catalysts

The structural composition of Fe-N-C catalysts is one important aspect that determines the number of ORR active sites that can be present in these catalysts. While for acidic electrolyte structure-activity correlations make it most likely that the ORR activity can be attributed to specific FeN_4 sites [36–39], in alkaline electrolyte this assignment is not as straightforward as several different types of active sites (e.g. FeN_4 sites, Me-free N-/S-doped carbons) were found to contribute significantly to the activity [17,40–42].

In Fig. 1a–c the XPS survey scan as well as the fine scans of the N 1s region are given for the sulfur-free and sulfur-added catalysts. The S2p region of the S-added catalyst is given in Fig. 1d. The different elements are assigned in the survey scan. Table 1 presents the surface elemental composition determined by XPS for both catalysts. It can be seen that the atomic ratio of N/C for Fe-(+S)-N-C (0.14) is much higher than that on Fe-(−S)-N-C (0.09), indicating that the presence of sulfur is beneficial to keep more nitrogen within the sample. The S2p region shows that sulfur is basically found as species embedded in the carbon matrix and not in interaction with the metal species [18].

The spectrum contains an unknown peak that could be originated by SiO_2 as a possible residual/artifact from the synthesis (the synthesis is performed in quartz boats). Regardless of the fact that a different N precursor (porphyrin) was used for synthesizing Fe-N-C samples, the results on S-addition are in line with our previous work. However, herein the enhancement of surface N content by adding sulfur was not as pronounced as for porphyrin-based catalysts [18,19]. As the Mößbauer spectrum of the sulfur-added catalyst (Fig. 2b) still indicated large fractions of iron carbide, one might assume that an optimization of the sulfur-content in the precursor mixture should enable catalysts free of iron carbide and consequently with higher nitrogen contents in relation to the findings for porphyrin-based catalysts. Furthermore, the sulfur-added catalyst has an unexpected large content of iron that remains even after the acid leaching. In Fig. 2a and b the Mößbauer spectra of the catalysts are given. Both catalysts can be fitted with FeN_4 sites and the same kind of inorganic iron species. Table 2 summarizes the Mößbauer parameters as well as the assignment to iron species. The calculation of iron contents was done based on iron contents provided by XPS and the Lamb-Mößbauer factors f_{LM} given in Sougrati et al. [43].

Please note that there is no Lamb-Mößbauer factor available for our doublet D3. As the parameters are closer to D1 we did this calculation assuming a similar Lamb-Mößbauer factor for D3. It becomes clear that the absolute fraction of iron assigned to ORR active FeN_4 sites (related to D1) is seven times larger in the sulfur-added catalysts than in the sulfur-free catalyst. As it will be shown below, this increase in the number of ORR active sites might be the main reason for the improved performance of the unmodified catalyst due to sulfur addition (see Fig. 4, below).

In order to get further insights on the carbon morphology of the catalysts, Raman spectroscopy was performed and pore size distribution and surface area were determined. The N_2 sorption measurements, pore-size distribution and the Raman spectra (1st order) of both catalysts are given in Fig. 3.

The resulting isotherms are shown in Fig. 3a. Both catalysts exhibit similar isotherms that can be assigned to type IV with H3 hysteresis loops according to IUPAC classification. This shape indicates the presence of slit-shaped mesopores. The BET area calculated for the sulfur-containing catalyst of 442 $m^2\ g^{-1}$ is slightly higher than for the sulfur free catalyst (416 $m^2\ g^{-1}$). In order to gain further insights into the porous structure, pore size distributions were calculated (see Fig. 3b, Table 1). Both catalysts show similar pore size distributions with two maxima in the microporous range centered at around 0.5 and 0.9 nm and one broad peak in the mesoporous region centered at 4.1 nm. The sulfur-containing sample shows a higher amount of ultramicropores (pores below 0.7 nm), resulting in a microporous surface area of 299 $m^2\ g^{-1}$ that is approximately 37% larger than for the sulfur-free catalyst. In some papers by Dodelet's group it was found that micropores are of importance for the formation of ORR active sites [46–48]. In addition, here, a higher activity and larger number of FeN_4 sites appears in parallel with a higher micropore surface area. Also Kicinski et al. attributed an enhanced porosity of the carbon to sulfur addition to their precursors [21].

The Raman spectra as given in Fig. 3c and d were fitted with four bands assigned as G-band (1580 cm^{-1}), D-band (1360 cm^{-1}), D_3-band (1500 cm^{-1}) and D_4-band (1200 cm^{-1}). In our recent publication, we investigated a group of Me-N-C catalysts and found a correlation of the D_3-band/G-band intensity with the nitrogen contents that were assigned to ORR active sites attributed to $N_{pyrid.}$ and $N_{Me\text{-}N}$ [49]. While for Pt/C based catalyst a carbon oxidation basically causes a decrease of D-band intensity we were able to show that for these Me-N-C catalysts the change in current density correlated with the change of this D_3-band/G-band intensity. Due to the aforementioned correlation of the D_3-band/G-band intensity with the nitrogen content assigned to active sites, it was concluded that MeN_4 sites seem to contribute to the D_3-band intensity - most likely by changes of the vibrational frequencies due to the interaction of the carbon atoms with the integrated MeN_4 sites (via the C-N-coordination).

Our results here are in line with our recent publication: The D_3-band/G-band intensity is significantly larger for the sulfur-added catalyst that contains significantly more nitrogen assigned to these two species and FeN_4 sites (compare Tables 1 and 2 and Fig. 1b and c).

3.2. Modification of the as-prepared catalysts with [BMMIM][NTf_2]

As described in the Experimental, IL modification of these two catalysts was performed in order to study the effect on ORR activity

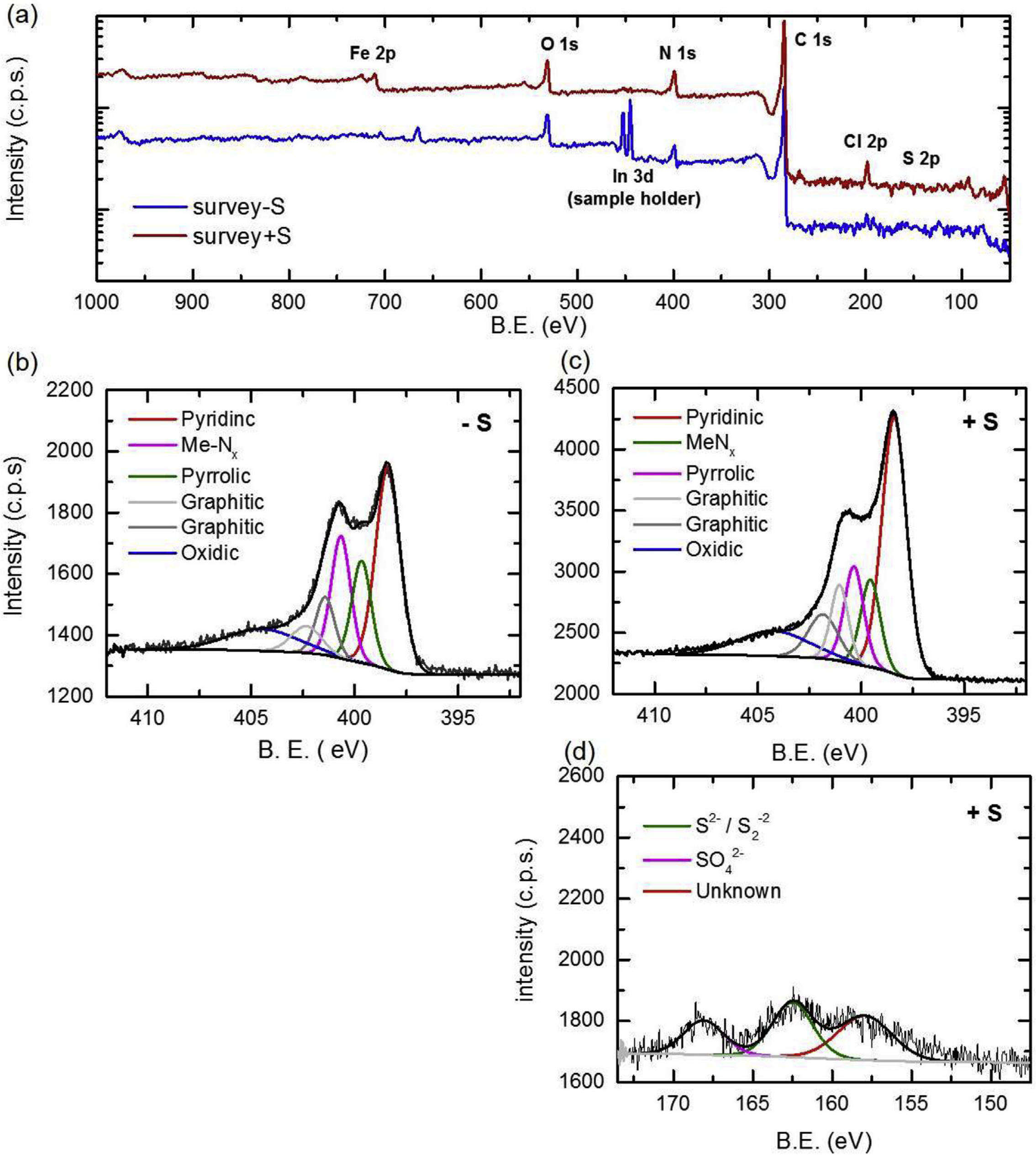

Fig. 1. XPS survey scans (a) and N1s fine scans of the sulfur-free (b) and sulfur-added (c) catalysts. In (d) the S2p fine scan of the S-added catalyst is shown.

Table 1
Summary of the surface elemental composition and specific surface area as determined by XPS and N_2-sorption, respectively for the unmodified catalysts.

Sample	XPS (wt%)					N_2-sorption (m^2 g^{-1})					
	Fe	N	C	O	S	S_{BET}	S_{DFT}	$S_{Micropore}$	$S_{Mesopore}$	Pore Volume (cm^3/g)	Density IL (g cm^{-3})
Fe-N-C (−S)	1.9	7.0	80.8	10.3	–	416	419	218	201	0.49	1.43
Fe-N-C (+S)	6.1	10.5	72.8	9.5	1.2	442	464	299	165	0.44	1.43

and stability. Fig. 4a shows the cyclic voltammograms (CV) of the sulfur-free and sulfur-added catalysts with different IL pore filling degrees. It can be clearly seen from these CV curves that the double layer capacitance, which is commonly used as tool for determining the electrochemical accessible surface area (ECSA) of an electrode material, is highly sensitive to the IL pore filling degree especially for the sulfur-free samples. Attempts were made to compare the double layer capacitance (evaluated at U = 0.8 V) for catalysts with different pore filling degrees, and the results are summarized in Fig. 5a. Even though the total specific surface area of both unmodified catalysts were almost identical (Table 1) the electrochemical accessible surface was nearly four times larger for the sulfur modified catalyst. The order of changing capacitance due to increasing IL pore filling degree differs for both sample series. For

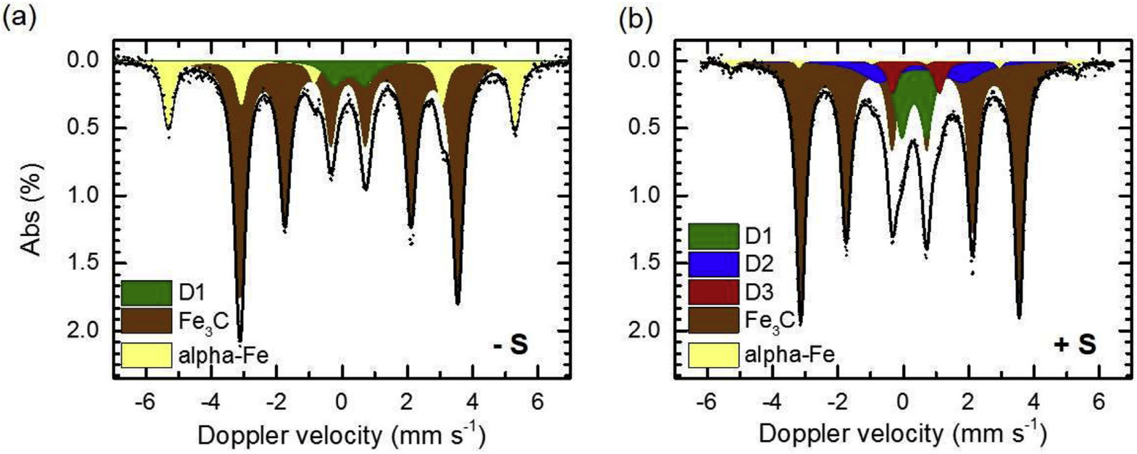

Fig. 2. Mößbauer spectra of the S-free (a) and S-added (b) catalysts.

Table 2
Summary of the Mößbauer parameters as well as assignment to iron sites and calculation of iron contents by using the Lamb-Mößbauer factors for RT provided in Sougrati et al. [43] ($f_{LM}(D1) = 0.46$, $f_{LM}(D2) = 0.52$, $f_{LM}(D3) \approx 0.46$, f_{LM}(alpha-Fe) $= 0.67$, $f_{LM}(Fe_3C) = 0.77$).

	δ_{iso}	ΔE_Q or ε	whm	H_0 (T)	Sulfur-free		Sulfur-added		Assignment
	(mm s^{-1})				A (%)	Fe (wt%)	A (%)	Fe (wt%)	
D1	0.28 (0.05)	0.85 (0.09)	0.57 (0.08)	–	6.4 (0.6)	0.12	14.1 (0.4)	0.86	FeN_4 (2+, LS) [9]
D2	0.54 (0.04)	2.55 (0.17)	1.32	–	–		10.7 (2.0)	0.76	FePc-like (2+, MS) [44]
D3	0.39 (0.03)	1.43 (0.04)	0.38	–	–		4.9 (1.4)	0.30	N-FeN_4-CN (3+,MS) [45]
Sext1	−0.03 (0.02)	0.008 (<0.01)	0.18	32.8 (<0.1)	18.9 (1.0)	0.35	1.7 (0.4)	0.10	Alpha-Fe [45]
Sext2	0.19 (<0.01)	0.011	0.19 (0.01)	20.7 (<0.1)	74.8 (1.0)	1.38	68.7 (0.6)	4.20	Fe_3C [45]

the sulfur-free catalyst a significant increase by in maximum a factor of about two for S-free_IL35 resulted. Contrary the sulfur-added catalyst showed a smaller increase of a factor of 1.5 for S-added_IL20.

Pore fillings above this maximum resulted in a drop of the capacitance for both type of catalysts. In case of the sulfur-added catalyst even a reduction of the capacitance was observed, with only 0.6 times the capacity for S-added_IL50 compared to the unmodified S-added catalyst. The electrocatalytic properties of the sulfur-free and sulfur-added catalysts with different IL pore filling degrees towards ORR are investigated by using RDE technique.

Fig. 4b and c shows the RDE curves and also Tafel plots recorded in O_2-saturated 0.1 M NaOH electrolyte at room temperature. It is evident that the presence of IL has dramatically changed the electrocatalytic behavior of both sulfur-free and sulfur-added catalysts, and the catalytic activity in terms of half-wave potential is highly depending on the IL pore filling degree, while the absolute trend is different for the two investigated catalysts.

We recognize that the capacitance and activity of both sample series appear to exhibit similar dependent behavior on the IL pore filling degree. While Fig. 5a and b give the capacitance and kinetic current density (both for $U = 0.8$ V) as a function of the pore-filling degree, in Fig. 5c the kinetic current density is correlated with the capacity. Both sample series belong to one single group of Non-PGM catalysts. Interestingly the effect of the sulfur addition as also the IL modification follow both the same linear increase in kinetic current density as a function of capacitance.

This result is in contrast to Bogdanoff et al. [50] who found an exponential correlation with an exponent of 2.3 for a group of cobalt porphyrin based catalysts prepared under oxalate addition. However, our samples showed the expected trend where the increasing electrochemical accessible surface area correlates with the kinetic current density. It is very interesting to note that the enhancement in activity due to sulfur addition not only correlates very well to the capacity but also perfectly reflects the increase in the number of ORR active FeN_4 sites (both factor of seven larger for the sulfur-added catalyst). This might be interpreted as a result of an improved accessibility of the active sites (increasing utilization factor [6]) in case of the sulfur-free catalyst, while for the sulfur-added catalyst the utilization factor seems already close to its maximum. The role of the pore size distribution on ORR was recently reported by Gupta et al. [22] and is in agreement with observed trends by Kicinki [21].

In order to evaluate the effect of the ionic liquid on the stability in accelerated stress tests we adapted the protocol for the load cycles (AST_LC) as provided by the Fuel Cell Commercialization Conference Japan [30] Fig. 6a gives a scheme of the load cycle protocol, in Fig. 6b the relative fraction of remaining activity is plotted as function of pore-filling degree and in Fig. 6c and d kinetic current densities at Beginning of Life (B.o.L.) and after 1650 cycles are given for both sample series. The data are extracted from Fig. 7 in which the RDE curves after further continuing to 15.000 cycles were added. We also gave the values of the change in half-wave potential $\Delta E_{1/2}$ in parenthesis for these catalysts.

It becomes apparent that the IL modification improves the stability of the non-PGM catalysts. For the S-free sample series the maximum improvement in stability was found for a pore-filling degree of 20% (IL20), where the catalysts lost only 15% of its initial activity. In case of S-added catalysts; however, the stability is either similar to the original catalyst or worse with almost no further change up to 15.000 cycles.

Considering the absolute activity values after the AST_LC, the maximum in activity was found for the sulfur-free catalyst with IL20 (almost identical to IL35) and for the sulfur-added catalyst with a pore-filling degree of 10% (IL10). For these four catalysts the BoL and EoL RDE curves are compared in Fig. 6a–d together with

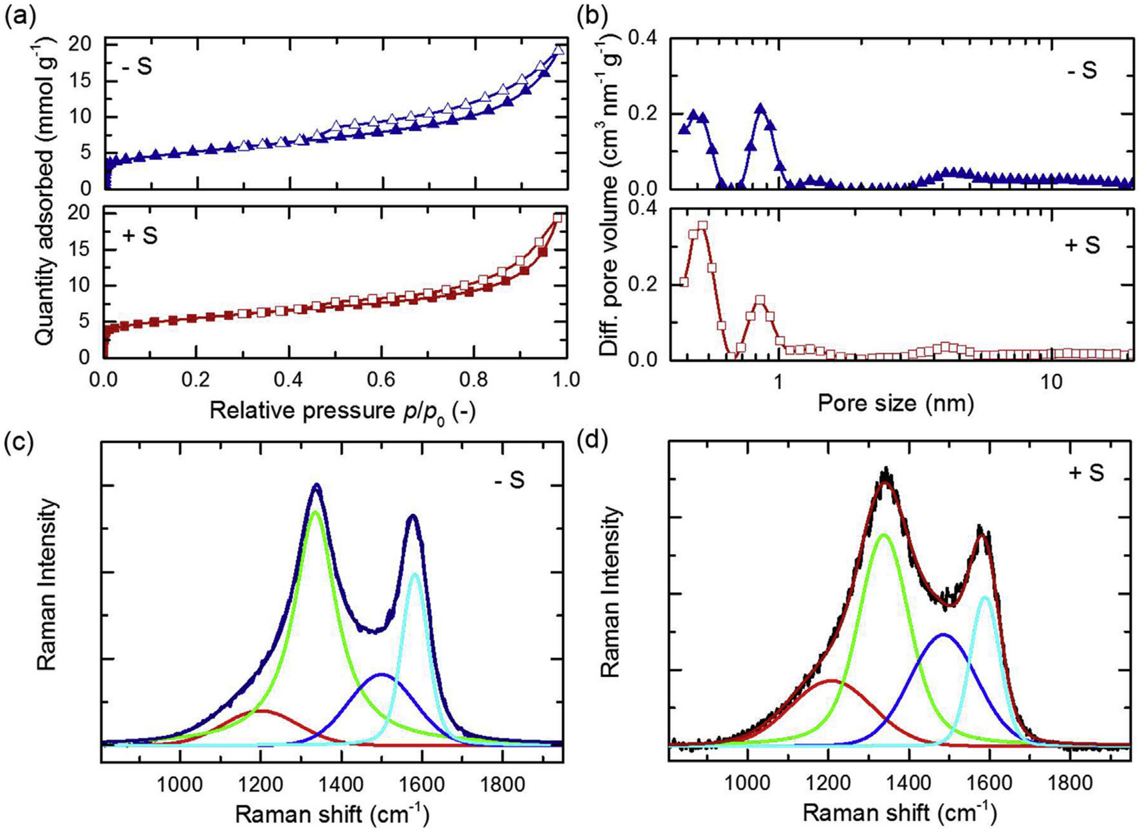

Fig. 3. N_2 sorption isotherms at 77 K (a), DFT-N_2 pore size distribution (b), and Raman spectra (c, d) of the sulfur-free and sulfur-added catalysts.

possible changes in capacity (as inserts). The least stable catalyst was the unmodified sulfur-free catalyst. The change in half-wave potential was about 36 mV after 1650 cycles. Both, IL-modification and S-addition resulted in changes of the diffusion limiting plateau.

This effect was also recognized before for other Me-N-C catalysts investigated in acidic electrolyte and could possibly be attributed to a change in the reduction mechanism [9,49]. The change in half-wave potential for S-free_IL20 was only 4 mV after 1650 cycles. However, in case of the sulfur-added catalyst, for both samples (with and without IL modification) almost the same changes in half-wave potentials were found (about 12 mV). Hence, our results specified that the ionic liquid modification was beneficial for the activity and stability of one Non-PGM catalyst, while for the S-added catalyst already the S-addition seems to improve the activity and stability.

Based on these results, we have learned that introducing ILs can be employed as an efficient approach to improving both the catalytic activity and stability of NPMCs towards ORR in alkaline electrolyte. The presence of ILs could significantly increase the electrochemical accessible surface area for the sulfur free samples, which might also be the origin of the boosting effect by using ILs. Nevertheless, we have to admit that it is still a mystery how the IL could make the surface more accessible to the electrolyte.

What are the main differences between the sulfur-free and the sulfur-added catalyst and their response to the IL modification? From the characterization of the unmodified catalysts in part 3.1 main differences between both catalysts were found in a) the content of sulfur, b) the number of ORR active FeN_4 sites, c) the contents of different nitrogen species and d) the pore size distribution.

If one of the three aforementioned factors a-c had an impact on the possibility to modify a Non-PGM catalyst with an ionic liquid we might assume that an interaction of either sulfur, FeN_4 sites or different nitrogen species with the ionic liquid was at the origin of the hindered modification of the sulfur-added catalyst with the ionic liquid. Such interactions could be possibly visible in the infrared (IR) spectra by a change of the position of the vibrational modes assigned to the ionic liquid. Hence, in order to evaluate this, in Fig. 8 the difference spectra of the unmodified catalyst and those with a pore-filling degree of 20% was determined and compared to the IR spectrum of the ionic liquid itself.

The spectra of the modified samples show features that can be assigned to the features of pure IL without a shift of vibrational modes. Thus, IR does not give evidence for a chemical interaction between the IL and the catalyst. Differences in the pore structure especially the presence of ultramicropores in the S-added catalyst might thus be responsible for the different response to IL modification. A further hint, that the pore structure difference is of major importance arises also from the different influence of the IL pore filling degree on the capacitance. For both catalysts the capacitance increases initially, with IL addition, goes through a maximum and decreases then with higher IL pore filling degrees. But for the catalysts with sulfur addition the maximum is earlier and the later decrease harsher. Accounting the size of the ionic liquid molecule (e.g., 2.9 × 7.9 Å for $[NTf_2]$ anion) [26] it might be too large to penetrate ultramicropores. As the sulfur-added catalyst shows a higher amount of ultramicropores, a smaller amount of IL might block the entrance to these pores. For bottle neck pores then also the accessibility of bigger sized pores is hindered by the IL. If so the optimum amount of IL for the modification will differ for varying pore structures. In previous IL modification studies, mainly

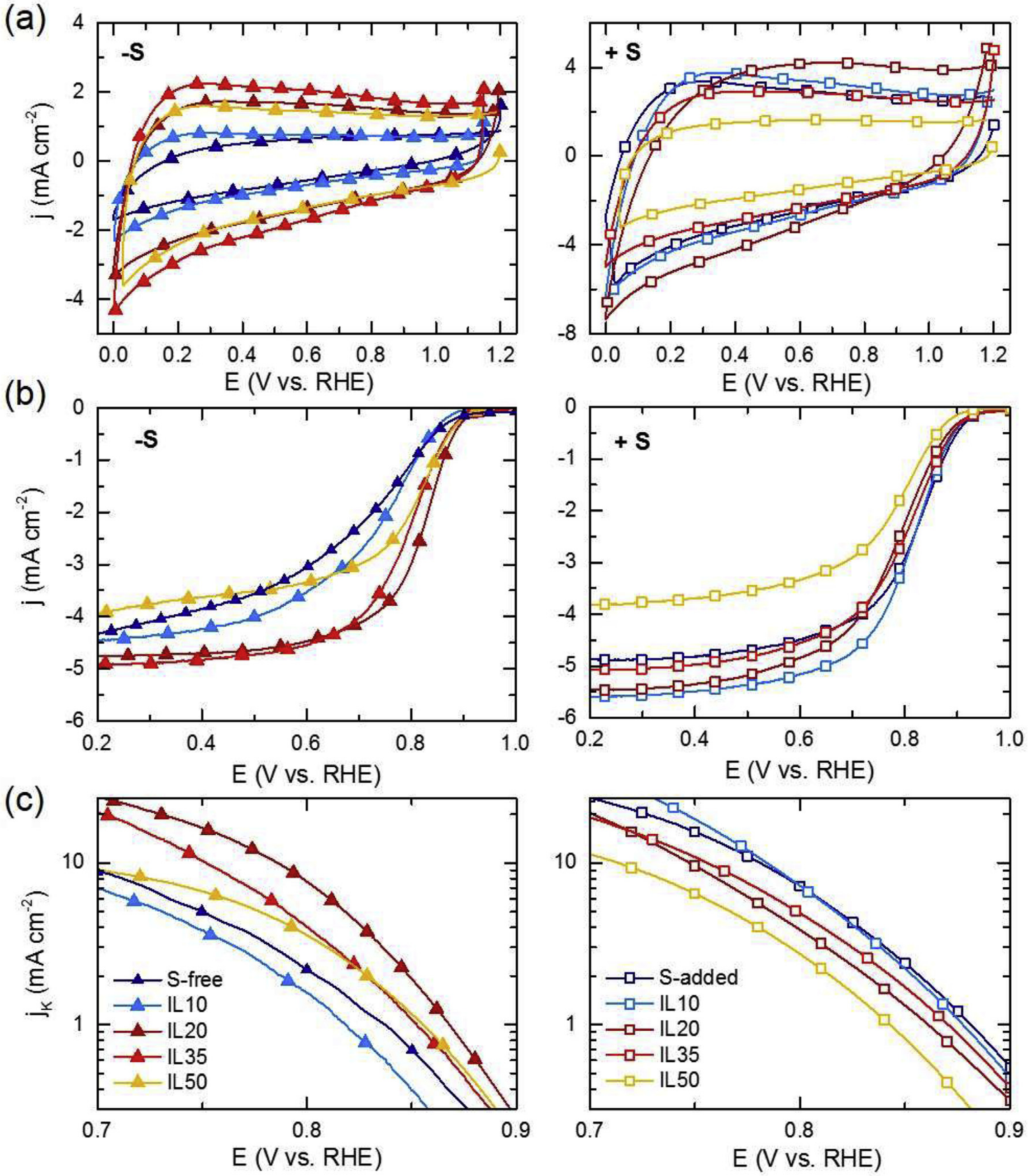

Fig. 4. Cyclic voltammograms (a) in N_2-saturated 0.1 M NaOH with 100 mV s^{-1}, (b) linear sweep voltammograms in O_2-saturated electrolyte at 1500 rpm with a scanning rate of 10 mV s^{-1} and (c) obtained Tafel plots for the sulfur-free and sulfur-added catalysts with different IL pore filling degrees, respectively. All measurements are made with a catalyst loading of 0.5 mg cm^{-2}.

catalysts without ultramicropores were employed, where this influence was most likely not obvious [31–33]. If the ultramicropores (d < 7 Å) are not considered in the calculation of the pore filling degree, the amount of IL added would be shifted to 11% higher values for S-free and 33% for S-added catalysts.

Further experiments would be required to finally proof this hypothesis but this is beyond the scope of this publication.

One aspect that need to be discussed in more detail is the correlation of the double layer capacitance and the kinetic current density. This very good correlation indicates that the capacitance seems either to be dominated by ORR active species or the share of ORR active species towards the surface contribution to capacitance is constant. Having a view to Tables 1 and 2 one possible explanation could be the attribution of ORR activity exclusively to the FeN_4 species assigned to the D1 doublet, as its change in content nearly perfectly fits to the change in ORR activity and capacity.

Based on the observed trends in capacity, the number of electrochemical accessible species can be enhanced on the one hand by the addition of sulfur to the precursor mixture, and on the other hand by the modification with the ionic liquid.

4. Conclusions

In this work, we have discussed the impact of an IL modification

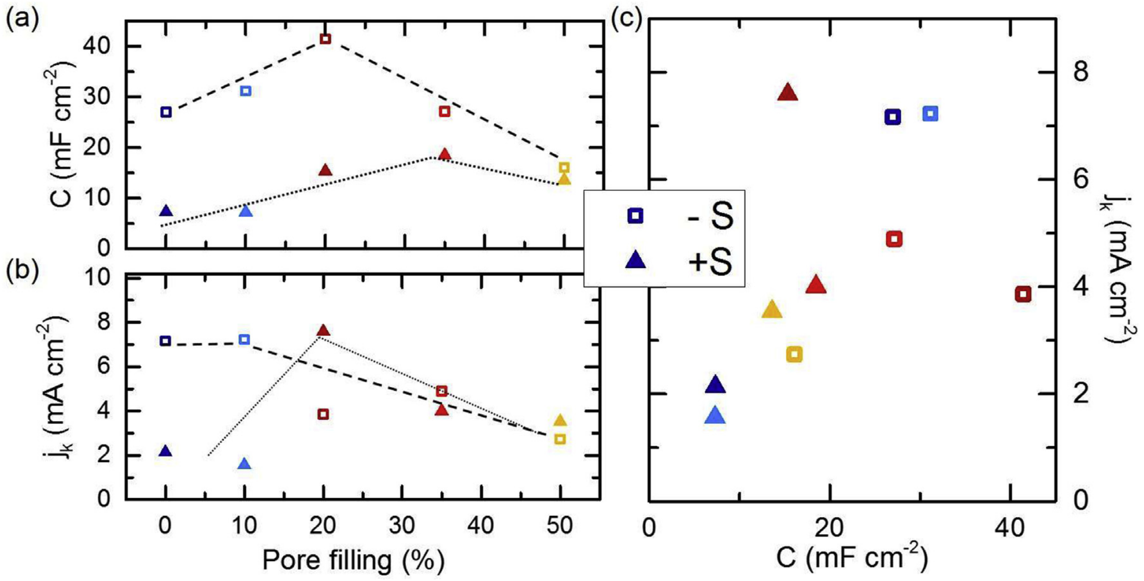

Fig. 5. Double layer capacitance (a) and kinetic current density (b) at 0.8 V vs. pore filling degree. The correlation between kinetic current density and capacitance is given in (c). Data were extracted from Fig. 4.

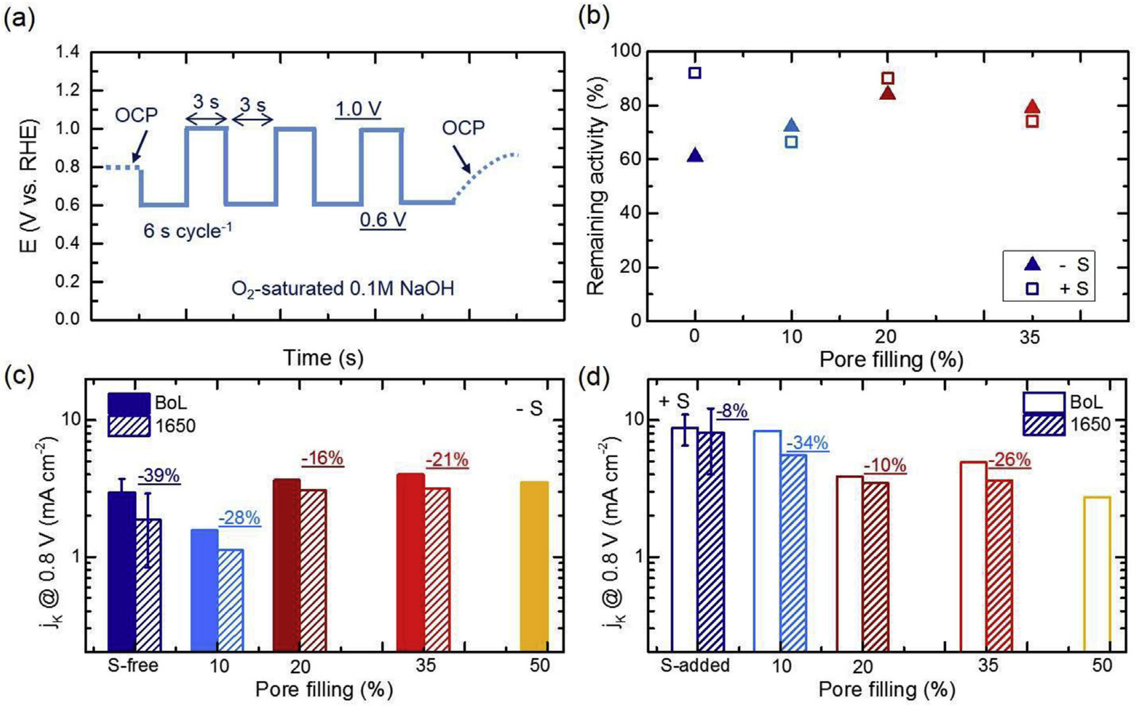

Fig. 6. Applied accelerated stress test protocol (AST_LC) for stability evaluation (a), correlation between the relative remaining activity and the pore-filling degree (b) as well as the BoL and EoL kinetic current densities for the sulfur-free (c) and sulfur-added (d) catalysts with different IL modifications (Data extracted from Fig. 7).

on the ORR activity and stability in alkaline electrolyte for a sulfur-free and a sulfur-added Fe-N-C catalyst. The structural characterization of the unmodified catalyst gave a significant larger number of ORR active FeN$_4$ sites, with only slightly larger micropore surface area for the unmodified sulfur-added catalyst compared to the sulfur-free catalyst.

The pore filling degree of the catalysts by IL had a significant effect on the double layer capacitance of the catalysts. At low IL loadings both, capacitance and activity increased. The study furthermore revealed, that the amount of IL must be carefully adjusted. Exceeding a certain degree of pore filling a decrease of capacitance and activity was observed. This decrease seems to be especially sensitive to the catalyst pore structure and the presence of ultramicropores (<0.7 nm), which might be prone to pore blocking. Pore blocking also explains why different trends were observed for the sulfur-free and sulfur-added catalyst. Herein a pronounced boosting of the ORR activity could only observed for the sulfur-free sample, where the maximum activity was obtained for a pore filling degree of 20–35%. In contrast, as a higher portion of the porosity of the sulfur-added catalyst is attributed to

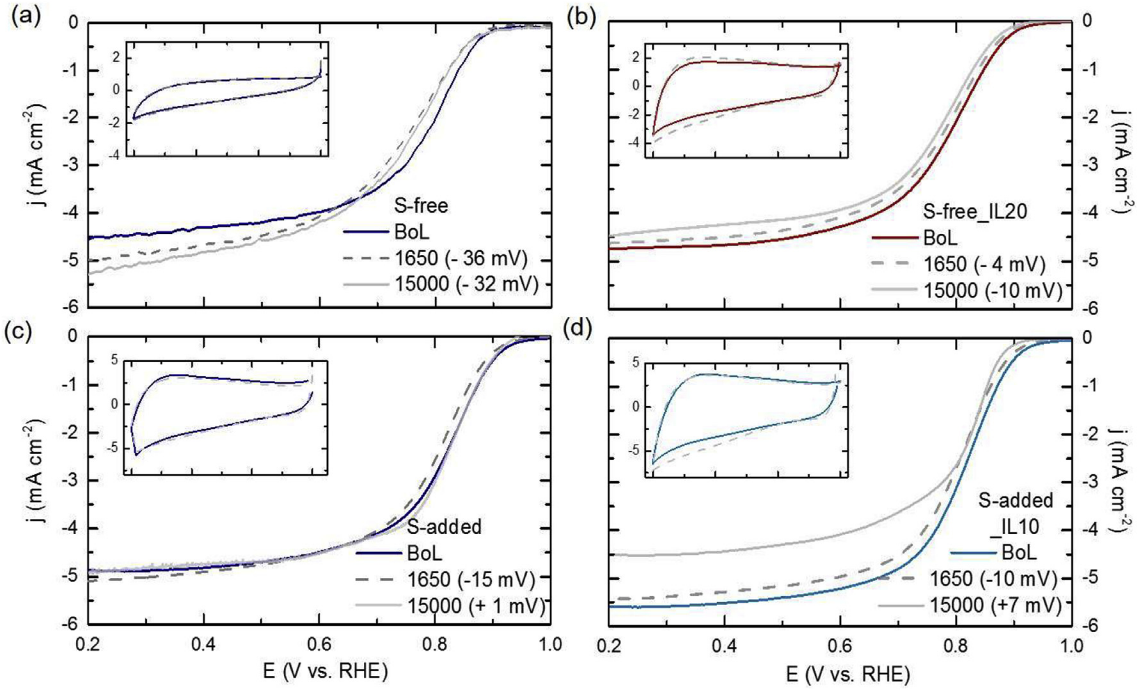

Fig. 7. RDE measurements at BoL and EoL (+1650 AST_LC cycles) for the unmodified and modified sulfur-free catalyst (a and b), the unmodified and modified sulfur-added catalyst (c and d).

ultramicropores the optimal pore-filling degree is shifted to smaller values.

While a clear improvement in activity and stability was found for the S-free catalyst, already S-addition to the precursor enabled a significant improvement of the catalytic activity (as known from previous work) and stability. Based on this, no clear improving effect that might be attributed to the IL modification of S-added catalyst was found.

Nevertheless, of particular interest was the universality of correlation between capacitance and kinetic current density of S-free and S-added catalyst ± IL that needs to be investigated in more detail in future work.

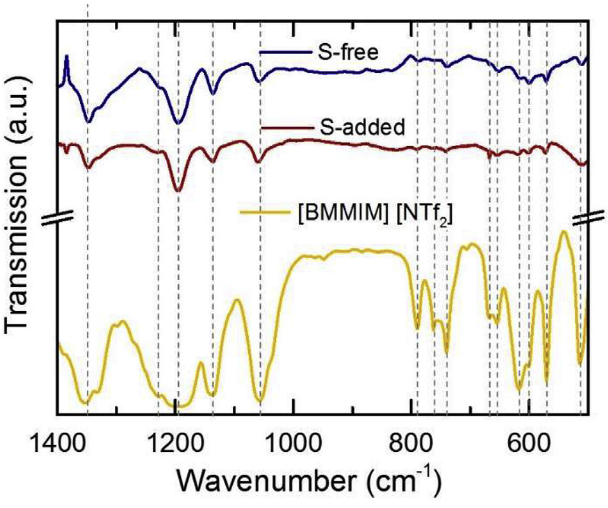

Fig. 8. Infrared transmission spectra of the pure IL and difference spectra for both catalysts modified with the IL (20%). The spectra of the as-prepared catalysts were subtracted as background.

Acknowledgement

Financial supports by the German research foundation via the Graduate School of Excellence Energy Science and Engineering (GSC1070), the federal ministry of education and research via the joint project NUKFER (05K16RD1) and the NanoMatFutur young researcher group (03XP0092) are gratefully acknowledged by UIK and her group. TW, GRZ and BE acknowledge that this project has received funding from the European Research Council (ERC) under the European Union's Horizon 2020 research and innovation program (grant agreement No 681719).

In addition, we would like to thank W. Jaegermann and his group for the possibility to do XPS and S. Hesse for the assistance with Raman spectroscopy.

References

[1] M.K. Debe, Nature 486 (2012) 43–51.
[2] H. Tributsch, U.I. Koslowski, I. Dorbandt, Electrochim. Acta 53 (2008) 2198–2209.
[3] E. Proietti, F. Jaouen, M. Lefèvre, N. Larouche, J. Tian, J. Herranz, J.-P. Dodelet, Nat. Comms 2 (2011) 416.
[4] G. Wu, K.L. More, C.M. Johnston, P. Zelenay, Science 332 (2011) 443–447.
[5] C.H. Choi, C. Baldizzone, J.-P. Grote, A.K. Schuppert, F. Jaouen, K.J.J. Mayrhofer, Angew. Chem. Int. Ed. 54 (2015) 12753–12757.
[6] N.R. Sahraie, U.I. Kramm, J. Steinberg, Y. Zhang, A. Thomas, T. Reier, J.-P. Paraknowitsch, P. Strasser, Nat. Commun. 6 (2015).
[7] A. Serov, K. Artyushkova, E. Niangar, C. Wang, N. Dale, F. Jaouen, M.-T. Sougrati, Q. Jia, S. Mukerjee, P. Atanassov, Nano Energy 16 (2015) 293–300.
[8] J. Shui, C. Chen, L. Grabstanowicz, D. Zhao, D.-J. Liu, Proc. Natl. Acad. Sci. U. S. A. 112 (2015) 10629–10634.
[9] U.I. Kramm, A. Zana, T. Vosch, S. Fiechter, M. Arenz, D. Schmeißer, J. Solid State Electrochem. 20 (2016) 969–981.
[10] G. McLean, Int. J. Hydrogen Energy 27 (2002) 507–526.
[11] S. Brocato, A. Serov, P. Atanassov, Electrochim. Acta 87 (2013) 361–365.
[12] L. Osmieri, A.H. Monteverde Videla, S. Specchia, Int. J. Hydrogen Energy 41 (2016) 19610–19628.
[13] S. Gojković, S. Gupta, R. Savinell, J. Electroanal. Chem. 462 (1999) 63–72.
[14] D. Malko, A. Kucernak, T. Lopes, Nat. Commun. 7 (2016) 13285.
[15] Q. He, X. Yang, X. Ren, B.E. Koel, N. Ramaswamy, S. Mukerjee, R. Kostecki, J. Power Sources 196 (2011) 7404–7410.

[16] G.A. Ferrero, K. Preuss, A. Marinovic, A.B. Jorge, N. Mansor, D.J.L. Brett, A.B. Fuertes, M. Sevilla, M.-M. Titirici, ACS Nano 10 (2016) 5922–5932.
[17] H.-W. Liang, X. Zhuang, S. Brüller, X. Feng, K. Müllen, Nat. Commun. 5 (2014) 4973.
[18] I. Herrmann, U.I. Kramm, J. Radnik, S. Fiechter, P. Bogdanoff, J. Electrochem. Soc. 156 (2009) B1283.
[19] U.I. Kramm, I. Herrmann-Geppert, S. Fiechter, G. Zehl, I. Zizak, I. Dorbandt, D. Schmeißer, P. Bogdanoff, J. Mater. Chem. A 2 (2014) 2663.
[20] G. Wu, H.T. Chung, M. Nelson, K. Artyushkova, K.L. More, C.M. Johnston, P. Zelenay, in: 220th ECS Meeting, ECS, 2011, pp. 1709–1717.
[21] W. Kiciński, B. Dembinska, M. Norek, B. Budner, M. Polański, P.J. Kulesza, S. Dyjak, Carbon 116 (2017) 655–669.
[22] S. Gupta, S. Zhao, O. Ogoke, Y. Lin, H. Xu, G. Wu, ChemSusChem 10 (2017) 774–785.
[23] R. Jinnouchi, A.B. Anderson, Phys. Rev. B 77 (2008).
[24] K.-Y. Yeh, S.A. Wasileski, M.J. Janik, Phys. Chem. Chem. Phys. PCCP 11 (2009) 10108–10117.
[25] A.S. Bondarenko, I.E.L. Stephens, H.A. Hansen, F.J. Perez-Alonso, V. Tripkovic, T.P. Johansson, J. Rossmeisl, J.K. Norskov, I. Chorkendorff, Langmuir ACS J. Surf. Colloids 27 (2011) 2058–2066.
[26] G.-R. Zhang, B.J. Etzold, J. Energy Chem. 25 (2016) 199–207.
[27] U. Kernchen, B. Etzold, W. Korth, A. Jess, Chem. Eng. Technol. 30 (2007) 985–994.
[28] J. Arras, M. Steffan, Y. Shayeghi, D. Ruppert, P. Claus, Green Chem. 11 (2009) 716.
[29] J. Lemus, J. Palomar, M.A. Gilarranz, J.J. Rodriguez, Adsorption 17 (2011) 561–571.
[30] J. Snyder, T. Fujita, M.W. Chen, J. Erlebacher, Nat. Mater. 9 (2010) 904–907.
[31] J. Snyder, K. Livi, J. Erlebacher, Adv. Funct. Mater 23 (2013) 5494–5501.
[32] G.-R. Zhang, M. Munoz, B.J.M. Etzold, ACS Appl. Mater. Interfaces 7 (2015) 3562–3570.
[33] G.-R. Zhang, M. Munoz, B.J.M. Etzold, Angewandte Chemie Int. ed. Engl. 55 (2016) 2257–2261.
[34] A. Ohma, K. Shinohara, A. Iiyama, T. Yoshida, A. Daimaru, ECS Trans. 41 (2011) 775–784.
[35] M.S. Dresselhaus, A. Jorio, M. Hofmann, G. Dresselhaus, R. Saito, Nano Lett. 10 (2010) 751–758.
[36] U.I. Kramm, J. Herranz, N. Larouche, T.M. Arruda, M. Lefèvre, F. Jaouen, P. Bogdanoff, S. Fiechter, I. Abs-Wurmbach, S. Mukerjee, J.-P. Dodelet, Phys. Chem. Chem. Phys. 14 (2012) 11673.
[37] U.I. Kramm, I. Herrmann-Geppert, P. Bogdanoff, S. Fiechter, J. Phys. Chem. C 115 (2011) 23417–23427.
[38] U.I. Koslowski, I. Abs-Wurmbach, S. Fiechter, P. Bogdanoff, J. Phys. Chem. C 112 (2008) 15356–15366.
[39] A. Zitolo, V. Goellner, V. Armel, M.-T. Sougrati, T. Mineva, L. Stievano, E. Fonda, F. Jaouen, Nat. Mater. 14 (2015) 937–942.
[40] G.A. Ferrero, A.B. Fuertes, M. Sevilla, M.-M. Titirici, Carbon 106 (2016) 179–187.
[41] J.L. Oberst, M.S. Thorum, A.A. Gewirth, J. Phys. Chem. C 116 (2012) 25257–25261.
[42] K. Gong, F. Du, Z. Xia, M. Durstock, L. Dai, Sci. (New York, N.Y.) 323 (2009) 760–764.
[43] M.T. Sougrati, V. Goellner, A.K. Schuppert, L. Stievano, F. Jaouen, Catal. Today 262 (2016) 110–120.
[44] U.I. Kramm, I. Herrmann-Geppert, J. Behrends, K. Lips, S. Fiechter, P. Bogdanoff, J. Am. Chem. Soc. 138 (2016) 635–640.
[45] U.I. Kramm, M. Lefèvre, N. Larouche, D. Schmeisser, J.-P. Dodelet, J. Am. Chem. Soc. 136 (2014) 978–985.
[46] F. Jaouen, F. Charreteur, J.P. Dodelet, J. Electrochem. Soc. 153 (2006) A689.
[47] F. Jaouen, S. Marcotte, J.-P. Dodelet, G. Lindbergh, J. Phys. Chem. B 107 (2003) 1376–1386.
[48] F. Charreteur, F. Jaouen, S. Ruggeri, J.-P. Dodelet, Electrochim. Acta 53 (2008) 2925–2938.
[49] I. Martinaiou, A. Shahraei, F. Grimm, H. Zhang, C. Wittich, S. Klemenz, S.J. Dolique, H-J. Kleebe, R.W. Stark, U.I. Kramm, Electrochim. Acta 243 (2017) 183–196.
[50] P. Bogdanoff, I. Herrmann, M. Hilgendorff, I. Dorbandt, S. Fiechter, H. Tributsch, J. New Mater. Electrochem. Syst. 7 (2004) 85–92.

4.4 Activity and Degradation Study of a Fe-N-C catalyst for ORR in Direct Methanol Fuel cell (DMFC)

Activity and Degradation Study of a Fe-N-C catalyst for ORR in Direct Methanol Fuel Cell (DMFC)

Ioanna Martinaiou[a,b] , Alessandro HA Monteverde Videla[e] , Natascha Weidler[a], Markus Kübler[c], David C.D. Wallace[c], Stephan Wagner[a], Ali Shahraei[c], Robert W. Stark[d], Peter Bogdanoff[e], Stefania Specchia[f], Ulrike I. Kramm[a,b,c]

[a]TU Darmstadt, Department of Materials and Earth Science, Otto-Berndt-Str. 3, 64287 Darmstadt, Germany
[b]Graduate School of Excellence Energy Science and Engineering, Otto-Berndt-Str. 3, 64287 Darmstadt, Germany
[c]TU Darmstadt, Department of Chemistry, Otto-Berndt-Str. 3, 64287 Darmstadt, Germany
[d]TU Darmstadt, Physics on Surfaces, Department of Materials- and Earth Science. Alarich-Weiss-Str. 16, 64287 Darmstadt, Germany
[e]Helmholtz-Zentrum Berlin für Materialien und Energie GmbH, Institute for Solar Fuels, Hahn-Meitner-Platz 1, 14109 Berlin, Germany
[f]Politecnico di Torino, Dipartimento di Scienza Applicata e Tecnologia, Corso Duca degli Abruzzi 24, 10129, Torino, Italy

Abstract

In this work a comprehensive study of the activity and stability of a non-precious metal catalyst ^{57}Fe-N-C (+S) in acidic media is reported. The combination of fundamental rotating-disk electrode studies and Direct Methanol Fuel Cell (DMFCs) investigations with spectroscopic techniques such as Raman and Mössbauer spectroscopy provide valuable information on the structural and chemical changes of the catalyst. The catalytic performance goes along with the loss of active sites as evidenced by post mortem Mössbauer spectroscopy.

Introduction

In recent decades, significant commercial efforts have been made to meet world's growing energy demand. The replacement of fossil fuels with solar and wind power is the most attractive option in terms of sustainability and low environmental impact. Fuel cells as clean-energy conversion devices have drawn a great deal of attention due to their high efficiency and low or zero emissions.

To date, several kinds of fuel cells, including Direct Methanol Fuel Cells (DMFCs) have shown great promise for near-term commercialization. DMFCs use liquid methanol as a fuel due to its high energy density, low price, storage, and handling [1]. Methanol can be produced by many different methods, from feedstocks such as coal and natural gas (by means of the gasification and steam reforming processes)[2], however, in order to comply with environmental requirements, methanol has to be produced by renewable sources.

In addition, the most important advantage is that methanol can integrate effectively with transmission and distribution systems that are already in existence. However, there are many technical challenges for the commercialization of DMFCs that remain unsolved. Methanol crossover is defined as methanol transport through the membrane from anode to the cathode side, the sluggish kinetics of the methanol oxidation reaction (MOR) and oxygen reduction reaction (ORR) as seen below , and in the anode the catalyst poisoning by irreversible CO adsorption on Pt [3,4].

$$\begin{array}{llr} CH_3OH + H_2O & \rightarrow \; CO_2 + 6H^+ + 6e^- & (E_0 = 0.02\ V) \\ 3/2\ O_2 + 6H^+ + 6e^- & \rightarrow \; 3H_2O & (E_0 = 1.23\ V) \\ \hline CH_3OH + 3/2\ O_2 & \rightarrow \; CO_2 + 2H_2O & (E_0 = 1.21\ V) \end{array}$$

Today, alloyed or pure Pt catalysts show the highest activity in DMFCs for MOR and ORR respectively [5–7]. In the anode, to overcome CO deactivation, alloys of Pt with more oxophilic elements have been investigated. PtRu bifunctional catalysts are presently the most active for methanol oxidation. It is proven that Ru serves the role of oxidizing CO_{ads} to CO_2 [8,9].

In the cathodic part, due to the crossover effect, methanol reacts with oxygen via combustion reaction, resulting in a mixed potential region which consequently leads to lower cell performance and fuel efficiency, when using platinum-based cathode catalysts in DMFCs [10,11].

This crossover effect has been acknowledged as the most notable technical barrier causing major performance losses of DMFC [12]. Therefore, the high cost of the cathode and the effect of methanol crossover can be avoided by developing highly methanol-tolerant and platinum-free cathode catalysts. In this regard, non-precious metal catalysts (NPMCs) provide the best alternative to Pt for the ORR. Over the last decade, significant progress on NPMCs has been made in terms of activity and stability, especially in acidic electrolytes. Among several types of NPMC studied in literature, most of them originate from sacrificial support methods with silica, activated carbon supports, polymer precursors, graphene oxide materials [11,13–21] or by , similarly synthesized Me-N-C catalysts which are tested mainly in PEMFCs [22–28].

Me-N-C catalysts exhibit an extremely low methanol oxidation reactivity as discussed by many authors. Briefly, Park et al [11] prepared a graphene-based Fe/Co-N-C catalyst which showed that it is tolerating methanol concentrations of up to 10.0 M in a DMFC without considerable activity loss from methanol crossover. On the contrary, the Pt-based cathode catalyst which was also tested for reasons of comparison showed that the open circuit voltage (OCV) was significantly decreased from initially 0.67 V to 0.55 V and 0.48 V when the methanol feed concentration was increased to 1.0 and 5.0 M, respectively. The maximum power density achieved with the non-precious catalyst was ca. 32 mW cm^{-2} and 110 mW cm^{-2} with the Pt cathode, with 1.0 M methanol feed concentration at 80 °C. Although the NPMC has the benefit of the methanol tolerance, the fuel cell performance is still very low compared to that of Pt-based catalyst.

Methanol tolerance on NPMCs was also studied by Sebastián et al [17], the authors prepared a Fe-N-C catalyst which was triple heat-treated and studied the methanol concentration influence on this catalyst and a Pt-based catalyst in an acidic electrolyte. Increasing the concentration of MeOH the NPMC remain unaffected whereas Pt loses about 200 mV of half-wave potential ($E_{1/2}$) for concentrations above 0.01 M. The maximum power density achieved was 48 mW cm^{-2} for methanol feed concentrations of 2.0-10.0 M. Additionally, a 100 h stability experiment at 0.3 V, 90°C, and 5.0 M methanol feed showed 50 % performance decay (in terms of power density) in the case of the Fe-N-C-THT cathode and about 45 % in the case of the Pt/C cathode indicating the similar behaviour between the benchmark and the non-precious catalyst, even though the origin of instability between the catalysts is different. The highest power density to date, has been reported by Wei et al [14], achieving 58 mW cm^{-2} at 60 °C and 2.0 M MeOH feed concentration by using a melamine-formaldehyde aerogel mixed with an iron salt resulting to a Fe-C-N electrocatalyst.

One of the main concerns associated with the commercial development of DMFCs is the long-term stability of a cell. The desired lifetime is near 5000 operating hours for portable applications [29]. DMFC is now far away from this requirement, because of the severe performance decay during operation. Therefore, durability and stability play a significant role in the commercialization of DMFC [30]. Although in most DMFC studies the initial performance and/or methanol- tolerance of non-precious metal cathode catalysts are tested in an actual DMFC, the durability/stability is often tested in rotating disk electrode configurations [10] or not tested at all [14]. There have been only a few reports on the durability/stability of non-precious metal catalysts at the cathode of DMFCs, probably due to the recent research interest in the topic [16,17,31–33].

The motivation of this work is to study the viability of using highly active non-precious metal catalyst for DMFC application. Thus, a PANI-based Fe-N-C catalyst was prepared which was characterized electrochemically by the RDE method in an acidic electrolyte by varying the temperature and investigated towards methanol tolerance by applying a durability protocol in the presence and absence of methanol resulting to the same performance decay. Subsequently, the catalyst was tested in a single cell DMFC also with varied temperature. Moreover, post mortem Mössbauer spectroscopy was applied in order to get insights on the degradation of the ^{57}Fe-N-C (+S) catalyst.

Experimental

Catalyst synthesis

One Fe-based catalyst, named ^{57}Fe-N-C (+S) was investigated in the present work. For the preparation of polyaniline, 90 mmol aniline was mixed with 264 mmol of the oxidant ammonium peroxydisulfate (APS) $(NH4)_2S_2O_8$, in 0.5 M HCl and let to polymerize for 24 h below 4 °C. The solvent evaporated at 150 °C for 24 h. In the following, 116 mmol of the PANI compound (Aniline:APS 1:3) was mixed with 3.4 mmol iron acetate and 1.1 mmol iron (57) acetate and 418 mmol dicyandiamide (DCDA) in a mortar until a homogeneous powder was obtained. The powder mixture was first heat-treated up to 800 °C with a ramping rate of 300 °C $\cdot$ h^{-1} for 1 h under inert atmosphere. After cooling down the catalyst was transferred in 2 M HCl for acid treatment for 12 h. In the following, the product was filtered and washed with distilled water until a neutral pH was achieved. After drying at 80 °C overnight the catalyst was heat-treated again at 800 °C for 1 hour with a heating ramp of 600 °C $\cdot$ h^{-1} in inert atmosphere resulting in a pure nanoparticle- free ^{57}Fe-N-C (+S) catalyst (Figure 1).

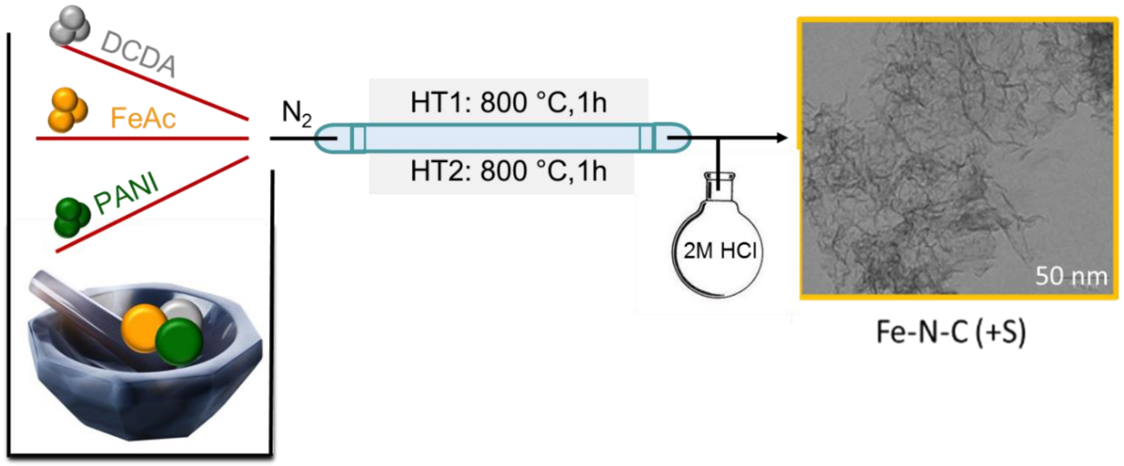

Figure 1. Scheme of the catalyst synthesis with a TEM image of the resulting ^{57}Fe-N-C (+S) catalyst.

Rotating disk electrode (RDE) measurements

The RDE measurements were performed in a three-electrode cell with a glassy-carbon rod as the counter electrode, an Ag/AgCl/(3 M KCl) electrode was used as reference. A drop of catalyst ink on the glassy carbon disk was used as working electrode. 0.1 M H_2SO_4 was used as electrolyte solution to test for the ORR activity and durability. The catalyst loading was kept at 0.5 mg cm^{-2} and the Nafion to catalyst ratio was 0.25.

For ORR- activity measurements firstly the capacitive current is measured by performing cyclic voltammetry between 1.0 and 0.0 V vs. RHE with sweep rates of 300 mV s^{-1} (20 scans), 100 mV s^{-1} (1 scan) and 10 mV s^{-1} (1 scan) in N_2–saturated electrolyte. After saturation with O_2, the open circuit potential (OCP) was determined and the activity measurements were applied in the same potential range as given above with a sweep rate of 10 mV s^{-1} with a disk rotation of 0 rpm, 900 rpm, and 1500 rpm. In this work, all activity data are plotted for 1500 rpm and the potential is measured experimentally prior to each test with a voltmeter, and then transferred versus the Reversible Hydrogen Electrode (RHE). The parameters used in this work for ORR-activity evaluation, are the onset potential, the half-wave potential ($E_{1/2}$) and for the calculation of the activation energy (E_A) the mass activity. Onset potential is defined as the potential in which a current density of <-0.1 mA cm^{-2} is generated and $E_{1/2}$ is the potential required to have half of the maximum diffusion current.

To define ORR activity, we used the mass-based kinetic current density, in units of A g^{-1} that was calculated according to equation (1):

$$j_{(A\,g^{-1})} = \frac{j_{kin}}{m_{cat}} \tag{1}$$

In this equation j_{kin} is the kinetic current density and m_{cat} the catalyst loading (0.5 mg cm^{-2}). The kinetic current density j_{kin} (mA cm^{-2}) was determined according to equation (2):

$$j_{kin}(U) = \frac{j(U) \times j_{Diff,lim}}{j_{Diff,lim} - j(U)} \tag{2}$$

In this equation $j_{kin}(U)$ represents the current density corrected for the capacity current and $j_{Diff,lim}$ is as-measured diffusion limiting current density.

For ORR-durability evaluation the Load Cycle protocol (LC) as proposed by the Fuel Cell Commercialization Conference in Japan in 2011 [34,35] was applied with a few modifications (O_2-saturated instead of N_2-saturated electrolyte, and 5000 cycles in total in contrast to 60000 cycles). In Figure 2 the conditions of the Load Cycle protocol are shown, in which the potential, at 0.6 and 1.0 V, holds for 3 sec at each. The lowest potential corresponds to the potential at peak power (about 0.6 V) and the upper potential (1.0 V) corresponds roughly to open circuit potential (OCP). The upper potential is known to have a significant impact on catalyst degradation [34].

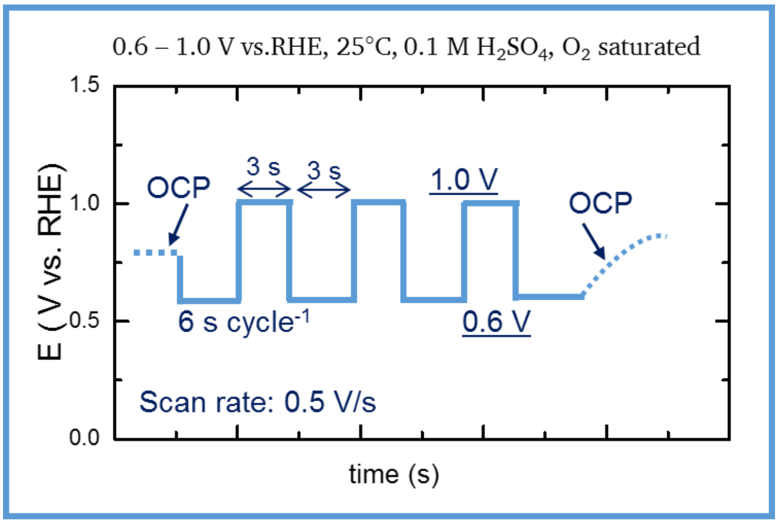

Figure 2: Conditions for the Load Cycle (LC) test protocol mimicking the peak load and open circuit voltage.

After each 1000 cycles, the activity protocol is performed in order to keep track on the activity decay of the studied catalyst. (Due to the observed changes in the RDE curves, only 5000 cycles were performed.)

MEA fabrication

For single cell experiments, membrane-electrode assemblies (MEA) were prepared with Nafion®115 membrane (~130mm thickness) as the solid electrolyte, commercial Pt-Ru/C nominally 40% platinum and 20% ruthenium on carbon black was used as the anode catalyst and ^{57}Fe-N-C (+S) as the cathode catalyst. The inks were prepared by mixing the catalyst powder with an isopropanol/deionized water solution (2:1) and Nafion ionomer solution (5 wt.%) with a Nafion to Platinum ratio of 0.14 for the anode and a Nafion to catalyst ratio of 0.4 for the cathode. After spraying the inks on the commercial hydrophobic gas diffusion layers (GDLs) Sigracet SGL 25BC, the three-compartment system formed the MEA by a hot pressing procedure at 135 °C and 50 bar for three minutes. The MEA was then installed in a 5 cm^2 single fuel cell (Electrochem. Inc).

DMFC tests

A fuel cell test bench (MITS Pro-FCTS, Arbin Instruments, USA) was used for the evaluation.
The anodic compartment was fed with 1.0 M methanol solution with a flow rate of 1mL min^{-1}. The cathodic compartment was fed with 100 N ml min^{-1} pure O_2 flow with a backpressure controller. The cell temperature was varied from room temperature to 80 °C. The polarization curves were recorded at 5 mV s^{-1} from open circuit potential down to 0.05 V. For temperatures higher than 60 °C the backpressure was controlled at 1 bar. In addition, a stability test was performed at 0.25 V (which corresponds to the maximum power density achieved), at 60 °C and 1 bar backpressure for in total 24 -h. Polarization curves were performed after 12 and 24 h, all polarization curves are not iR corrected.

N_2-sorption measurements

In order to determine the BET specific surface area and an estimate of the micropore surface area N_2-sorption measurements were performed with an Autosorb-3B test station from Quantachrome. Prior to the sorption experiment, the sample was degassed at 200 °C for 16 hours. Adsorption and desorption isotherms were measured at 77 K with N_2 as adsorbate down to relative pressures of P/P_0 of 0.1. The exact mass was determined afterwards and used for final determination of the surface areas. The adsorption data were analysed with the Brunauer-Emmett-Teller theory with the Autosorb software from Quantachrome Instruments.

Transmission Electron Microscopy (TEM)

In this work, the catalyst powder was immersed in ethanol and sonicated for 10 minutes in an ultrasonic bath, afterwards a small drop was placed on a copper grid (Plano S147-4) and kept for drying at room temperature. Measurements were conducted by a FEI CM 20 ST system equipped with a LaB6 Filament and a SDD-EDS detector.

Scanning Electron Microscopy with EDX

In order to get some ideas of the changes in iron concentration, SEM/EDX measurements were performed at the cross sections of the MEAs. The change in iron concentration was monitored by the Fe/Pt ratio of the MEA after degradation (as measured) in relation to the expected calculated Fe/Pt ratio based on MEA preparation.

X-ray photoelectron spectroscopy

X-ray photoelectron spectra (XPS) were measured with a Specs Phoibos 150 hemispherical analyzer and a Specs XR50M Al Ka X-ray source (E = 1486.7 eV). Before the measurements, the catalyst powder was pressed on an indium foil and transferred into the high-vacuum system. Spectra were analyzed using CasaXPS. Peaks were fitted using a Shirley background and a mixed Gauss/Lorentz peak.

Raman spectroscopy

In order to perform Raman measurements a drop of the catalyst ink- or the scratched remaining catalyst from the working electrode after the durability test- was placed onto a silica wafer. Raman spectra were obtained at room temperature with an alpha 300R confocal Raman microscope from WiTec (Ulm, Germany) with a grid of 600 lines mm^{-1} using an excitation laser (532.2 nm) with a laser power of 1 mW. The range of the measured spectra spreads from 0 to 4000 cm^{-1}. The spectra were acquired by performing 10 scans, each with integration time of 10 s. The fitting was done assuming the presence of four bands for the catalysts using voigtian lines. The bands can be assigned as G band (1580 cm^{-1}), D band (1360 cm^{-1}), D_3 band (1500 cm^{-1}) and D_4 band (1200 cm^{-1}). The assignment of these bands to different carbon contributions is given in the discussion part.

^{57}Fe Mössbauer spectroscopy

The Mössbauer measurements were performed with a Wissel instrument with a ^{57}Co/Rh source of an activity A ≈ 25 mCi to the time of measurements. The samples were prepared and measured at room temperature and the isomer shifts were determined relative to α-Fe. In case of the catalyst powder 100 mg were filled into a PTFE sample holder. In case of the MEAs after 12 and 24 h stability test, the 5 cm^2 MEAs were fixed in front of the detector with the cathode facing the gamma radiation beam. All Mössbauer spectra were fitted with Lorentzian lines using the program Recoil.

Results and discussion

Structural Characterization of the ^{57}Fe-N-C (S) catalyst

The physicochemical characterization of the ^{57}Fe-N-C (S) catalyst was performed using TEM (microscopy technique), N_2-physisorption (BET surface area), XPS (surface chemical composition analysis), Raman spectroscopy and Mössbauer spectroscopy. In Figure 3a and b, the XPS survey scan and the N1s narrow scan are given for the ^{57}Fe-N-C (S) catalyst, respectively. The different elements are assigned in the survey scan and the near surface N contributions of N deconvolved for six peaks are given: N_{pyrid},(397.5–398.8 eV), N-Fe_x (N_{N-Fex} 398.5–400.5 eV), pyrrolic (N_{pyrrol}, 400–401.5 eV), graphitic peak (N_{graph}, 401–403 eV), and two oxidic peaks (N_{ox}, 402.5–405 eV).

In Figure 3c and d the TEM images of the catalyst are shown. It becomes apparent that the ^{57}Fe-N-C (S) catalyst is a pure nanoparticle–free catalyst with mixed carbon structure. Parts are shown to be dominated by amorphous carbon but also parts are shown with graphene sheets. Probably this is due to the addition of sulfur in the precursor. As reported by Kramm et al. [36] sulfur prevents iron-carbide formation during the heating process. It is also reported that the iron carbide formation causes the inhibition of FeN_4 sites as shown by structural characterization [37,38]. In addition, this catalyst is acid leached in 2 M HCl for approx. 12 hours, which means that inactive Fe nanoparticles are leached out.

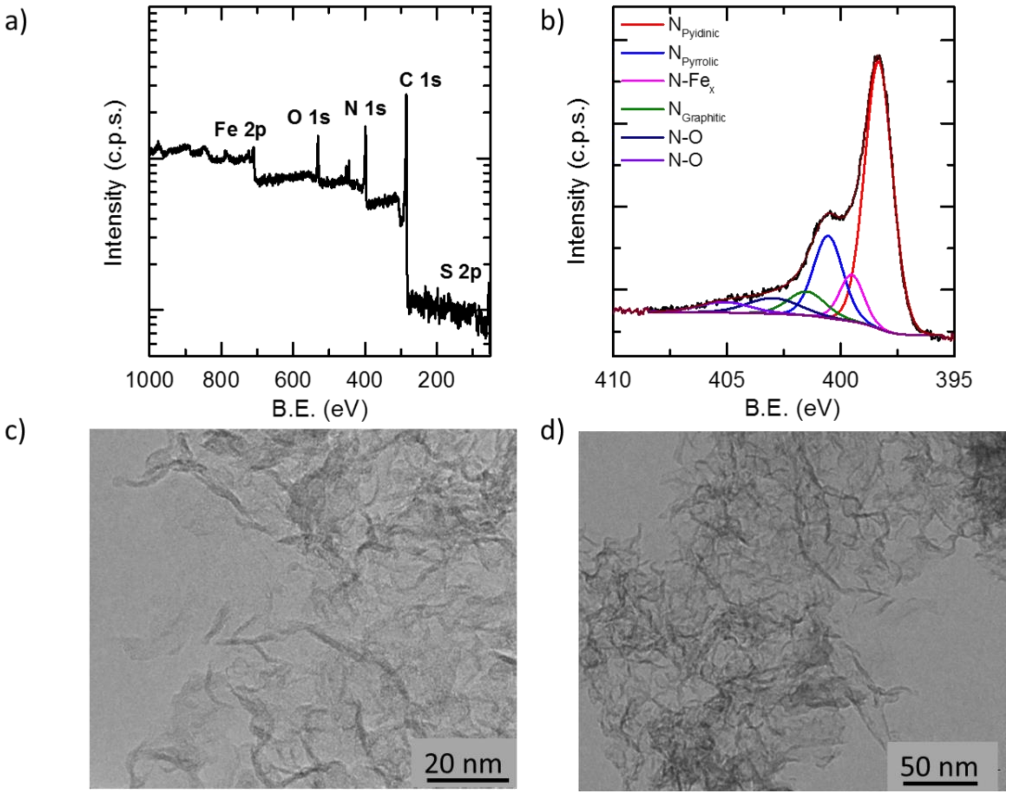

Figure 3: XPS survey scan (a), N1s narrow scan spectra (b) and TEM images (c) of ^{57}Fe- N- C (S) catalyst.

The surface elemental composition of the ^{57}Fe-N-C (+S) catalyst, obtained by XPS analysis, is shown in Table 1 as well as the results by N_2-sorption measurements.

Table 1: Surface elemental composition provided by XPS and specific surface area provided by N2-sorption measurements.

Sample	XPS (wt %)					N_2-sorption (m^2 g^{-1})		
	Fe	**N**	**C**	**O**	**S**	S_{BET}	$S_{Micropore}$	$S_{Mesopore}$
^{57}Fe-N-C (+S)	9.5	18.4	60.8	8.9	2.3	548	-	548

In order to get further insights on the carbon morphology especially on porosity and the role of micropores on ORR activity of the ^{57}Fe-N-C (+S) catalyst, N_2-sorption measurements were performed. The BET area was found 548 m^2 g^{-1} and is attributed to mesopore surface area as micropores were not detected by the t-method. These large pores are due to in situ-formed FeS being leached during the acid treatment, leaving behind open pores [39].

In Figure 4 the Raman spectrum of the ^{57}Fe-N-C (S) catalyst is shown. The spectrum is typical for amorphous carbon with two very prominent first-order bands corresponding to the D (1360 cm^{-1}) and G band (1580 cm^{-1}), indicating the formation of graphitized carbon with various dislocations/defects present [40,41].

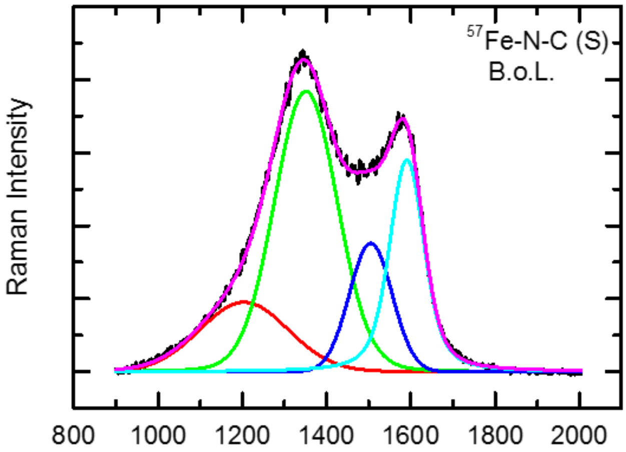

Figure 4: Raman spectrum of the ^{57}Fe-N-C (S) catalyst in the B.o.L.

In order to perform a more detailed analysis, it is necessary to deconvolute and fit the Raman spectrum and reveal all the components present in the system. The fitting was done by including four bands. The G band at around 1580 cm^{-1} and the D band at around 1360 cm^{-1}, which correspond to the planar motion of sp^2-hybridized carbon atoms in an ideal graphene layer and from carbon atoms close to the edge of a graphene sheet, or beside defects as curvatures, respectively [42–44].

Because perfect graphite only shows a G band [45] the ratio of the D to G band intensity (I_D/I_G) was used to characterize the graphene layer extension [46–49]. In this study, it was calculated by the fitted intensities and was found to be 1.32. Values above 1 are indicative of low graphene layer extensions typically found for amorphous carbon.

Additionally, two broad signals at ca. 1200 (D4) and 1500 cm^{-1} (D3) are also present in the Raman spectrum. These bands are associated with carbon atoms outside of a perfectly planar graphene network (such as aliphatic or amorphous structures) (D4) and integrated five-member rings, heteroatoms or FeN_4 active sites integrated into graphene-sheet structures (D3), respectively [38,43,44,46].

Electrochemical evaluation of the ^{57}Fe-N-C (S) catalyst

The catalytic activity, methanol tolerance, the effect of temperature and the durability via a load cycle protocol towards the ORR were determined in acidic solution (0.1M H_2SO_4). In Figure 5a and Figure 5b the polarisation curves obtained by RDE technique show the effect of methanol addition and temperature, respectively. The ^{57}Fe-N-C (S) catalyst shows initially a high catalytic performance with an onset potential of 0.83 V and a half-wave potential ($E_{1/2}$) of 0.73 V, as depicted in Figure 5a. The tolerance of the catalyst towards methanol was studied by adding 0.1 M, and 1.0 M methanol to the electrolyte. Even though the onset potential remains the same, the half-wave potential decreases by about 20 mV with methanol concentration of 1.0 M. It was described by Sebastian et al [17], that such potential changes might be caused by changes in O_2-saturation concentration and oxygen diffusivity induced by methanol addition.

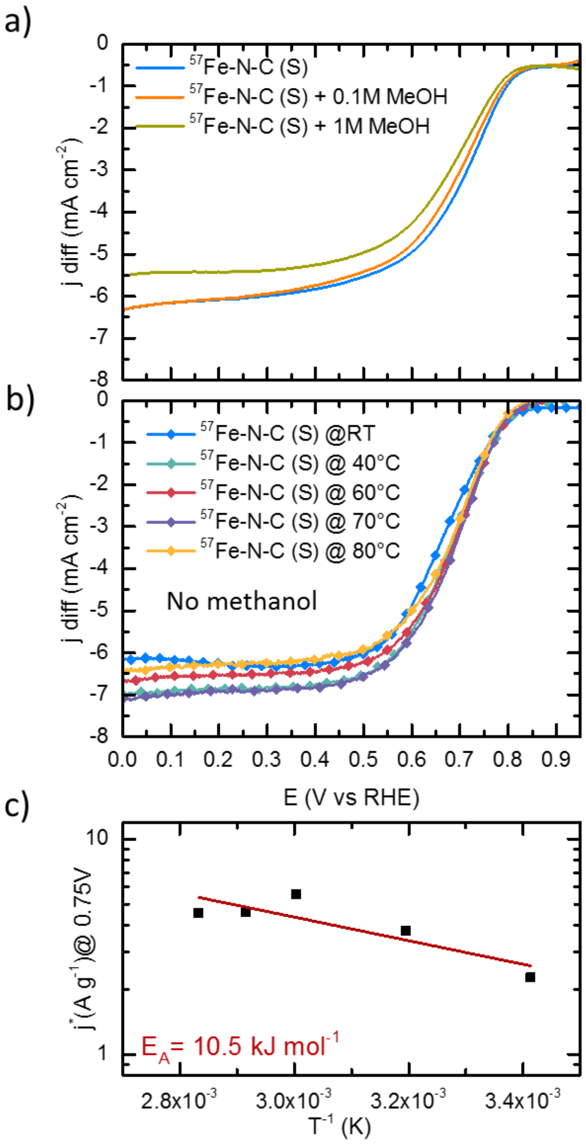

Figure 5: a) Methanol concentration and b) temperature effect on the RDE curves in O_2-saturated 0.1 -M H_2SO_4 electrolyte in the absence of methanol, recorded at 1500 rpm and 10 mVs^{-1}. c) Arrhenius plot for the ORR activity in terms of mass-related kinetic current density at 0.75 V with calculated activation energy.

Figure 5b shows the effect of temperature on ORR activity. As shown, by increasing the temperature from room temperature to 80 °C the onset potential remains unaffected while an increase in the kinetic region in terms of $E_{1/2}$ by 10 mV suggests that the temperature effect on this ^{57}Fe-N-C (S) catalyst is minor. In order to investigate the effect of temperature on the ORR activity it is necessary to consider the change in O_2 solubility, as also suggested by Jaouen et al. [50]. It is known that O_2 solubility decreases with increasing temperature. Wakabayashi et al [51] calculated the O_2 solubility at different temperatures. It is 1.38 mM at room temperature, 0.95 mM at 40 °C, 0.61 at 60 °C, 0.80 mM at 70 °C and 0.61 at 80 °C. Hence, for the ORR activity data given in Figure 5c, the activity is recalculated for an O_2 concentration of 1mM according to Neyerlin et al. [52].

$$j^{*}= j \cdot \left(\frac{C_{O2}^{*}}{C_{O2}}\right)^{0.79} \quad [50] \qquad (3)$$

where j* is the mass activity at 0.75 V vs. RHE and * is for an O_2 concentration of 1mM in the electrolyte solution. j is the mass activity calculated as mentioned in the experimental part, and C_{O_2} is the actual O_2 concentration in the electrolyte at the corresponding temperature. The exponent 0.79 is calculated for Pt/C on ORR in the work of Neyerlin et al [52], and is used in the work of Jaouen et al [50] for Fe-N-C catalysts. Thus it is assumed that the same law applies to this catalyst as well. The temperature dependence on oxygen diffusion coefficient (D) is described by the ratio of temperature (in K), and the dynamic viscosity, η [53] thus from the Levich equation (4) the diffusion limited current densities are predicted to increase with increasing temperature. However, the oxygen solubility is decreasing with increasing temperature. Considering the experimental results, one can conclude that the increase of the oxygen diffusion coefficient with temperature was higher than the decrease of oxygen solubility.
Equation 4 gives the Levich equation

$$j_{Diff} = 0.62 \cdot z \cdot c_O \cdot F \cdot D^{\frac{2}{3}} \cdot v^{-\frac{1}{6}} \cdot \omega^{\frac{1}{2}} = B \cdot c_O \cdot \omega^{1/2} \quad (4)$$

where z is the number of exchanged electrons, c_0 is the concentration of dissolved oxygen in the electrolyte, F is the Faraday constant, ω is the rotation velocity, v is the kinematic viscosity of the electrolyte and B is the Levich constant.

In Figure 5c the Arrhenius plot is shown with the logarithm of the corrected mass activity at 0.75 V for a fixed O_2 concentration versus the reciproke of the studied temperature in Kelvin. The Arrhenius law is expressed as

$$j^*(T) = j^*(T_\infty)\exp\left(\frac{-E_A}{RT}\right) \text{ [50]} \qquad (5)$$

From equation 5, the activation energy can be determined by taking the slope of the linear fit, which is $-E_A/(R \ln 10)$. The activation energy was found to be 10.5 kJ mol^{-1} for the ^{57}Fe-N-C (S) catalyst which is close to activation energies calculated for other Fe-N-C catalysts (8.9 kJ mol^{-1}) [50] and also similar to activation energies obtained for Pt/C catalysts (10 kJ mol^{-1}) [52] and Pt crystalline faces (12 kJ mol^{-1}) [54].

Load Cycle durability tests and its correlation to carbon morphology

Another important aspect besides activity is the durability of the non-precious metal catalysts for the fuel cell application. In order to investigate the catalyst durability and the effect of methanol concentration on it, we applied a durability protocol according to the Load Cycle (LC) protocol proposed by the Fuel Cell Commercialization Conference Japan ([34,35]. In Figure 6a the RDE curves at Beginning of Life (B.o.L.) and End of Life (E.o.L.) which corresponds to 5000 cycles, are shown, with intermediate evaluations of activity in every 1000 cycles (not shown). In Figure 6b the exact same protocol is applied in the presence of 1.0 M methanol in the electrolyte. Comparing Figures 6a and 6b it becomes apparent that the methanol addition has no effect on the durability behaviour of the catalyst. In both cases, a similar performance loss of $\Delta E_{1/2}$ less than 80 mV is reported.

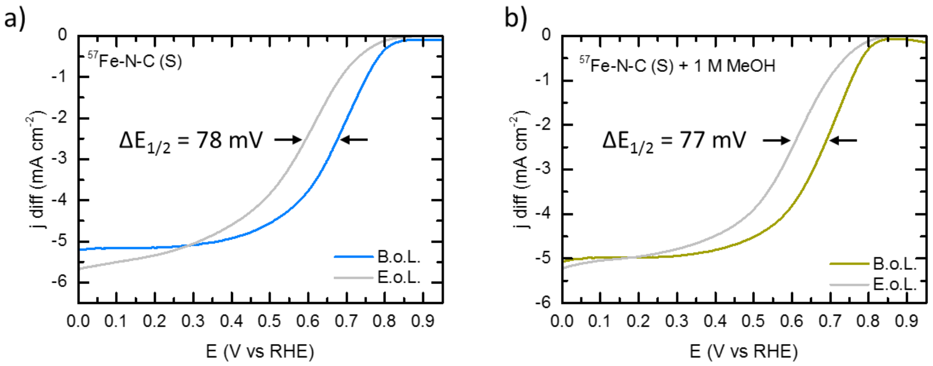

Figure 6: RDE curves at B.o.L and E.o.L (+ 5000 LC cycles) in O_2- saturated 0.1 M H_2SO_4 electrolyte for the ^{57}Fe-N-C (S) catalyst in the absence (a) and in the presence of 1.0 M methanol (b), with 1500 rpm and 10 mV s^{-1}.

In Figure 7 the deconvolution of the Raman spectra of the ^{57}Fe-N-C (S) catalyst for the first order region at B.o.L and E.o.L is shown.

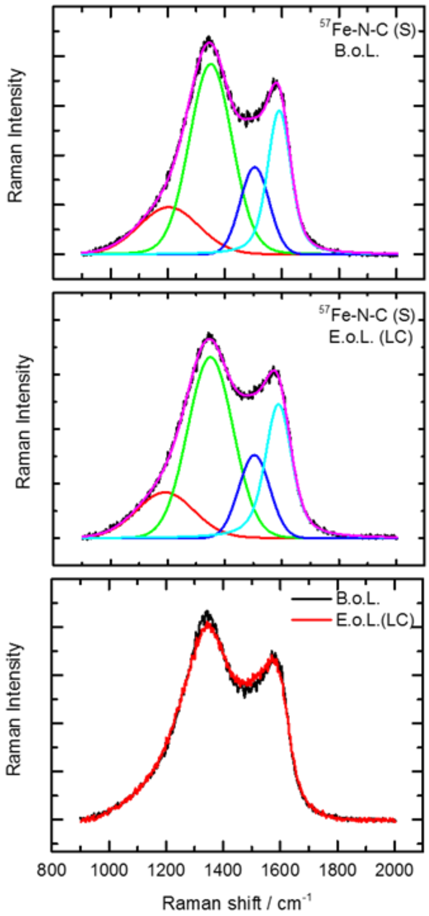

Figure 7: Raman spectra of the ^{57}Fe-N-C (S) catalyst in the B.o.L (a), and E.o.L (b) including the fitting are shown. c) Shows the comparison of the normalized spectra before and after the durability protocol.

The fitting of the Raman spectra was done as discussed previously. The Raman spectrum at B.o.L was added for easier comparison. The degree of graphitization (I_D/I_G) at E.o.L was found 1.35 (B.o.L.: 1.32). This slight increase in the graphitization degree indicates a slightly higher order after the durability test. For higher graphitization degree the ratio of D to G band should be smaller than 1, however in both cases was found higher.

The D_3 to G ratio was also determined. In our previous work [46] a decrease of the D_3 to G band ratio was also observed after applying a Start/Stop durability test (cycling between 1.0 to 1.5 V) and this decrease was linked with the disintegration of the active MeN_4 sites. This can be caused either by the oxidation of the graphene sheets or by leaching of the metal that was found more likely for a displacement of the metal out of the N_4 plane. A decrease from 0.61 (B.o.L) to 0.51 (E.o.L) was observed for this catalyst.

Instability during LC protocols is usually attributed to the gradual leaching of the metal centres and in some cases when a change in the diffusion current is also visible, to the change of mechanism from direct 4e$^-$ to indirect 2e$^-$ process. Choi et al, [55] suggested the Fe demetallation as the main instability cause for potentials up to 0.7 V. Carbon oxidation, which is another degradation effect, is kinetically hindered below 1.1 V especially in the absence of metal nanoparticles as in the case of the studied catalyst and for the given temperature [26,55].

DMFC performance and its correlation to the Fe content

For the application of DMFCs, it is desirable for the cathode catalyst to exhibit a high tolerance to the presence of methanol. As shown above, methanol has a very low impact on the ^{57}Fe-N-C (S) catalyst, especially in terms of durability.

Single cell performance of two similar prepared MEAs (Table 2) was measured in a methanol/O_2 fuel cell. An additional MEA was prepared as a reference for Fe/Pt ratio determination by SEM/EDX but was not tested. The non-precious metal catalyst was studied at the cathode side of these two MEAs. The polarization curves were recorded from open circuit potential (OCP) to 0.05 V with 5 mV s^{-1}, at different temperatures as shown in Figure 7.

Table 2: Information on MEA preparation.

	catalyst loading / mg cm^{-2}		Membrane	OCP / mV @ RT
	Anode (Pt-Ru)	Cathode (^{57}Fe-N-C (S))		
MEA#12	1.25	2.97	Nafion®115, 135°C, 50 bar	520
MEA#13	1.54	1.74		560
MEA#14	0.31 (Pt/C)	2.12	Nafion®117, 135°C, 50 bar	unused

The DMFC polarization and power density curves obtained at five different temperatures (25, 40, 60, 70, and 80 °C) are shown for the two MEAs in Figure 8. For the measurements of 60 °C and higher the backpressure was controlled at 1 bar. It can be observed that increasing the temperature, the fuel cell performance of both MEAs is significantly increasing, as expected from the Arrhenius equation (5). The open circuit potential slightly changes for both MEAs at room temperature, with the OCP of MEA#13 to be 40 mV higher than the OCP of MEA#12. With increasing temperature, the OCP increases for both MEAs. In the activation controlled region (here 0.6 to 0.4 V) most of the differences in the cell behaviour come from the kinetic control of MOR and ORR. The activation energy of both MEAs was also determined as described previously (here with the mass activity taken at 0.4 V). For

MEA#12 the activation energy was found 49.1 kJ mol^{-1} whereas for MEA#13 it was found 44.9 kJ mol^{-1}.

It is clear that the activation energies obtained by the DMFC tests are significantly higher in comparison to the activation energy obtained by the RDE measurements. A mayor difference is the electrode setup. In RDE, a three-electrode setup was used, hence E_A is just related to the intrinsic properties of our Fe- N-C (S) catalyst. Here in DMFC, a two-electrode setup was used. Hence, the measured current densities reflect the theoretical difference between methanol oxidation reaction (MOR) and oxygen reduction reaction (ORR) minus the overpotentials related to both half-cell reactions and potential (i·R) drop due to the resistance of the membrane.

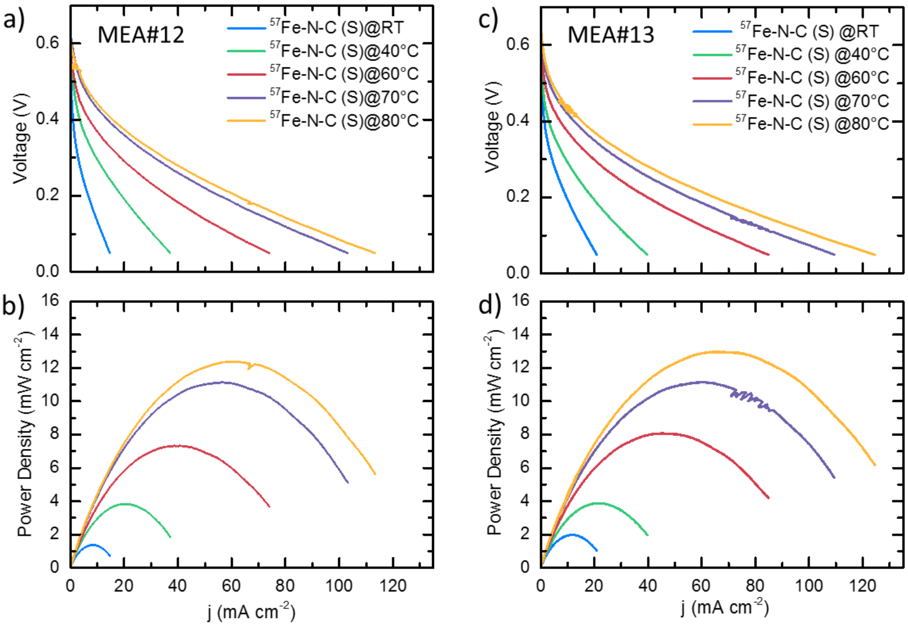

Figure 8: Polarization (a,c) and power density (b,d) curves of DMFC for both MEAs at different temperatures. Methanol feed concentration was 1.0 M with 1.0 mL min^{-1} flow rate in the anode and O_2 in the cathode.

The maximum power density achieved at 80 °C is equal for both MEAs with 12 mW cm^{-2} for MEA#12 and 13 mW cm^{-2} for MEA#13 (both at 0.2 V). The observed power densities are similar to reports on other NPMCs operated with similar low loadings on the anodic side, as summarized in Table 3.

The performance analysis in the high power density region (0.2 V) shows larger differences than those derived from the activation-controlled region (0.6 to 0.4 V). At 0.2 V, the effect of temperature is even more pronounced on the performance of both MEAs where the cell performance increases significantly with higher temperature. Thus, this stronger improvement at low voltages indicates improvements in the mass transport at higher potentials as originating from higher diffusion coefficients [53].

Table 3: DMFC performance results with NPMC as cathode.

Reference	NPMC	Max. Power Density / mW cm^{-2}	Temp. / °C	Cathode load. / mg cm^{-2}	Anode load. / mg cm^{-2}
[31]	CoZn	15.2	90	2.5	1 (Pt)
[32]	FePc	19.6	90	2.5	1 (Pt)
[20]	FePc	11.2	110	2.5	2.5 (Pt-Ru)
[14]	Fe/N/C aerogels	58	60	10	4.5 (Pt-Ru)
	Co/N/C aerogels	53	60	10	4.5 (Pt-Ru)
[16]	Fe-ABZIM	23	90	3	1(Pt-Ru)
[17]	Fe-ABZIM (THT)	48	90	3	1(Pt-Ru)
This work	**^{57}Fe-N-C (S)**	**13**	**80**	**1.7**	**1.5 (Pt-Ru)**

Even though durability is a very important aspect in the development of H_2-PEMFCs as well as of DMFCs, there have been only a few reports on the durability/stability of non-precious metal catalysts at the cathode of DMFCs [16,17,31–33].

Figure 9a shows a stability test at 0.25 V, 60 °C, 1 bar backpressure and 1 M methanol feed performed on the two MEAs with ^{57}Fe-N-C (S) as the cathode catalyst. Since there are not any suggested stability protocols particularly for DMFC applications, the conditions were chosen as described: the 0.25 V was chosen as it corresponds to 90 % of peak power density achieved for both MEAs while temperature and pressure were chosen as more suitable for portable applications.

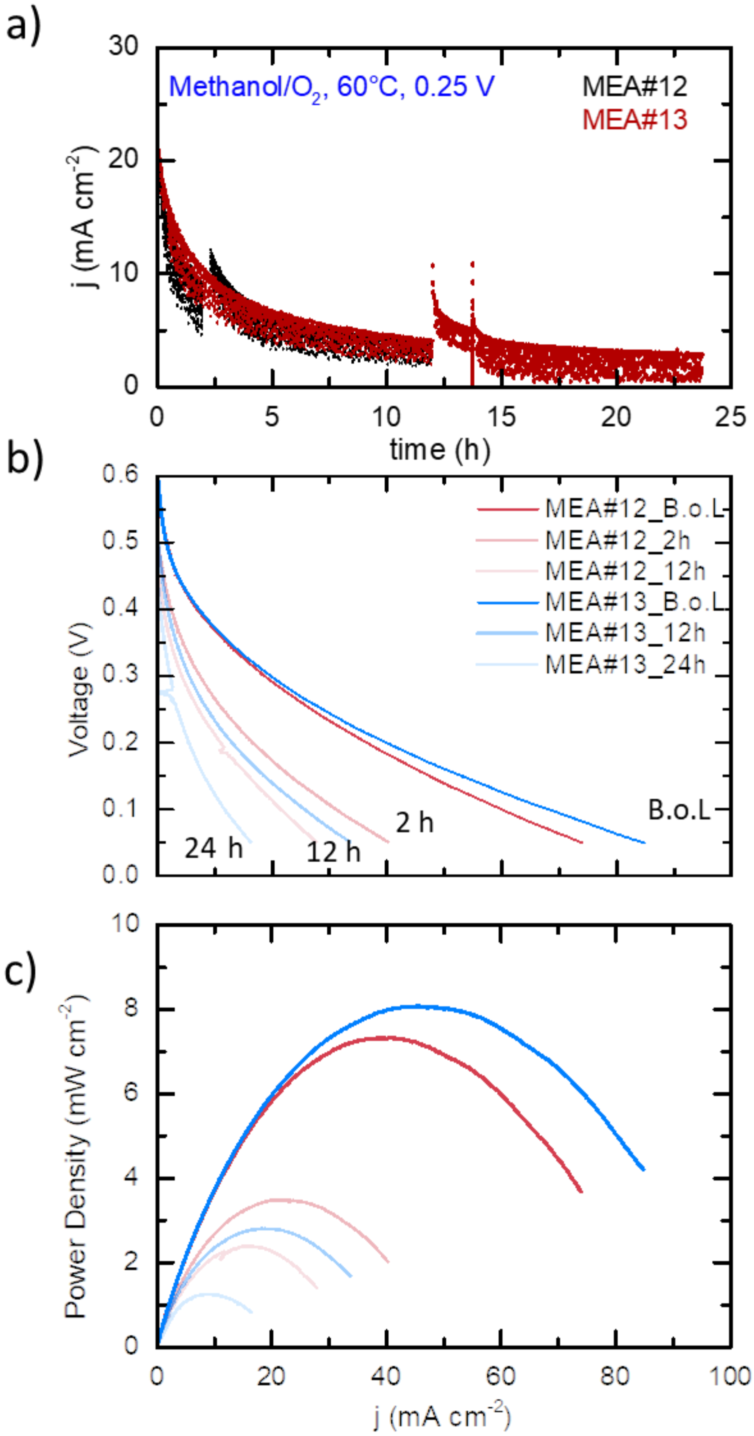

Figure 9: a) Stability test in DMFC at 0.25 V, 60 °C, 1.0 M methanol feed concentration and O_2 to the cathode, polarization (b) and power density(c) curves in the B.o.L. and E.o.L. of both MEAs.

In Figure 9b the polarization curves of MEA#12 and MEA#13 are shown at B.o.L, after 2 hours (MEA#12), after 12 hours (MEA#12 and MEA#13) and after 24 hours (MEA#13). MEA#12 was tested for 12 h with an intermediate activity evaluation after 2 h whereas MEA#13 was tested for in total 24 h with an intermediate activity evaluation after 12 h. In Figure 9c the power density versus the kinetic current density of both MEAs can be seen. The initial maximum power density of MEA#12 was 7.3 mW cm^{-2} at 41 mA cm^{-2} whereas after only 2 h of stability testing the achieved maximum power density was found to be the half (3.5 mW cm^{-2} at 22.6 mA cm^{-2}) pointing out the rapid initial fast decay. The End of Life (E.o.L.) maximum power density of the MEA#12 was found to be 2.4 -mW -cm^{-2} at 15.8 mA cm^{-2}) indicating that there is a more gradual performance loss.

MEA#13 was tested under the same conditions as MEA#12 however the duration of the test was different (24 h in total). The performance loss in terms of maximum power density was 8.1 mW cm^{-2} at 45.4 mA cm^{-2} down to 2.8 mW cm^{-2} at 18.3 mA cm^{-2}) within the first 12 hours and to 1.2 mW cm^{-2} at 9.3 mA cm^{-2} at the E.o.L.

For better comparison, the performance loss was determined by the loss in current density at 0.25 V. For the MEA#12 the initial current density was 26.9 mA cm^{-2}, after 2 hours was 11.4 mA cm^{-2} and after 12 hours was 7.19 mA cm^{-2}. It is obvious that the performance of the catalyst is severely decreasing in just two hours. The overall performance loss (in terms of current density) is 73 % at 0.25 V after 12 hours. For the MEA#13 the initial current density was 28.8 mA cm^{-2}, after 12 hours 8.7 mA cm^{-2} and after 24 h 3.3 mA cm^{-2}. The performance loss for the MEA#13 after 12 hours is 70 -% and after 24 hours is 88 %. The same initial rapid decay is observed as in the case of MEA#12.

Several authors also observed this initial rapid decay. Osmieri et al [32] performed a short stability test using a Fe-N-C catalyst as a cathode in the DMFC. The potential was kept constant at 0.4 V and the performance was evaluated every 30 minutes for in total 3 hours. The authors observed a large performance loss in terms of maximum power density (loss of 24 %) in the first hour of the test. In the following, a slower performance decrease occurred which resulted in 49 % performance loss in terms of maximum power density after 3 hours. According to the authors, the performance loss was attributed to the high flow rate of methanol (5.0 mL min^{-1}), even though the catalyst used was found to be highly methanol tolerant, and to the flooding of the micropores which accounts 50 % of the total surface area of the Fe-N-C catalyst.

Similar performance loss behaviour was observed by Sebastian et al [33] in a 100 h stability test at 0.3 V, 90 °C and 5 M methanol concentration. The authors reported a major decrease of current within the first 3 hours of the test followed by a significantly slower decay rate with time. The origin of the instability was not discussed in this work.

Recently, Chenitz et al, [56] investigated this initial fast decay which occurred with different testing conditions (variation of potential from 0.2 to 0.8 V at two different temperatures 25 and 80 °C) with a Fe-N-C catalyst in an H_2-PEMFC. The authors attribute this effect to a specific demetallation mechanism. For catalysts with micropores (> 0.7 nm), any iron ions coordinated out-of plane would be immediately released and transferred by the water flux which goes through the open-end micropores, resulting to the demetallation of the Fe-N_4 sites in the micropores.

So far Mössbauer spectroscopy has been conducted mostly for the investigation of powder samples. In this study, besides the initial powder catalyst we performed post mortem Mössbauer spectroscopy of the MEAs after performing stability test in a DMFC. The Mössbauer spectra of the ^{57}Fe-N-C (S) catalyst initial, after 12 hours and after 24 hours stability test in a DMFC as described above, are shown in Figure 10. It should be noted that the number of polarisation curves applied to both MEAs was equal.

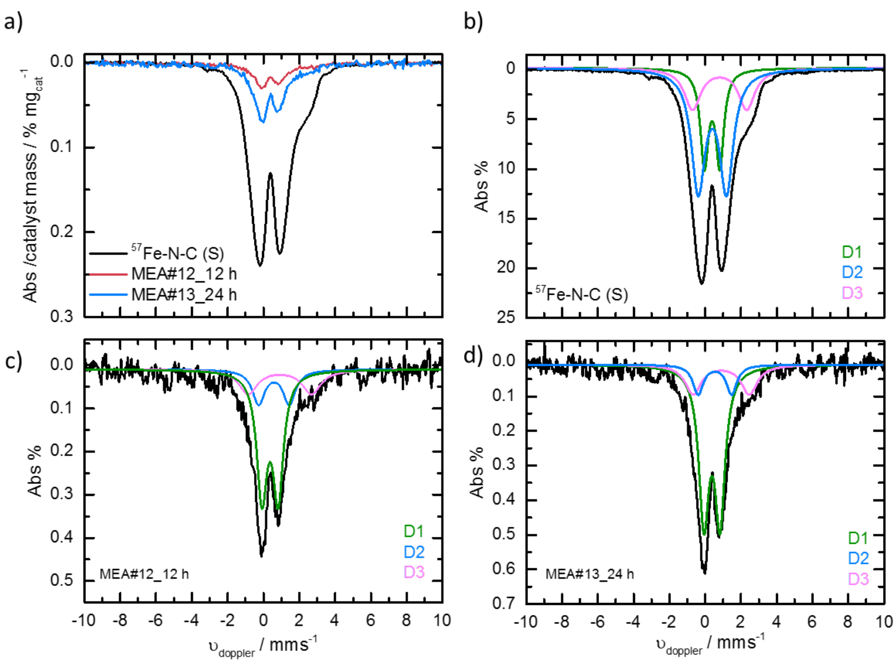

Figure 10: a) Comparison of the normalized to catalyst mass Mössbauer spectra and Mössbauer spectra including deconvolution of the as prepared ^{57}Fe-N-C (S) catalyst (b), MEA#12_12h (c) and MEA#13_24h (d).

In Figure 10a, the absorbance per mg of catalyst is used in order to compare the as-prepared catalyst with the used MEAs. From the comparison of the Mössbauer spectra, it becomes apparent that the Mössbauer absorbance of both MEAs significantly decreases. According to Kramm et al, [57] this decrease is related to iron leaching, and/ or water adsorption.

The obtained three spectra were deconvoluted into three doublets with the presence of only FeN_4 sites. Table 4 summarizes the Mössbauer parameters as well as the assignment to iron species. The calculation of iron contents was done based on iron contents provided by XPS and the Lamb-Mössbauer factors f_{LM} given in Sougrati et al. [58].

Table 4: Summary of the Mössbauer fitted parameters for the ^{57}Fe-N-C (S) catalyst, MEA#12_12h and MEA#13_24h. Lamb-Mössbauer factors for RT provided in Sougrati et al. [58] (f_{LM}(D1) = 0.46, f_{LM}(D2) = 0.52, f_{LM}(D3) ≈ 0.52).

	$δ_{iso}$	**$ΔE_Q$ or ε**	**whm**	**^{57}Fe-N-C (S)**		**MEA#12_12h**		**MEA#13_24 h**		**Assignment**
		(mm s^{-1})		**A (%)**	**Fe (wt%)**	**A (%)**	**Fe (wt%)**	**A (%)**	**Fe (wt%)**	
D1	0.37	0.89	0.64	24.7	2.35	59.9	2.19	66.4	1.95	Fe^{2+}N4, LS [24]
D2	0.50	1.66	0.80	53.5	5.08	19.1	0.70	13.2	0.39	$FePc^{2+}$, MS [26]
D3	0.87	3.23	1.12	21.8	2.07	21.0	0.77	20.4	0.60	$FeSO_4 \cdot 7\ H_2O$ [59]

It should be noted that there is no Lamb-Mössbauer factor available for the doublet D3. As the parameters are closer to D2 the calculation was done assuming a similar Lamb-Mössbauer factor for D3.

The first two doublets (D1 and D2) are assigned to FeN_4 centres that differ in their local environment and with Fe^{II} characterized by low spin (D1, S = 0), and mid spin (D2, S = 1) [57], another doublet with a large isomer shift (D3) is assigned to ferrous sulfate heptahydrate ($FeSO_4 \cdot 7\ H_2O$) [59]. Obviously, this species is formed due to the presence of the residuals from APS that was used as oxidation agent in the polymerisation of aniline and not removed. The absence of sextets and /or singlet proves the absence of elemental iron and iron carbides.

Figure 11 provides a comparison of the remaining Fe content of the different iron species, normalised to Platinum content, with time as determined by Mössbauer spectroscopy.

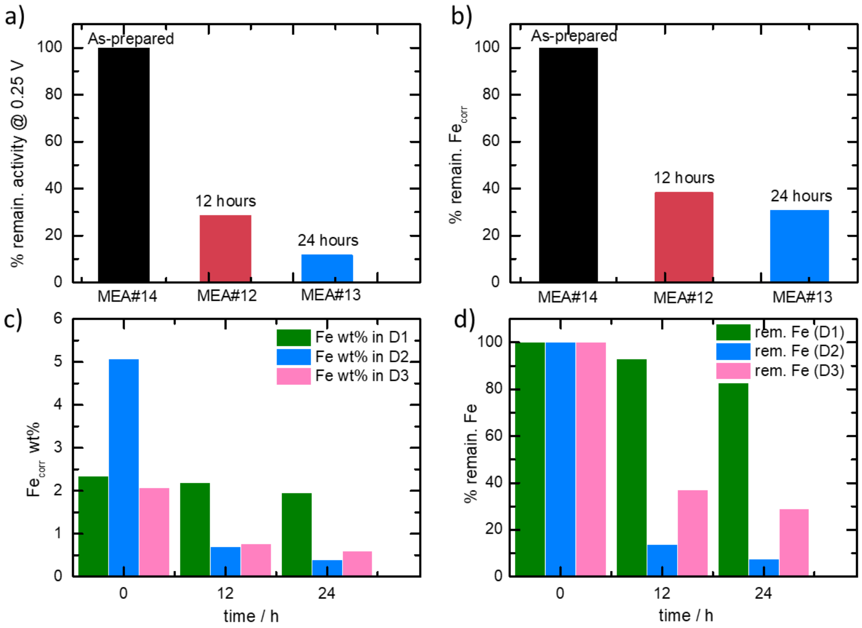

Figure 11: a) Percentage of remaining activity of the untreated, after 12 and 24 hours MEAs, b) percentage of remaining Fe content, normalised to Pt content, of the untreated, after 12 and 24 hours MEAs, c) Fe content and d) and remaining Fe content of the different iron species as determined by Mössbauer spectroscopy vs time.

From Figure 11 it becomes clear that the remaining Fe content as well as the remaining activity decrease with time.

The highest initial population (t=0 h) is attributed to Fe phthalocyanine ($FePc^{2-}$) like structure. The decrease of the population in D2 doublet indicates that iron in the form of $FePc^{2-}$ is removed during the stability test. The Fe content assigned to D1 seems to reveal a more stable behaviour. However, our recent low temperature measurements on MEAs treated under different conditions, show that some iron oxide/hydroxide species are formed, most probably from the remaining iron ions in the MEA, when the FC run is stopped (manuscript in preparation, beamline report ESRF).

Thus, it is evident from the results, that at 0.25 V significant fractions of FeN_4 sites are removed from the catalysts, even though this catalyst does not contain micropores. Furthermore, even iron sulfate seems more stable under the given operating conditions as visible from the less pronounced decrease in the related iron concentration.

Conclusions

In this work, the activity and the influence of methanol concentration of a nanoparticle-free ^{57}Fe-N-C (+S) catalyst was evaluated in a half-cell set up in acidic media. The influence of temperature on activity (in the absence of methanol) was studied from RT to 80 °C in order to determine the activation energy of this catalyst which was found to be 10.5 kJ mol^{-1}.
The durability performance of this catalyst under Load Cycle conditions showed that the addition of methanol has no negative impact on the durability. Raman spectroscopy was performed before and after the durability protocol, whereas only minor changes were observed.

In DMFC the activation energy assigned to the overall cell performance was a factor of ~ five higher and might indicate that there is stronger kinetic hindrance for the MOR on PtRu compared to ORR on our catalyst. A stability protocol was applied at 0.25 V, 60 °C and with 1.0 M methanol. Mössbauer spectroscopy was performed before and after 12 and 24 hours of operation. It is shown that the decrease in the catalytic performance goes along with the loss of active sites.

References

[1] P. Joghee, J.N. Malik, S. Pylypenko, R. O'Hayre, MRS Energy & Sustainability 2 (2015).
[2] G.A. Olah, A. Goeppert, G.K.S. Prakash (Eds.), Beyond Oil and Gas: The Methanol Economy, Wiley-VCH Verlag GmbH & Co. KGaA, Weinheim, Germany, 2009.
[3] C.Y. Du, T.S. Zhao, W.W. Yang, Electrochimica Acta 52 (2007) 5266–5271.
[4] J. Prabhuram, T.S. Zhao, H. Yang, Journal of Electroanalytical Chemistry 578 (2005) 105–112.
[5] V.R. Stamenkovic, B. Fowler, B.S. Mun, G. Wang, P.N. Ross, C.A. Lucas, N.M. Marković, Science (New York, N.Y.) 315 (2007) 493–497.
[6] V.R. Stamenkovic, B.S. Mun, M. Arenz, K.J.J. Mayrhofer, C.A. Lucas, G. Wang, P.N. Ross, N.M. Markovic, Nature materials 6 (2007) 241–247.
[7] J. Greeley, I.E.L. Stephens, A.S. Bondarenko, T.P. Johansson, H.A. Hansen, T.F. Jaramillo, J. Rossmeisl, I. Chorkendorff, J.K. Nørskov, Nature chemistry 1 (2009) 552–556.
[8] H.A. Gasteiger, N.M. Markovic, P.N. Ross, J. Phys. Chem. 99 (1995) 8290–8301.
[9] C. Lamy, A. Lima, V. LeRhun, F. Delime, C. Coutanceau, J.-M. Léger, Journal of Power Sources 105 (2002) 283–296.
[10] Q. Li, T. Wang, D. Havas, H. Zhang, P. Xu, J. Han, J. Cho, G. Wu, Advanced science (Weinheim, Baden-Wurttemberg, Germany) 3 (2016) 1600140.
[11] J.C. Park, C.H. Choi, Journal of Power Sources 358 (2017) 76–84.
[12] Q. Li, Y. Chen, J.R. Rowlett, J.E. McGrath, N.H. Mack, Y.S. Kim, ACS applied materials & interfaces 6 (2014) 5779–5788.
[13] B. Piela, T.S. Olson, P. Atanassov, P. Zelenay, Electrochimica Acta 55 (2010) 7615–7621.
[14] Y. Wei, C. Shengzhou, L. Weiming, International Journal of Hydrogen Energy 37 (2012) 942–945.
[15] D. Sebastián, A. Serov, I. Matanovic, K. Artyushkova, P. Atanassov, A.S. Aricò, V. Baglio, Nano Energy 34 (2017) 195–204.
[16] D. Sebastián, A. Serov, K. Artyushkova, P. Atanassov, A.S. Aricò, V. Baglio, Journal of Power Sources 319 (2016) 235–246.
[17] D. Sebastián, A. Serov, K. Artyushkova, J. Gordon, P. Atanassov, A.S. Aricò, V. Baglio, ChemSusChem 9 (2016) 1986–1995.
[18] L. Osmieri, R. Escudero-Cid, A.H.A. Monteverde Videla, P. Ocón, S. Specchia, Applied Catalysis B: Environmental 201 (2017) 253–265.
[19] A.H.A. Monteverde Videla, S. Ban, S. Specchia, L. Zhang, J. Zhang, Carbon 76 (2014) 386–400.
[20] A.H.A. Monteverde Videla, D. Sebastián, N.S. Vasile, L. Osmieri, A.S. Aricò, V. Baglio, S. Specchia, International Journal of Hydrogen Energy 41 (2016) 22605–22618.

[21] Y.J. Sa, D.-J. Seo, J. Woo, J.T. Lim, J.Y. Cheon, S.Y. Yang, J.M. Lee, D. Kang, T.J. Shin, H.S. Shin, H.Y. Jeong, C.S. Kim, M.G. Kim, T.-Y. Kim, S.H. Joo, Journal of the American Chemical Society 138 (2016) 15046–15056.
[22] M. Lefèvre, E. Proietti, F. Jaouen, J.-P. Dodelet, Science (New York, N.Y.) 324 (2009) 71–74.
[23] E. Proietti, F. Jaouen, M. Lefèvre, N. Larouche, J. Tian, J. Herranz, J.-P. Dodelet, Nature communications 2 (2011) 416.
[24] U.I. Kramm, M. Lefèvre, N. Larouche, D. Schmeisser, J.-P. Dodelet, Journal of the American Chemical Society 136 (2014) 978–985.
[25] N.R. Sahraie, U.I. Kramm, J. Steinberg, Y. Zhang, A. Thomas, T. Reier, J.-P. Paraknowitsch, P. Strasser, Nature communications 6 (2015) 8618.
[26] U.I. Kramm, A. Zana, T. Vosch, S. Fiechter, M. Arenz, D. Schmeißer, J Solid State Electrochem 20 (2016) 969–981.
[27] J. Shui, C. Chen, L. Grabstanowicz, D. Zhao, D.-J. Liu, Proceedings of the National Academy of Sciences of the United States of America 112 (2015) 10629–10634.
[28] G. Wu, K.L. More, C.M. Johnston, P. Zelenay, Science (New York, N.Y.) 332 (2011) 443–447.
[29] A. Mehmood, M.A. Scibioh, J. Prabhuram, M.-G. An, H.Y. Ha, Journal of Power Sources 297 (2015) 224–241.
[30] Z. Guo, A. Faghri, International Communications in Heat and Mass Transfer 35 (2008) 225–239.
[31] L. Osmieri, R. Escudero-Cid, M. Armandi, P. Ocón, A.H.A. Monteverde Videla, S. Specchia, Electrochimica Acta 266 (2018) 220–232.
[32] L. Osmieri, R. Escudero-Cid, M. Armandi, A.H.A. Monteverde Videla, J.L. García Fierro, P. Ocón, S. Specchia, Applied Catalysis B: Environmental 205 (2017) 637–653.
[33] D. Sebastián, V. Baglio, A.S. Aricò, A. Serov, P. Atanassov, Applied Catalysis B: Environmental 182 (2016) 297–305.
[34] A. Ohma, K. Shinohara, A. Iiyama, T. Yoshida, A. Daimaru, Boston, MA, October 9 - October 14, 2011.
[35] S.S. Kocha, in: K.-D. Kreuer (Ed.), Fuel Cells, Springer New York, 2013, pp. 473–518.
[36] U.I. Kramm, I. Herrmann-Geppert, S. Fiechter, G. Zehl, I. Zizak, I. Dorbandt, D. Schmeißer, P. Bogdanoff, J. Mater. Chem. A 2 (2014) 2663–2670.
[37] M. Ferrandon, A.J. Kropf, D.J. Myers, K. Artyushkova, U. Kramm, P. Bogdanoff, G. Wu, C.M. Johnston, P. Zelenay, J. Phys. Chem. C 116 (2012) 16001–16013.
[38] I. Herrmann, U.I. Kramm, J. Radnik, S. Fiechter, P. Bogdanoff, J. Electrochem. Soc. 156 (2009) B1283.
[39] Q. Li, G. Wu, D.A. Cullen, K.L. More, N.H. Mack, H.T. Chung, P. Zelenay, ACS Catal. 4 (2014) 3193–3200.
[40] A. Sadezky, H. Muckenhuber, H. Grothe, R. Niessner, U. Pöschl, Carbon 43 (2005) 1731–1742.
[41] R.J. Nemanich, S.A. Solin, Phys. Rev. B 20 (1979) 392–401.
[42] F. Tuinstra, J.L. Koenig, The Journal of Chemical Physics 53 (1970) 1126–1130.
[43] T. Jawhari, A. Roid, J. Casado, Carbon 33 (1995) 1561–1565.
[44] A. Cuesta, P. Dhamelincourt, J. Laureyns, A. Martínez-Alonso, J.M.D. Tascón, Carbon 32 (1994) 1523–1532.
[45] M.J. Matthews, M.A. Pimenta, G. Dresselhaus, M.S. Dresselhaus, M. Endo, Phys. Rev. B 59 (1999) R6585-R6588.
[46] I. Martinaiou, A. Shahraei, F. Grimm, H. Zhang, C. Wittich, S. Klemenz, S.J. Dolique, H.-J. Kleebe, R.W. Stark, U.I. Kramm, Electrochimica Acta 243 (2017) 183–196.
[47] G. Wu, C.M. Johnston, N.H. Mack, K. Artyushkova, M. Ferrandon, M. Nelson, J.S. Lezama-Pacheco, S.D. Conradson, K.L. More, D.J. Myers, P. Zelenay, J. Mater. Chem. 21 (2011) 11392.
[48] S. Gupta, S. Zhao, O. Ogoke, Y. Lin, H. Xu, G. Wu, ChemSusChem 10 (2017) 774–785.
[49] A.C. Ferrari, J. Robertson, Phys. Rev. B 61 (2000) 14095–14107.
[50] F. Jaouen, V. Goellner, M. Lefèvre, J. Herranz, E. Proietti, J.P. Dodelet, Electrochimica Acta 87 (2013) 619–628.
[51] N. Wakabayashi, M. Takeichi, H. Uchida, M. Watanabe, The journal of physical chemistry. B 109 (2005) 5836–5841.

[52] K.C. Neyerlin, W. Gu, J. Jorne, H.A. Gasteiger, J. Electrochem. Soc. 153 (2006) A1955.
[53] U.A. Paulus, T.J. Schmidt, H.A. Gasteiger, R.J. Behm, Journal of Electroanalytical Chemistry 495 (2001) 134–145.
[54] C.F. Zinola, A.M. Castro Luna, A.J. Arvia, Electrochimica Acta 39 (1994) 1951–1959.
[55] C.H. Choi, C. Baldizzone, J.-P. Grote, A.K. Schuppert, F. Jaouen, K.J.J. Mayrhofer, Angewandte Chemie (International ed. in English) 54 (2015) 12753–12757.
[56] R. Chenitz, U.I. Kramm, M. Lefèvre, V. Glibin, G. Zhang, S. Sun, J.-P. Dodelet, Energy Environ. Sci. 11 (2018) 365–382.
[57] U.I. Kramm, M. Lefèvre, P. Bogdanoff, D. Schmeißer, J.-P. Dodelet, The journal of physical chemistry letters 5 (2014) 3750–3756.
[58] M.T. Sougrati, V. Goellner, A.K. Schuppert, L. Stievano, F. Jaouen, Catalysis Today 262 (2016) 110–120.
[59] E. Fluck, W. Kerler, W. Neuwirth, Angew. Chem. Int. Ed. Engl. 2 (1963) 277–287.

4.5 Summary of the Results and Contribution to the Field

Non-precious metal catalysts (NPMCs) have evolved greatly from cobalt phthalocyanine, whose ORR activity in alkaline media was firstly reported in 1965, [45] to more recent high-temperature treated transitional metal-nitrogen-carbon (Me-N-C) materials with high performance [2,3,58].
Significant progress in activity and durability has been made especially in acidic electrolyte, by using several precursors such as 1,10 phenanthroline (Phen) [2,57], polyaniline (PANI) [204], metal-organic framework (MOF) [2,3,97], and the combination of different precursors [2,3,97]. (A summary of today's most active and durable catalysts can be found in Table 2.2 and Table 2.4, respectively.)

In this work, four differently prepared Fe-N-C catalysts were reported. Based on the different synthesis routes (chapter 3.1) the Fe-based catalysts exhibit different structures, and different performance. To the time when the different working topics started, they displayed the state of the art in the Catalysts and Electrocatalyst group (ECAT group). In this chapter, the activity and durability behaviour in correlation with structural analysis of these Fe-N-C catalysts under identical conditions will be discussed.

Electrochemical characterization

As described in chapter 2.2.2 and 3.1 the synthesis of the non-precious metal catalysts has a major influence on the resulting morphology, thus to the active sites of the catalysts. Briefly, all catalysts were prepared by a first heat-treatment followed by an acid leaching, and by a second heat-treatment. The detailed preparation of each catalyst can be found in chapter 3.1. Each of these preparation routes represents the status of the progress of catalyst development in the ECAT group of Prof. U.I.Kramm. In Table 4.1, the preparation steps are summarized.

Table 4.1: Summary of preparation routes of all Fe-N-C catalysts studied.

Name	Precursors	Preparation route
Fe-N-C (MOF+ Phen)	FeAc+MOF+Phen	HT1: 950 °C (2 h), AL, HT2: 950 °C (2 h)
Fe-N-C (DCDA+Phen)	FeAc+DCDA+Phen	HT1: 800 °C (1 h), AL, HT2: 800 °C (3 h)
Fe-N-C (DCDA+Phen+S)	FeAc+DCDA+Phen+ S	HT1: 800 °C (1 h), AL, HT2: 800 °C (3 h)
^{57}Fe-N-C (DCDA+ PANI(S))	^{57}FeAc+DCDA+PANI(S)	HT1: 800 °C (1 h), AL, HT2: 800 °C (1 h)

In Figure 4.1 the cyclic voltammograms (CV) obtained in N_2-saturated electrolyte with 100 mV sec^{-1} of the studied catalysts are shown. When cyclic voltammetry is performed on this type of catalyst in the absence of oxygen, many iron-containing catalysts exhibit a reversible redox peak at around 0.6–0.8 V versus RHE [166,167].
As many metal free catalysts do not exhibit this peak, some publications associate the peak with the metal centred Fe^{2+} / Fe^{3+} redox peak of the active site [166,167].

Ramaswamy et al. reported a relationship with the position of the redox peak and the activity of the catalyst. The charge associated with this peak was used to determine the number of active sites and hence the site density.

In this study, a pair of peaks around 0.7 V can observed only for the Fe-N-C (DCDA+Phen+S) catalyst attributed to the Fe^{3+}/Fe^{2+} transition.

It has to be pointed out that this peak can also be associated with a quinone/hydroquinone couple on the carbon surface [168].

In addition, from CV curves the double layer capacitance can be determined by extracting the anodic current density at 0.5 V. It can be seen from Figure 4.1 that the double layer capacitance increases in the order of Fe-N-C (MOF+ Phen) < Fe-N-C (DCDA+Phen+S) < Fe-N-C (DCDA+Phen) < ^{57}Fe-N-C (DCDA+ PANI(S)). The actual values can be found in Table 4.2 below.

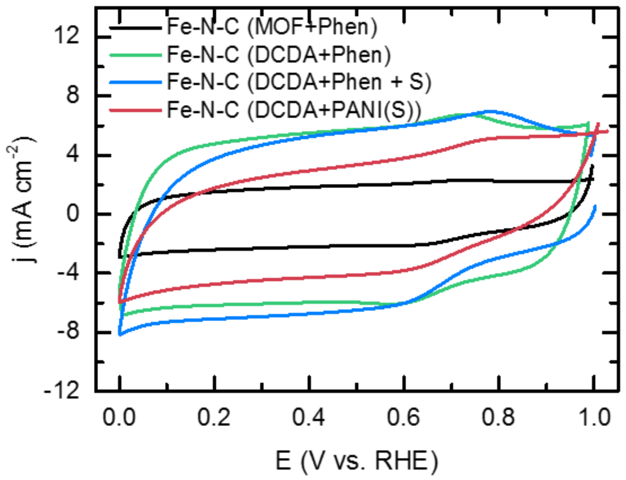

Figure 4.1: Cyclic voltammograms in N_2-saturated 0.1 M H_2SO_4 with 100 mV sec^{-1}.

In Figure 4.2, the RDE curves and the Tafel plots of the studied catalysts are shown. From the RDE curves the diffusion limiting current density (J_{Diff}), the onset (E_{Onset}) and the half-wave potential ($E_{1/2}$) can be extracted. As for the kinetic current density (J_{kin}) it can be extracted from the Tafel plots. The data are summarized in Table 4.2 together with the error percentage assigned to each of these values.

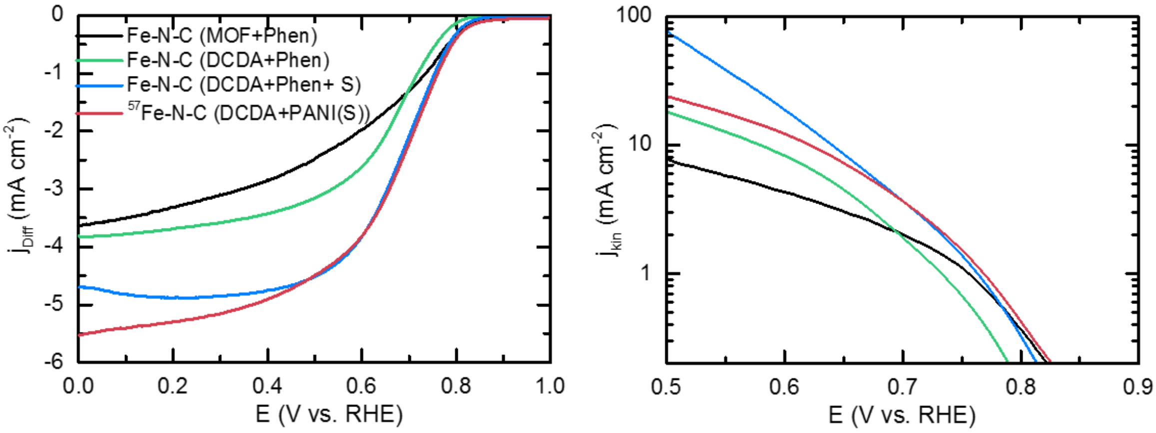

Figure 4.2: RDE and Tafel plots of all studied catalysts in 0.1 M H_2SO_4, rpm 1500 and 10 mV s^{-1}.

In principle, the high onset potential reveals the reaction initiation; the high half-wave potential indicates faster kinetics and the higher diffusion limiting current density (in this case more negative) implies larger number of electron transfer. From the comparison of the obtained data, it becomes apparent that the most active catalysts are the ones with sulfur in the precursor. This is in accordance with literature where it was found that sulfur addition increases the activity by suppressing the formation of inactive species (such as iron carbides) [171].

Table 4.2: Summary of catalytic performance of all Fe-N-C catalysts studied (in brackets, the percentage error is given).

Name	E_{Onset} (V)	$E_{1/2}$ (V)	J_{Diff} @ 0.0 V (mA cm^{-2})	J_{kin} @ 0.75 V (mA cm^{-2})	Capacity @0.5 V (mF cm^{-2})
Fe-N-C (MOF+ Phen)	0.86 ± 2.2%	0.66 ± 6.5%	3.54 ± 7.3%	1.51± 37%	19.6
Fe-N-C (DCDA+Phen)	0.80 ± 0.5%	0.67 ± 1.6%	4.41 ± 11.0%	0.93± 37%	57.4
Fe-N-C (DCDA+Phen+S)	0.85 ± 3.6%	0.70 ± 2.8%	4.79 ± 1.9%	1.85± 35%	56.4
^{57}Fe-N-C (DCDA+ PANI(S))	0.85 ± 1.1%	0.68 ± 1.4%	5.40 ± 3.8%	1.45± 10%	59.5

Physicochemical characterization

In order to investigate the structure and composition of these catalysts, several physicochemical characterization techniques were employed.

The catalysts were characterized by TEM (microscopy technique), N_2 physisorption (BET surface area), XPS (surface chemical composition analysis), Raman spectroscopy and Mössbauer spectroscopy.

In Table 4.3, the surface elemental composition and specific surface area as determined by XPS and N_2-sorption measurements are shown.

It can be observed that the difference in the precursors and preparation routes leads to different compositions. The highest iron and nitrogen content corresponds to the S-added catalysts. Besides its role to prevent the formation of iron carbides [161], the addition of sulfur according to Hermann et al. [148] was found to lower the iron content for their catalysts. This is not the case when comparing the Fe-N-C (DCDA+Phen) and Fe-N-C (DCDA+Phen+S) catalysts.

The formation of FeN_4 sites requires a Fe to N weight ratio of < 1 due to the relation of the molar masses of Fe to N (1:4). Comparing the four catalysts it becomes clear that the active site formation is not limited by the nitrogen content as the ratio is below one for all catalysts.

In the case of the Fe-N-C (DCDA+Phen+S) catalyst, it is 0.58, whereas for the ^{57}Fe-N-C (DCDA+ PANI(S)) catalyst is 0.52. This means that for both catalysts the Fe to N ratio is found similar and roughly translated to one iron atom corresponds to 8 nitrogen atoms. Therefore, the absolute increase in Fe content indicates that more active sites can be formed.

From the N_2-sorption measurements, the highest specific surface area corresponds to the ^{57}Fe- N-C (DCDA+ PANI(S))) which is in agreement with the highest kinetic current density obtained for thiscatalyst. According to Hermann et al. [148] and Kicinski et al. [163], the addition of sulfur extends the electrochemical active surface area. This is in good agreement with the present results. The absence of micropores is in contrast to findings from other groups where it is reported that active sites are hosted in micropores [172]. In this case, the ^{57}Fe-N-C (DCDA+ PANI(S)) catalyst which consists of mainly mesopores exhibits similarly high activity as the Fe-N-C (DCDA+Phen+S) catalyst which contains micropores and mesopores. That leads us to the conclusion that active sites can be present in micropores as well as in mesopores. This conclusion is supported by previous findings of Hermann et al. [171], and Kramm et al. [161] a correlation between the mesopore surface area and the kinetic current density was found.

Table 4.3: Summary of surface elemental composition provided by XPS and specific surface area provided by N_2- sorption measurements.

Sample	XPS (wt%)					N_2-sorption (m^2 g^{-1})		
	Fe	**N**	**C**	**O**	**S**	S_{BET}	$S_{Micropore}$	$S_{Mesopore}$
Fe-N-C (MOF+ Phen)	3.0	8.6	75.2	13.2	-	252	-	25
Fe-N-C (DCDA+Phen)	1.9	7.0	80.8	10.3	-	416	218	201
Fe-N-C (DCDA+Phen+S)	6.1	10.5	72.8	9.5	1.2	442	299	165
^{57}Fe-N-C (DCDA+ PANI(S))	9.5	18.4	60.8	8.9	2.3	548-	-	548

The morphology of the catalyst after the second heat-treatment was studied using TEM. From Figure 4.3 it becomes apparent that in all cases the catalysts contain mixed carbon morphologies.

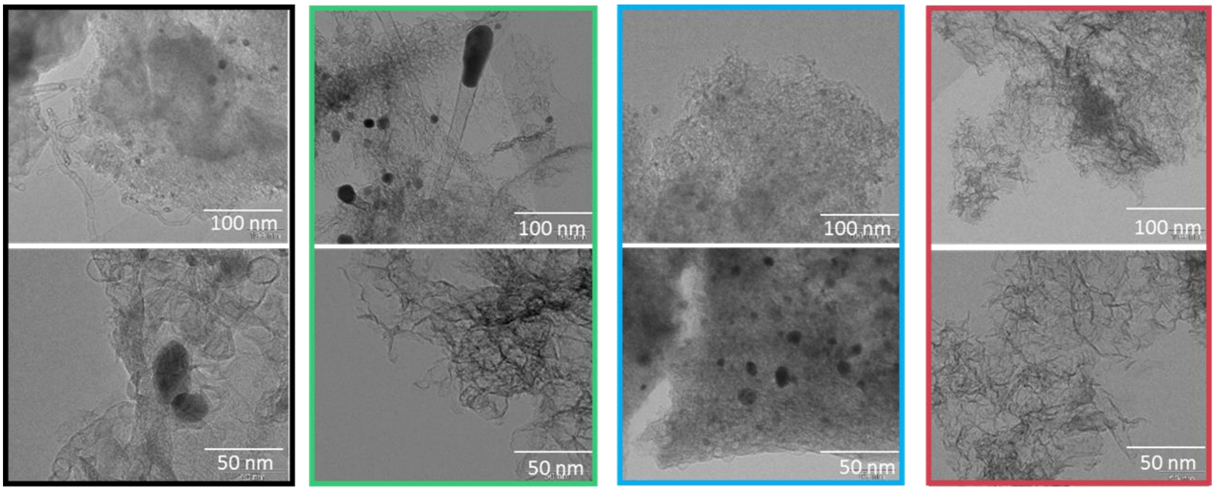

Fe-N-C (MOF+ Phen) Fe-N-C (DCDA+Phen) Fe-N-C (DCDA+Phen+S) ^{57}Fe-N-C(DCDA+ PANI(S))

Figure 4.3: TEM images of the Fe-N-C catalysts (scale bar is 100 nm for the above images and 50 nm for the below).

The Fe-N-C (MOF+ Phen) sample seems to contain iron particles embedded in the carbon as well as some carbon nanotubes/nanofibrous network. In the case of the Fe-N-C (DCDA+Phen) catalyst, a mixed morphology is observed with areas containing iron particles embedded in carbon nanotubes (CNTs) and areas free of iron nanoparticles. This indicates the heterogeneous distribution of iron present in the catalyst. The introduction of sulfur in the case of the Fe-N-C (DCDA+Phen+S) catalyst was not able to remove the excess iron species. Interestingly, in the case of ^{57}Fe-N-C (DCDA+ PANI(S)), a catalyst free or quasi-free of crystallographic iron nanoparticles is observed.
In general, pure catalysts are preferred as the performance can be easier attributed to the catalytic sites present. Moreover tuning the properties of a pure catalyst will be easier than for a catalyst with a complex morphology.

The evaluation of the carbon morphology was further followed with Raman spectroscopy.
Figure 4.4 shows the Raman spectra of all investigated catalysts are shown. These are typical for amorphous carbons. The Raman spectrum is divided in the first-order region (< 2200 cm^{-1}) and in the second-order region (between 2200 and 3500 cm^{-1}) [205] .
Briefly, the G (graphite) band corresponds to an ideal graphitic lattice vibration mode with E_{2g} symmetry [183]. For single graphitic crystals, it is the only peak observed. The D (Defect) band is of

A_{1g} symmetry. The carbon atoms at the edges of the graphene layers are considered the origin of the D band [182,188]. Moreover, additional bands appear at about 1200 cm^{-1} (D_4) due to polyenes and at 1500 cm^{-1} (D_3) due to defective carbon that possibly includes organic molecules, molecular fragments, functional groups [206] or as we recently suggested MeN_4 sites which reflect defects within graphene layers contributing towards the D_3 band intensity [207].

All observed second-order Raman bands are assigned to overtones and combination modes of the first-order bands [185,188].

The second order bands occur at ~ 2700 cm^{-1} (2*D), ~ 2450 cm^{-1} (2*D4) and ~ 2950 cm^{-1} (G + D). Besides the Fe-N-C (DCDA+Phen+S) catalyst which exhibits a small band at around 2700 cm^{-1}, most of the catalysts do not show additional bands in the second order range (or only a broad band).

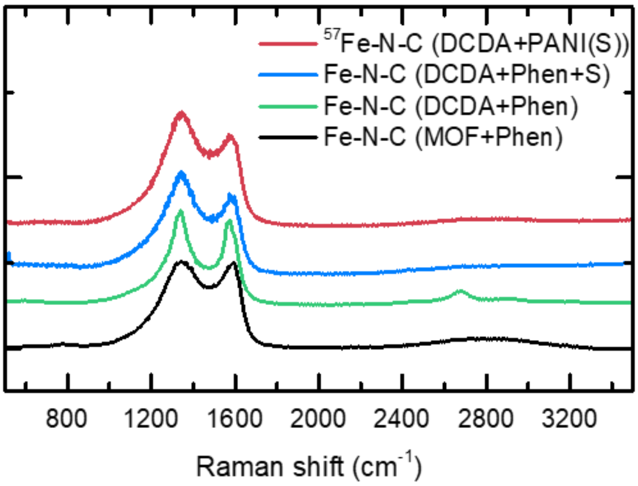

Figure 4.4: Raman spectra of all investigated catalysts.

In Figure 4.5 the first-order Raman spectra of all catalysts deconvolved into four components, are shown. It becomes clear that the Raman spectra of the catalysts differ in the intensity of the main bands. This is expected as the precursors and the preparation route was different, resulting in different carbon morphologies and graphitization levels. The contribution of each band can be better acknowledged by the ratio of the D to G and D_3 to G bands.

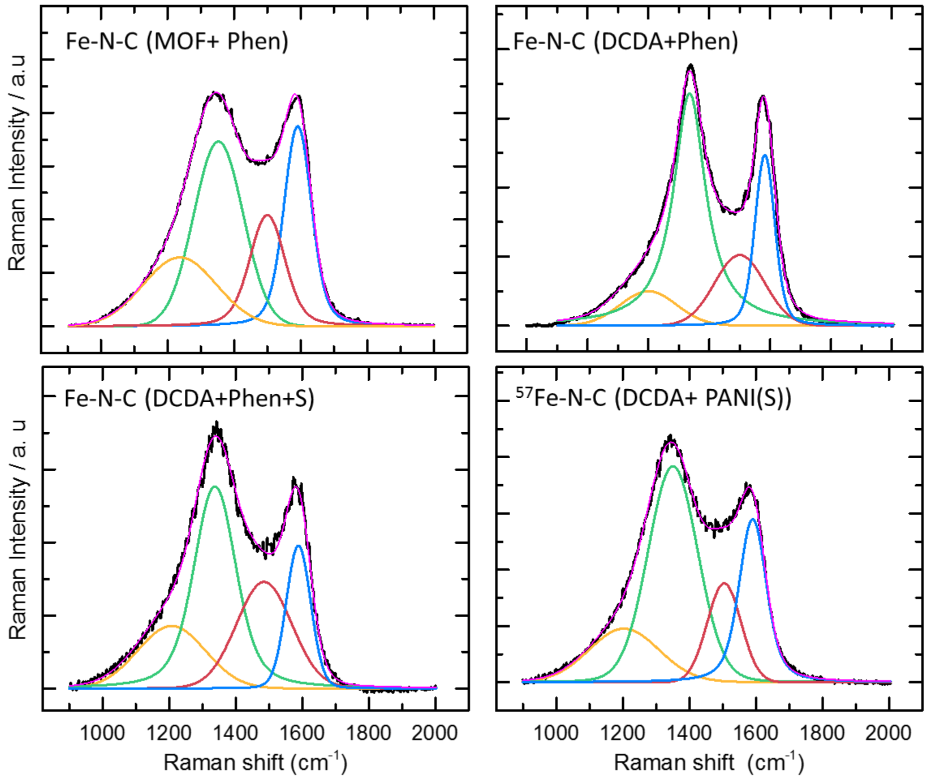

Figure 4.5: First-order Raman spectra of the studied catalysts including the deconvolution.

In this study the D to G ratio and the D_3 to G ratio were calculated by the fitted curves and used to describe the degree of graphitization (I_D/I_G) and the defects in the graphene layer, respectively. The data obtained can be found in Table 4.4. High degree of graphitization (low I_D/I_G) corresponds only to the Fe-N-C (MOF+ Phen) catalyst because it was prepared at significantly higher temperature (950 °C in comparison to 800 °C). Graphitized carbon leads to the reduction of edge defects/dislocations that are favorable for nitrogen doping, thus reducing the potential active sites for adsorption of ORR intermediates. The relatively low degree of graphitization (high I_D/I_G) of Fe-N-C (DCDA+Phen), Fe-N-C (DCDA+Phen+S), and ^{57}Fe-N-C (DCDA+ PANI(S)) is in good agreement with the high amount of surface nitrogen, sulfur (for the S-added catalysts) and iron doping. In fact, Grabke et al. [208] suggested that the addition of sulfur hinders the graphitization process.

Table 4.4: Degree of graphitization and Defect ratio.

Name	D to G ratio I_D/I_G	D_3 to G ratio I_{D3}/I_G
Fe-N-C (MOF+ Phen)	0.92	0.55
Fe-N-C (DCDA+Phen)	1.36	0.41
Fe-N-C (DCDA+Phen+S)	1.41	0.74
^{57}Fe-N-C (DCDA+ PANI(S))	1.46	0.61

Kramm et al. [94] also reported a lower degree of graphitization for an S-added in contrast to an S-free catalyst.

The D_3 to G ratio as we suggested in Martinaiou et al. [207] could be an indicator of the activity if the MeN_4 are recognised as defects in the graphene layers. In this respect, the D_3 to G ratio was plotted vs. the kinetic current density, the half-wave potential, and the Fe to N ratio (Figure 4.6). Regarding the J_{kin} and the $E_{1/2}$ both parameters are indicators of activity, and a good correlation was obtained. No correlation was found for the D to G ratio vs. $E_{1/2}$ and J_{kin}. In addition, a correlation was obtained between the Fe to N ratio and the D_3 to G ratio, indicating that in the graphene layer when more coordination of Fe to N is present, this can be evidenced by the D_3 to G ratio where higher values are obtained. Such correlation was not found for the D to G ratio pointing out the sensitivity of the D_3 band to the metal surrounding.

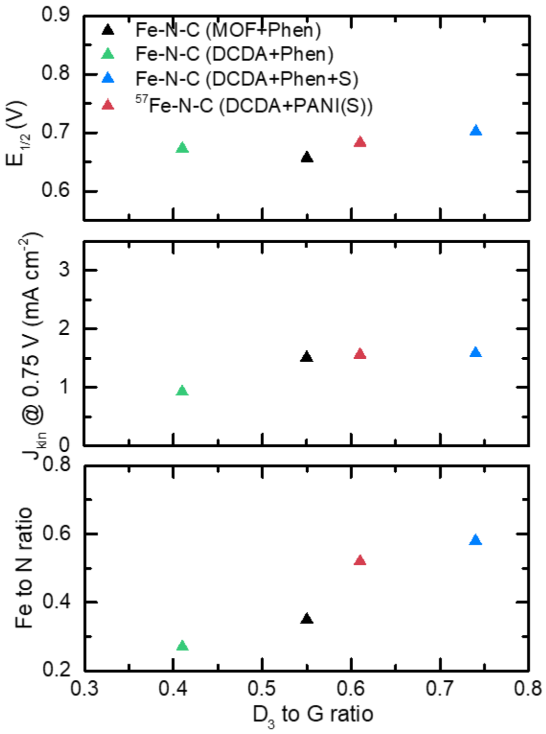

Figure 4.6: D_3 to G band vs. the half wave potential ($E_{1/2}$), the kinetic current density (J_{kin}), and the Fe to N ratio.

In the following, the Mössbauer spectra will be presented.
Mössbauer spectroscopy offers a deeper view of the iron species present in the catalysts. In Figure 4.7, the obtained spectra of the described catalysts are shown. Mössbauer spectroscopy has proven to be most suitable for identification of any Fe containing species because of the unique physical properties, which give access to coulombic interactions, oxidation states, electronegativity, spin states and characterization of bonds as well as magnetic interactions.

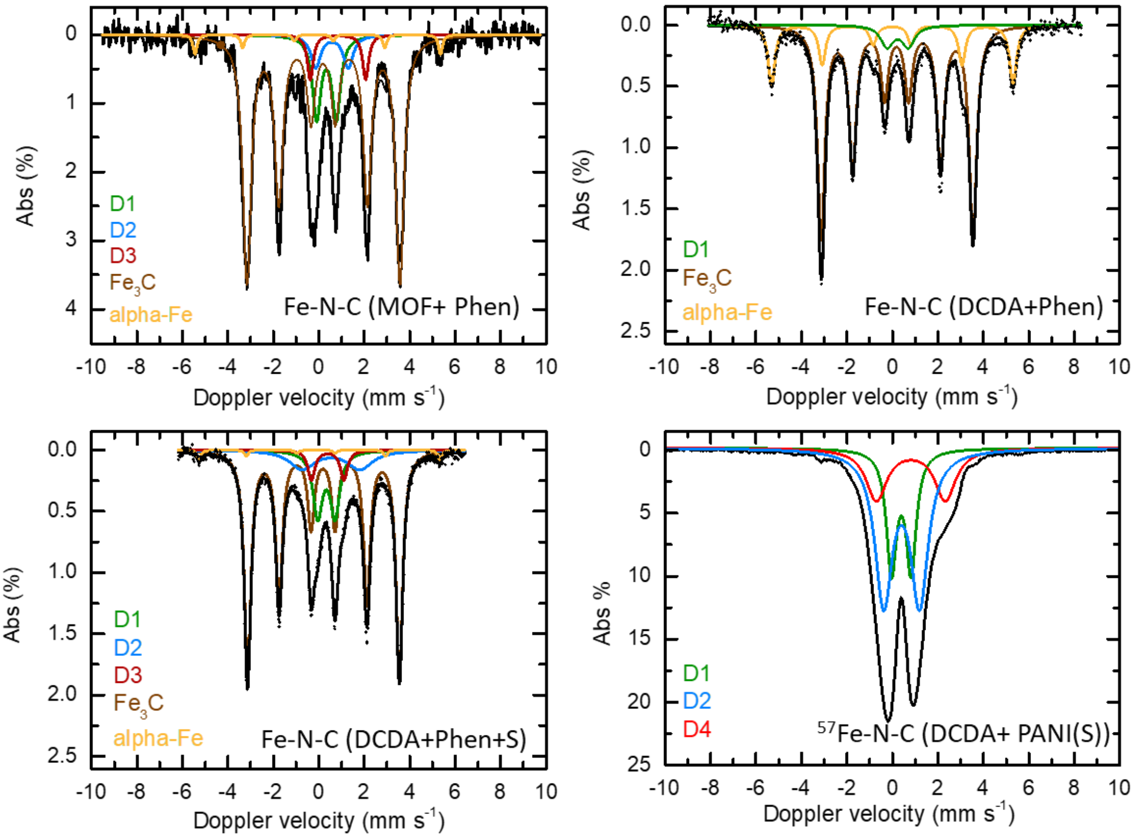

Figure 4.7: Mössbauer spectra with deconvolved species of all studied catalysts.

It becomes apparent from Figure 4.7 that the samples consist of FeN$_4$ sites (2^+, low-spin (LS)) as depicted by D1 [209], Fe-Phthalocyanine-like (2^+, mid-spin (MS)) as depicted by D2 [142,210], N-FeN$_4$-CN (3^+, MS) as depicted by D3 [142] and iron sulfate heptahydrate (FeSO$_4$· 7 H$_2$O) as depicted by D4 [211]. In addition, most samples are dominated by iron encapsulated in carbon species as seen by the presence of the two sextets (Sext1-Fe$_3$C and Sext2- alpha-iron) [142] with the exception of the ^{57}Fe-N-C (DCDA+ PANI(S)) catalyst. These data are in accordance with TEM measurements where the existence of iron particles in the graphene layers was already shown for all catalysts with the exception of ^{57}Fe-N-C (DCDA+ PANI(S)). In principle, the presence of Fe-nanoparticles in the catalysts have been found to be inactive for ORR in acidic media [96,142] and to correlate with poor catalytic performance [212]. It is believed that the formation of these iron nanoparticles originate from the synthesis parameters, such as incomplete acid leaching due to the fact that Fe particles encapsulated by carbon are hardly accessible during the acid leaching [142] or due to poor milling (or mixing) before the acid treatment [212] or even before the first heat treatment which hinders (in some degree) the formation of iron-phenanthroline complex [Fe(phen)$_3$]$^{2+}$.

In the case, of the ^{57}Fe-N-C (DCDA+ PANI(S)) catalyst it is believed that the sulfur addition was successful in restraining the formation of any Fe carbides. From our previous results [213] it was suggested that another parameter besides S to Fe ratio could influence the hindrance of iron carbide formation. Further investigations must follow in order to clarify the extent of the influence of the sulfur and/or the combination with the nitrogen precursor (phenanthroline or polyaniline), and/or the oxygen to sulfur ratio, or the oxygen content.

In the following, the Mössbauer parameters as obtained by the fitting process are shown.

Table 4.5: Summary of the Mössbauer fitted parameters for all catalysts. Lamb-Mössbauer factors for RT provided in Sougrati et al. [214] (f_{LM}(D1) = 0.46, f_{LM}(D2) = 0.52, f_{LM}(D3) ≈ 0.52).

	δ_{iso}	ΔE_Q or ε	whm	H_0	Fe-N-C (MOF + Phen)		Fe-N-C (DCDA+ Phen)		Fe-N-C (DCDA+ Phen + S)		^{57}Fe-N-C (DCDA+ PANI (S))		Assignment
	(mm s^{-1})			(T)	A (%)	Fe (wt%)	A (%)	Fe (wt%)	A (%)	Fe (wt%)	A (%)	Fe (wt%)	
D1	0.32	0.86	0.55	-	12.7	0.51	6.4	0.12	14.1	0.86	24.7	2.35	FeN_4 (2+,LS)
D2	0.56	2.49	0.65	-	4.9	0.17	-	-	10.7	0.76	53.5	5.08	FePc-like (2+,MS)
D3	0.45	1.48	0.60	-	5.9	0.24	-	-	4.9	0.30	-	-	N-FeN_4-CN (3+,MS)
D4	0.87	3.23	1.1	-	-	-	-	-	-	-	21.8	2.07	$FeSO_4 \cdot 7H_2O$
Sext1	0.19	0.03	0.36	32.8	73.6	2.02	18.9	0.35	1.7	0.10	-	-	Alpha-Fe
Sext2	-0.02	0.05	0.26	20.7	2.9	0.07	74.8	1.38	68.7	4.20	-	-	Fe_3C

It can be seen by Table 4.5, that the Fe-N-C (MOF+ Phen) catalyst is dominated by alpha-iron (Sext1), whereas the iron content in the FeN_4 sites is smaller. In the case of Fe-N-C (DCDA+Phen) catalyst, the iron content which corresponds to the active FeN_4 sites, exists exclusively in the form of $Fe^{II}N_4$(LS) sites, as iron species attributed to other doublets where not detected. Interestingly, the addition of sulfur (Fe-N-C (DCDA+Phen+S)) to the latter catalyst led to the formation of additional FeN_4 sites as confirmed by the additional doublets. Although, the introduction of sulfur in the precursor did not hinder the iron carbide formation, it promoted the presence of additional active sites. The ^{57}Fe-N-C (DCDA+ PANI(S)) catalyst was successfully prepared resulting in a pure-structured catalyst.

Although, activity has been attributed to iron carbides (due to the absence of D1 species from Mössbauer spectroscopy) by other groups (chapter 2.2.2) in this study all samples contain the D1 doublet but not the Sext2 and/or Sext1. Therefore, exclusive ORR activity attributed to iron carbides can be excluded.

The catalysts with the highest iron content in FeN_4 sites are the S-added ones. Kramm et al. [60,91,161] assigned the D1 doublet as ORR active site. Considering only the $Fe^{II}N_4$ LS) sites (doublet D1) it can be seen that the S-added catalyst contain the highest content of iron in these sites. The FeN_4 as depicted by D1 increases in the order of Fe-N-C (DCDA+Phen) < Fe- N- C (MOF+ Phen) < Fe-N-C (DCDA+Phen+S)) < ^{57}Fe-N-C (DCDA+ PANI(S) which is in total agreement with the activity behaviour of the catalysts.

However, in the case of the Fe-N-C (DCDA+Phen+S) catalyst, the addition of sulfur did not prevent the iron carbide formation. The question here arises on what is the exact role of sulfur and how does the addition of sulfur really affects the structure and the activity of the catalysts. From the comparison of Fe to S ratio of the Fe-N-C (DCDA+Phen+S) and ^{57}Fe-N-C (DCDA+ PANI(S)) catalyst the obtained values are 5.1 and 4.1, respectively. These values seem close and are reflected in the activity behaviour of both catalysts as shown in Figure 4.6.

In this case, the oxygen to sulfur ratio or nitrogen to sulfur ratio could also be considered. The N to S ratio for the Fe-N-C (DCDA+Phen+S) catalyst is 8.7 and for the ^{57}Fe-N-C (DCDA+ PANI(S)) is 8. These values are very close and this leads us to the assumption that the oxygen to sulfur ratio must be the one that accounts for the difference reflected on the structure of the catalysts but not so much on the activity. The O to S ratio for the Fe-N-C (DCDA+Phen+S) catalyst is 7.9 whereas for the ^{57}Fe-N-C (DCDA+ PANI(S)) is 3.8. It is obvious that the O to S ratio for the first catalyst is almost the double. This could indicate that there is a relation between formed sulfur oxides and the resulting structure of the catalysts. This will need further evaluation before certain conclusions can be drawn

Further investigation on durability was done for the S-added catalysts, namely Fe-N-C (DCDA+Phen+S) and ^{57}Fe-N-C (DCDA+ PANI(S)), as these were found to be the best performing catalysts.

Durability was evaluated with the Load cycle protocol (as discussed in chapter 2.2.3); briefly, this protocol is applied as it represents the running conditions of a fuel cell in automotive applications. The protocol includes a 3 sec hold at 0.6 V and a 3sec hold at 1.0 V, thus a "cycle" accounts for 6 sec. In this durability evaluation, both catalysts were tested in 0.1M H_2SO_4 acidic media for 5000 cycles (10 hours).

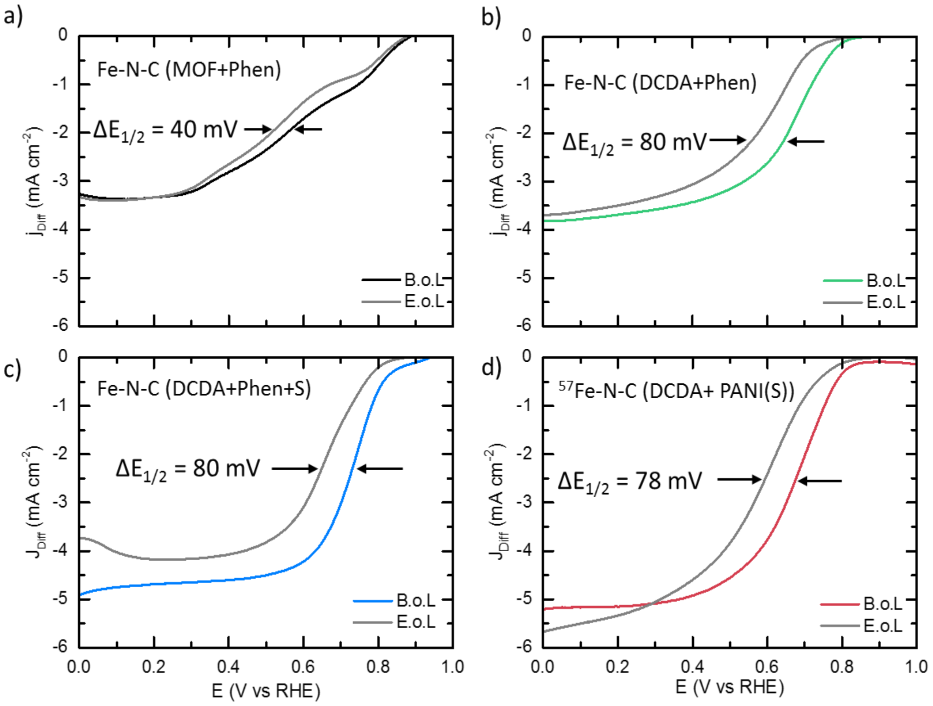

Figure 4.8: Load cycle protocol: RDE curves at BoL and EoL (+ 5000 LC cycles) in O_2- saturated 0.1 M H_2SO_4 electrolyte for the Fe-N-C (DCDA+Phen+S) and ^{57}Fe-N-C (DCDA+ PANI(S)) catalysts with 1500 rpm and 10 mV s^{-1}.

In Figure 4.8 the RDE curves of Beginning of Life (B.o.L) and End of Life (E.o.L) of each catalyst are shown.

The degradation of the catalysts was measured by the loss in the half-wave potential ($\Delta E_{1/2}$). From Figure 4.8 it becomes apparent that the catalysts show the same loss in durability. In the case of Fe- N- C (DCDA+Phen+S) the loss in $E_{1/2}$ is 80 mV and in the case of ^{57}Fe-N-C (DCDA+ PANI(S)) is 78 mV. These values are very similar indicating that even though the structure of the catalysts is different (Mössbauer results) the performance is similar. This confirms the view that iron carbides do not contribute to the activity or durability of the catalysts (case of Fe-N- C (DCDA+Phen+S)). The origin of instability in this potential region has been attributed mainly to the demetalation of the catalysts [136,144,151].

Fe ions dissolving in the electrolyte solution at low electrochemical potential leads to the deactivation of the active centres (FeN_4) but also could react with even minute amounts of H_2O_2 and can oxidize the active moieties like the N heteroatoms, which can be responsible for catalyst deactivation and decomposition.

In order to investigate further the durability of these catalysts, the Start/Stop Cycle (SSC) protocol was employed. This protocol suggests cycling in a high potential region from 1.0 to 1.5 V. This durability protocol was also applied with harsh conditions in O_2-saturated 0.1 M H_2SO_4 electrolyte. The durability protocol was stopped after 1000 cycles (as the degradation of the catalysts was already obvious). In Figure 4.9 the RDE curves of Beginning of Life (B.o.L.) and End of Life (E.o.L.) of each catalyst are shown. In this potential region, the primary origin of instability is the carbon oxidation. Interestingly, the Fe-N-C (MOF+Phen) and the Fe-N-C (DCDA+Phen±S) exhibit lower durability loss in terms of half-wave potential. The loss was found to be 40 and about 50mV, respectively, whereas for the ^{57}Fe- N- C (DCDA+ PANI(S)) was found 80 mV. In this case, the difference in performance is larger in comparison to the Load cycle durability test.

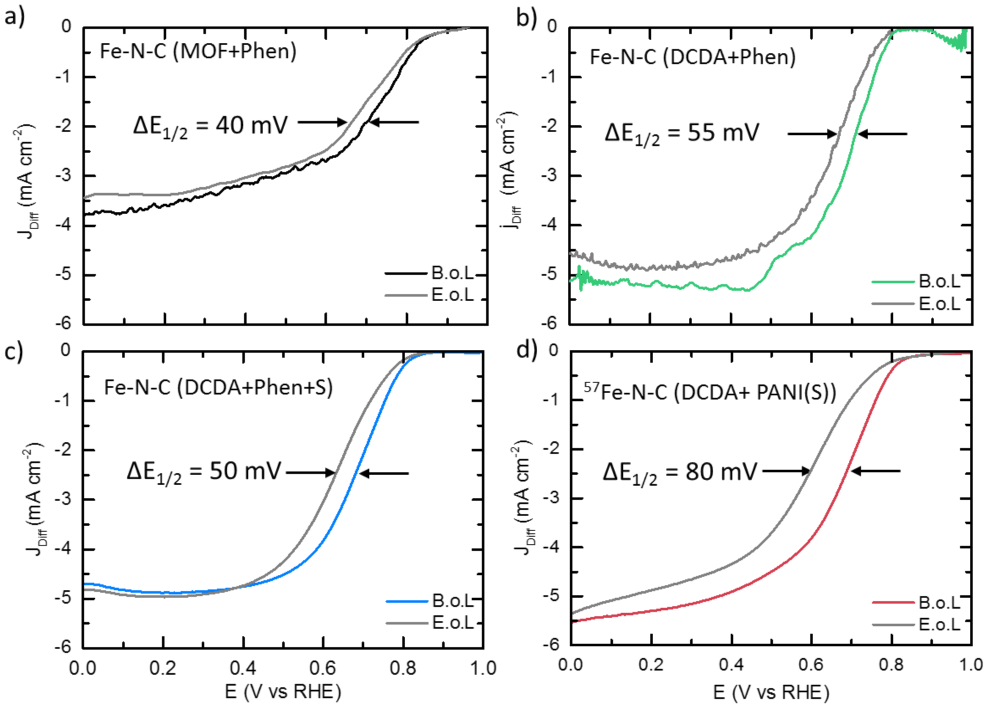

Figure 4.9: Start/Stop Cycle (SSC) protocol: RDE curves Beginning of Life (BoL) and End of Life (EoL) (1000 cycles) of Fe-N-C (DCDA+Phen+S) and ^{57}Fe-N-C (DCDA + PANI(S)) catalysts in 0.1 M H_2SO_4 O_2-saturated electrolyte, with 1500 rpm and 10 mV s^{-1}.

For the Fe-N-C (MOF+ Phen) catalyst, one would expect such a behaviour, as this catalyst was synthesized with prolonged heat treatment (in total 4 hours). Reduced initial ORR activity after extended heat treatment can be explained by the loss of active species such as N species and the FeN_4 sites. The loss of these sites results in a more ordered carbon matrix (low I_D/I_G). The higher graphitized structure is more stable and not so prone to be destroyed by carbon corrosion. Hence, a better durability performance during the SSC conditions is obtained.

How to explain the large difference in the durability behaviour between the Phen-based samples and the PANI-based sample? Is the N-precursor responsible for this?

In our previous work [207] we found from correlations between electrochemical evaluation and Raman spectroscopy that in this potential region, the carbon oxidation is related to the disintegration of active MeN_4 sites that might be initiated either by: the oxidation of the surrounding graphene sheets and by a displacement of the metal out of the N_4 plane, the release was evidenced by a decrease in the D_3 band.

In addition, FeN_4 sites located near the surface but covered by graphene layers (or even hindered by the presence of Fe_3C) of the catalyst could be exposed after the cycling in such harsh conditions, contributing in the remaining activity of the catalyst. This would justify the difference in durability loss, as the main structure difference of these catalysts is the presence or absence of iron carbides [108].

Another possible reason for the higher decay of the ^{57}Fe-N-C (DCDA+ PANI(S)) sample in this potential region, could be that, heteroatom doping (as shown by XPS this catalyst contains higher nitrogen and sulfur atoms) in the graphene layer (which is beneficial for activity) can cause a more pronounced degradation due to removal of heteroatoms thus creating "holes" in the graphene layer leading to increased corrosion rates and FeN_4 disintegration.

Furthermore, according to Grabke et al. [208] the addition of sulfur hinders the iron carbide formation and the graphitization process. This is in agreement with the results obtained by Raman spectroscopy, where the I_D/I_G ratio is used as graphitization indicator.

The higher I_D/I_G ratio of the ^{57}Fe-N-C (DCDA+ PANI(S)) catalyst (1.46) in comparison to the Fe-N-C (DCDA+Phen+S) catalyst (1.41) indicates a correlation between the graphitization of carbon and the durability of the catalysts. It is well known that more graphitized (low I_D/I_G) Me-N-C catalysts are more stable during durability tests due to higher resistance to corrosion [193].

To conclude, the temperature and the heat–treatment duration strongly affect the structure and thus the performance of the catalysts. In the following chapter a summary of the most important conclusions related to each project is given.

5

Summary and Outlook

In the present thesis, the activity, the durability and the degradation mechanisms of Me-N-C (chapter 4.1) and especially of Fe-N-C (chapters 4.2 to 4.4) catalysts under different conditions were evaluated. In order to enable a more general statement, the four different preparation approaches were compared for the same conditions in chapter 4.5. In the following, the main conclusions for each project will be summarized.

The motivation regarding the first project was to get a better understanding on the effect of the metal centre on the durability of Me-N-C catalysts. While the impact of the metal species on the activity has been reported largely, our results showed that a Fe-N-C catalyst was the most stable when investigated by a durability protocol following the Start-up and Shut-down conditions. In addition, a decrease of the D_3 band in the Raman spectra was related with the activity loss [207].

In the following, the influence of sulfur on the structure and thus on activity and durability was studied, by adapting a novel synthesis route. While the maximum in activity was similar in comparison to previous studies, our S-added most active catalyst still contained iron carbides, in contrast to previous reports [213]. Furthermore, the investigation of the addition of an Ionic Liquid to a S-free and a S-added catalyst under a Load Cycle durability protocol for application in alkaline media showed that this modification improved the activity and the stability of the S-free catalyst, however it did not further improve the performance of the S-added catalyst [215].

Subsequently, a new synthesis approach lead to an active Fe-N-C catalyst with sulfur on the precursor free or quasi-free of iron carbides. This catalyst was evaluated regarding the stability on a Direct Methanol Fuel Cell and the resulting data point out that the greatest performance loss occurs in the first two hours followed by a more gradual loss (chapter 4.4).

As mentioned above, to enable a systematic comparison of the different preparation approaches in chapter 4.5 all four catalysts were compared under identical conditions. The activity loss under a Load Cycle durability protocol in this potential region is attributed to the demetallation of the catalyst. When applying a Start-up and Shut-down protocol carbon oxidation of the surrounding graphene sheets and the release of the metal out of the MeN_4 are at the origin of the catalyst's instability. In both cases, the pyrolysis conditions affect the performance of the catalysts.

To conclude, further investigations are required in order to obtain pure-structured catalysts with high activity and stability. Post mortem spectroscopic analysis will enable accurate conclusions and optimize the structure to property correlations. The extent of carbon oxidation to CO and CO_2 could be investigated by in-situ differential electrochemical mass spectrometry (DEMS) in order to quantify the loss of carbon surface. Further analysis of the used electrolyte with inductively coupled plasma mass spectrometry (ICP-MS) would give information on the iron amount, which is leached out of the catalysts. Especially in the case of a pure catalyst, (only FeN_4 sites present), the assignments and the conclusions will be more accurate

It is necessary to point out that degradation mechanisms in aqueous electrochemical cell vs. MEA studies are intrinsically different. MEA in situ characterization techniques need to be developed and implemented with all fuel cell performance studies in order to establish degradation mechanisms and propose mitigation strategies.

Large-scale commercialization of fuel cells is currently limited by the challenges in the design of efficient catalysts for Oxygen Reduction Reaction, which directly affects the cost of the devices. The main challenges are related to the activity of the catalysts, where even Pt-based catalysts exhibit significant overpotentials, the stability due to the fact that catalysts in the cathode (where ORR occurs) are exposed to harsh conditions that are harmful to the overall long term-performance of the catalysts and also to the abundance of the catalysts currently used. The latter is because the most active catalysts for fuel cell application are noble metal-based catalysts, which are in general scarce and expensive. The replacement of noble based catalysts is a research topic, which has drawn significant attention the past years. The activity progress of non-precious metal catalysts, especially earth-abundant Fe-based catalysts, has brought them to a level where they are becoming industrially relevant. Unfortunately, the poor stability of these catalysts hinders them from being considered as a viable alternative to noble metal catalysts for fuel cell application. Due to the variety of synthetic approaches and designs in literature, the difficulty of understanding and identifying the complex fundamental degradation mechanisms of these catalysts rises. To be able to develop mitigation strategies and overcome the durability problems it is essential to unravel the real structure and composition of the catalysts and to design durability tests, which can lead to accurate conclusions. In order to do so, highly active non-precious metal catalysts free of metal crystalline phases are necessary for a precise identification of active sites towards ORR. The number of active sites in a catalyst can be determined by poisoning experiments. Especially when performed both at beginning and end of life can aid in solving the challenge of determining active site density and provide information about vulnerable active site structures lost during the catalyst operation. A further development and implementation of in-situ methods regarding their structure, composition and changes in electronic structure at all stages will be of particular importance. The design of in situ experiments can be demanding, however with the utilization of techniques sensitive to the surface area or in the bulk, a breakthrough development can be achieved. Electrochemical cells coupled with X-Ray Photoelectron Spectroscopy, and/or Mössbauer spectroscopy would give important information and therefore promising strategies could eventually develop.

In conclusion, if the required durability can be reached, NPMCs will replace noble materials and lead to the widespread commercialization of fuel cell technology.

References

[1] B. D. James, J. A. Kalinoski, U.S. Department of Energy-Hydrogen Program, (2008) Annual Progress Report.

[2] E. Proietti, F. Jaouen, M. Lefèvre, N. Larouche, J. Tian, J. Herranz, J.-P. Dodelet, Nature communications 2 (2011) 416.

[3] J. Shui, C. Chen, L. Grabstanowicz, D. Zhao, D.-J. Liu, Proceedings of the National Academy of Sciences of the United States of America 112 (2015) 10629–10634.

[4] M. Chokai, T. Daidou, Y. Nabae, ECS Transactions 64 (2014) 261–270.

[5] X. Wang, H. Zhang, H. Lin, S. Gupta, C. Wang, Z. Tao, H. Fu, T. Wang, J. Zheng, G. Wu, X. Li, Nano Energy 25 (2016) 110–119.

[6] Key World Energy Statistics 2016, 10.1787/key_energ_stat-2016-en, IEA, 2016.

[7] Intergovernmental Panel on Climate Change IPCC.

[8] European Commission,

https://ec.europa.eu/clima/policies/international/negotiations/paris_en.

[9] J.O. Bockris, Science (New York, N.Y.) 176 (1972) 1323.

[10] I. Katsounaros , M.T.M Koper, Electrocatalysis for the Hydrogen Economy. In: Uosaki K. (eds) Electrochemical Science for a Sustainable Society. Springer, Cham. (2017).

[11] H. Watanabe, ECS Transactions, Cancun, Mexico, October 29-November 3, (2006).

[12] B.G. Pollet, I. Staffell, J.L. Shang, Electrochimica Acta 84 (2012) 235–249.

[13] S.J. Hamrock, A.M. Herring, in: R.A. Meyers (Ed.), Encyclopedia of Sustainability Science and Technology, Springer New York, (2012) 8328–8347.

[14] F. Barbir, PEM fuel cells: Theory and practice, Elsevier Academic, Amsterdam, London, (2005).

[15] W.R. Grove, The London, Edinburgh, and Dublin Philosophical Magazine and Journal of Science 14 (2009) 127–130.

[16] L. Carrette, K.A. Friedrich, U. Stimming, Fuel Cells 1 (2001) 5–39.

[17] A.J. Appleby, F.R. Foulkes, Fuel cell handbook, Van Nostrand Reinhold, New York, (1989).

[18] J. Herranz Salañer, PhD Thesis (2011) Université du Québec.

[19] M.K. Debe, Nature 486 (2012) 43–51.

[20] U.A. Paulus, A. Wokaun, G.G. Scherer, T.J. Schmidt, V. Stamenkovic, V. Radmilovic, N.M. Markovic, P.N. Ross, The journal of physical chemistry. B 106 (2002) 4181–4191.

[21] J. Garche and L. Jörissen, The Electrochemical Society Interface (2015) 39-43.

[22] N.V. Long, Y. Yang, C. Minh Thi, N. van Minh, Y. Cao, M. Nogami, Nano Energy 2 (2013) 636–676.

[23] R. Dillon, S. Srinivasan, A.S. Aricò, V. Antonucci, Journal of Power Sources 127 (2004) 112–126.

[24] B.D. McNicol, D.A.J. Rand, K.R. Williams, Journal of Power Sources 83 (1999) 15–31.

[25] M. Watanabe, S. Motoo, Journal of Electroanalytical Chemistry and Interfacial Electrochemistry 60 (1975) 267–273.

[26] A.H.A. Monteverde Videla, D. Sebastián, N.S. Vasile, L. Osmieri, A.S. Aricò, V. Baglio, S. Specchia, International Journal of Hydrogen Energy 41 (2016) 22605–22618.

[27] D. Sebastián, A. Serov, K. Artyushkova, P. Atanassov, A.S. Aricò, V. Baglio, Journal of Power Sources 319 (2016) 235–246.

[28] D. Sebastián, A. Serov, K. Artyushkova, J. Gordon, P. Atanassov, A.S. Aricò, V. Baglio, ChemSusChem 9 (2016) 1986–1995.

[29] S. Kakaç, A. Pramuanjaroenkij, L.L. Vasil′ev, Mini-micro fuel cells: Fundamentals and applications / edited by S. Kakaç, A. Pramuanjaroenkij, L. Vasiliev, Springer, Dordrecht, London, 2008.

[30] G. McLean, International Journal of Hydrogen Energy 27 (2002) 507–526.

[31] L. Wang, W. Jia, X. Liu, J. Li, M.M. Titirici, Journal of Energy Chemistry 25 (2016) 566–570.

[32] G.A. Ferrero, A.B. Fuertes, M. Sevilla, M.-M. Titirici, Carbon 106 (2016) 179–187.

[33] R.A. Meyers (Ed.), Encyclopedia of Sustainability Science and Technology, Springer New York, New York, NY, 2012.

[34] S. Gottesfeld, D.R. Dekel, M. Page, C. Bae, Y. Yan, P. Zelenay, Y.S. Kim, Journal of Power Sources 375 (2018) 170–184.

[35] R. O'Hayre, S.-W. Cha, W. Colella, F.B. Prinz (Eds.), Fuel Cell Fundamentals, John Wiley & Sons, Inc, Hoboken, NJ, USA, 2016.

[36] V. Ramani, H. Russel-Kunz, J.M. Fenton, The Electrochemical Society Interface 13 (Fall 2004), 17-19, 45.

[37] B. Bladergroen, H. Su, S. Pasupathi, V. Linkov, in: J. Kleperis (Ed.), Electrolysis, InTech, 2012.

[38] A. Steinbach, 2014 Annual Merit Review

https://www.hydrogen.energy.gov/pdfs/review14/fc104_steinbach_2014_o.pdf.

[39] F. Jaouen, E. Proietti, M. Lefèvre, R. Chenitz, J.-P. Dodelet, G. Wu, H.T. Chung, C.M. Johnston, P. Zelenay, Energy Environ. Sci. 4 (2011) 114–130.

[40] J.H. Zagal, F. Bedioui, J.-P. Dodelet (Eds.), N4-Macrocyclic Metal Complexes, Springer New York, New York, NY, 2006.

[41] A.L. Wijnoltz, Oxygen reduction catalysed by carbon supported metal chelates, Technische Universiteit Eindhoven, 1995.

[42] J.A.R. van Veen, H.A. Colijn, Berichte der Bunsengesellschaft für physikalische Chemie 85 (1981) 700–704.

[43] F. Calle-Vallejo, J.I. Martínez, J. Rossmeisl, Physical chemistry chemical physics PCCP 13 (2011) 15639–15643.

[44] R. Boulatov, in: J.H. Zagal, F. Bedioui, J.-P. Dodelet (Eds.), N4-Macrocyclic Metal Complexes, Springer New York, New York, NY, 2006, pp. 1–40.

[45] R. Jasinski, J. Electrochem. Soc. 112 (1965) 526.

[46] R. Jasinski, Nature 201 (1964) 1212–1213.

[47] H. Jahnke, M. Schönborn, G. Zimmermann, in: F.P. Schäfer, H. Gerischer, F. Willig, H. Meier, H. Jahnke, M. Schönborn, G. Zimmermann (Eds.), Physical and chemical applications of dyestuffs, Springer, Berlin, 1976, pp. 133–181.

[48] V.S. Bagotzky, M.R. Tarasevich, K.A. Radyushkina, O.A. Levina, S.I. Andrusyova, Journal of Power Sources 2 (1978) 233–240.

[49] S. Gupta, D. Tryk, I. Bae, W. Aldred, E. Yeager, J Appl Electrochem 19 (1989) 19–27.

[50] L.T. Weng, P. Bertrand, G. Lalande, D. Guay, J.P. Dodelet, Applied Surface Science 84 (1995) 9–21.

[51] J.H. Zagal, S. Griveau, J.F. Silva, T. Nyokong, F. Bedioui, Coordination Chemistry Reviews 254 (2010) 2755–2791.

[52] X. Yuan, L. Li, Z. Ma, X. Yu, X. Wen, Z.-F. Ma, L. Zhang, D.P. Wilkinson, J. Zhang, Scientific reports 6 (2016) 20005.

[53] V. Trapp, P. Christensen, A. Hamnett, Faraday Trans. 92 (1996) 4311.

[54] R.J. Toh, Z. Sofer, M. Pumera, Chemphyschem a European journal of chemical physics and physical chemistry 16 (2015) 3527–3531.

[55] M. Chen, J. Liu, W. Zhou, J. Lin, Z. Shen, Scientific reports 5 (2015) 10389.

[56] H. Yin, C. Zhang, F. Liu, Y. Hou, Adv. Funct. Mater. 24 (2014) 2930–2937.

[57] M. Lefèvre, E. Proietti, F. Jaouen, J.-P. Dodelet, Science (New York, N.Y.) 324 (2009) 71–74.

[58] G. Wu, K.L. More, C.M. Johnston, P. Zelenay, Science (New York, N.Y.) 332 (2011) 443–447.

[59] H. Meng, N. Larouche, M. Lefèvre, F. Jaouen, B. Stansfield, J.-P. Dodelet, Electrochimica Acta 55 (2010) 6450–6461.

[60] U.I. Kramm, I. Abs-Wurmbach, I. Herrmann-Geppert, J. Radnik, S. Fiechter, P. Bogdanoff, J. Electrochem. Soc. 158 (2011) B69.

[61] M. Park, J. Lee, K. Hembram, K.-R. Lee, S. Han, C. Yoon, S.-W. Nam, J. Kim, Catalysts 6 (2016) 86.

[62] J.-L. Shui, N.K. Karan, M. Balasubramanian, S.-Y. Li, D.-J. Liu, Journal of the American Chemical Society 134 (2012) 16654–16661.

[63] F. Jaouen, V. Goellner, M. Lefèvre, J. Herranz, E. Proietti, J.P. Dodelet, Electrochimica Acta 87 (2013) 619–628.

[64] K. Wiesener, Electrochimica Acta 31 (1986) 1073–1078.

[65] S. Maldonado, K.J. Stevenson, The journal of physical chemistry. B 109 (2005) 4707–4716.

[66] G. Liu, X. Li, J.-W. Lee, B.N. Popov, Catal. Sci. Technol. 1 (2011) 207.

[67] D. Singh, J. King, U. S. Ozkan, Modified Carbon Materials for O2 Reduction Reaction Electrocatalysts in Acid PEM Fuel Cells, Wiley-VCH, Weinheim, 2014.

[68] K. Mamtani, U.S. Ozkan, Catal Lett 145 (2015) 436–450.

[69] N.P. Subramanian, X. Li, V. Nallathambi, S.P. Kumaraguru, H. Colon-Mercado, G. Wu, J.-W. Lee, B.N. Popov, Journal of Power Sources 188 (2009) 38–44.

[70] F. Jaouen, J.-P. Dodelet, Electrochimica Acta 52 (2007) 5975–5984.

[71] V. Nallathambi, J.-W. Lee, S.P. Kumaraguru, G. Wu, B.N. Popov, Journal of Power Sources 183 (2008) 34–42.

[72] Z. Wen, S. Ci, F. Zhang, X. Feng, S. Cui, S. Mao, S. Luo, Z. He, J. Chen, Advanced materials (Deerfield Beach, Fla.) 24 (2012) 1399–1404.

[73] J. Wei, Y. Liang, Y. Hu, B. Kong, G.P. Simon, J. Zhang, S.P. Jiang, H. Wang, Angewandte Chemie (International ed. in English) 55 (2016) 1355–1359.

[74] D. Deng, L. Yu, X. Chen, G. Wang, L. Jin, X. Pan, J. Deng, G. Sun, X. Bao, Angewandte Chemie (International ed. in English) 52 (2013) 371–375.

[75] W.-J. Jiang, L. Gu, L. Li, Y. Zhang, X. Zhang, L.-J. Zhang, J.-Q. Wang, J.-S. Hu, Z. Wei, L.-J. Wan, Journal of the American Chemical Society 138 (2016) 3570–3578.

[76] Y. Hu, J.O. Jensen, W. Zhang, L.N. Cleemann, W. Xing, N.J. Bjerrum, Q. Li, Angewandte Chemie (International ed. in English) 53 (2014) 3675–3679.

[77] Y. Hu, J.O. Jensen, W. Zhang, S. Martin, R. Chenitz, C. Pan, W. Xing, N.J. Bjerrum, Q. Li, J. Mater. Chem. A 3 (2015) 1752–1760.

[78] K. Strickland, E. Miner, Q. Jia, U. Tylus, N. Ramaswamy, W. Liang, M.-T. Sougrati, F. Jaouen, S. Mukerjee, Nature communications 6 (2015) 7343.

[79] V. Goellner, C. Baldizzone, A. Schuppert, M.T. Sougrati, K. Mayrhofer, F. Jaouen, Physical chemistry chemical physics PCCP 16 (2014) 18454–18462.

[80] J.A.R. van Veen, J.F. van Baar, K.J. Kroese, J. Chem. Soc., Faraday Trans. 1 77 (1981) 2827.

[81] A.L. Bouwkamp-Wijnoltz, W. Visscher, J.A.R. van Veen, E. Boellaard, A.M. van der Kraan, S.C. Tang, The journal of physical chemistry. B 106 (2002) 12993–13001.

[82] A. Biloul, F. Coowar, O. Contamin, G. Scarbeck, M. Savy, D. van den Ham, J. Riga, J.J. Verbist, Journal of Electroanalytical Chemistry and Interfacial Electrochemistry 289 (1990) 189–201.

[83] A. Biloul, F. Coowar, O. Contamin, G. Scarbeck, M. Savy, D. van den Ham, J. Riga, J.J. Verbist, Journal of Electroanalytical Chemistry 328 (1992) 219–232.

[84] A. Biloul, F. Coowar, O. Contamin, G. Scarbeck, M. Savy, D. van den Ham, J. Riga, J.J. Verbist, Journal of Electroanalytical Chemistry 350 (1993) 189–204.

[85] S.L. Gojković, J. Electrochem. Soc. 145 (1998) 3493.

[86] S.L. Gojković, S. Gupta, R.F. Savinell, Electrochimica Acta 45 (1999) 889–897.

[87] G. Faubert, R. Côté, J.P. Dodelet, M. Lefèvre, P. Bertrand, Electrochimica Acta 44 (1999) 2589–2603.

[88] M. Lefèvre, J.P. Dodelet, P. Bertrand, The journal of physical chemistry. B 106 (2002) 8705–8713.

[89] F. Jaouen, S. Marcotte, J.-P. Dodelet, G. Lindbergh, The journal of physical chemistry. B 107 (2003) 1376–1386.

[90] F. Charreteur, S. Ruggeri, F. Jaouen, J.P. Dodelet, Electrochimica Acta 53 (2008) 6881–6889.

[91] U.I. Koslowski, I. Abs-Wurmbach, S. Fiechter, P. Bogdanoff, J. Phys. Chem. C 112 (2008) 15356–15366.

[92] U.I. Kramm, J. Herranz, N. Larouche, T.M. Arruda, M. Lefèvre, F. Jaouen, P. Bogdanoff, S. Fiechter, I. Abs-Wurmbach, S. Mukerjee, J.-P. Dodelet, Physical chemistry chemical physics PCCP 14 (2012) 11673–11688.

[93] U.I. Kramm, PhD Thesis (2009) Technische Universität Berlin.

[94] U.I. Kramm, I. Herrmann-Geppert, S. Fiechter, G. Zehl, I. Zizak, I. Dorbandt, D. Schmeißer, P. Bogdanoff, J. Mater. Chem. A 2 (2014) 2663–2670.

[95] M. Ferrandon, A.J. Kropf, D.J. Myers, K. Artyushkova, U. Kramm, P. Bogdanoff, G. Wu, C.M. Johnston, P. Zelenay, J. Phys. Chem. C 116 (2012) 16001–16013.

[96] C.H. Choi, W.S. Choi, O. Kasian, A.K. Mechler, M.T. Sougrati, S. Brüller, K. Strickland, Q. Jia, S. Mukerjee, K.J.J. Mayrhofer, F. Jaouen, Angewandte Chemie (International ed. in English) 56 (2017) 8809–8812.

[97] A. Zitolo, V. Goellner, V. Armel, M.-T. Sougrati, T. Mineva, L. Stievano, E. Fonda, F. Jaouen, Nature materials 14 (2015) 937–942.

[98] U.I. Kramm, I. Herrmann-Geppert, J. Behrends, K. Lips, S. Fiechter, P. Bogdanoff, Journal of the American Chemical Society 138 (2016) 635–640.

[99] F. Charreteur, F. Jaouen, S. Ruggeri, J.-P. Dodelet, Electrochimica Acta 53 (2008) 2925–2938.

[100] R. Bashyam, P. Zelenay, Nature 443 (2006) 63–66.

[101] G. Wu, Z. Chen, K. Artyushkova, F.H. Garzon, P. Zelenay, ECS Transactions, Honolulu, HI, October 12 - October 17, 2008, 2008.

[102] G. Wu, K. Artyushkova, M. Ferrandon, A.J. Kropf, D. Myers, P. Zelenay, ECS Transactions, Vienna, Austria, October 4 - October 9, 2009, 2009.

[103] A. Serov, K. Artyushkova, P. Atanassov, Adv. Energy Mater. 4 (2014) 1301735.

[104] Y.-C. Wang, Y.-J. Lai, L. Song, Z.-Y. Zhou, J.-G. Liu, Q. Wang, X.-D. Yang, C. Chen, W. Shi, Y.-P. Zheng, M. Rauf, S.-G. Sun, Angewandte Chemie (International ed. in English) 54 (2015) 9907–9910.

[105] C. Zhang, Y.-C. Wang, B. An, R. Huang, C. Wang, Z. Zhou, W. Lin, Advanced materials (Deerfield Beach, Fla.) 29 (2017).

[106] D. Zhao, J.-L. Shui, C. Chen, X. Chen, B.M. Reprogle, D. Wang, D.-J. Liu, Chem. Sci. 3 (2012) 3200.

[107] J. Li, S. Ghoshal, W. Liang, M.-T. Sougrati, F. Jaouen, B. Halevi, S. McKinney, G. McCool, C. Ma, X. Yuan, Z.-F. Ma, S. Mukerjee, Q. Jia, Energy Environ. Sci. 9 (2016) 2418–2432.

[108] N.R. Sahraie, U.I. Kramm, J. Steinberg, Y. Zhang, A. Thomas, T. Reier, J.-P. Paraknowitsch, P. Strasser, Nature communications 6 (2015) 8618.

[109] M. Lefèvre, J.P. Dodelet, P. Bertrand, The journal of physical chemistry. B 104 (2000) 11238–11247.

[110] U.I. Kramm, A. Zana, T. Vosch, S. Fiechter, M. Arenz, D. Schmeißer, J Solid State Electrochem 20 (2016) 969–981.

[111] A. Serov, K. Artyushkova, E. Niangar, C. Wang, N. Dale, F. Jaouen, M.-T. Sougrati, Q. Jia, S. Mukerjee, P. Atanassov, Nano Energy 16 (2015) 293–300.

[112] H. Tributsch, U.I. Koslowski, I. Dorbandt, Electrochimica Acta 53 (2008) 2198–2209.

[113] N. Markovic, Surface Science Reports 45 (2002) 117–229.

[114] K. Gong, F. Du, Z. Xia, M. Durstock, L. Dai, Science (New York, N.Y.) 323 (2009) 760–764.

[115] G. Wu, H.T. Chung, M. Nelson, K. Artyushkova, K.L. More, C.M. Johnston, P. Zelenay, Boston, MA, October 9 - October 14, 2011, 2011.

[116] H.-W. Liang, X. Zhuang, S. Brüller, X. Feng, K. Müllen, Nature communications 5 (2014) 4973.

[117] J.C. Park, C.H. Choi, Journal of Power Sources 358 (2017) 76–84.

[118] B. Piela, T.S. Olson, P. Atanassov, P. Zelenay, Electrochimica Acta 55 (2010) 7615–7621.

[119] Q. Li, T. Wang, D. Havas, H. Zhang, P. Xu, J. Han, J. Cho, G. Wu, Advanced science (Weinheim, Baden-Wurttemberg, Germany) 3 (2016) 1600140.

[120] D. Papageorgopoulos, in 2015 Annual Merit Review Proceedings.

[121] M.K. Debe, DOE Hydrogen and Fuel Cells Program 2012 Annual Progress Report.

[122] T. Zhang, P. Wang, H. Chen, P. Pei, Applied Energy 223 (2018) 249–262.

[123] Y. Yu, H. Li, H. Wang, X.-Z. Yuan, G. Wang, M. Pan, Journal of Power Sources 205 (2012) 10–23.

[124] S.S. Kocha, in: K.-D. Kreuer (Ed.), Fuel Cells, Springer New York, New York, NY, 2013, pp. 473–518.

[125] A. Ohma, K. Shinohara, A. Iiyama, T. Yoshida, A. Daimaru, Boston, MA, October 9 - October 14, 2011, 2011.

[126] C.A. Reiser, L. Bregoli, T.W. Patterson, J.S. Yi, J.D. Yang, M.L. Perry, T.D. Jarvi, Electrochem. Solid-State Lett. 8 (2005) A273.

[127] J.C. Meier, C. Galeano, I. Katsounaros, A.A. Topalov, A. Kostka, F. Schüth, K.J.J. Mayrhofer, ACS Catal. 2 (2012) 832–843.

[128] I. Katsounaros, S. Cherevko, A.R. Zeradjanin, K.J.J. Mayrhofer, Angewandte Chemie (International ed. in English) 53 (2014) 102–121.

[129] E. Proietti, S. Ruggeri, J.-P. Dodelet, J. Electrochem. Soc. 155 (2008) S5.

[130] K. Kinoshita, in “Electrochemical oxygen technology”, John Wiley & Sons, Inc., New York (1992), pp. 19-29.

[131] A.B. Anderson, R.A. Sidik, The journal of physical chemistry. B 108 (2004) 5031–5035.

[132] E.S. Dy, T.A. Roman, Y. Kubota, K. Miyamoto, H. Kasai, Journal of Physics: Condensed Matter 19 (2007) 445010.

[133] P. Gouérec, A. Biloul, O. Contamin, G. Scarbeck, M. Savy, J. Riga, L.T. Weng, P. Bertrand, Journal of Electroanalytical Chemistry 422 (1997) 61–75.

[134] S. Baranton, C. Coutanceau, C. Roux, F. Hahn, J.-M. Léger, Journal of Electroanalytical Chemistry 577 (2005) 223–234.

[135] J. Herranz, F. Jaouen, M. Lefèvre, U.I. Kramm, E. Proietti, J.-P. Dodelet, P. Bogdanoff, S. Fiechter, I. Abs-Wurmbach, P. Bertrand, T.M. Arruda, S. Mukerjee, The journal of physical chemistry. C, Nanomaterials and interfaces 115 (2011).

[136] H. Schulenburg, S. Stankov, V. Schünemann, J. Radnik, I. Dorbandt, S. Fiechter, P. Bogdanoff, H. Tributsch, J. Phys. Chem. B 107 (2003) 9034–9041.

[137] C.H. Choi, C. Baldizzone, G. Polymeros, E. Pizzutilo, O. Kasian, A.K. Schuppert, N. Ranjbar Sahraie, M.-T. Sougrati, K.J.J. Mayrhofer, F. Jaouen, ACS Catal. 6 (2016) 3136–3146.

[138] J.A. Varnell, E.C.M. Tse, C.E. Schulz, T.T. Fister, R.T. Haasch, J. Timoshenko, A.I. Frenkel, A.A. Gewirth, Nature communications 7 (2016) 12582.

[139] R. Chenitz, U.I. Kramm, M. Lefèvre, V. Glibin, G. Zhang, S. Sun, J.-P. Dodelet, Energy Environ. Sci. 11 (2018) 365–382.

[140] V.P. Glibin, J.-P. Dodelet, J. Electrochem. Soc. 164 (2017) F948-F957.

[141] M.M. Mench, E.C. Kumbur, T.N. Veziroğlu, Polymer electrolyte fuel cell degradation, Academic Press, Amsterdam, Boston, 2012.

[142] U.I. Kramm, M. Lefèvre, N. Larouche, D. Schmeisser, J.-P. Dodelet, Journal of the American Chemical Society 136 (2014) 978–985.

[143] M. Ferrandon, X. Wang, A.J. Kropf, D.J. Myers, G. Wu, C.M. Johnston, P. Zelenay, Electrochimica Acta 110 (2013) 282–291.

[144] C.H. Choi, C. Baldizzone, J.-P. Grote, A.K. Schuppert, F. Jaouen, K.J.J. Mayrhofer, Angewandte Chemie (International ed. in English) 54 (2015) 12753–12757.

[145] T. Schilling, M. Bron, Electrochimica Acta 53 (2008) 5379–5385.

[146] J.-Y. Choi, D. Higgins, Z. Chen, J. Electrochem. Soc. 159 (2012) B87.

[147] F. Charreteur, F. Jaouen, J.-P. Dodelet, Electrochimica Acta 54 (2009) 6622–6630.

[148] I. Herrmann, U.I. Kramm, J. Radnik, S. Fiechter, P. Bogdanoff, J. Electrochem. Soc. 156 (2009) B1283.

[149] F. Jaouen, J.-P. Dodelet, The journal of physical chemistry. C, Nanomaterials and interfaces 113 (2009) 15422–15432.

[150] L. Gubler, S.M. Dockheer, W.H. Koppenol, J. Electrochem. Soc. 158 (2011) B755.

[151] M. Bron, S. Fiechter, P. Bogdanoff, H. Tributsch, Fuel Cells 2 (2002) 137–142.

[152] Y. Shao, S. Zhang, C. Wang, Z. Nie, J. Liu, Y. Wang, Y. Lin, Journal of Power Sources 195 (2010) 4600–4605.

[153] H.-J. Zhang, Q.-Z. Jiang, L. Sun, X. Yuan, Z. Shao, Z.-F. Ma, International Journal of Hydrogen Energy 35 (2010) 8295–8302.

[154] R. Borup, J. Meyers, B. Pivovar, Y.S. Kim, R. Mukundan, N. Garland, D. Myers, M. Wilson, F. Garzon, D. Wood, P. Zelenay, K. More, K. Stroh, T. Zawodzinski, J. Boncella, J.E. McGrath, M. Inaba, K. Miyatake, M. Hori, K. Ota, Z. Ogumi, S. Miyata, A. Nishikata, Z. Siroma, Y. Uchimoto, K. Yasuda, K.-I. Kimijima, N. Iwashita, Chemical reviews 107 (2007) 3904–3951.

[155] J.-Y. Choi, L. Yang, T. Kishimoto, X. Fu, S. Ye, Z. Chen, D. Banham, Energy Environ. Sci. 10 (2017) 296–305.

[156] D. Banham, T. Kishimoto, Y. Zhou, T. Sato, K. Bai, J.-I. Ozaki, Y. Imashiro, S. Ye, Science advances 4 (2018) eaar7180.

[157] D. Banham, S. Ye, K. Pei, J.-I. Ozaki, T. Kishimoto, Y. Imashiro, Journal of Power Sources 285 (2015) 334–348.

[158] V. Goellner, V. Armel, A. Zitolo, E. Fonda, F. Jaouen, J. Electrochem. Soc. 162 (2015) H403-H414.

[159] M. Lefèvre, J.-P. Dodelet, Electrochimica Acta 48 (2003) 2749–2760.

[160] G. Zhang, R. Chenitz, M. Lefèvre, S. Sun, J.-P. Dodelet, Nano Energy 29 (2016) 111–125.

[161] U.I. Kramm, I. Herrmann-Geppert, P. Bogdanoff, S. Fiechter, The journal of physical chemistry. C, Nanomaterials and interfaces 115 (2011) 23417–23427.

[162] L. Yang, N. Larouche, R. Chenitz, G. Zhang, M. Lefèvre, J.-P. Dodelet, Electrochimica Acta 159 (2015) 184–197.

[163] W. Kiciński, B. Dembinska, M. Norek, B. Budner, M. Polański, P.J. Kulesza, S. Dyjak, Carbon 116 (2017) 655–669.

[164] C.H. Hamann, A. Hamnett, W. Vielstich, Electrochemistry, 2nd ed., Wiley-VCH; [Chichester John Wiley, Weinheim, 2007.

[165] A.J. Bard, L.R. Faulkner, Electrochemical methods: Fundamentals and applications / Allen J. Bard, Larry R. Faulkner, 2nd ed., John Wiley, New York, Chichester, 2000.

[166] J. Chlistunoff, The journal of physical chemistry. C, Nanomaterials and interfaces 115 (2011) 6496–6507.

[167] N. Ramaswamy, U. Tylus, Q. Jia, S. Mukerjee, Journal of the American Chemical Society 135 (2013) 15443–15449.

[168] K. Kinoshita, J.A.S. Bett, Carbon 11 (1973) 403–411.

[169] S. Brunauer, P.H. Emmett, E. Teller, Journal of the American Chemical Society 60 (1938) 309–319.

[170] M.D. Donohue, G.L. Aranovich, Advances in Colloid and Interface Science 76-77 (1998) 137–152.

[171] I. Herrmann, U.I. Kramm, S. Fiechter, P. Bogdanoff, Electrochimica Acta 54 (2009) 4275–4287.

[172] F. Jaouen, M. Lefèvre, J.-P. Dodelet, M. Cai, J. Phys. Chem. B 110 (2006) 5553–5558.

[173] D.B. Williams, C.B. Carter, Transmission Electron Microscopy, Springer US, Boston, MA, 2009.

[174] S. Dimovski, A. Nikitin, H. Ye, Y. Gogotsi, J. Mater. Chem. 14 (2004) 238.

[175] J.F. Watts, J. Wolstenholme, An introduction to surface analysis by XPS and AES, J. Wiley, New York, Chichester, 2003.

[176] S. Hüfner, Photoelectron Spectroscopy: Principles and Applications, Springer, Berlin, Heidelberg, 2003.

[177] U. I. Kramm, Spectroscopic Analysis of Nanocarbon-Based non-precious Metal Catalyst for ORR. In Nanocarbons for Advanced Energy Conversion, (2015) X. Feng (Ed.).

[178] P. Gütlich, Z. anorg. allg. Chem. 638 (2012) 15–43.

[179] N.N. Greenwood, T.C. Gibb, Mössbauer Spectroscopy, Springer Netherlands, Dordrecht, 1971.

[180] McMillan, Paul F.,Hofmeister, Anne, Reviews in Mineralogy and Geochemistry 18 (1988) 99–159.

[181] E. Smith, G. Dent (Eds.), Modern Raman Spectroscopy - A Practical Approach, John Wiley & Sons, Ltd, Chichester, UK, 2004.

[182] J. Robertson, Materials Science and Engineering: R: Reports 37 (2002) 129–281.

[183] F. Tuinstra, J.L. Koenig, The Journal of Chemical Physics 53 (1970) 1126–1130.

[184] M.A. Pimenta, G. Dresselhaus, M.S. Dresselhaus, L.G. Cançado, A. Jorio, R. Saito, Physical chemistry chemical physics PCCP 9 (2007) 1276–1291.

[185] A. Sadezky, H. Muckenhuber, H. Grothe, R. Niessner, U. Pöschl, Carbon 43 (2005) 1731–1742.

[186] N. Larouche, B.L. Stansfield, Carbon 48 (2010) 620–629.

[187] A.C. Ferrari, J. Robertson, Phys. Rev. B 61 (2000) 14095–14107.

[188] Y. Wang, D.C. Alsmeyer, R.L. McCreery, Chem. Mater. 2 (1990) 557–563.

[189] Z. Chen, Y. Zhou, Y. Li, J. Liu, Z. Zou, Progress in Natural Science: Materials International 27 (2017) 452–459.

[190] M. Ghazinejad, S. Holmberg, O. Pilloni, L. Oropeza-Ramos, M. Madou, Sci Rep 7 (2017) 16551.

[191] X. Cheng, L. Zhang, L. Chen, Y. Zhang, Q. Fan, San Francisco, CA, May 24 - May 29, 2009, 2009.

[192] P.Bogdanoff, I. Herrmann, M. Hilgendorff, I. Dorbandt, S. Fiechter, H. Tributsch, Journal of new materials for electrochemical systems 7 (2004) 85–92.

[193] S. Gupta, S. Zhao, O. Ogoke, Y. Lin, H. Xu, G. Wu, ChemSusChem 10 (2017) 774–785.

[194] M. Ramsteiner, J. Wagner, Appl. Phys. Lett. 51 (1987) 1355–1357.

[195] C.A. Melendres, J. Phys. Chem. 84 (1980) 1936–1939.

[196] I. V. Aleksandkov, Y. S. Bobovich, Opt. Spectrosc. (Engl.Trans/.), 37 (1974).

[197] C. de Silva, K. Czarnecki, M.D. Ryan, Inorganica Chimica Acta 287 (1999) 21–26.

[198] M. Aydin, Vibrational Spectroscopy 68 (2013) 141–152.

[199] I. Herrmann, U.I. Kramm, S. Fiechter, V. Brüser, H. Kersten, P. Bogdanoff, Plasma Processes Polym. 7 (2010) 515–526.

[200] F. Jaouen, F. Charreteur, J.P. Dodelet, J. Electrochem. Soc. 153 (2006) A689.

[201] B. Hammer, J.K. Nørskov, in: B.C. Gates, H. Knözinger (Eds.), Impact of surface science on catalysis, Academic, San Diego, Calif., London, 2000, pp. 71–129.

[202] A. Nilsson, L. Pettersson, J.K. Nørskov, Chemical bonding at surfaces and interfaces, Elsevier Science, Place of publication not identified, 2011.

[203] B. Hammer, J.K. Norskov, Nature 376 (1995) 238–240.

[204] H.T. Chung, J.H. Won, P. Zelenay, Nature communications 4 (2013) 1922.

[205] R.J. Nemanich, S.A. Solin, Phys. Rev. B 20 (1979) 392–401.

[206] T. Jawhari, A. Roid, J. Casado, Carbon 33 (1995) 1561–1565.

[207] I. Martinaiou, A. Shahraei, F. Grimm, H. Zhang, C. Wittich, S. Klemenz, S.J. Dolique, H.-J. Kleebe, R.W. Stark, U.I. Kramm, Electrochimica Acta 243 (2017) 183–196.

[208] H.J. Grabke, D. Moszynski, E.M. Müller-Lorenz, A. Schneider, Surf. Interface Anal. 34 (2002) 369–374.

[209] J. Blomquist, H. Lång, R. Larsson, A. Widelöv, J. Chem. Soc., Faraday Trans. 88 (1992) 2007–2011.

[210] R. Taube, Pure and Applied Chemistry 38 (1974) 427–438.

[211] E. Fluck, W. Kerler, W. Neuwirth, Angew. Chem. Int. Ed. Engl. 2 (1963) 277–287.

[212] M.J. Workman, M. Dzara, C. Ngo, S. Pylypenko, A. Serov, S. McKinney, J. Gordon, P. Atanassov, K. Artyushkova, Journal of Power Sources 348 (2017) 30–39.

[213] A. Janßen, I. Martinaiou, S. Wagner, N. Weidler, A. Shahraei, U.I. Kramm, Hyperfine Interact 239 (2018) 629.

[214] M.T. Sougrati, V. Goellner, A.K. Schuppert, L. Stievano, F. Jaouen, Catalysis Today 262 (2016) 110–120.

[215] I. Martinaiou, T. Wolker, A. Shahraei, G.-R. Zhang, A. Janßen, S. Wagner, N. Weidler, R.W. Stark, B.J.M. Etzold, U.I. Kramm, Journal of Power Sources 375 (2018) 222–232.

Curriculum Vitae Martinaiou Ioanna

WORK EXPERIENCE

December 2014 – April 2015	Globe Williams,Operations

EDUCATION AND TRAINING

June 2015-currently	PhD candidate Title: Degradation studies of Me-N-C catalysts for the Oxygen Reduction Reaction in Fuel Cells.Supervisor: Ulrike I. Kramm Darmstadt Graduate School of Excellence Energy Science and Engineering, Darmstadt, Germany
2014	Diploma in Chemical Engineering, Department of Chemical Engineering, University of Patras, Greece Direction: Process Engineering and Environment

RESEARCH AND TEACHING EXPERIENCE

October 2015-currently	Graduate Teaching Assistant, Exercises Chemistry for Energy Scientists and Engineers, Master program
October 2015-currently	Graduate Teaching Assistant, Exercises Electrochemistry , Department of Chemistry, Master program
October2017-November 2017	Funded scholarship for an international research stay. Project: Investigating the durability performance of a non noble cathode catalyst operating in DMFC. Supervisor: Stefania Specchia Department of Materials Science and Chemical Engineering, Politecnico di Torino, Torino, Italy
January 2017	Accepted proposal with high evaluation in Bessy Synchrotron, Helmholtz Zentrum Berlin. Project: Investigation of catalysts degradation during Accelerated Stress Tests under oxygen reduction conditions via in situ XANES and EXAFS measurements. Proposer: Ioanna Martinaiou, Ulrike I. Kramm
February2010-June 2010	Diploma Thesis, Electrochemistry Laboratory, Helmholtz Institute for Materials and Energy Title: New Preparation Approaches to obtain Fe/N/C-catalysts for the Oxygen Reduction Reaction in Polymer-Electrolyte-Membrane Fuel Cells (PEM-FC) Supervisor: Koutsoukos Petros, Kramm I. Ulrike
August2009-October 2009	Participation in summer student program of Helmholtz Institute for Materials and Energy. Electrochemistry Laboratory Project title: Influence of the pyrolysis temperature on the turn over frequency of porphyrin-based electrocatalysts.

PUBLICATIONS

Metall-N-C- Katalysatoren in der Elektrokatalyse
Article, November 2017, Nachrichten aus der Chemie 65(11):1096-1099
Ulrike I. Kramm, Ali Shahraei, **Ioanna Martinaiou**

Effect of rf-Plasma Treatment on the Activity and Selectivity of Me-N-C Electrocatalysts for the Oxygen Reduction Reaction
Conference paper, October 2017, ECS Transactions 80(8)
Natascha Weidler, Deepu J. Babu, **Ioanna Martinaiou** [...] Ulrike I. Kramm

Improved electrochemical performance of Fe-N-C catalysts through ionic liquid modification in alkaline media
Journal of Power Sources, (2018), 375, 222
Ioanna Martinaiou, Thomas Wolker, Ali Shahraei [...] Ulrike I. Kramm

Elucidating the Origin of HER Activity in Mono- and Bimetallic Metal- and Nitrogen-doped Carbon Catalysts (Me-N-C)
ACS Applied Materials & Interfaces,(2017), 9, 25184
Ali Shahraei, Ashkan Moradabadi, **Ioanna Martinaiou** [...]Ulrike I. Kramm

Effect of metal species on the stability of Me-N-C catalysts during accelerated stress tests mimicking the start-up and shut-down conditions
Special Issue Electrochimica Acta, (2017) 243,183
Ioanna Martinaiou, Ali Shahraei, Fabian Grimm [...]Ulrike I. Kramm

Effect of Sulfite Ions on the Structural Composition and ORR Activity of Fe-N- C Catalysts
Hyperfine Interactions, (2018), 239, 1
Stephan Wagner, **Ioanna Martinaiou**, Ali Shahraei [...] Ulrike I. Kramm

Influence of sulfur in the precursor mixture on the structural composition of Fe-N-C catalysts
Hyperfine Interactions, (2018), 239, 7
Arne Janßen, **Ioanna Martinaiou**, Stephan Wagner, [...] Ulrike I. Kramm

CONFERENCE PRESENTATIONS

Influence of the structural composition on the activity and stability of Me-N-C catalysts,
Ioanna Martinaiou, Fabian Grimm, Andreas Huber, Dieter Schmeisser, Ulrike I. Kramm
Electrolysis and Fuel Cell Discussions 2015-Challenges Towards Zero Platinum for Oxygen Reduction, La Grande Motte, France 13-15 September 2015

Forschungsgruppe Katalysatoren und Elektrokatalysatoren
Nina Erini, Ioanna Martinaiou, Ali Shahraei, Ulrike I. Kramm
Energie Konferenz, Darmstadt, Germany 03 March 2016

Correlating the structural characterization and stability of Me-N-C catalysts during accelerated stress tests.
Ioanna Martinaiou, Ali Shahraei, Fabian Grimm [...]Ulrike I. Kramm
49. Jahrestreffen Deutscher Katalytiker, Weimar, Germany 16-18 March 2016

Influence of metal species on the stability of Me-N-C catalysts during accelerated stress tests mimicking the start-up and shut-down conditions
Ioanna Martinaiou, Ali Shahraei, Fabian Grimm [...]Ulrike I. Kramm
67th Annual Meeting of the International Society of Electrochemistry, The Hague, 22-26 August 2016

Correlating the structural characterization and stability of Me-N-C catalysts during accelerated stress tests.
Ioanna Martinaiou, Ali Shahraei, Fabian Grimm [...]Ulrike I. Kramm
Electrochemistry 2016, Goslar, Germany, 26-28 September